



THÈSE DE DOCTORAT DE L'ÉTABLISSEMENT UNIVERSITÉ BOURGOGNE FRANCHE-COMTÉ
PRÉPARÉE AU LABORATOIRE INTERDISCIPLINAIRE CARNOT DE BOURGOGNE

École doctorale n°553

Carnot Pasteur

Doctorat de Physique

Par

Mme Saharyan Astghik

Modèles effectifs pour l'optique quantique à photon unique

Thèse à présenter et à soutenir, le 19 Février 2024, en salle D115

Composition du Jury :

M. JAUSLIN Hans-Rudolf	Professeur, Laboratoire ICB, Université de Bourgogne, France	Président
M. GARRAWAY Barry	Professeur, University of Sussex, Royaume-Uni	Rapporteur
M. KELLER Arne	Professeur, Université Paris-Saclay, France	Rapporteur
M. KUHN Axel	Professeur, University of Oxford, Royaume-Uni	Examineur
M. CHEN Xi	Chargé de recherche, University of the Basque Country, Espagne	Examineur
Mme. GOGYAN Anahit	Chargée de recherche, Institute for Physical Research, Arménie	Examinatrice
M. GUÉRIN Stéphane	Professeur, Laboratoire ICB, Université de Bourgogne, France	Directeur de thèse

Effective models for single-photon quantum optics

by

Astghik Saharyan

February, 2024

*PhD THESIS FROM UNIVERSITE DE BOURGOGNE
PREPARED IN LABORATOIRE INTERDISCIPLINAIRE
CARNOT DE BOURGOGNE*

Committee in charge:

M. JAUSLIN Hans-Rudolf	Professor, Laboratoire ICB, Université de Bourgogne, France	President
M. GARRAWAY Barry	Professor, University of Sussex, UK	Referee
M. KELLER Arne	Professor, Université Paris-Saclay, France	Referee
M. KUHN Axel	Professor, University of Oxford, UK	Examiner
M. CHEN Xi	Researcher, University of the Basque Country, Spain	Examiner
Mme. GOGYAN Anahit	Researcher, Institute for Physical Research, Armenia	Examiner
M. GUÉRIN Stéphane	Professor, Laboratoire ICB, Université de Bourgogne, France	Thesis supervisor

Résumé

Au cours des dernières décennies, l'optique quantique a évolué des cavités à facteur de qualité élevé des premières expériences vers de nouvelles conceptions de cavités impliquant des modes à fuite. Bien que les modèles utilisés dans des expériences standard soient efficaces pour reproduire ces expériences, les fuites de photons sont la plupart du temps traitées de manière phénoménologique ce qui limite l'interprétation des résultats et ne permet pas une étude systématique. Dans ce manuscrit, nous adoptons une approche différente et, à partir des premiers principes, nous dérivons des modèles effectifs qui permettent la caractérisation complète d'un photon unique produit dans la cavité et se propageant dans l'espace libre. Nous proposons un schéma atome-cavité pour la génération de photons uniques et analysons rigoureusement le photon unique sortant dans les domaines temporel et fréquentiel pour différents régimes de couplage. Nous étendons l'analyse en étudiant des modèles de cavités plus réalistes, prenant notamment en compte la structure diélectrique multicouche des miroirs de la cavité. Nous évaluons la force du couplage dipolaire entre un seul émetteur et le champ de rayonnement dans une telle cavité optique. Notre modèle permet de faire varier librement la fréquence de résonance de la cavité, la fréquence de la transition lumineuse ou atomique, ainsi que la longueur d'onde associée à la mise en forme du miroir diélectrique. En particulier, nous montrons qu'en raison des effets induits par la nature multicouche du miroir de la cavité, même dans le régime de cavité haute finesse tel que défini habituellement, la description du système cavité-réservoir peut différer de celle où la structure du miroir est négligée. Pour les cavités très courtes, la longueur effective utilisée pour déterminer le volume du mode de la cavité et les longueurs définissant les résonances sont différentes, et diffèrent notablement de la longueur géométrique de la cavité. Ce n'est que pour des cavités beaucoup plus longues que leur longueur d'onde de résonance que le volume du mode se rapproche asymptotiquement de celui normalement supposé à partir de leur longueur géométrique. Sur la base de ces résultats, nous définissons une fonction de réponse généralisée de la cavité et une fonction de couplage cavité-réservoir, qui tiennent compte de la structure géométrique du miroir de la cavité. Cela nous permet de définir une réflectivité effective pour la cavité avec un miroir multicouche comme si elle avait une structure négligeable. Nous estimons l'erreur d'une telle définition en considérant des cavités de différentes longueurs et structures de miroir. Enfin, nous appliquons ce modèle pour caractériser un photon unique produit dans une telle cavité et se propageant à l'extérieur dans l'espace libre.

Abstract

Over the last decades, quantum optics has evolved from high-quality-factor cavities in the early experiments toward new cavity designs involving leaky modes. Despite efficient models to describe standard experiments, photon leakage is most of the time treated phenomenologically, which restricts the interpretation of the results and does not allow systematic studies. In this manuscript, we take a different approach, and starting from first principles, we derive effective models that allow complete characterization of a leaking single photon produced in the cavity and propagating in free space. We propose an atom-cavity scheme for single-photon generation, and we rigorously analyze the outgoing single photon in time and frequency domains for different coupling regimes. We extend the analysis by studying more realistic cavity models, namely taking into account the multilayer dielectric structure of cavity mirrors. We evaluate the dipole coupling strength between a single emitter and the radiation field within such an optical cavity. Our model allows one to freely vary the resonance frequency of the cavity, the frequency of light or atomic transition addressing it, and the design wavelength of the dielectric mirror. In particular, we show that due to the effects induced by the multilayer nature of the cavity mirror, even in the standardly defined high-finesse cavity regime, the cavity-reservoir system description might differ from the one where the structure of the mirror is neglected. For very short cavities, the effective length used to determine the cavity mode volume and the lengths defining the resonances are different, and also found to diverge appreciably from the geometric length of the cavity. Only for cavities much longer than their resonant wavelength does the mode volume asymptotically approach that normally assumed from their geometric length. Based on these results, we define a generalized cavity response function and cavity-reservoir coupling function, which account for the geometric structure of the cavity mirror. This allows us to define an effective reflectivity for the cavity with a multilayer mirror as if it had a negligible structure. We estimate the error of such a definition by considering cavities of different lengths and mirror structures. Finally, we apply this model to characterize a single photon produced in such a cavity and propagating outside in free space.

Acknowledgements

Words cannot express my gratitude to my supervisor Prof. Stéphane Guérin who always had confidence in my abilities even when I did not believe in myself. You gave me the opportunity of a lifetime that opened doors I never thought possible, your continuous encouragement and patience has kept my spirits and motivation high during this challenging process. Our inspiring discussions have shaped my academic and personal growth, and for this I will be forever grateful.

Thanks should also go to the ITN LIMQUET that financed my research and the amazing people I met there. Being part of this project was a unique and invaluable experience. I am deeply indebted to Prof. Axel Kuhn for being so welcoming during my secondment in Oxford, and for the opportunities and continuous support he has provided me throughout our collaboration. Working with you and the time spent in your group was one of the most rewarding experiences of my PhD. Special thanks to Juan-Rafael Álvarez for the stimulating academic exchange and much more. I would also like to extend my gratitude to Prof. Hans R. Jauslin, who generously shared his knowledge and expertise to help in advancing my research project. Big thanks to Maxime Federico for reading my manuscript with great diligence and for offering helpful comments.

I would like to express my deepest appreciation to my committee members: Prof. Barry Garraway, Prof. Arne Keller, Prof. Axel Kuhn, Dr. Xi Chen, Dr. Anahit Gogyan, and Prof. Hans R. Jauslin for their time and effort, I am honored to have your insight on my thesis work.

I can not stress enough how thankful I am for my exceptional labmates who became my family in Dijon. Being so far from my home and my family, I could not have made it to the end if it were not for them and all the great moments we shared in and outside the lab. I am extremely fortunate to have found a loving and caring friend such as Gohar: you helped me get through more than you know it. Special thanks should go to my officemates: Xavier, who has been there for me since the day I joined the group and made it so much easier to become a part of our wonderful community in the lab; Rodolphe, who, despite all my jokes, is still willing to be my good friend - I appreciate your friendship a lot, and Pierre, who is my office karaoke partner and supplier of the much-needed chocolate. Massive thanks to the rest of our gang, especially Maxime, Georgiy, Sigg, Colm and Benjamin. Friendship with all of you is one of the highlights of my PhD journey. I am also thankful to my friends Ani, Yeva, Feyva, and Lily, who, despite being far away, were always there for me and were willing to support me in any way they could. Special thanks to Lily and Vahan for introducing baby Emily into my life: playing with her was my anti-stress treatment during this stressful period. Thank you all for your friendship and for being a part of my life.

Last but not least, I am extremely grateful to my family, to whom I dedicate this thesis. Without their unconditional love and support, I would not be where I am now. Mom, thank you for your endless love and care, you have always looked out for me and made sure that I had no worries other than following my dreams. Dad, thanks for always having my back, you introduced me to the world of science and have always been my biggest inspiration. Your constant encouragement and support gave me the strength I needed in order not to give up. Special thanks to my sister Nvard, who has always been my biggest cheerleader. You always encouraged me to take risks, and without your push I would not have taken on this endeavor in the first place. You and Valeri have given me the greatest gift of my life - the joy of being an aunt to such a wonderful kid like Alex; he brings so much positivity and happiness into my life. Lastly, I am grateful to my younger brother Azat, who is the most special person in my life and who keeps me going in more ways than one. I want to express my sincere thanks to my extended family for always being there for me and for my parents, especially during the times when I could not be there for them. I am the luckiest person to have a family like you; I love you all so much. I would also like to dedicate this work to the memory of my aunt Nano - you gave me so much love and care since the day I was born and were by my side through all my ups and downs, I am sorry for not being there for you when you needed it the most.

List of Publications

Astghik Saharyan, Juan-Rafael Álvarez, Axel Kuhn, and Stéphane Guérin. Effective models for quantum optics with multilayer open cavities. *to be submitted*

A. Saharyan, B. Rousseaux, Z. Kis, S. Stryzhenko, and S. Guérin. Propagating single photons from an open cavity: Description from universal quantization. *Phys. Rev. Res.*, 5:033056, Jul 2023

Astghik Saharyan, Juan-Rafael Álvarez, Thomas H. Doherty, Axel Kuhn, and Stéphane Guérin. Light-matter interaction in open cavities with dielectric stacks. *Applied Physics Letters*, 118(15):154002, 2021

Gian Luca Giorgi, Astghik Saharyan, Stéphane Guérin, Dominique Sugny, and Bruno Bellomo. Microscopic and phenomenological models of driven systems in structured reservoirs. *Phys. Rev. A*, 101:012122, Jan 2020

Table of Contents

Résumé	iii
Abstract	v
Acknowledgements	vii
List of Publications	ix
Table of Contents	xi
I Introduction	1
1 Quantum technologies: Opportunities and challenges	3
1.1 Quantum information processing	7
1.2 Photonic quantum computing	9
1.3 Quantum nanophotonics: plasmonics and single plasmons	13
1.4 Driven open quantum systems	14
2 Cavity QED Approaches to Quantum Information Processing	17
II Propagating single photons from an open cavity	23
3 Introduction	25
3.1 Electromagnetic field: from classical to quantum description	26
3.2 Open cavity with a single-layered dielectric mirror: the true modes	28
4 Production of a single photon from a trapped atom	33
4.1 Derivation of the model	34
4.2 Heisenberg-Langevin equations, Poynting vector, photon density, and photon flux	43
5 Single photon shaping	51
5.1 The model	51
5.2 The scheme for a large detuning	53
Summary	57
APPENDIX A	58
A.1 Quantization of the electromagnetic field	59

A.2	Boundary conditions for a cavity with a single-layered dielectric mirror	63
A.3	Lorentzian structure of cavity response function	64
A.4	Input-output relation with the use of a Dirac delta distribution .	65
A.5	Derivation of the pseudomode representation	67
A.6	Discretization of the continuous integrals	70
A.7	Single photon spatial distribution	71
A.8	Evaluation of the integral (4.68b)	73
A.9	Derivation of the master equation	75
 III Light-matter interaction in open cavities with dielectric stacks		77
6	Cavities with multilayer dielectric stacks	79
6.1	The model	80
6.2	Effective cavity response function	81
6.3	Trapped atom interacting with a multilayer cavity	84
7	Effective models for multilayer cavity dynamics	87
7.1	True-mode representation for a multilayer cavity	88
7.2	Inside-outside representation	91
7.3	Cavity-reservoir coupling function	93
7.4	Numerical verification of the inside-outside representation	97
 Summary		103
 APPENDIX B		104
B.1	Effective single-layered cavity response function	105
B.2	Discrete cavity modes in terms of to the true modes	107
B.3	Continuous reservoir modes in terms of the true modes	108
B.4	Coefficients relating the true modes to the inside-outside modes .	110
B.5	Commutation relation for the separated modes	111
B.6	Hamiltonian representation	113
 IV Conclusion and perspectives		117
 APPENDIX C		120
C.1	Microscopic and phenomenological models of driven systems in structured reservoirs	121
C.2	Discussion and conclusions	130
C.3	Derivation of the microscopic master equation	131
 Bibliography		135

Part I
Introduction

Quantum technologies: Opportunities and challenges

Nothing in life is to be feared, it is only to be understood. Now is the time to understand more, so that we may fear less.

Marie Curie

Ever since the idea of using the properties of quantum physics in developing quantum technologies, there have been significant advancements in the field, starting from the Nobel Prize award-winning discoveries (1997: Steven Chu, Claude Cohen-Tannoudji, William D. Phillips; 2001: Eric Cornell, Wolfgang Ketterle, Carl E. Wieman; 2005: John L. Hall, Theodor W. Hänsch, Roy J. Glauber; 2012: Serge Haroche, David J. Wineland, 2022: Alain Aspect, John F. Clauser, Anton Zeilinger) to the first prototypes of a quantum computer (2018: the 72-qubit processor built by Google, 2021: 433-qubit processor by IBM). The word *quantum* already indicates that, unlike classical computers, quantum computers rely on the laws of quantum physics. Quantum features such as superposition and entanglement allow the quantum computer to approach problems very differently - essentially attacking them simultaneously rather than sequentially. This ability of quantum computers to effectively explore thousands of combinations in parallel leads to dramatic increases in speed when solving certain classes of problems. These problems include some of society's most pressing issues, such as geophysical analysis, weather and financial forecasting, chemical and materials science, pharmaceutical drug discovery and enhanced security. This potential impact of quantum computers has attracted worldwide interest in developing quantum technologies contributing to the rapid development of the field at the fundamental as well as at the industrial level.

The invention of the quantum computer plays a particularly significant role in the security of our information-based society. The long-term secure management of data is of the highest importance for society and the economy. Development of the quantum computer makes current data encryption protocols, which are based

on math, vulnerable and poses a threat to long-term security. Using advantages provided by quantum technologies, such as quantum random number generation and quantum key distribution, offers a way to overcome these vulnerabilities. Quantum encryption is currently being developed for the ultimate uncrackable and quantum-safe computing environment. The existing prototypes of quantum computers provide a test environment for experimentation and innovation with quantum algorithms. In particular, there have been major developments in cloud-based quantum computing, with available platforms such as Quandela Cloud by Quandela, Xanadu Quantum Cloud by Xanadu, IBM Quantum Experience by IBM, Quantum Inspire by Qutech, etc.

The discussion above highlights that quantum technologies have the potential to change our world beyond recognition. However far we may be from fully benefiting from the advent of quantum technologies, an important step toward it is the common understanding of the challenges and the goals of the field. The scientific community worldwide has provided us with the state of the art reviews and roadmaps toward reaching the ultimate goal [1, 4, 24, 73, 110, 140, 177, 193]. Following some of these summaries, here we separate the study of quantum technologies into four different categories: quantum communication, quantum computation, quantum simulation, and quantum metrology (see Fig. 1.1). The main results of this thesis contribute to the study of quantum information processing, which comprises two of the domains mentioned above: quantum communication and quantum computation. Thus, in the following, we briefly represent the study of quantum simulation and quantum metrology, while later mainly focusing on quantum information processing.

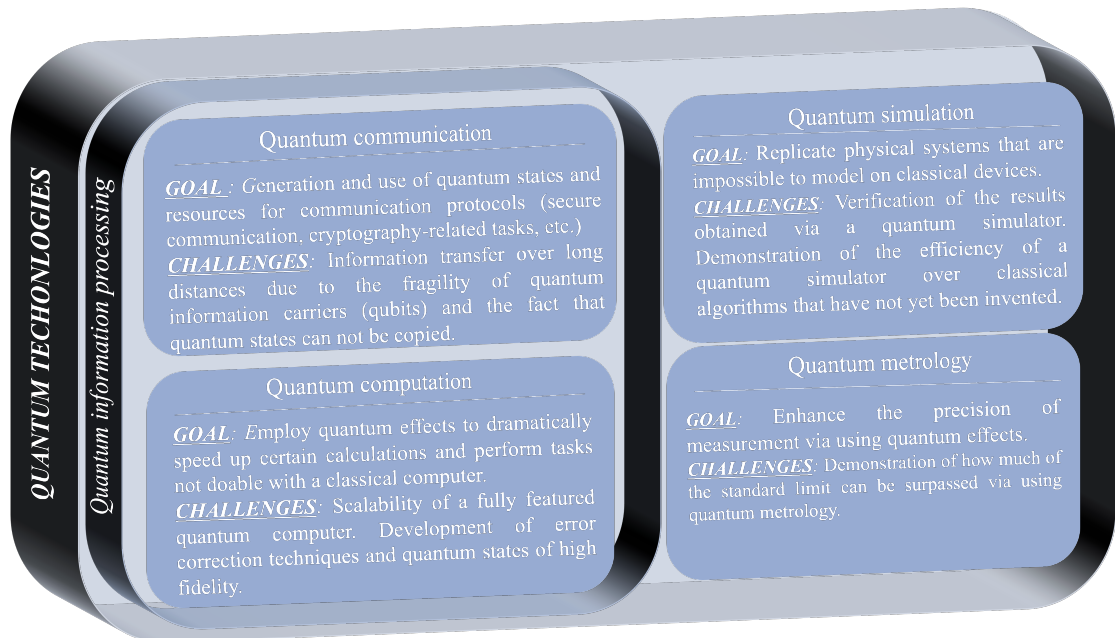


Figure 1.1: Different domains of the study of quantum technologies. While all these domains share common goals and challenges, here we highlight the most relevant ones for each of them.

Quantum simulation

Simulating models of the physical world is important in advancing scientific knowledge and developing technologies. The purpose of a simulator is to reveal information about another real system, i.e., we simulate an idealized model describing the system of interest. The fact that the simulator reveals features of an idealized model is less demanding than a full simulation of a real model since, typically, a simulated model attempts to capture only the most relevant properties of the real system of interest. There are numerous important questions to which simulations would provide answers but which remain beyond current technological capabilities [90]. These span a multitude of scientific research areas, from nuclear, atomic [206] and condensed matter physics [121] to molecular energies in chemistry [93, 128]. Here comes the idea of using a quantum device to mimic such systems that are impossible to model on a classical device [63, 90]. While building fully fledged universal quantum computer is difficult (if not impossible), it is possible to develop on the experimental advances made so far, a simulator that can imitate certain physically interesting systems that can not be simulated with classical computers [123]. The difference between a simulator and a computer can be defined by the accuracy level of the results provided. If the accuracy with which a device simulates a model can be arbitrarily controlled and guaranteed without the need to compare it to a real system, then that device can be called a computer. While a simulator is a part of a real system, that simulates an idealized model of it, that then has to be compared with the real system.

This potential of quantum simulators to simulate problems that can not be modelled on a classical device poses a question: how can one verify that the result of quantum simulation is correct? In other words, can one trust the results obtained with a quantum simulator, and under what conditions are they reliable to a known degree of uncertainty? An answer to this question, for instance, can be that the simulator could first be benchmarked with problems with known solutions. Alternatively, the results of simulations of different methods and systems could be compared. Apart from this reliability issue, real-world implementations of a quantum simulation will always face experimental imperfections, such as noise due to finite precision instruments and interactions with the environment. Can one predict in advance where the results of quantum simulators are more sensitive to errors? These and other important questions led to the notion that a successful quantum simulator has to satisfy a set of conditions [32, 84]: *relevance* – the simulated models should be of some relevance for applications and/or for research in the areas mentioned before, *controllability* – certain control of the parameters of the simulated model should be possible, *reliability* – one should be ensured that the observed physics of the simulation corresponds faithfully to the ideal model whose properties are of the interest, *efficiency* – it is expected that the quantum simulation should solve problems more efficiently than is practically possible with a classical simulation.

It is difficult to prove that a specific problem can not be simulated efficiently using classical computers, via algorithms that have not been yet invented, but is possible to simulate on a quantum simulator. The advantage of a quantum device is that the size of problems that can be tackled in a reasonable time grows significantly more quickly with the size of the simulating device than it does for a classical device, thus it is expected that quantum devices will one day be able to solve larger problems than

their classical counterparts. It is, however, possible that the experimental difficulty of scaling up quantum simulation hardware might cause an overhead such that a quantum device does not surpass the accuracy obtained by a classical algorithm [90].

Apart from all the challenges to build efficient quantum simulators, this emerging field of research harbours a number of interesting theoretical questions and promises to have a pivotal influence on tackling challenges of different research fields.

Quantum metrology

One of the essential processes of physical science is the measurement process. Originally, metrology focused on measurements using classical or semiclassical systems, such as mechanical systems described by classical physics or optical systems modelled by classical wave optics. Quantum metrology and sensing, on the other hand, deal with the measurement through the use of quantum effects that lead to some kind of enhancement, e.g., in precision, efficiency, or simplicity of implementation.

The goal of a measurement is to associate a value with a physical quantity, giving an estimate of it. The challenge is to achieve the highest precision in these estimations and find measurement schemes that reach that precision. The precision, however, can never reach 100% due to the errors of different natures: technical or fundamental. The technical ones are mostly represented by accidental errors caused by out-of-control imperfections in the measurement process. Conversely, there are fundamental limits on the uncertainty imposed by physical laws. In the classical measurement process, one can reduce errors by repeating the measurement and averaging the results. The central limit theorem implies that the reduction of the error is proportional to the square root of the number of repetitions. On the other hand, the exploitation of quantum systems to estimate unknown parameters overcomes the precision limits that can be, in principle, obtained by using only classical resources [44]. This idea is at the basis of the continuously growing research area of quantum metrology and sensing that aims at reaching the ultimate fundamental bounds on estimation precision by exploiting quantum probes [67]. The latest advancement in theoretical and experimental techniques have already led to measuring devices, such as the gravitational interferometer LIGO [2, 3] exceeding the classical limits. Nevertheless, in quantum metrology, there are still ultimate limits in precision described by Heisenberg-like uncertainty relations. Further theoretical study is needed to examine these limits in order to determine how close, in principle, one can get to the fundamental limits.

Besides the fundamental interest in ultimate precision limits, quantum metrology presents different applications. Different research branches can benefit from quantum - enhanced sensitivity, such as atomic clocks for synchronization purposes in data-center operations and navigation (GPS, GNSS) [17, 29, 102], plasmonic sensing for chemical and biological studies [118], microscopy and imaging [126, 141], etc. Different platforms that are used to implement quantum measurements involve measurements with trapped ions [119], interferometry with photons [53], and magnetometry with cold atomic ensembles [196]. Each of these fields faces different challenges, such as the fact that these systems experience losses during the implementation of the measurement process, which makes it difficult to experimentally demonstrate how close to the fundamental limit one can get. Nonetheless, there are already considerable improvements when using quantum features over classical ones,

and further development of theoretical and experimental techniques will lead to new methods to overcome these challenges and broaden the potential impact of this field.

1.1 Quantum information processing

In today's technologies, the manipulation of information is carried out using physical machines (computers, routers, scanners, etc.) which are governed by the laws of classical physics. Considering that the classical physics is a special limit of quantum physics, it leads to the natural question, why should the information processing be limited to classical physics. Motivated by such thoughts, Feynman [63] and others [41] pointed the way toward quantum computers. Looking at information processing from the quantum mechanical point of view allows the use of quantum features such as superposition and entanglement for applications that are not possible with classical devices. This offers the potential of improving information processing quantitatively, e.g., increase in computational power, as well as qualitatively such as quantum random number generation and quantum cryptography, which are not doable classically. It is not trivial to say how much one will gain by computing via quantum computer over classical one, as quantum information processors currently have only a limited number of known applications. For certain tasks there might be no advantage in choosing quantum computer over the classical one, while for others one can reach to exponential speed up, e.g., Shor's algorithm [172], where a quantum computer would be able to factor large numbers exponentially faster than any known classical computer algorithm [140].

According to Shannon [169], in classical computing, in order to quantify the information, a binary digit or bit is taken as the fundamental unit of information. Analogous to this, in quantum information processing the fundamental unit of information is the quantum bit or "qubit". Qubits are just quantum two-level systems such as the spin of an electron, the ground and excited states of an atom or the polarization of a photon, and, unlike classical bits, they can be prepared in a coherent superposition state [140]. This allows to store exponentially more information in qubits than in a comparable set of classical bits.

To implement quantum information processing, efficient and reliable state mapping between qubits and remote quantum devices is required. This interconnection is done using quantum as well as classical links, establishing the quantum internet. Quantum phenomena such as no-cloning, quantum measurement, entanglement and quantum teleportation, impose new challenging constraints for this network design. Specifically, classical network functionalities are based on the assumption that classical information can be safely read and copied [24]. However, this assumption does not hold in the case of quantum internet. Hence, the construction of a quantum network must carefully account for the constraints imposed by quantum nature, both in fundamental research as well as in engineering designs. To provide a better understanding of the advances in the field, in the following, we review some of the requirements and the proposed architectures for the realization of quantum information processing.

In his article [43], DiVincenzo provided a set of criteria that need to be satisfied for a successful realization of quantum computation. Those include:

1. *A scalable physical system with well characterized qubits.* This assumes having qubits with known physical parameters, as well as their interaction with each other and with the external fields, that are used to manipulate the state of qubits. Current architectures used to design such qubits include atom/ion traps, where individual atoms/ions are trapped in an ultra-high vacuum via applying controlled laser fields; superconductors, where superconducting circuits are used as qubits; diamonds, where the impurities of diamonds (NV centers) are used to trap single electrons; quantum dots, where individual electrons are trapped between the boundaries of different semiconductor materials. These architectures have been successfully realized for proof of principle, however establishing a scalable platform with these is still a major challenge.
2. *The ability to initialize the quantum system in a well-defined state.* This is a principal requirement for any type of computing; before the start of the computation, the system performing the computation algorithm should be in a known state. An example of an initial state can be the lowest energy state of the system, which, for some of the architectures described above, can be achieved via applying laser cooling techniques.
3. *Long relevant decoherence times.* Decoherence times characterize the dynamics of a quantum system in contact with its environment. Reading or writing operations with qubits for communication and computation purposes means interaction between the qubits and the environment, hence decoherence is unavoidable. Decoherence causes the loss of quantum properties, i.e., due to system-environment interaction, after some time (decoherence time) the quantum computer will not be so different from that of a classical machine. This puts a constraint on decoherence times; they should be long enough such that one can benefit from the quantum features of quantum computation. This raises a natural concern that depending on the duration of the computation required, there will be necessity of longer decoherence times. This is rectified via applying quantum error correction techniques [171, 178, 56], which require quantum repeaters to be placed periodically along the quantum network.
4. *A universal set of quantum gates.* Quantum gates act as unitary transformations applied on a small number of qubits. Unitary transformation implies that the process is reversible, i.e., the quantum system in principle should be perfectly isolated. However, not only the perfect isolation is not possible but, as mentioned above, it is also not desired when one wants to extract information from the quantum system. Hence, quantum gates can not be implemented perfectly; there are both systematic and random errors caused by imperfections and random fluctuations. These type of errors can be seen as another source of decoherence and thus error correction techniques can be effective for producing reliable computations from imperfect quantum operations. To characterize these imperfections the quantum fidelity is introduced as a fundamental figure of merit. The larger is the imperfection of the physical implementation of an arbitrary quantum operation, the lower is the fidelity.
5. *A qubit-specific measurement capability.* Extraction of information in a quantum computer is nontrivial. To extract the result of the computation, efficient measurements of specific qubits must be performed. This requires

strong and controllable interaction of the qubit with its environment, causing additional constraints on the hardware designs. Measurements on these kind of quantum systems can never be 100% efficient, however it is still possible to make reliable quantum computation with less measurement efficiency, via some tradeoff with other resources (e.g. implementing limited number of repeated measurements). For these tradeoffs to work, one should keep in mind the decoherence time of the system. If the time required to perform the measurement is faster than the decoherence time, then the error correction is more simplified.

6. *The ability to interconvert stationary and flying qubits.* Here there is a classification of two types of qubits: stationary qubits and flying qubits. This separation indicates that the qubits used to transfer information from place to place can be different from the qubits used for information processing/storing within a computing devices. Thus, there is a need of efficient interconnection of these flying and stationary qubits. Some of the examples introduced in point 1 are the main examples of stationary qubits, while for a flying qubit, as discussed in the following section, the state or the polarization of a photon is used.
7. *The ability to faithfully transmit flying qubits between specified locations.* Following the previous point, once there is a successful connection between the flying and the stationary qubits, the flying qubit now has to faithfully transfer the information to the distant stationary qubit, using classical, as well as quantum channels. One method is to simply move the qubits through space, similar to the transmission of classical bits with electrical currents. However, this can be very difficult in practice, especially over long distances, as it must be done without disturbing or measuring the qubit state. Quantum teleportation, discovered by Bennett [12], offers an alternative method of transmission without physical contact [140]. This, however, requires entangled qubits both in the sending and receiving ends.

Whichever channel one uses for the information transfer, they are going to be noisy, hence the degradation of quantum information will be unavoidable. This, again, will require quantum error correction to be implemented.

Having these criteria in mind, in the following, we focus on using the properties of photons as information carriers for quantum information processing.

1.2 Photonic quantum computing

Creating verified communication links capable of sharing and transmitting entanglement is essential for networking quantum computers and securing quantum communication [177]. As mentioned before, the aim of the flying qubits is to transport qubits out of the physical quantum devices through the network for conveying quantum information from the sender to the receiver. Photons are very attractive to be used for this purpose. The rationale for this choice lays in the advantages provided by photons: weak interaction with the environment (thus, reduced decoherence), easy control with standard optical components as well as high-speed

low-loss transmissions [24]. Photons can be used as flying qubits regardless of the local quantum system chosen for processing. Moreover, using photons as qubits in processing devices means that the interconversion between a stationary and a flying qubit can be skipped [177].

In long-distance entanglement distribution, regardless of the qubit chosen, there is a decay of the entanglement distribution rate as a function of the distance. Therefore, computing and networking tasks may need photons to be delayed or stored, so extra devices such as quantum memory and quantum repeater may sometimes be needed. A full-scale error-corrected universal quantum computer remains a challenging quest today in any quantum system [177]. One of the first demonstrations of the possible scalability of quantum processing was the scheme proposed by Knill, Laflamme, and Milburn [100], which inspired a push toward a universal quantum computer with photons. An important point is the use of a few photons, ideally a single photon, to benefit from quantum properties (otherwise leading to classical coherent states in the limit of a laser).

With all the advantages that photons offer, there are, however, some drawbacks too because of the fact that photons do not easily interact with each other or with the quantum systems in the limit of interest of a few photons. This gives rise to photon losses due to imperfect detection and the problem of photon generation techniques.

Deterministic generation of single photons

A photon is defined as an elementary excitation of a single mode of the quantized electromagnetic field [35, 52]. Photon's life in quantum computation starts with its generation and concludes with its detection. Both processes can not be perfectly implemented, but they can be efficient enough to provide reliable computing [177]. Advanced single-photon applications require high-performance sources that produce photons of high quality. The quality of the photons can be described by the following merits:

- **Single-photon purity:** quantifies to what extent an emitted pulse contains only one photon. The absence of any two-photon coincidence event signifies an ideal single-photon source [124].
- **Identical photons (most often referred to as photon indistinguishability):** quantifies to what extent the individual photons in a photon stream are identical. Two identical photons can increase the number of photons used simultaneously in an experiment.
- **Single-photon generation rate:** specifies the number of photons that can be created per second. The operation speed of the sources is ultimately limited by the radiative lifetime of the emitter.

High-quality photon states can be produced from sources such as trapped ions and atoms, color centers in diamonds, semiconductors and quantum dots. In experimental quantum optics spontaneous parametric down-conversion [23, 96] is widely used to produce photon pairs that are naturally entangled in polarization [112], transverse spatial modes [38], or frequency [111]. Nonetheless, the disorganized individual radiators of these sources, in general, produce nondeterministic, incoherent radiation.

We can expect them to produce single photons at random or uncorrelated crowds of photons. However, quantum computing requires that the photon generation is deterministic and operates at high generation probabilities [109]. Moreover, computing tasks require the capability of simultaneously generating a large number of such individual photon states [31, 122]. The obvious way to achieve this is to have a large number of deterministic sources that can simultaneously produce one and only one photon each at the push of a button [177]. Apart from all these requirements, single photons should be efficiently collected, such that they are not lost by absorption, scattering, diffraction, etc.

In this thesis, we focus on the creation of single photons from trapped atoms. In the simplest case of an atom with two energy levels, a photon is produced each time the atom decays from the upper energy state to the lower state. In free space, photons are emitted in all directions or into a continuum of optical modes. A useful source, however, creates photons in just one optical mode. To develop such a source, two approaches can be pursued, based on either cavities or waveguides. For tightly confined modes, the atom decays preferentially into a single mode in the cavity or waveguide. The collected photon can be subsequently coupled into a single-mode optical fiber to be transferred to a distant quantum node [19, 42, 124, 155].

Photon detection

One of the key enabling technology for long-distance quantum communication is the development of quantum repeaters [138, 165]. Quantum repeaters work by breaking the total communication distance into a series of shorter links [81, 99, 132, 184]. This process critically depends on the performance of both single-photon generation and single-photon detection, ensuring faithful information read-out [144]. At least one quantum repeater protocol has been developed that relies only on single-photon sources and single-photon detectors [7].

A single-photon detector is an extremely sensitive device capable of registering an absorbed increment of radiation energy [82]. An ideal photon detector clicks every time a photon hits it and immediately restarts its operation. It does not produce false positive signals when no real photons were detected (so-called “dark counts”) and it also tells exactly how many photons were detected in the same spatiotemporal mode [177]. While such an ideal photon detector does not exist, it is still possible to do quantum computing without having an ideal detector [175]. Nonetheless, improving the performance of the detector to very high levels is important for a realistic and scalable platform.

Existing photon detectors are characterized by the following parameters:

- **Detection efficiency:** This is a quantity that measures the sensitivity of a detector. Almost all single-photon detectors involve the conversion of a photon into an electrical signal of some sort. The overall conversion factor from photons to such detectable photoelectrons characterizes the detection efficiency.
- **Reset time:** This is the time between two consecutive detections, i.e, the time needed to restart the detector. This puts a limit on the detection rate marking that during this time no further detection is possible: photons that arrive during this interval will not be detected.

- **Detection time jitter:** This characterizes the uncertainty on the time delay between the photon arrival and the detector response. In other words, it describes the deviation between the photon absorption and the appearance of the change in the parameter of interest, being detected by the detector.
- **Dark count rate:** This is the average rate of registered counts without any incident light. The false detection events are mostly of thermal origin. Dark counts are characterized by their statistical properties. This rate also depends on the other parameters of the detector such as the efficiency and reset time.
- **Photon-number-resolving capabilities:** This characterizes the ability to distinguish the number of photons in an incident pulse. Conventional single-photon detectors are based on photomultipliers and avalanche photodiodes, which are not photon-number resolving and can only distinguish between zero photons and more than zero photons.

Over the past few decades, a number of techniques with sufficient sensitivity have been rapidly developed to detect single and few photons at room temperature, such as the use of avalanche photodiodes (APDs) [37], photomultiplier tubes (PMTs) [65], frequency up-conversion devices [91], quantum dot field-effect transistors (QD-FETs) [92], superconducting nanowire single-photon detectors (SNSPD) [75, 82] or single electron transistors [94]. However, combining the overall performance parameters of these techniques to reach the stringent requirements of optical quantum information applications remains a challenge.

Manipulating a photon

Controlled manipulation of single-photon states – in particular of their central frequency, their shape and polarization – is crucial for quantum information processing and especially for quantum internet [99]. The essential physical resource for enabling quantum information systems to outperform classical ones is quantum entanglement. Therefore, precise and accurate control of material and photonic qubits that provide the entanglement is necessary. Numerous optical techniques are available to alter characteristics of photons after they have been launched, and use those characteristics to encode quantum bits in them.

The ability to coherently modify the time and frequency shape of the produced single photon is of great importance when interfacing the flying and stationary qubits. For example, a quantum-memory element such as an atom, ion, or quantum dot typically emits a photon wavepacket with an exponentially decaying tail. For propagation in a fiber or for writing into a different memory, one may need to convert that shape into a Gaussian packet or an exponential packet with a decay or growth that differs from the original one, hence photon reshaping will be required. Several approaches for modifying the temporal profile of the single-photon emission have been proposed by temporally modulating the excitation or emission pulses of quantum emitters, e.g., the shaping of a produced photon via shaping the driving field [183, 190, 195, 199].

Photons that are created by transitions between discrete quantum states acquire a carrier frequency equal to the Bohr transition frequency. The creation procedure alters the envelope of the field but not its carrier frequency. However, various techniques can be used to shift the carrier frequency. For example, in optics, the

parameter to be varied is typically a medium's electronic susceptibility. If strong light fields cause the susceptibility to oscillate, then energy can be redistributed between optical modes of various frequencies [176]. When a photon undergoes frequency conversion, its shape may be altered as a result of changes in its spectral content and phase structure. However, this does not always have to be considered as a negative effect: as mentioned above, the reshaping of the photon can be necessary for qubit interfacing, hence this technique can also be used to alter the shape of the photon.

In addition to its central frequency and shape, a single-photon is characterized by its polarization. The advantage of polarization based qubit encoding is that modern electro-optic elements allow efficient polarization control, such as transparent materials that have suitable structure can rotate the direction of the electric vector in controllable ways. Two orthogonal polarization modes can easily be separated by means of using polarizing beam splitters and this can be used to create polarization-entangled Bell states [113, 146, 158].

The characteristic parameters of photons and manipulation techniques are not limited to those discussed here. As mentioned above, the techniques used to alter one of the parameters can lead to the modification of another. Thus, these techniques can be used to transfer information from one parameter to another.

1.3 Quantum nanophotonics: plasmonics and single plasmons

As discussed above, quantum information carriers and high-performance single-photon sources are essential in quantum computation. The emission of light by quantum emitters strongly depends on the environment in which they are placed, thus, it can be controlled by placing emitters in a designed resonator. While in this manuscript we primarily focus on the use of optical cavities to enhance light-matter interaction, there have been significant efforts in extending the concepts for optical cavities to the fields of nanophotonics and plasmonics [50, 194]. A major motivation to explore the nanoscale regime lies in the fact that the electric field scales inversely proportional to the volume in which the field is confined. Thus, at this scale, one can, in principle, achieve strong light-matter coupling that is not attainable with optical resonators. Such strong coupling opens up new opportunities for the quantum control of light and the exploration of nonlinear effects with very few photons [136, 208].

One way to achieve such light-matter coupling at the nanoscale is by placing an emitter next to a plasmonic structure. Plasmons are collective oscillations of free electrons localized at the surface of a metallic structure. Such structures are capable of confining light far below the diffraction limit. When interacting with an electromagnetic field, in metallic particles smaller than the wavelength of the field, the confinement of conduction electrons provides a restoring force that leads to oscillation of the electron cloud. The frequency of this oscillation is determined by the density of electrons, as well as the size and shape of the charge distribution. This phenomenon is known as a localized surface plasmon (LSP) resonance. Unlike LSPs which do not propagate, when interfacing a metallic film with a dielectric, charge oscillations can propagate along the metal-dielectric interface at frequencies below

the material plasmon resonance. These propagating surface plasmon polaritons (SPPs) have a well-defined propagation direction and they can be waveguided and manipulated like photons. Compared with a free-space photon of the same frequency, an SPP has greater spatial confinement. The ability to concentrate light to arbitrarily small dimensions opens the door to both strong coupling with quantum emitters and the prospect of designing integrated plasmonic devices and circuits, analogous to integrated photonics and electrical circuits [18, 21, 40].

In order to perform quantum optics with surface plasmons, a source of a single plasmon is needed. Such a source can be achieved by illuminating a metallic structure acting as a plasmon launcher with single photons [25, 58, 135]. One of the major challenges when realizing this scheme is the momentum mismatch between SPPs and free-space photons, which makes it difficult to couple into and out of SPP modes. Another challenge associated with plasmonic structures is that surface plasmons suffer from large intrinsic losses: the shorter the plasmon wavelength, the higher the loss. These losses in metallic systems limit propagation lengths for confined modes. For some applications, such as efficient generation of single SPPs, achieving low losses is essential; for others, the losses can be put to good use, e.g., when controlling the dissipative quantum dynamics [181, 197]. The promising features of plasmonic structures make them an attractive platform for quantum information processing. This, in turn, motivates the ongoing effort to gain a deeper understanding of such systems.

1.4 Driven open quantum systems

To successfully implement quantum computation related tasks, one should be able to efficiently manipulate and control the dynamical processes at the level of the quantum system under consideration. This is typically done by applying properly designed external electromagnetic fields that drive the quantum system into a desired target state. As discussed previously, the quantum systems are inherently influenced by the environment they are in contact with, giving rise to dissipation and decoherence [20, 69]. Thus, no quantum system can be considered completely isolated; they are open. Dissipative processes originating from the interaction with the environment could negatively influence the control protocols designed to manipulate the quantum system, hence, to efficiently benefit from the quantum features of the system, it is necessary to be able to accurately characterize the behaviour of the system, specifically by exploring the balance between control and interaction with the environment. Moreover, by properly engineering the characteristics of the environment, the dissipative dynamics can be strongly modified and tuned into a useful tool, e.g., to generate specific states [11, 105].

In the context of modeling open quantum systems, the description of such systems is often derived under certain approximations, such as the weak-coupling regime between the system and the environment (which is usually considered as a bosonic bath) known as Born approximation, and for memoryless dynamics with time-independent dissipation rates (Markovian approximation). Other common assumptions concern the absence of initial correlations between the system and its environment. An alternative route to take into account environmental effects relies on a phenomenological description of standard dissipative mechanisms, where the

dissipator is built “by hand,” for instance, by inferring the decay rates from experimental data. This approach may lead to a drastic simplification of the dynamics; however, there are scenarios for which the phenomenological technique may not be reliable, as it may not be able to capture all the relevant aspects of the dynamics. In particular, this problem becomes significant when an external control field is exerted on the system. When modeling the dynamics of such systems, a standard assumption called fixed-dissipator (FD) assumption is applied [114, 116, 166]. This assumes that the dissipative part of the system is not affected by the control term. In particular, in Appendix C.1, we study the case of a driven qubit interacting with a structured environment and analyze the consequences of the FD assumption. We show that manipulating the environment through reservoir engineering, which is possible when the environment spectrum is not flat, allows one to obtain a collection of stationary states that can be very different from the ones given by the model with FD assumption. This serves as an extra motivation to derive effective models describing the dynamics of open quantum systems that do not rely on phenomenological approaches.

Cavity QED Approaches to Quantum Information Processing

As mentioned before, quantum information processing requires quantum memories for long-term information storage and quantum state transmitters for long-distance communication [140]. Due to their weak interaction with the environment, neutral atoms are attractive candidates to be used in various quantum computing architectures [78, 87, 159], ensuring longer decoherence time and providing the possibility of manipulating and measuring the qubit state using resonant laser pulses. The weak interaction with the environment is beneficial for information storage, however, for information extraction and transfer, the atom-environment interaction should be enhanced in a controlled and coherent manner, such that one can efficiently interface the stationary qubits (atoms) and the flying qubits (photons). In neutral atom-based architectures, qubits are expressed in terms of the internal electronic states of the atom, e.g., ground and excited energy levels. The decay of the electronic state of the atom from the excited to the ground state produces radiation known as spontaneous emission, which, in general, is an incoherent radiation. The discovery of Purcell that the decay rate of an emitter depends strongly on the environment the emitter is placed in [76, 151], paved the way towards the study of light-matter interaction with the use of an optical cavity, known today as cavity quantum electrodynamics (cavity QED) [52, 83]. In a properly designed cavity, atoms and photons interact much more strongly than they do in free space, and this enhancement leads to interesting applications in quantum information processing [51, 147].

The word cavity in quantum optics means a resonator for electromagnetic radiation. In this manuscript, we mainly focus on Fabry-Pérot type cavities, which are optical cavities made from two parallel reflecting surfaces, namely mirrors [57] (see Fig. 2.1). Furthermore, from a quantum optics point of view, a photon is the excitation of the modes of the electromagnetic radiation field [52]. This leads to the definition of a vacuum as a state with no photons, i.e., no excitation of the field. The presence of a cavity in a vacuum alters the mode structure of the vacuum, specifically, the structure of electromagnetic field modes propagating in the vacuum. This is because the cavity, having a finite length, imposes boundaries on the electromagnetic field, which results in the confinement of the field inside the cavity, giving rise to resonances. Having such resonances is at the basis of enhanced light-matter interaction with cavities,

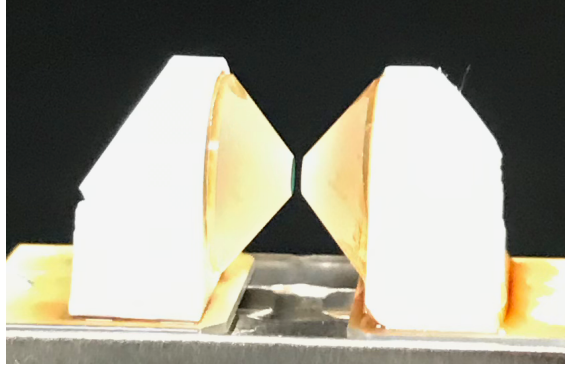


Figure 2.1: Fabry-Pérot cavity used in quantum optics experiments. The picture is taken at the Clarendon Laboratory at University of Oxford [143].

where, ideally, the cavity is loaded with an emitter, e.g. an atom on its excited level (which can be achieved via applying an appropriate laser pulse that excites the atom), and is tuned such that the atom couples to one of the cavity resonances, thus it decays and produces a photon [109]. If the atom is far detuned from the cavity resonances, then the decay rate will not be as enhanced, and the atom can not emit a photon into the cavity mode, since the cavity is not able to accept it. The atom-cavity interaction not only causes the modification of the spontaneous emission rate but can also result in atomic energy level shifts (also known as Lamb shift [22]). This is analogous to the Casimir effect, when the presence of metallic boundaries alter the modes of the vacuum field around the atom [27, 83].

Taking into account all these effects, the cavity-atom interaction is separated into two main regimes: the weak and the strong coupling regimes. The weak coupling implies that the cavity is such that apart from the atom-cavity coupling, there are other processes in the system that can result in significant losses, such as the escape of the produced photon through the cavity mirrors (cavity decay) or atomic spontaneous emission non resonant with the cavity (atomic decay). The strong coupling regime, on the other hand, requires the atom-cavity field interaction to be the dominant one such that it overwhelms any loss or decoherence rate (on the time-scale of the operation designed for the system to perform), including the atomic level shifts [117]. The strong coupling regime can be achieved with cavities of small volume and high reflectivity such that the electric field inside the cavity is enhanced providing single photon-single atom coupling, leading to coherent conversion between the qubit state of the atom into the qubit state spanned by the number of photons in the cavity [66, 98, 192]. This periodic exchange of excitation between the atom and the cavity creates entanglement between them, allowing to perform various quantum information processing schemes and gate operations [5, 55, 152, 203]. Proof-of-principle experiments featuring cavity QEDs have been realized by several groups [143, 148, 185, 205], in some of which laser-cooled Rydberg atoms are used as emitters trapped in a cavity.

With regard to DiVincenzo criteria, cavity QED systems are promising candidates in the realization of quantum computation, satisfying most of the criteria via offering certain advantages over other architectures as well as facing significant challenges that are yet to be overcome [1, 110]. One of the strengths of such systems is that

they allow straightforward interfacing of matter and flying qubits: photons are relatively easier to produce and transmit than to store them, while atoms are good for trapping, hence storing information. Moreover, the techniques for initialization of stationary qubits as well as flying qubits in cavity QED systems are relatively mastered. The state of the atomic qubit can be initialized using optical pumping techniques, exciting the atom to desired energy level, while the initial state of the photonic qubit is simply the vacuum state of the cavity.

A major advantage of cavity QEDs over other systems is that they are well understood from a theoretical standpoint, and the various interactions present in such systems (coupling to the external field, coupling to the environment) are, in principle, well describable, providing a clear understanding of decoherence mechanisms of such systems. Given the fact that the photon is the excitation of the cavity mode, single-photons produced from such systems can be characterized by a well-defined frequency, polarization, and mode profile. Apart from theoretical advancement, there has been significant progress in the experimental realization of such systems for various applications in quantum information processing. In particular, thanks to the magneto-optical trapping and cooling techniques, in current experiments one can observe single atom-cavity mode interaction [129, 137, 145]. Quantum phase gate operations acting on the emitter as well as on the produced photon have been realized in such systems [152, 156]. Success rates of these operations are very dependent on the cavity geometry and mirror quality. This poses a challenge on efficient experimental realization of cavity QED based schemes, where the proper cavity design (mirror coating, optimized mirror curvature) is required, such that one can have the desired light-matter coupling. Additionally, while in theoretical models the atom is mainly considered as a two or three level system, in practice the entire level structure of the atom needs to be considered, since the emitter is subject to external fields that can cause level splittings (Stark effect, non-linear Zeeman effect) [10].

As mentioned before, cavity QED systems can serve as a platform for long distance information transfer. Once a single photon is produced in a cavity, it can readily be transported between sites using optical fibers, therefore providing information transfer between two distant stationary qubits. This assumes considering the reverse process of the photon generation, i.e., the arriving photon that is generated from the first cavity couples to the second cavity and then gets absorbed by the atom trapped in that cavity. This reversed process of mapping the qubits state from photon to atomic states can be used as a qubit measurement scheme [129] as well as to create quantum memory and quantum repeaters. Completing this full cycle of information transfer, however, is experimentally challenging. Coupling of a single photon into an outside mode and an outside single photon into a cavity mode with negligible losses is not straightforward. It is direct when coupling into free space, but much harder when coupling to a fiber mode. This requires an asymmetric cavity of low losses perfectly mode-matched with an output/input mode, i.e., the mode and the polarization of the fiber used as an output for the sending and an input for the receiving cavity [110]. Unlike the photon generation process that has been successfully demonstrated [143], this reverse process lacks experimental implementation, due to these difficulties to provide perfect mode matching between the input channel and the cavity mode.

Another experimental challenge, that limits the performance of the cavity QED based quantum computer is the efficient trapping of individual atoms inside a cavity and the rate of errors arising from the motion of those trapped atoms [45]. The dimensions of optical cavities are quite small ($1\text{-}100\mu\text{m}$) which makes trapping of individual atoms inside a cavity challenging. In current cavity QED experiments the way the atoms appear inside the cavity is via intersecting atomic beams through the cavity, making this process stochastic. This makes it challenging to localize and control the atom, so that the coupling with the cavity is well defined. In particular, in the strong coupling regime, since there is a repeated exchange of excitation between the atom and the cavity field, the atom gets heated (due to momentum kicks to the atom) which can lead to its escape from the trap. One proposed way to reduce this kind of noise is to use adiabatic elimination techniques. Adiabatic passage schemes are intrinsically fault tolerant [192], i.e., applying such scheme allows one to avoid errors that otherwise would have to be treated via error correcting techniques. An example of adiabatic passage scheme is the stimulated Raman adiabatic passage (STIRAP), found to be very robust against atomic motion and spontaneous emission [13, 200]. The idea of STIRAP is to make complete transfer of the atomic population from an initial state to a target state by coupling them via an intermediate state, which is radiatively decaying (excited state) [198, 200]. This allows one to avoid spontaneous emission that would be present if one would consider only the initial state and the radiative excited state as a two level system. Other strategies involve error correcting techniques that are system specific and revolve around characterizing the errors that occur in a given physical realization of a quantum computer. Such error correcting techniques have been described by Shor and Steane [171, 178, 191].

The main issue that the cavity QED based architectures are facing is the scalability. For achieving the ultimate quantum networking, the model should be advanced involving many more qubits and quantum registers than the ones used in proof-of-principle experiments. This includes reproducing the cavity system with nearly identical parameters such that the produced photons can be considered identical. Moreover, it will be challenging to preserve the spatial and spectral purity of the photons that are cascaded through many of such cavities in a row. Additionally, the Fabry-Pérot cavities used in quantum optics experiments are bulky, and combined with the rest of experimental setup are not the ideal platforms for scalable systems. Nevertheless, the environmental isolation that these systems offer is difficult to reach in other platforms, therefor making cavity systems leading candidates for achieving robust and controllable processes [14, 31, 108, 109].

There are other types of resonator designs [46] and other types of material qubits that can play the same role as a Fabry-Pérot cavity with neutral atoms, such as linear ion traps with optical cavities [150], semiconductor quantum dots systems [9], solid state ion vacancy systems [134, 168] and photonic band gap cavities [202]. In particular, the physics of cavity QED has been employed in the study of circuits that opened the field of circuit QED [15]. This approach for example has been used by Google to run simple quantum algorithms on a machine operating on superconducting qubits [15, 182]. All these advancements prove the worth of the fundamental study of such cavity QED systems and one can hope that the future advancement of the field will overcome the challenges mentioned above leading to the development of integrated hardware platforms with well-understood decoherence mechanisms and

sufficient fidelity of control required for quantum information processing.

Motivated by the discussion above, in this manuscript, we study the light-matter interaction in optical cavities. We focus on deriving effective models for efficiently characterizing the dynamics and the properties of a single-photon produced in such systems and to study the limit of the model for producing single photons (otherwise unpredictable for phenomenological models). The manuscript is organized as follows: in Part II we introduce different representations for deriving the dynamics of a leaky cavity. In particular, starting from first principles, we derive effective models that allow us to characterize the dynamics of the cavity, separated from its environment, while still providing the complete characterization of the field propagating outside the cavity. We apply these models to study the production of shaped single-photon wave packets, using a nonresonant laser pulse scheme for a three-level atom. In Part III, we extend the analysis by taking into account the geometric structure of the cavity. We revise the concept of mode volume and cavity resonance frequency for a cavity formed with multilayered dielectric mirrors. This allows for a discussion on a more realistic specification of characteristic parameters of the cavity, particularly for short cavities used to achieve strong coupling. Taking into account these effects induced by the multilayer nature of the cavity mirror, starting from first principles, we derive a generalized cavity-reservoir coupling function that accounts for the effects caused by the actual structure of the mirror. The explicit form of this function allows us to characterize the spectral and spatial properties of the photon produced in the cavity and propagating outside. Finally, in Part IV, we provide discussion and perspective of the results demonstrated in this manuscript.

Part II

Propagating single photons from an open cavity

Introduction

As we discussed in the previous chapter, cavities play an important role not only in classical, but also in quantum optics [139]. Cavities are essentially open systems, i.e., they are in contact with the continuous field of environment and the radiation field generated inside the cavity propagates outside it through its partially transparent mirrors. This means that the models used to describe the dynamics of such systems have to take into account the losses of the system, including the leakage of the radiation field through the cavity mirrors. In the ideal case of lossless cavities, i.e., cavities with perfectly reflecting mirrors, the situation is simple in the sense that such a perfect cavity supports well-defined discrete frequencies, and the emitter trapped in such a cavity interacts with those discrete modes with well-defined emitter cavity coupling. A well-known model to describe such systems is the Jaynes-Cummings model [88, 156], where a two-level emitter is coupled to a single quantized mode of a perfect cavity, with well-defined dipole interaction. In the models where the cavity can be treated as an isolated system, with the mirrors separating the field inside the cavity from the environment outside, there is a nearly periodic exchange of energy between the atom and the cavity mode, and the Jaynes-Cummings model is an accurate approximation. In reality, however, the cavities can never be perfect. A common approach to model open/leaky optical cavities, in which the input from the environment and the output into it are taken into account, is based on the phenomenological construction of the cavity leakage by assuming the environment to be a reservoir with flat spectrum, thus featuring a constant reservoir-cavity coupling (Markov approximation) [20, 69]. In this formalism, known as input-output formalism, the properties of the field exiting the cavity (the output) can be determined based on knowledge of the input field and the dynamics of the emitter-cavity system alone. This formalism, however, does not provide the complete characteristics of the outgoing field, namely its spectral and spatial properties. Moreover, these phenomenological models have been used not only for characterizing optical cavities but also to model other type of cavities, such as plasmonic cavities. This, however, led to misinterpretations in nanophotonics [187]. Thus, to explicitly provide the validity limits of well-known phenomenological models and to provide a complete description of the system, a derivation from first principles is highly desirable and will be discussed throughout this manuscript.

In this chapter, we review the quantization of the electromagnetic field based on the

solutions of classical Maxwell's equations. Following the models introduced in the literature, we derive the classical modes of an open cavity formed by a perfect mirror and a partially reflecting dielectric mirror. We review the concept of cavity response function and its approximate Lorentzian behavior. Finally, we apply this analysis to quantize the open cavity field together with its surroundings as a single closed system, which we refer to as a “universal quantization”. Having this quantized model, in Chapter 4, we derive the dynamics of a system consisting of a trapped atom in a cavity from first principles and connect this derivation to the phenomenological models commonly used in the literature.

3.1 Electromagnetic field: from classical to quantum description

As mentioned before, our aim here is to provide a first principle derivation of the dynamics of an open cavity. To ensure such a first principle derivation means to construct the model starting from the fundamental laws, i.e., we start by solving the classical Maxwell's equations and quantize the system using those solutions (the details of the following derivation is presented in Appendix A.1) [59]. The classical Maxwell's equations for linear, passive, and inhomogeneous medium, where there are no free charges and no electric current, read as follows ¹ [80]:

$$\nabla \times \mathbf{B} = \frac{\varepsilon(\mathbf{r})}{c^2} \frac{\partial}{\partial t} \mathbf{E}, \quad (3.1)$$

$$\nabla \times \mathbf{E} = -\frac{\partial}{\partial t} \mathbf{B}, \quad (3.2)$$

$$\nabla \cdot (\varepsilon(\mathbf{r})\mathbf{E}) = 0, \quad (3.3)$$

$$\nabla \cdot \mathbf{B} = 0, \quad (3.4)$$

where $c = 1/\sqrt{\varepsilon_0\mu_0}$ is the speed of light, with ε_0 and μ_0 being the free space permittivity and permeability, respectively. $\varepsilon(\mathbf{r})$ is the relative permittivity with $n^2 = \varepsilon$ being the refraction index of the media. \mathbf{E} and \mathbf{B} represent the electric and magnetic field vectors. We proceed by introducing the scalar and vector potentials associated with the electromagnetic field: U, \mathbf{A} ; such that $\nabla \times \mathbf{A} = \mathbf{B}$ and $(\partial/\partial t)\mathbf{A} + \mathbf{E} = -\nabla U$. With these definitions, the above Maxwell's equation can be written as:

$$\left(\frac{\partial^2}{\partial t^2} + \frac{c^2}{\varepsilon(\mathbf{r})} \nabla \times \nabla \times \right) \mathbf{A}(\mathbf{r}, t) = -\frac{\partial}{\partial t} \nabla U. \quad (3.5)$$

Moreover, we can introduce the following operator: $\hat{\Omega}^2 = \frac{c}{\sqrt{\varepsilon(\mathbf{r})}} \nabla \times \nabla \times \frac{c}{\sqrt{\varepsilon(\mathbf{r})}}$, and by applying the Coulomb gauge (i.e., $\nabla \cdot (\varepsilon(\mathbf{r})\mathbf{A}) = 0$ (transversality condition), $U = 0$ [34]) and defining $\tilde{\mathbf{A}} = \sqrt{\varepsilon_0\varepsilon(\mathbf{r})}\mathbf{A}(\mathbf{r})$, from Eq. (3.5) we can get the following eigenvalue equation

$$\left(\hat{\Omega}^2 - \omega_k^2 \right) \tilde{\mathbf{A}}(\mathbf{r}) = 0, \quad (3.6)$$

$$(3.7)$$

¹The parameters written in bold represent vectors, the product “.” represents the scalar product and “×” is the vector product.

where ω_k are the eigenvalues of the operator $\hat{\Omega}$, with the index $k = (\mathbf{k}, \sigma)$, where \mathbf{k} represents the wavevector with $|\mathbf{k}| = \omega_k/c$, and σ represents a possible degeneracy.

Having the full classical description of the field, we now can quantize it via defining canonically conjugate variables $\tilde{\mathbf{\Pi}} = -\sqrt{\varepsilon_0\varepsilon(\mathbf{r})}\mathbf{E}$ such that the pair $(\tilde{\mathbf{A}}, \tilde{\mathbf{\Pi}})$ forms a Hamiltonian system. However, these variables are not independent, due to the constraint $\nabla \cdot \sqrt{\varepsilon(\mathbf{r})}\tilde{\mathbf{A}} = 0$ and $\nabla \cdot \sqrt{\varepsilon(\mathbf{r})}\tilde{\mathbf{\Pi}} = 0$ imposed by Coulomb gauge. Thus, they can not be directly used for quantization and be replaced by their corresponding operators. Instead, to have independent parameters for quantization, we perform a canonical transformation $(\tilde{\mathbf{A}}, \tilde{\mathbf{\Pi}}) \rightarrow (q_k, p_k)$, where the parameters q_k and p_k are independent, canonically conjugate variables. The latter can be quantized using the principle of correspondence, and this leads to the expressions of the quantized field variables in terms of the eigenfunctions $\Phi_k(\mathbf{r})$, the eigenvalues ω_k , and the creation/annihilation operators $\hat{a}_k^\dagger, \hat{a}_k$:

$$\tilde{\mathbf{A}}(\mathbf{r}) = \sum_k \sqrt{\frac{\hbar}{2\omega_k}} \left(\Phi_k(\mathbf{r})\hat{a}_k + \Phi_k^*(\mathbf{r})\hat{a}_k^\dagger \right), \quad (3.8a)$$

$$\tilde{\mathbf{\Pi}}(\mathbf{r}) = -i \sum_k \sqrt{\frac{\hbar\omega_k}{2}} \left(\Phi_k(\mathbf{r})\hat{a}_k - \Phi_k^*(\mathbf{r})\hat{a}_k^\dagger \right), \quad (3.8b)$$

with

$$[\hat{a}_k, \hat{a}_{k'}^\dagger] = \delta_{kk'}, \quad (3.9a)$$

$$[\hat{a}_k, \hat{a}_{k'}] = [\hat{a}_k^\dagger, \hat{a}_{k'}^\dagger] = 0. \quad (3.9b)$$

The functions $\Phi_k(\mathbf{r})$ satisfy the transversality constraint: $\nabla \cdot (\varepsilon(\mathbf{r})\Phi_k(\mathbf{r})) = 0$, and are the solutions of the following eigenmode equation:

$$\hat{\Omega}^2 \Phi_k(\mathbf{r}) = \omega_k^2 \Phi_k(\mathbf{r}). \quad (3.10)$$

Taking the expressions in Eq. (3.8) into account, the Hamiltonian of the electromagnetic field can be written as follows:

$$H = \frac{1}{2} \sum_k \hbar\omega_k \left(\hat{a}_k^\dagger \hat{a}_k + \hat{a}_k \hat{a}_k^\dagger \right). \quad (3.11)$$

The above quantization is done for a field with discrete modes in the Hilbert space $L_2(R^N, d^N q)$. Direct transition from such discrete mode quantization to continuous ones is not trivial due to the fact that the Hilbert space with infinite degrees of freedom is not well defined. This, however, can be straightforwardly done if we move from finite-dimensional Hilbert space to an associated Fock space. The quantized expressions for the continuous electromagnetic field then read:

$$\tilde{\mathbf{A}}(\mathbf{r}) = \int d^3k \sqrt{\frac{\hbar}{2\omega_k}} \left(\boldsymbol{\psi}(k, \mathbf{r})\hat{a}(k) + \boldsymbol{\psi}^*(k, \mathbf{r})\hat{a}^\dagger(k) \right), \quad (3.12)$$

$$\tilde{\mathbf{\Pi}}(\mathbf{r}) = -i \int d^3k \sqrt{\frac{\hbar\omega_k}{2}} \left(\boldsymbol{\psi}(k, \mathbf{r})\hat{a}(k) - \boldsymbol{\psi}^*(k, \mathbf{r})\hat{a}^\dagger(k) \right). \quad (3.13)$$

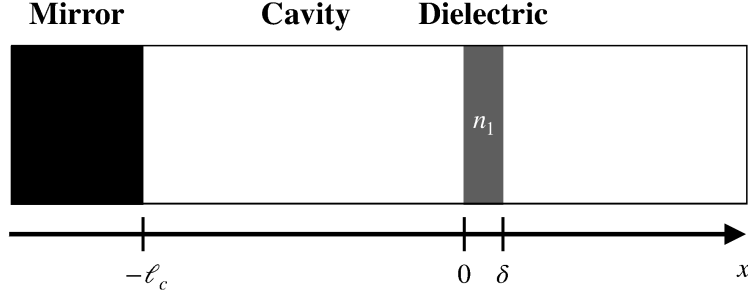


Figure 3.1: Description of the single-layered cavity model. A perfect mirror stands at $x = -\ell_c$, delimiting a cavity of length ℓ_c with a partially transparent dielectric material from $x = 0$ to $x = \delta$.

where the explicit definition of $\boldsymbol{\psi}(k, \mathbf{r})$ is given in Appendix A.1 and

$$[\hat{a}(k), \hat{a}^\dagger(k')] = \delta(k - k'), \quad (3.14a)$$

$$[\hat{a}(k), \hat{a}(k')] = [\hat{a}^\dagger(k), \hat{a}^\dagger(k')] = 0. \quad (3.14b)$$

Similarly, for the Hamiltonian we obtain:

$$H = \frac{1}{2} \int d^3k \hbar\omega_k (\hat{a}^\dagger(k)\hat{a}(k) + \hat{a}(k)\hat{a}^\dagger(k)). \quad (3.15)$$

Finally, the quantized electric field expression becomes:

$$\mathbf{E} = -\frac{1}{\sqrt{\varepsilon_0\varepsilon(\mathbf{r})}}\tilde{\boldsymbol{\Pi}} = i \int d^3k \sqrt{\frac{\hbar\omega_k}{2\varepsilon_0\varepsilon(\mathbf{r})}} (\boldsymbol{\psi}(k, \mathbf{r})\hat{a}(k) - \boldsymbol{\psi}^*(k, \mathbf{r})\hat{a}^\dagger(k)). \quad (3.16)$$

Taking this analysis into account, below we review the derivation and quantization of the modes of an open cavity.

3.2 Open cavity with a single-layered dielectric mirror: the true modes

To analyse the modes of an open cavity, we study the longitudinal propagation of the field (paraxial approximation [164]) through the cavity (we omit writing explicitly the transverse mode structure, any inclusion of which can be absorbed in the mode function obtained below). Let us model a cavity with flat mirrors and of mirror spacing ℓ_c . In this analysis, we neglect any polarization effect that may arise within the cavity. A targeted application of our model is the production of single photons leaking out from one side of the cavity, thus, we assume that such a cavity has a perfect mirror on the left side, positioned at $x = -\ell_c$, and a partially transparent dielectric placed at the origin, with a refractive index n_1 and a thickness δ . The dielectric layer thickness is designed to support a target wavelength, λ_0 . Typically, $\delta = \lambda_0/4n_1$, with n_1 being the refractive index of the dielectric. This structure can be seen in Fig. 3.1. To get the spatial distribution of the electromagnetic field modes for this structure, we solve Eq. (3.10) for one-dimensional case:

$$\left(\frac{d^2}{dx^2} + \varepsilon_r(x) \frac{\omega^2}{c^2} \right) \Phi_\omega(x) = 0, \quad (3.17)$$

where $\Phi_\omega(x)$ is the space-dependent field eigenmode of continuous, positive index $\omega = 2\pi c/\lambda$, with λ being the wavelength of the travelling wave. $\varepsilon_r(x)$ is the relative permittivity of the structure having the following form:

$$\varepsilon_r(x) = \begin{cases} 1 & x \in [-\ell_c, 0] \cup [\delta, \infty) \\ n_1^2 & x \in (0, \delta) \end{cases}. \quad (3.18)$$

The ortho-normalization condition for these modes is given by:

$$\langle \Phi_\omega(x), \Phi_{\omega'}(x) \rangle = \int dx \varepsilon_r(x) \Phi_\omega^*(x) \Phi_{\omega'}(x) = \delta(\omega - \omega'). \quad (3.19)$$

Under these conditions, Eq. (3.17) is solved by a superposition of plane waves of the form

$$\Phi_\omega(x) = A_+ e^{i\frac{\omega}{c}\sqrt{\varepsilon_r(x)}x} + A_- e^{-i\frac{\omega}{c}\sqrt{\varepsilon_r(x)}x}. \quad (3.20)$$

The distinct solutions are then stitched together by the boundary condition that $\Phi_\omega(x)$ and its derivative must ensure continuity throughout the points of discontinuity of $\varepsilon_r(x)$, thus fixing the values of the coefficients A_+ and A_- for every region (see the details in Appendix A.2). For a single-layered mirror, the solution has the form

$$\Phi_\omega(x) = \Phi_{\omega,\text{ins}}(x) \chi_{[-\ell_c, 0]} + \Phi_{\omega,\text{mirror}}(x) \chi_{(0, \delta)} + \Phi_{\omega,\text{outs}}(x) \chi_{[\delta, \infty)}. \quad (3.21)$$

Here, $\chi_{\mathcal{D}}$ represents the indicator function within a domain $\mathcal{D} \subset \mathbb{R}$, i.e., $\chi_{\mathcal{D}}(x) = 1$ for $x \in \mathcal{D}$ and 0 otherwise. The normalized mode is described in the three regions by:

$$\begin{aligned} \Phi_{\omega,\text{ins}}(x) &= \frac{2i}{\sqrt{2\pi c \mathcal{A}}} e^{i\frac{\omega}{c}\ell_c} T(\omega) \sin\left[\frac{\omega}{c}(x + \ell_c)\right], \\ \Phi_{\omega,\text{mirror}}(x) &= \frac{e^{i\frac{\omega}{c}\ell_c}}{\sqrt{2\pi c \mathcal{A}}} \frac{T(\omega)}{1 + r_1} \left[(e^{i\frac{\omega}{c}\ell_c} - r_1 e^{-i\frac{\omega}{c}\ell_c}) e^{i\frac{\omega}{c}n_1 x} + (r_1 e^{i\frac{\omega}{c}\ell_c} - e^{-i\frac{\omega}{c}\ell_c}) e^{-i\frac{\omega}{c}n_1 x} \right], \\ \Phi_{\omega,\text{outs}}(x) &= \frac{1}{\sqrt{2\pi c \mathcal{A}}} e^{2i\frac{\omega}{c}\ell_c} \frac{T(\omega)}{T^*(\omega)} e^{i\frac{\omega}{c}x} - e^{-i\frac{\omega}{c}x}, \end{aligned} \quad (3.22)$$

where \mathcal{A} is the transverse area of the mode (a quantity which is calculated when the mode is normalized in three dimensions), and r_1 is the single-layer reflectivity:

$$r_1 = \frac{n_1 - 1}{n_1 + 1}. \quad (3.23)$$

$T(\omega)$ is the cavity spectral response function, which describes the ratio of intensity between the inside and outside of the cavity, with respect to a particular frequency ω :

$$T(\omega) = \frac{t(\omega)}{1 + r(\omega) e^{2i\frac{\omega}{c}(\ell_c + \frac{\delta}{2})}}. \quad (3.24)$$

It depends on the cavity spectral transmission response function $t(\omega)$ [201]:

$$t(\omega) = \frac{(1 - r_1^2) e^{i(n_1 - 1)\frac{\omega}{c}\delta}}{1 - e^{2in_1\frac{\omega}{c}\delta} r_1^2} = |t(\omega)| e^{i\phi_t(\omega)}, \quad (3.25)$$

and spectral reflection response function $r(\omega)$:

$$r(\omega) = e^{-i\frac{c}{\ell_c}\delta} r_1 \frac{(e^{2in_1\frac{c}{\ell_c}\delta} - 1)}{1 - e^{2in_1\frac{c}{\ell_c}\delta} r_1^2} = |r(\omega)| e^{i\phi_r(\omega)}. \quad (3.26)$$

It is important to stress that both of these parameters are complex and have associated phases: $\phi_r(\omega)$, $\phi_t(\omega)$. Together, $t(\omega)$ and $r(\omega)$ satisfy the beam splitter relations

$$|t(\omega)|^2 + |r(\omega)|^2 = 1, \quad (3.27a)$$

$$r^*(\omega)t(\omega) + t^*(\omega)r(\omega) = 0. \quad (3.27b)$$

With the definitions provided above, the modes (3.22) represent the true modes leading to the so-called universal quantization.

The absolute value squared of the cavity response function can be decomposed as a sum of Lorentzian-like functions [52, 201], still having $\tilde{\omega}_m$ and γ_1 depending on ω : (see the details in Appendix A.3):

$$|T(\omega)|^2 = \sum_{m=-\infty}^{\infty} \frac{c}{2L_1} \frac{\gamma_1(\omega)}{(\omega - \tilde{\omega}_m(\omega))^2 + \left(\frac{\gamma_1(\omega)}{2}\right)^2}, \quad (3.28)$$

where

$$\gamma_1(\omega) = -\frac{c}{L_1} \ln |r(\omega)|, \quad (3.29a)$$

$$\tilde{\omega}_m(\omega) = m\frac{\pi c}{L_1} + \frac{c}{2L_1} (\pi - \phi_r(\omega)), \quad (3.29b)$$

$$L_1 = \ell_c + \frac{\delta}{2}. \quad (3.29c)$$

Index 1 in L_1 and γ_1 indicates that in the considered model the mirror is made of a single dielectric layer.

These results for a single-layered cavity are commonly used to model the dynamics of cavities with highly reflecting mirrors, assuming that the mirror thickness is negligible with respect to the cavity length such that $L_1 \approx \ell_c$. Such a high reflectivity with a single-layered mirror can be achieved if we assume a dielectric material with a fictitiously high refractive index. In particular, at the perfect cavity limit, i.e., taking the limit $n_1 \rightarrow \infty$, Eq. (3.23) leads to $r_1 \rightarrow 1$, and the reflection function in Eq. (3.26) becomes $r(\omega_m) \approx -1 = e^{i\pi}$, making the phase $\phi_r(\omega_m) = \pi$, with $\omega_m = m\pi c/\ell_c$ being the perfect cavity resonances. Taking these into account, for a highly reflective cavity the parameters in decomposition (3.28) can be evaluated at the resonance frequency ω_m leading to

$$|T(\omega)|^2 \approx \sum_{m=-\infty}^{\infty} \frac{c}{2\ell_c} \frac{\Gamma_m}{(\omega - \omega_m)^2 + \left(\frac{\Gamma_m}{2}\right)^2}, \quad (3.30)$$

where

$$\Gamma_m = \gamma_1(\omega_m) = -\frac{c}{\ell_c} \ln |r(\omega_m)|, \quad (3.31a)$$

$$\tilde{\omega}_m = \omega_m + \frac{c}{2\ell_c} (\pi - \phi_r(\omega_m)) \approx \omega_m. \quad (3.31b)$$

At this stage, each term in the sum in Eq. (3.30) becomes Lorentzian, each being centred around the resonance frequency ω_m . Additionally, assuming that the width Γ_m is much smaller than the spacing $\Delta_{\omega_m} = \pi c/\ell_c$ between the neighbouring resonances ($-\frac{c}{\ell_c} \ln |r(\omega_m)| = \Gamma_m \ll \frac{\pi c}{\ell_c}$, i.e., $-\ln |r(\omega_m)| \ll \pi$, defining a *high finesse* cavity, which results from a high reflectivity), the cavity response function can be written as

$$T(\omega) \approx \sum_{m=-\infty}^{\infty} \sqrt{\frac{c}{2\ell_c}} \frac{\sqrt{\Gamma_m}}{(\omega - \omega_m) + i\frac{\Gamma_m}{2}} = \sum_{m=-\infty}^{\infty} T_m(\omega), \quad (3.32)$$

where $T_m^*(\omega)T_{m'}(\omega) = \delta_{mm'}|T_m(\omega)|^2$. Moreover, defining a high quality (high- Q) cavity as $\Gamma_m \ll \omega_m$, we can conclude that high reflectivity results in high finesse, which itself implies a high- Q cavity. Thus, high reflectivity is the quantity characterizing the targeted features of the cavity. In practice, the reflectivity is finite and can not be made high using a single dielectric layer. Realistic cavities feature a multilayer structure which offers high reflectivity, as seen in Part III.

Finally, using the modes (3.22) we can write the quantized expression of the field corresponding to the semi-infinite system composed of the open cavity and its environment:

$$E(x) = i \int_0^{\infty} d\omega \sqrt{\frac{\hbar\omega}{2\varepsilon_0}} \left(\Phi_{\omega}(x)a_{\omega} - \Phi_{\omega}^*(x)a_{\omega}^{\dagger} \right), \quad (3.33)$$

with the corresponding Hamiltonian

$$H = \frac{1}{2} \int_0^{\infty} d\omega \hbar\omega \left(a_{\omega}^{\dagger}a_{\omega} + a_{\omega}a_{\omega}^{\dagger} \right) = \int_0^{\infty} d\omega \hbar\omega \left(a_{\omega}^{\dagger}a_{\omega} + \frac{1}{2} \right). \quad (3.34)$$

The term $\frac{1}{2}\hbar\omega$ is often omitted with the argument that the zero of the energy can be chosen at will in non-relativistic quantum physics (otherwise leading to an infinite quantity), reducing the Hamiltonian to

$$H = \int_0^{\infty} d\omega \hbar\omega a_{\omega}^{\dagger}a_{\omega}. \quad (3.35)$$

The quantization (3.33) is known as the universal quantization [52, 101, 142, 201], since the modes a_{ω} describe a closed system that incorporates the cavity and everything else surrounding it.

In the following we use this decomposition of the cavity response function to derive different models for cavity induced light-matter interaction and single photon production.

Production of a single photon from a trapped atom

Coherent atom-cavity interaction needed to produce a photon inside the cavity is achieved in a so-called strong coupling regime, where the atom-cavity coupling rate surpasses incoherent decay mechanisms [98]. The enhancement to the spontaneous emission rate of a quantized emitter within a resonant cavity is described by the Purcell effect. When compared to spontaneous emission into free space, the rate of emission into the cavity mode for an atom localized at the field maximum is enhanced by the factor [151]:

$$F_p = \frac{3\lambda^3 Q}{4\pi^2 V}, \quad (4.1)$$

where Q is the quality factor of the resonator, λ is the transition wavelength and V is the optical mode volume of the resonator. As discussed before, the suppression of photonic decay within the cavity generally requires the use of highly reflective mirrors, leading to a large cavity finesse. Given the representation of finesse as the ratio of cavity free spectral range to its linewidth, a high finesse additionally ensures good spectral resolution of each resonance. Therefore, when an emitter with a comparable transition linewidth is coupled to a high finesse cavity, interaction with only a single field mode can be assumed.

Taking into account the quantization and the cavity (true) modes derived in the previous chapter, in this chapter, we demonstrate the first principle derivation of the dynamics of a photon produced from an atom trapped in an optical cavity. We consider the cavity structure depicted in Fig. 3.1 and the universal quantization of the true modes (3.22). Our aim is to have the complete characterization of the produced photon so that it can be used in quantum information transfer and storage. This implies that we need to have the description of the photon inside as well as outside the cavity. To reach this goal, we discuss different representations of the light-matter interaction in an optical cavity. In particular, we introduce the true-mode representation, corresponding to the universal quantization, and introduce the inside-outside representation, which, unlike the true-mode representation, assumes a separation between the cavity (inside) and its environment (outside) modes. This representation allows us to obtain the complete characterization of the leaking photon in time as well as in the frequency domain. We analyze the validity of this

separation by comparing the dynamics obtained via inside-outside representation to that obtained from the true-mode representation. We demonstrate, that one can straightforwardly derive the well-known phenomenological models from the inside-outside and true-mode representations while having the explicit definitions of the parameters and the approximations applied. To characterize the propagation of the photon outside the cavity, we derive the quantized Poynting vector from the true-mode representation, which we then write in terms of the reservoir operators corresponding to the inside-outside representation. We derive the condition of correspondence of this reservoir photon number operator to the standard output photon number operator derived in the input-output formulation [69]. Finally, we derive the master equation [20, 69, 71, 149] by tracing out the reservoir degrees of freedom, which allows one to determine the state of the atom-cavity system necessary to obtain the quantum averages describing the relevant physical observables. This derivation provides the explicit limit at which the approximate models coincide with the actual true-mode representation.

4.1 Derivation of the model

We start by considering a single Λ atom with ground $|g\rangle$, metastable $|f\rangle$, and excited $|e\rangle$ states trapped in a cavity, which is designed to sustain a field of wavelength λ_0 and frequency $\omega_0 = 2\pi c/\lambda_0$. The $|f\rangle \leftrightarrow |e\rangle$ transition, with frequency ω_{ef} and dipole moment d_{fe} , is assumed to be nearly resonant with a cavity mode, introducing the detuning $\Delta_c = \omega_{ef} - \omega_0$; the $|g\rangle \leftrightarrow |e\rangle$ transition, with frequency ω_{eg} and dipole moment d_{ge} is assumed to be independently driven by a classical laser field $\mathcal{E}(t) \cos(\omega_L t + \varphi_L)$, corresponding to the time-dependent Rabi frequency $\Omega(t) = -\mathcal{E}(t)d_{ge}/2\hbar$, with a detuning $\Delta = \omega_{eg} - \omega_L$.

4.1.1 True-mode representation

As demonstrated earlier, the universal quantization procedure, featuring the true modes (3.22) is a derivation from first principles, which allows the treatment of the cavity as part of the environment and the derivation of true (exact) modes for such a closed system (see Fig. 4.1(a)). Here we consider the same physical situation as the one in Fig. 3.1 while considering that the length of the dielectric layer can be neglected with respect to the cavity length [52]. By introducing an atom in such a cavity, we can write the Hamiltonian for the full atom-environment system: $\mathcal{A} \oplus \mathcal{E}$, in a rotating frame defined by the unitary operator $U_{RW} = \exp(-i\omega_L t) \sigma_g + \sigma_e + \sigma_f$:

$$\tilde{H}(t) = H_A(t) + H_{\text{int}} + H_E \quad (4.2a)$$

$$H_A(t) = \hbar(\Delta - \Delta_c - \omega_0)\sigma_f + \hbar\Delta\sigma_e + \hbar\Omega(\sigma_{ge} + \sigma_{eg}), \quad (4.2b)$$

$$H_E = \int_0^{+\infty} d\omega \hbar\omega a_\omega^\dagger a_\omega, \quad (4.2c)$$

$$H_{\text{int}} = i\hbar \int_0^{+\infty} d\omega \left(\eta(\omega)a_\omega\sigma^\dagger - \eta^*(\omega)a_\omega^\dagger\sigma \right), \quad (4.2d)$$

where $H_A \equiv H_A(t)$ denotes the atomic Hamiltonian in the rotating wave approximation (RWA). Here, we have introduced the atomic operators $\sigma_{k\ell} \equiv |k\rangle\langle\ell|$, $\sigma_k \equiv \sigma_{kk}$

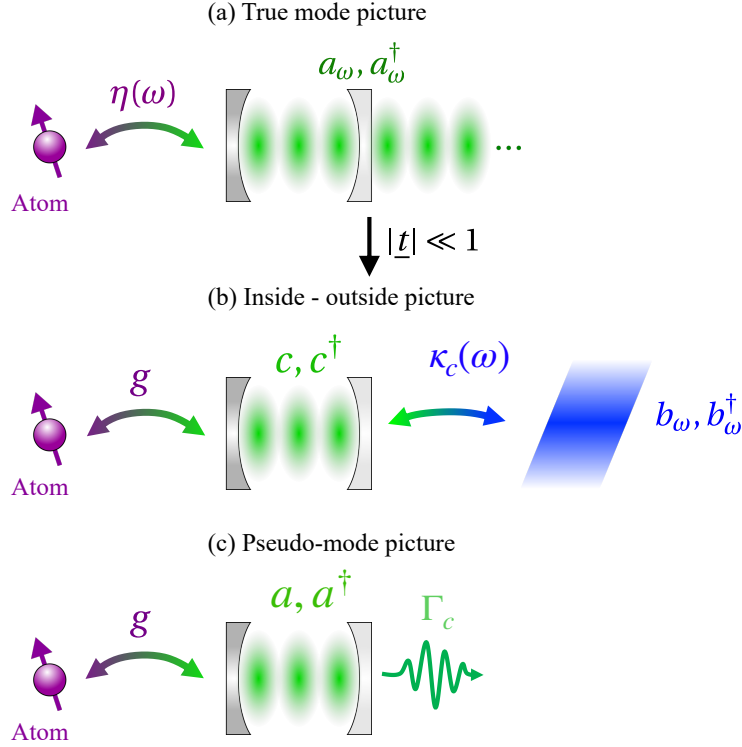


Figure 4.1: (a) True-mode picture corresponding to the modes obtained from universal quantization, where the cavity is treated as part of the environment. In such a representation, the atom is coupled to the universal modes a_ω with a frequency-dependent coupling strength $\eta(\omega)$. (b) For cavities with sufficiently small transmission it is possible to approximately separate modes into cavity (inside) and reservoir (outside) modes, with an effective frequency-dependent coupling $\kappa_c(\omega)$. In this picture, the atom couples mainly to the cavity mode c , to which it is resonant (or near resonant), with coupling strength g . (c) Unlike the two other representations, in the pseudomode picture, the reservoir is eliminated and accounted for via the cavity linewidth Γ_c , in a non-Hermitian description.

and $\sigma \equiv \sigma_{fe}$. H_E describes the environment with the cavity as part of it. Operators $a_\omega, a_\omega^\dagger$ are the annihilation and creation operators for the true modes, satisfying the commutation relation

$$[a_\omega, a_{\omega'}^\dagger] = \delta(\omega - \omega'). \quad (4.3)$$

H_{int} represents the interaction between the atom and the structured environment, which is evaluated via calculating the atom-field dipolar interaction at the position of the atom x_A : $V = (d_{\text{ef}}\sigma + d_{\text{ef}}^*\sigma^\dagger)E(x_A)$. Since the atom is placed inside the cavity, to evaluate $E(x_A)$, we use the expression of the mode function $\Phi_{\omega, \text{ins}}(x_A)$ in Eq. (3.22)

$$E(x_A) = i \int_0^\infty d\omega \sqrt{\frac{\hbar\omega}{2\varepsilon_0}} (\Phi_{\omega, \text{ins}}(x_A)a_\omega - \Phi_{\omega, \text{ins}}^*(x_A)a_\omega^\dagger), \quad (4.4)$$

leading to the following coupling factor:

$$\eta(\omega) = i \sqrt{\frac{\omega}{\hbar\varepsilon_0\pi c\mathcal{A}}} d_{\text{ef}} e^{i\frac{\omega}{c}\ell_c} \sin\left[\frac{\omega}{c}(x_A + \ell_c)\right] T(\omega). \quad (4.5)$$

Furthermore, by using the approximate expression (3.32) for the response function, and assuming that the atom couples to a single cavity mode ω_0 , we get the following coupling function

$$\eta(\omega) \approx i \sqrt{\frac{\omega}{\hbar \varepsilon_0 \ell_c \mathcal{A}}} d_{\text{eff}} e^{i \frac{\omega}{c} \ell_c} \sin \left[\frac{\omega}{c} (x_A + \ell_c) \right] \sqrt{\frac{\Gamma_c}{2\pi}} \frac{1}{\omega - \omega_0 + i \frac{\Gamma_c}{2}}, \quad (4.6)$$

where Γ_c is the cavity linewidth corresponding to the mode ω_0 . In the literature, the assumptions leading to such a Lorentzian-like coupling function (namely, the Lorentzian structure of the response function) usually correspond to applying the high quality factor (high- Q) cavity limit. However, as we show below, the high- Q assumption by itself is not sufficient, by definition. Instead, we should require a high-finesse cavity induced by a high reflectivity, which satisfies all the conditions necessary to perform the above approximations. Additionally, we can note, that the product $\ell_c \mathcal{A}$ appearing in this coupling strength can be interpreted as the cavity mode volume. In the case considered here, it happens to be identical to the mode volume determined by the geometric parameters of the cavity: its mirror separation (or geometric length, ℓ_c), and mirror area, \mathcal{A} . However, we emphasise that here, the mode volume was not introduced by normalizing the field in a perfect resonator of length ℓ_c . Instead, it is a result of the finite width of the resonances in Eq. (3.32). As we show in Chapter 6, where we study more realistic cavity models, recovering ℓ_c only appears in the case of a long, high-finesse resonator and this may not prevail when such condition is not met.

The Hamiltonian (4.2) with the coupling (4.5) describes a true-mode representation, i.e., with continuous frequencies, but with a structured reservoir [39]. In the following we break these true modes into inside and outside modes, which allow one to quantize the cavity and the reservoir separately.

4.1.2 Mode separation into inside and outside modes

We now consider an approximately equivalent model to the one obtained in Section 4.1.1 via splitting the modes a_ω into two parts: cavity modes c (inside) and the continuum of reservoir modes b_ω (outside) [Fig. 4.1(b)]. The derivation is formally shown in Ref. [52], exhibiting an error of order $\mathcal{O}(|\underline{t}|^2)$, where \underline{t} is the transmission rate of the (single-layered) mirror. In Chapter 7, we explicitly demonstrate this derivation for more realistic cavities made of multilayer dielectric mirrors. This representation can be interpreted as replacing the semitransparent mirror with a perfect one, forming a perfect cavity (\mathcal{C}), which is coupled to the reservoir (\mathcal{R}) (see Fig. 4.2 for the coupling scheme of the atom with the cavity). We refer to it as the inside-outside representation. The RWA Hamiltonian of the full system $\mathcal{A} \oplus \mathcal{C} \oplus \mathcal{R}$ reads, in the Schrödinger picture:

$$H(t) = H_A(t) + H_{AC} + H_C + H_{RC} + H_R \quad (4.7a)$$

$$H_C = \hbar \omega_0 c^\dagger c, \quad (4.7b)$$

$$H_{AC} = \hbar g (c^\dagger \sigma + \sigma^\dagger c), \quad (4.7c)$$

$$H_R = \int_0^{+\infty} d\omega \hbar \omega b_\omega^\dagger b_\omega, \quad (4.7d)$$

$$H_{RC} = i\hbar \int_0^{+\infty} d\omega (\kappa_c(\omega) b_\omega^\dagger c - \kappa_c^*(\omega) c^\dagger b_\omega), \quad (4.7e)$$

with the atom-cavity coupling factor $g = -d_{\text{ef}}\sqrt{\omega_0/\hbar\varepsilon_0\ell_c\mathcal{A}}$ (one-photon Rabi frequency), assuming the atom is localized at the field maximum. The coupling factor $\eta(\omega)$ for the true mode picture [Eq. (4.6)] can then be approximated in the limit of high reflectivity as

$$\eta(\omega) \approx \hat{\eta}(\omega) = -ig\sqrt{\frac{\Gamma_c}{2\pi}} \frac{1}{\omega - \omega_0 + i\frac{\Gamma_c}{2}}, \quad (4.8)$$

which is obtained by evaluating the term $g_\omega := -d_{\text{ef}}\sqrt{\omega/\hbar\varepsilon_0\ell_c\mathcal{A}}e^{i\frac{\omega}{c}\ell_c}\sin\left[\frac{\omega}{c}(x_A + \ell_c)\right]$ in Eq. (4.6) at the resonance frequency ω_0 : $g = g_{\omega_0}$. The form (4.8) allows the direct derivation of the pseudomode representation described in Section 4.1.3.

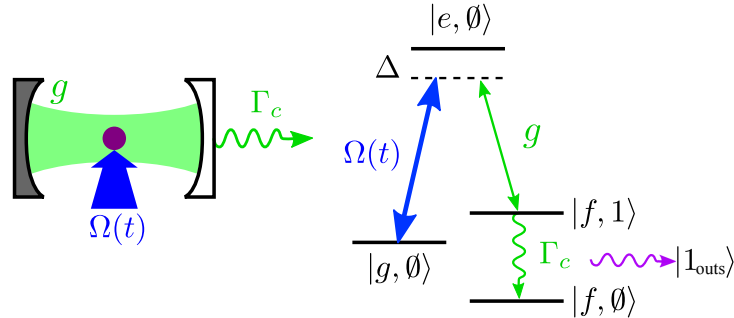


Figure 4.2: Atom-field interaction in the cavity. Left panel: A single Λ atom is driven by an external classical laser field of Rabi frequency Ω and a quantized cavity field with coupling strength g . Right panel: The fields are in two-photon resonance ($\Delta = \Delta_c$), and the one-photon detuning is Δ . Initially, the atom is in the ground state $|g\rangle$. In the course of the excitation process, one photon is taken from the laser field and transferred to the cavity, which eventually leaks out of the cavity through a semitransparent mirror characterized by the leakage Γ_c .

In Eq. (4.7), $H_A(t)$ is the same as Eq. (4.2b), H_C is the free-cavity Hamiltonian, H_{AC} describes the coupling between the atom and the cavity, H_R is the free-reservoir Hamiltonian, and H_{RC} describes the coupling between the empty cavity and the free reservoir. The reservoir annihilation and creation operators $b_\omega, b_\omega^\dagger$ satisfy the commutation relation

$$[b_\omega, b_{\omega'}^\dagger] = \delta(\omega - \omega'). \quad (4.9)$$

The cavity-reservoir coupling function $\kappa_c(\omega)$ can be evaluated in the limit of small transmission and near resonance as [52] (explicit derivation of this function for multilayered cavity is presented in Part III, Appendix B.6)

$$\kappa_c(\omega) = -i\sqrt{\frac{\Gamma_c}{2\pi}} e^{-i\frac{\omega}{c}\ell_c} \text{sinc}\left((\omega - \omega_0)\frac{\ell_c}{c}\right). \quad (4.10)$$

To derive this function, as it is demonstrated in [52], one should equate the modes derived in true-mode representation to the modes derived for the model where the actual single-layered open cavity is replaced by a perfect one which is then coupled to the semi-infinite reservoir delimited by the perfect cavity. From this equivalence the expression in (4.10) can be obtained for cavities with sufficiently small transmission.

We highlight that in this derivation there is no emitter initially considered in the system, and the coupling function $\kappa_c(\omega)$ describes the coupling of the empty cavity to the environment.

One can notice that the derived inside-outside representation does not feature the constant cavity-reservoir coupling that is generally assumed in the standard derivation under certain conditions [69]. The standard approach, albeit leading to physically accurate results in some limits that are analyzed in the next section, can lead to mathematical inconsistencies (see Appendix A.4). Here, however, the cavity-reservoir coupling has a specific form (4.10), which is obtained under mathematically explicitly defined conditions (see the details in Chapter 7) and can be treated straightforwardly.

4.1.3 Pseudomode representation

We can define a pseudomode representation [Fig. 4.1(c)] via

$$\hat{H}(t) = H_A(t) + \hat{H}_{AC} + \hat{H}_C \quad (4.11a)$$

$$\hat{H}_{AC} = \hbar g (a^\dagger \sigma + \sigma^\dagger a), \quad (4.11b)$$

$$\hat{H}_C = \hbar \left(\omega_0 - i \frac{\Gamma_c}{2} \right) a^\dagger a, \quad (4.11c)$$

where, for a single mode,

$$a^\dagger |\emptyset\rangle = |1\rangle, \quad (4.12a)$$

$$[a, a^\dagger] = 1. \quad (4.12b)$$

As we demonstrate below, this representation can be derived directly from the true-mode picture with the approximate coupling (4.8). The cavity modes c in (4.7) and a in (4.11) are different since they apply on different space. c is the perfect cavity mode, while a is defined as:

$$a = \frac{1}{g} \int d\omega \hat{\eta}(\omega) \hat{a}_\omega, \quad (4.13)$$

where \hat{a}_ω is the annihilation operator of the true mode defined for the approximate coupling $\hat{\eta}(\omega)$.

We highlight that Hamiltonian (4.11) is for the open system $\mathcal{A} \oplus \mathcal{C}$, where the reservoir is eliminated, while Hamiltonians (4.2) and (4.7) both describe closed systems. Here, we expect that the annihilation operators a and c represent physically the same approximate modes. In the following we analyze these different representations by comparing the dynamics obtained via each Hamiltonian.

4.1.4 Comparison and validity of the different representations

We numerically analyze the validity of different representations described in Fig. 4.1. We consider a single atom trapped in the cavity and assume an initial condition with zero photons. To differentiate the parameters of different representations, we denote the quantities corresponding to the true-mode picture and the pseudomode

picture with a tilde and a hat, respectively. We commence by deriving the dynamics corresponding to the true-mode representation. Here, one can denote the basis as $|i\rangle|\alpha\rangle \equiv |i, \alpha\rangle$, with i labeling the atomic states and α describing the state of the continuum. The state in this basis can then be given by the following:

$$|\tilde{\psi}\rangle = \tilde{c}_{g,0}(t)|g, \emptyset\rangle + \tilde{c}_{e,0}(t)|e, \emptyset\rangle + \int_0^{+\infty} d\omega \tilde{c}_{f,1}(\omega, t)|f, \mathbf{1}_\omega\rangle, \quad (4.14)$$

with

$$a_\omega^\dagger|\emptyset\rangle = |\mathbf{1}_\omega\rangle, \quad (4.15a)$$

$$a_\omega|\mathbf{1}_{\omega'}\rangle = \delta(\omega - \omega')|\emptyset\rangle. \quad (4.15b)$$

Using Hamiltonian (4.2) in the time-dependent Schrödinger equation with state (4.14):

$$i\hbar \frac{\partial}{\partial t}|\tilde{\psi}\rangle = \tilde{H}|\tilde{\psi}\rangle, \quad (4.16)$$

we obtain the following dynamical equations:

$$i \frac{d}{dt} \tilde{c}_{g,0}(t) = \Omega \tilde{c}_{e,0}(t), \quad (4.17a)$$

$$i \frac{d}{dt} \tilde{c}_{e,0}(t) = \Delta \tilde{c}_{e,0}(t) + \Omega \tilde{c}_{g,0}(t) + i \int_0^{+\infty} d\omega \eta(\omega) \tilde{c}_{f,1}(\omega, t), \quad (4.17b)$$

$$i \frac{d}{dt} \tilde{c}_{f,1}(\omega, t) = (\Delta - \Delta_c + \omega - \omega_0) \tilde{c}_{f,1}(\omega, t) - i\eta^*(\omega) \tilde{c}_{e,0}(t), \quad (4.17c)$$

where $\eta(\omega)$ is the actual coupling function (4.5).

Pseudomode dynamics

If we take into account the approximation in (4.6), we can define the following coefficient:

$$\hat{c}_{f,1} = \frac{1}{\hat{g}} \int_0^{+\infty} d\omega \eta(\omega) \tilde{c}_{f,1}(\omega, t) = \frac{1}{\hat{g}} \int_0^{+\infty} d\omega \eta(\omega) e^{-i(\Delta - \Delta_c + \omega - \omega_0)t} \tilde{\underline{c}}_{f,1}(\omega, t), \quad (4.18)$$

where \hat{g} is the normalization factor and we have defined the quantity $\tilde{\underline{c}}_{f,1}(\omega, t) = e^{i(\Delta - \Delta_c + \omega - \omega_0)t} \tilde{c}_{f,1}(\omega, t)$. With this definition Eq. (4.17c) becomes

$$\frac{d}{dt} \tilde{\underline{c}}_{f,1}(\omega, t) = -\eta^*(\omega) e^{i(\Delta - \Delta_c + \omega - \omega_0)t} \tilde{c}_{e,0}(t). \quad (4.19)$$

Calculating the time derivative of Eq. (4.18) using the relation (4.19), and inverting the order of time and frequency integration we obtain:

$$\begin{aligned} \frac{d}{dt} \hat{c}_{f,1}(t) &= \frac{d}{dt} \hat{c}_{f,1}^{(0)}(t) - \frac{1}{\hat{g}} \int_0^{+\infty} d\omega |\eta(\omega)|^2 \tilde{c}_{e,0}(t) \\ &\quad + \frac{i}{\hat{g}} \int_0^t dt' \tilde{c}_{e,0}(t') \int_0^{+\infty} d\omega |\eta(\omega)|^2 (\Delta - \Delta_c + \omega - \omega_0) e^{-i(\Delta - \Delta_c + \omega - \omega_0)(t-t')}, \end{aligned} \quad (4.20)$$

where we introduced the time derivative of the coefficient at an initial time, defined as

$$\hat{c}_{f,1}^{(0)}(t) = \frac{1}{\hat{g}} \int_0^{+\infty} d\omega \eta(\omega) e^{-i(\Delta - \Delta_c + \omega - \omega_0)t} \tilde{\underline{c}}_{f,1}(\omega, 0). \quad (4.21)$$

Two integrals appear in (4.20) that are evaluated in Appendix A.5, leading to

$$\mathcal{I}_1 = \int_0^{+\infty} d\omega |\eta(\omega)|^2 \approx \frac{\omega_0 |d_{fe}|^2}{\hbar \varepsilon_0 \mathcal{A} \ell_c} \sin^2 \left[\frac{\omega_0}{c} (x_A + \ell_c) \right], \quad (4.22)$$

$$\begin{aligned} \mathcal{I}_2 &= \int_0^{+\infty} d\omega |\eta(\omega)|^2 (\Delta - \Delta_c + \omega - \omega_0) e^{-i(\Delta - \Delta_c + \omega - \omega_0)(t-t')} \\ &\approx \frac{\omega_0 |d_{fe}|^2}{2\hbar \varepsilon_0 \mathcal{A} \ell_c} \left(\Delta - \Delta_c - i \frac{\Gamma_c}{2} \right) e^{-i(\Delta - \Delta_c - i \frac{\Gamma_c}{2})(t-t')} \sin^2 \left[\frac{\omega_0}{c} (x_A + \ell_c) \right], \end{aligned} \quad (4.23)$$

which are obtained under the approximation $\epsilon_1^2 \ll 1$, with $\epsilon_1 = \frac{\Gamma_c}{c} (x_A + \ell_c)$. From the value for the integral \mathcal{I}_1 , we can deduce the expression of the normalization coefficient \hat{g} :

$$|\hat{g}|^2 = \frac{\omega_0 |d_{fe}|^2}{\hbar \varepsilon_0 \mathcal{A} \ell_c} \sin^2 \left[\frac{\omega_0}{c} (x_A + \ell_c) \right] = \mathcal{I}_1, \quad (4.24)$$

leading to

$$\hat{g} = i \sqrt{\frac{\omega_0}{\hbar \varepsilon_0 \mathcal{A} \ell_c}} d_{fe} \sin \left[\frac{\omega_0}{c} (x_A + \ell_c) \right]. \quad (4.25)$$

Having the evaluation of these integrals, we can now rewrite the dynamical equation (4.20) as follows:

$$\frac{d}{dt} \hat{c}_{f,1} = \frac{d}{dt} \hat{c}_{f,1}^{(0)}(t) - \hat{g}^* \tilde{c}_{e,0}(t) + i \hat{g}^* \int_0^t dt' \tilde{c}_{e,0}(t') \left(\Delta - \Delta_c - i \frac{\Gamma_c}{2} \right) e^{-i(\Delta - \Delta_c - i \frac{\Gamma_c}{2})(t-t')}. \quad (4.26)$$

To evaluate the time integral appearing in this expression, we first formally integrate equation (4.19) and put the result in (4.18), it can be shown that

$$\hat{c}_{f,1}(t) - \hat{c}_{f,1}^{(0)} = -\frac{1}{\hat{g}} \int_0^\infty d\omega |\hat{\eta}(\omega)|^2 \int_0^t dt' \tilde{c}_{e,0}(t') e^{-i(\Delta - \Delta_c - i \frac{\Gamma_c}{2})(t-t')} \quad (4.27)$$

$$= -\hat{g}^* \int_0^t dt' \tilde{c}_{e,0}(t') e^{-i(\Delta - \Delta_c - i \frac{\Gamma_c}{2})(t-t')}, \quad (4.28)$$

hence Eq. (4.26) becomes

$$\frac{d}{dt} \hat{c}_{f,1}(t) = \frac{d}{dt} \hat{c}_{f,1}^{(0)}(t) - \hat{g}^* \tilde{c}_{e,0}(t) - i \left(\Delta - \Delta_c - i \frac{\Gamma_c}{2} \right) \left(\hat{c}_{f,1}(t) - \hat{c}_{f,1}^{(0)} \right). \quad (4.29)$$

Considering that at initial time $t = 0$ the atom is in its ground state and there is no photon in the environment ($\tilde{c}_{f,1}(\omega, 0) = 0$), the above equation reduces to

$$\frac{d}{dt} \hat{c}_{f,1}(t) = -\hat{g}^* \tilde{c}_{e,0}(t) - i \left(\Delta - \Delta_c - i \frac{\Gamma_c}{2} \right) \hat{c}_{f,1}(t). \quad (4.30)$$

Moreover, we can redefine the normalization factor \hat{g} : $g = i \hat{g}$, which is the atom-cavity coupling defined in Eq. (4.7), leading to the approximate atom-true mode coupling (4.8).

Taking these results into account, we can define the photon state of the cavity as:

$$|1\rangle = \frac{1}{g} \int_0^{+\infty} d\omega \hat{\eta}^*(\omega) \hat{a}_\omega^\dagger |\emptyset\rangle. \quad (4.31)$$

Consequently, recalling Eq. (4.17), we can get the dynamics corresponding to the pseudomode representation, on a reduced basis $\{|g, \emptyset\rangle, |e, \emptyset\rangle, |f, 1\rangle\}$, for the state given by

$$|\psi_{\text{eff}}\rangle = \hat{c}_{g,0}(t)|g, \emptyset\rangle + \hat{c}_{e,0}(t)|e, \emptyset\rangle + \hat{c}_{f,1}(t)|f, 1\rangle :$$

$$i\frac{d}{dt}\hat{c}_{g,0}(t) = \Omega\hat{c}_{e,0}(t), \quad (4.32a)$$

$$i\frac{d}{dt}\hat{c}_{e,0}(t) = \Delta\hat{c}_{e,0}(t) + \Omega\hat{c}_{g,0}(t) + g\hat{c}_{f,1}(t) \quad (4.32b)$$

$$i\frac{d}{dt}\hat{c}_{f,1}(t) = \left(\Delta - \Delta_c - i\frac{\Gamma_c}{2}\right)\hat{c}_{f,1}(t) + g\hat{c}_{e,0}(t), \quad (4.32c)$$

which leads to the Hamiltonian in (4.11).

Inside-outside dynamics

Unlike the case of the true-mode picture, in the inside-outside representation there is a separation of the photon state into inside and outside ones. Thus the basis splits into the following states: $\{|g, \emptyset\rangle, |e, \emptyset\rangle, |f, 1_{\text{ins}}, \emptyset_{\text{outs}}\rangle, |f, \emptyset_{\text{ins}}, 1_{\omega, \text{outs}}\rangle\}$, where the indices “ins” and “outs” indicate the photon state inside and outside the cavity, respectively, and

$$c^\dagger|\emptyset\rangle = |1_{\text{ins}}\rangle, \quad (4.33a)$$

$$c|1_{\text{ins}}\rangle = |\emptyset\rangle, \quad (4.33b)$$

$$b_\omega^\dagger|\emptyset\rangle = |1_{\omega, \text{outs}}\rangle, \quad (4.33c)$$

$$b_\omega|1_{\omega', \text{outs}}\rangle = \delta(\omega - \omega')|\emptyset\rangle. \quad (4.33d)$$

The dynamical equations corresponding to the Hamiltonian (4.7) with the state

$$|\psi\rangle = c_{g,0}(t)|g, \emptyset\rangle + c_{e,0}(t)|e, \emptyset\rangle + c_{f,1,0}(t)|f, 1_{\text{ins}}, \emptyset_{\text{outs}}\rangle + \int_0^{+\infty} d\omega c_{f,0,1}(\omega, t)|f, \emptyset_{\text{ins}}, 1_{\omega, \text{outs}}\rangle \quad (4.34)$$

become

$$i\frac{d}{dt}c_{g,0}(t) = \Omega c_{e,0}(t), \quad (4.35a)$$

$$i\frac{d}{dt}c_{e,0}(t) = \Delta c_{e,0}(t) + \Omega c_{g,0}(t) + g c_{f,1,0}(t), \quad (4.35b)$$

$$i\frac{d}{dt}c_{f,1,0}(t) = (\Delta - \Delta_c)c_{f,1,0} + g c_{e,0}(t) - i \int_0^{+\infty} d\omega \kappa_c^*(\omega) c_{f,0,1}(\omega, t), \quad (4.35c)$$

$$i\frac{d}{dt}c_{f,0,1}(\omega, t) = (\Delta - \Delta_c + \omega - \omega_0) c_{f,0,1}(\omega, t) + i\kappa_c(\omega) c_{f,1,0}(t). \quad (4.35d)$$

In order to examine the validity limits of the approximate models derived above, we compare the dynamics via solving Eqs. (4.17), (4.32), and (4.35) [see details of the integration of Eqs. (4.17) and (4.35) in Appendix A.6]. For this analysis, the way the atom is driven to its excited state is irrelevant. Thus we assume that

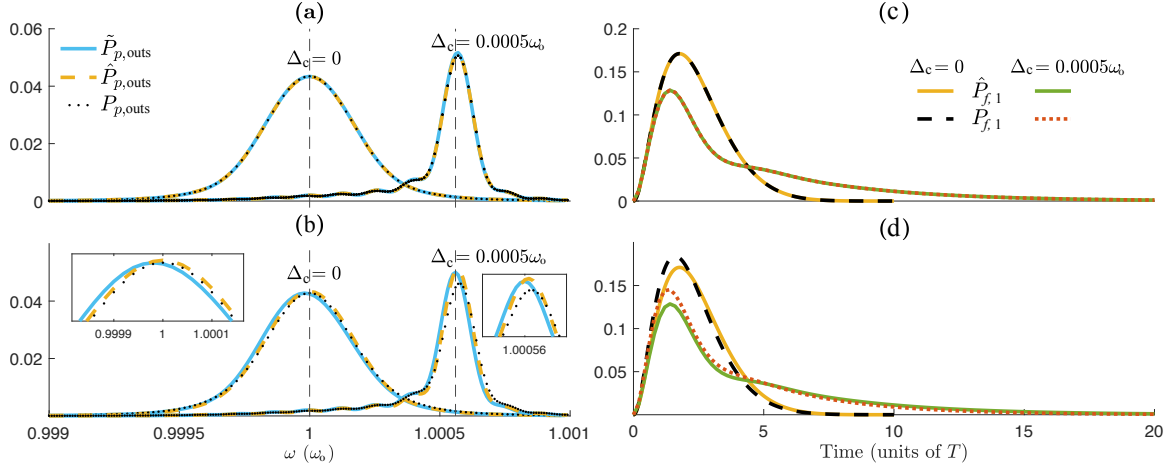


Figure 4.3: Comparison of the single-photon shape obtained via true-mode, inside-outside, and pseudomode pictures. (a) and (b) Spectral shape of the outgoing photon with $(g, \Gamma_c, \omega_m) \times T = (0.6, 2, 2416)$, where $\omega_m = m \frac{\pi c}{\ell_c}$, m being the number of antinodes inside the cavity. Each curve corresponds to a different representation: $\tilde{P}_{p,\text{outs}} = |\tilde{\mathbf{c}}_{f,1}(\omega, t_f)|^2$ (true-mode picture), $\hat{P}_{p,\text{outs}} = |\hat{\mathbf{c}}_{f,1}(\omega, t_f)|^2$ (pseudomode picture), and $P_{p,\text{outs}} = |\mathbf{c}_{f,0,1}(\omega, t_f)|^2$ (inside-outside picture; see the definition of the dimensionless parameters \mathbf{c}_i in Appendix A.6), where t_f is the final time when the photon is in its steady state. In (a), $t_f/T = 10$, $\Gamma_c = 2/T$ is obtained for a cavity with a length $\ell_c = \ell_0$ and a fictitious refractive index $n_1 = 27.735$, leading to the reflectivity $R = |r|^2 = e^{-2\ell_c \Gamma_c / c} \approx 0.995$ (with $\frac{\ell_0}{cT} = 0.0013$), where ℓ_0 is the length for which the cavity sustains a single fundamental mode, i.e., $m = 1$. In (b), $t_f/T = 20$, $\ell_c = 165\ell_0$ and $n_1 = 2.1756$, leading to the same $\Gamma_c = 2/T$, for the $m = 165$ th mode, with the reflectivity $R \approx 0.42$.

(c) and (d) Time profiles of the outgoing photon, with the figures (c) and (d) obtained via the same parameters introduced in (a) and (b), respectively. $\hat{P}_{f,1} = |\hat{\mathbf{c}}_{f,1}(t)|^2$, $P_{f,1} = |\mathbf{c}_{f,1,0}(t)|^2$ are the coefficients derived from the pseudo-mode and inside-outside representations, respectively.

the atom is initially in the excited state $|e\rangle$ and there is no laser field applied, i.e. $\Omega = 0$. We analyze a regime where there are no Rabi oscillations between the atom and the produced photon, i.e., the leakage from the cavity is stronger than the atom-cavity coupling: $\Gamma_c > g$. Both the effective Hamiltonian and the inside-outside representation are derived under the assumption of having a high- Q cavity, i.e., $\Gamma_c \ll \omega_0$. In Fig. 4.3, we present the results obtained via different representations for a cavity with a fixed quality factor: $\omega_0/\Gamma_c \approx 1200$. This factor is obtained either by fixing the mirror refractive index and changing the length of the cavity or vice versa. In Fig. 4.3(a), the cavity length is such that it sustains half a wavelength of cavity resonance wavelength λ_0 : $\ell_c = \ell_0 = \lambda_0/2$. Therefore, there is only a single mode that the atom can couple to, making the cavity finesse the same as the quality factor: $\Delta_{\omega_m}/\Gamma_c \approx 1200$. We recall that the spectral shape of the photon in pseudomode representation is recovered using the true-mode representation with a coupling $\hat{\eta}(\omega)$, taking into account the relation in Eq. (4.13). As we can see from the figure, both for detuned and nondetuned cases, the photons obtained with pseudomode and inside-outside representations match the true-mode representation obtained from eq. (4.17),

with the coupling (4.5)¹. Furthermore, in Fig. 4.3(b), we consider a cavity of longer length and a mirror of lower refractive index. To have the same atom-cavity coupling rate, we change the value of the dipole moment of the atom. While having the same quality factor, here we get a cavity finesse $\Delta_{\omega_m}/\Gamma_c \approx 7$. This low finesse makes the transition from eq. (4.5) to eq. (4.6) less accurate, i.e., the Lorentzians corresponding to each mode are not separated well enough to consider $\sqrt{\sum f_m} \approx \sum \sqrt{f_m}$. We emphasize that the approximation (4.6) is used in the derivation of the pseudo-mode picture as well as the inside-outside representation. Hence, it leads to a mismatch between the approximate and the actual representations. Equivalently, as shown in Appendix A.5, in order for the pseudomode derivation to work, the following condition should hold: $\left(\frac{\Gamma_c}{c}(x_A + \ell_c)\right)^2 \ll 1$. Evidently, when we increase the cavity length while keeping Γ_c the same, this condition is not well satisfied, breaking the validity of this representation. On the other hand, as mentioned before, the inside-outside representation is derived for the cavities with low transmission rate, given by $|t|^2 = 1 - e^{-2\ell_c\Gamma_c/c}$ [see Eq. (3.31a)]. For this long-cavity scenario, similar to the previous argument, this term fails to satisfy the condition $|t|^2 \ll 1$ ($|t|^2 \approx 0.58$), which leads to the mismatch between the inside-outside and the true-mode representations. Finally, we can notice that even in the case of $\Delta_c = 0$, the photon obtained from the actual model is slightly shifted from the resonance frequency ω_0 . This is because in the actual model where we use the response function $T(\omega)$, apart from the fundamental mode ω_0 , there are other modes, which, combined with the low finesse of the cavity, affect the produced photon.

In Figs. 4.3(c) and 4.3(d), we study the corresponding photon shape in the time domain. Here we compare the cavity photon obtained from the pseudo-mode $[\hat{c}_{f,1}(t)]$ and the inside-outside representations $[c_{f,1,0}(t)]$. As we can see from Eq. (4.32), the photon inside the cavity $\hat{c}_{f,1}(t)$ depends only on the parameters Γ_c and g , and these parameters are fixed, hence $\hat{P}_{f,1}$ is the same both for high (top figure) and low (bottom figure) finesse scenarios. On the other hand, in the inside-outside representation, the coupling $\kappa_c(\omega)$ explicitly depends on the cavity length, leading to different curves for the coefficient $P_{f,1}$. This, combined with the arguments introduced in the analysis of Figs. 4.3(a) and (b), lead to the differences between the photon obtained via pseudomode and inside-outside representations.

In the following, we derive the well-known master equation starting from the inside-outside representation. We use a method different from the standard derivation obtained by phenomenological use of the pseudo-mode Hamiltonian.

4.2 Heisenberg-Langevin equations, Poynting vector, photon density, and photon flux

We wish to derive the effective dynamics of the atom-cavity system $\mathcal{S} = \mathcal{A} \oplus \mathcal{C}$, coupled to the reservoir, from first principles. Our aim is to control the production of an outgoing photon leaking from the cavity by driving specifically the atom in the cavity by the external field. We will use the convenient inside-outside representation as it will allow a clear identification and characterization of the leaking photon

¹In the simulation we use the actual response function (3.24) derived for a single-layered mirror with the atom placed at $x_a = -\ell_c/2$.

propagating in free space. Here, we study the case presented in Fig. 4.2, where the atom is initially in the ground state, and we consider the two-photon resonance condition: $\Delta = \Delta_c$, leading to $\omega_{\text{gf}} = \omega_0 - \omega_L$. We use the Poynting vector that we derive from the true-mode representation and define in the Heisenberg picture. We highlight that one could use the Poynting vector derived in Ref. [16] in free space and apply it to the situation with the presence of a cavity; however, as we show below, the Poynting vector that we derive from first principles is different from this one. We then derive the effective model in two steps: We first define an outgoing flux of photons which is connected to the quantum average of the Heisenberg evolution of the cavity operator $c^\dagger c$. Next, we derive a master equation of the system \mathcal{S} by eliminating the reservoir degrees of freedom, which will allow the calculation of the quantum averages.

4.2.1 Derivation of the Poynting vector: photon number density and flux

During the photon detection process, the detector measures the energy density at its position [see Fig. 4.4]. Thus, considering that the energy carried by the photons leaking from the cavity can be characterized by the Poynting vector [52, 16], one can use this quantity to describe the photon profile. The Poynting vector of the photon produced in the cavity (placed at position $x = 0$) and propagating in the positive x direction can be calculated using the modes $\Phi_{\omega, \text{outs}}(x)$, derived for the outside of the cavity in the true-mode representation [Eq. (3.22)]:

$$S_{\text{outs}}(x) = -\frac{1}{2\mu_0}(B_{\text{outs}}(x)E_{\text{outs}}(x) + E_{\text{outs}}(x)B_{\text{outs}}(x)) \quad (4.36)$$

where

$$E_{\text{outs}}(x) = \frac{i}{\sqrt{2\pi c \mathcal{A}}} \int_0^\infty d\omega \sqrt{\frac{\hbar\omega}{2\epsilon_0}} \left((G(\omega)e^{i\frac{\omega}{c}x} - e^{-i\frac{\omega}{c}x}) a_\omega - H.C. \right), \quad (4.37)$$

$$B_{\text{outs}}(x) = -\frac{i}{c\sqrt{2\pi c \mathcal{A}}} \int_0^\infty d\omega \sqrt{\frac{\hbar\omega}{2\epsilon_0}} \left((G(\omega)e^{i\frac{\omega}{c}x} + e^{-i\frac{\omega}{c}x}) a_\omega - H.C. \right), \quad (4.38)$$

with

$$G(\omega) = e^{2i\frac{\omega}{c}\ell_c} \frac{T(\omega)}{T^*(\omega)} \approx \sqrt{\frac{2\pi}{\Gamma_c}} \sqrt{\frac{\omega_0}{\omega}} \alpha^*(\omega) \left(\omega - \omega_0 - i\frac{\Gamma_c}{2} \right). \quad (4.39)$$

$\alpha(\omega)$ is the coefficient linking the true mode a_ω to the discrete cavity mode c : $a_\omega = \alpha(\omega)c + \int_0^\infty d\omega' \beta(\omega, \omega') b_{\omega'}$ (the explicit derivation of this term for more realistic cavities is demonstrated in Part III, Chapter 7), and can be written as follows [see Eq. (7.23a)]:

$$\alpha(\omega) = \sqrt{\frac{\omega}{\omega_0}} \sqrt{\frac{\ell_c}{\pi c}} \text{sinc} \left((\omega - \omega_0) \frac{\ell_c}{c} \right) e^{-i\frac{\omega}{c}\ell_c} T^*(\omega). \quad (4.40)$$

Taking these into account we get the following Poynting vector, for the propagation in the positive x direction:

$$S_{\text{outs}}(x) = \frac{\hbar}{2\pi \mathcal{A}} \int_0^\infty d\omega d\omega' \sqrt{\omega\omega'} \text{Re} \left\{ G(\omega) G^*(\omega') e^{i\frac{(\omega-\omega')}{c}x} a_{\omega'}^\dagger a_\omega \right\}. \quad (4.41)$$

Furthermore, by moving from the true-mode representation to the inside-outside representation via writing a_ω in terms of the outside operator: $a_\omega = \int d\omega' \beta(\omega, \omega') b_{\omega'}$ and considering that [52]

$$i \int d\omega d\omega' \omega \alpha^*(\omega) \beta(\omega, \omega') b_{\omega'} = \int d\omega \kappa_c^*(\omega) b_\omega \quad (4.42)$$

(see Appendix B.6), we obtain the following:

$$S_{\text{outs}}(x) = \frac{\hbar \omega_0}{\mathcal{A} \Gamma_c} \int_0^\infty d\omega d\omega' \kappa_c^*(\omega) \kappa_c(\omega') e^{i \frac{(\omega - \omega')}{c} x} b_{\omega'}^\dagger b_\omega. \quad (4.43)$$

Via introducing the integrated reservoir operator defined as

$$b(x) = \frac{1}{\sqrt{\Gamma_c}} \int_0^\infty d\omega \kappa_c^*(\omega) e^{i \frac{\omega}{c} x} b_\omega, \quad (4.44)$$

the expression for the Poynting vector becomes

$$S_{\text{outs}}(x) = \frac{\hbar \omega_0}{\mathcal{A}} b^\dagger(x) b(x). \quad (4.45)$$

It shows that the Poynting vector includes the coupling between inside and outside the cavity.

Moreover, recalling the Poynting theorem [52, 70], for the expectation value of the Poynting vector corresponding to the energy flow of linearly polarized light propagating in one-dimensional space, we can write the following:

$$\frac{\partial}{\partial x} \langle S_{\text{outs}}(x) \rangle_{|\psi(t)\rangle} + \frac{\partial}{\partial t} \langle U_{\text{outs}}(x) \rangle_{|\psi(t)\rangle} = 0, \quad (4.46)$$

where $\langle U_{\text{outs}}(x) \rangle_{|\psi(t)\rangle}$ is the expectation value of the electromagnetic energy density and $|\psi(t)\rangle$ is the wavefunction (4.34) corresponding to the inside-outside representation. As we show below [Eq. (4.68b)], if we write the Poynting vector (4.45) in the Heisenberg representation, i.e., via operator $b(x, t)$ in Eq (4.63), it can be shown that this term depends only on $t - x/c$. Taking this into account, Eq. (4.46) can be equivalently written as

$$-\frac{\partial}{c \partial t} \langle S_{\text{outs}}(x) \rangle_{|\psi(t)\rangle} + \frac{\partial}{\partial t} \langle U_{\text{outs}}(x) \rangle_{|\psi(t)\rangle} = 0, \quad (4.47)$$

$$\frac{\partial}{\partial x} \langle S_{\text{outs}}(x) \rangle_{|\psi(t)\rangle} - c \frac{\partial}{\partial x} \langle U_{\text{outs}}(x) \rangle_{|\psi(t)\rangle} = 0, \quad (4.48)$$

leading to the following relation between the Poynting vector and the energy density:

$$\frac{\langle S_{\text{outs}}(x) \rangle_{|\psi(t)\rangle}}{c} = \langle U_{\text{outs}}(x) \rangle_{|\psi(t)\rangle}. \quad (4.49)$$

Using the fact that we are considering a quasi-monochromatic state, one can define an averaged coarse-grained photon number density propagating through the area \mathcal{A} at a position x by

$$\Phi_{\text{density}}(x, t) := \frac{\mathcal{A}}{\hbar \omega_0} \langle U_{\text{outs}}(x) \rangle_{|\psi(t)\rangle}, \quad (4.50)$$

which using (4.49) can be expressed in terms of the averaged Poynting vector as

$$\Phi_{\text{density}}(x, t) := \frac{\mathcal{A}}{\hbar\omega_0} \frac{\langle S_{\text{outs}}(x) \rangle_{|\psi(t)\rangle}}{c} = \frac{1}{c} \langle b^\dagger(x)b(x) \rangle_{|\psi(t)\rangle} = \langle b_x^\dagger b_x \rangle_{|\psi(t)\rangle}, \quad (4.51)$$

where we have defined the operator

$$b_x^\dagger = \frac{1}{\sqrt{c}} b^\dagger(x) = \frac{1}{\sqrt{c}\Gamma_c} \int_0^\infty d\omega \kappa_c(\omega) e^{-i\frac{\omega}{c}x} b_\omega^\dagger, \quad (4.52)$$

which satisfies the following commutation relations (see Appendix A.7):

$$[b_x, b_x^\dagger] = \frac{1}{2\ell_c}, \quad (4.53)$$

$$[b_x, b_{x'}^\dagger] = 0, \quad \text{when } |x - x'| > 2\ell_c. \quad (4.54)$$

Taking this definition into account, the total photon number outside the cavity ($x > 0$) can be written as follows:

$$N(t) = \int_0^\infty dx \langle b_x^\dagger b_x \rangle_{|\psi(t)\rangle}, \quad (4.55)$$

with $\langle b_x^\dagger b_x \rangle_{|\psi(t)\rangle}$ being the mean value of photon number density at a position x . We remark that this definition is possible due to the fact that we consider a one-dimensional model for the propagating light and limit the study to a single mode ω_0 , which is justified by the fact that when there is an emitter trapped in such a cavity, the cavity-emitter coupling is designed such that the emitter couples to a single cavity mode, therefore selecting single mode ω_0 . As discussed in literature [61, 70, 133], in a more general case, a definition of a local photon number operator or a local energy density is not possible since the process of projecting out the transverse and longitudinal part of a vector field is a nonlocal operation in position space. However in the particular case discussed here, we are able to define such a local operator in a so-called coarse-grained limit, due to the explicit form of $\kappa_c(\omega)$ in the definition (4.52) (see the discussion in Appendix A.7).

Furthermore, considering that for a given state, the amount of energy going through the field mode area \mathcal{A} , during the time dt , is the quantum average of the flux of the Poynting vector through this area: $\mathcal{A} \langle S_{\text{outs}}(x) \rangle_{|\psi(t)\rangle} dt = \hbar\omega_0 \langle b^\dagger(x)b(x) \rangle_{|\psi(t)\rangle} dt$, by normalizing this expression by $\hbar\omega_0$, we get the averaged number of photons $dn(x, t) \equiv \langle b^\dagger(x)b(x) \rangle_{|\psi(t)\rangle} dt$ going through the mode area during dt , defining the photon flux:

$$\Phi_{\text{flux}}(x, t) := \frac{dn(x, t)}{dt} = \left\langle b^\dagger(x)b(x) \right\rangle_{|\psi(t)\rangle}, \quad (4.56)$$

which is related to the photon number density (4.51) by the following relation

$$\Phi_{\text{flux}}(x, t) = c \Phi_{\text{density}}(x, t). \quad (4.57)$$

Additionally, we can define a general photon state outside the cavity as

$$|1_{\text{outs}}(t)\rangle = \int_0^{+\infty} d\omega \hat{\Psi}(\omega, t) b_\omega^\dagger |\emptyset\rangle, \quad (4.58)$$

with the shape $\hat{\Psi}(\omega, t)$, where the time dependence appears in the phase corresponding to the propagation such that at all times t

$$\int_0^\infty d\omega |\hat{\Psi}(\omega, t)|^2 = 1, \quad (4.59)$$

which satisfies

$$N = \int_0^\infty dx \left\langle b_x^\dagger b_x \right\rangle_{|1_{\text{outs}}(t)\rangle} = 1. \quad (4.60)$$

We remark that b_x^\dagger cannot be interpreted as an operator that creates a photon at position x ; such operator does not exist since the mode of the photon is non-local [61, 70].

4.2.2 Equations of motion for the operators – Heisenberg representation

In the above derivations, we have considered time-independent operators in the Schrödinger representation, where the time dependence is in the wavefunction. Here we move to the Heisenberg representation and derive the equations of motion in the Heisenberg picture for the time-dependent reservoir operator $b_\omega(t) \equiv \hat{U}^\dagger(t, t_0) b_\omega \hat{U}(t, t_0)$ with $\hat{U}(t, t_0)$ being the propagator of the total Hamiltonian $H(t)$, whose Heisenberg picture reads $H^{(H)}(t) = \hat{U}^\dagger(t, t_0) H(t) \hat{U}(t, t_0)$. From $\dot{\mathcal{O}} = -\frac{i}{\hbar} [\mathcal{O}(t), H^{(H)}(t)]$ for an operator \mathcal{O} , assumed to be time independent in the Schrödinger picture and written as $\mathcal{O}^{(H)}(t) \equiv \mathcal{O}(t) = \hat{U}^\dagger(t, t_0) \mathcal{O} \hat{U}(t, t_0)$ in the Heisenberg picture, we write the Heisenberg-Langevin equations:

$$\dot{b}_\omega(t) = -i\omega b_\omega(t) + \kappa_c(\omega) c(t), \quad (4.61a)$$

$$\dot{c}(t) = -i\omega_0 c(t) - \int_0^{+\infty} d\omega \kappa_c^*(\omega) b_\omega(t) - ig\sigma(t). \quad (4.61b)$$

In the following, we omit the “ (H) ” superscript for the Heisenberg picture Hamiltonian $H^{(H)}(t) \equiv H(t)$. The energy carried by the photons leaking from the cavity can be characterized by the Poynting vector operator in the Heisenberg or Schrödinger picture, thus, in the following, we write the expressions derived above for the Poynting vector in the Heisenberg picture:

$$S_{\text{outs}}(x, t) = \frac{\hbar\omega_0}{\mathcal{A}} b^\dagger(x, t) b(x, t), \quad (4.62)$$

where $b(x, t)$ is the Heisenberg representation of the integrated reservoir operator (4.44):

$$b(x, t) := \frac{1}{\sqrt{\Gamma_c}} \int_0^\infty d\omega \kappa_c^*(\omega) e^{i\frac{\omega}{c}x} b_\omega(t). \quad (4.63)$$

Similarly, relation (4.49) in the Heisenberg representation becomes

$$\frac{\langle S_{\text{outs}}(x, t) \rangle_{|\psi(t_0)\rangle}}{c} = \langle U_{\text{outs}}(x, t) \rangle_{|\psi(t_0)\rangle}, \quad (4.64)$$

where $|\psi(t_0)\rangle$ is the initial state. Furthermore, for the photon number density and flux, we can write

$$\Phi_{\text{density}}(x, t) = \frac{\mathcal{A}}{\hbar\omega_0} \frac{\langle S_{\text{outs}}(x, t) \rangle}{c} = \frac{1}{c} \langle b^\dagger(x, t)b(x, t) \rangle = \langle b_x^\dagger(t)b_x(t) \rangle, \quad (4.65)$$

$$\Phi_{\text{flux}}(x, t) = \frac{\mathcal{A}}{\hbar\omega_0} \langle S_{\text{outs}}(x, t) \rangle = \langle b^\dagger(x, t)b(x, t) \rangle, \quad (4.66)$$

where we have defined the Heisenberg representation of the operator b_x :

$$b_x^\dagger(t) = \frac{1}{\sqrt{c}} b^\dagger(x, t) = \frac{1}{\sqrt{c}\Gamma_c} \int_0^\infty d\omega \kappa_c(\omega) e^{-i\frac{\omega}{c}x} b_\omega^\dagger(t). \quad (4.67)$$

4.2.3 Integrated reservoir operators: Input-output relation

In eq. (4.63) we have defined the integrated reservoir operator, which we can evaluate by integrating (4.61a) from an initial time t_0 to t ,

$$b(x, t) := \frac{1}{\sqrt{\Gamma_c}} \int_0^{+\infty} d\omega \kappa_c^*(\omega) b_\omega(t) e^{i\omega\frac{x}{c}} \quad (4.68a)$$

$$= b_{\text{in}}\left(t - \frac{x}{c}\right) + \int_{t_0}^t dt' \int_0^{+\infty} d\omega \frac{|\kappa_c(\omega)|^2}{\sqrt{\Gamma_c}} c(t') e^{-i\omega(t-t')} e^{i\omega\frac{x}{c}}, \quad (4.68b)$$

with the *input* operator defined similarly:

$$b_{\text{in}}\left(t - \frac{x}{c}\right) := \frac{1}{\sqrt{\Gamma_c}} \int_0^{+\infty} d\omega \kappa_c^*(\omega) b_\omega(t_0) e^{-i\omega(t-t_0-\frac{x}{c})}. \quad (4.69)$$

One can notice that the definition (4.68a) is different from the standard definition, where $b(x, t)$ is defined via a Fourier transform of b_ω [69, 77, 153] and a flat continuum (see Appendix A.4). Instead, here, from the definition of the Poynting vector, we have the natural introduction of the function $\kappa_c(\omega)$ in the definition, and its explicit form allows one to straightforwardly derive the equation for the output operator.

In order to evaluate the integral over the frequency in (4.68b), we use the expression (4.10). This gives for the integrated reservoir operator (see details in Appendix A.8):

$$b(x, t) = b_{\text{in}}\left(t - \frac{x}{c}\right) + \sqrt{\Gamma_c} c \left(t - \frac{x}{c}\right), \quad (4.70)$$

where we have assumed $t \gg \frac{2\ell_c}{c}$, $t > t_0 + \frac{x}{c} + \frac{2\ell_c}{c}$. We further neglect the cavity length, assuming that the traveling distance of interest is much larger than the cavity length. Also, considering that the dynamics evolves over a much longer period of time than the round trip time $\frac{2\ell_c}{c}$ of the produced photon (coarse-grained approximation), we get $t \gg 0$, $t > t_0 + \frac{x}{c}$ and $x > 0$. We define the *output* operator

$$b_{\text{out}}(t - x/c) := b(x > 0, t); \quad (4.71)$$

hence,

$$b_{\text{out}}\left(t - \frac{x}{c}\right) = b_{\text{in}}\left(t - \frac{x}{c}\right) + \sqrt{\Gamma_c} c \left(t - \frac{x}{c}\right), \quad (4.72)$$

which is recognized as the input-output relation [69]. We highlight that the input-output relation here is a consequence of the concrete form of $\kappa_c(\omega)$ [Eq. (4.10)],

which justifies thus the Markov approximation. This formulation allows direct and transparent interpretation of the b_{out} operator through the Poynting vector as shown below [see Eq. (4.76)].

At the cavity position, $x = 0$, we obtain the integrated reservoir operator (see Appendix A.8):

$$b_0(t) \equiv b(x = 0, t) = b_{\text{in}}(t) + \frac{\sqrt{\Gamma_c}}{2} c(t). \quad (4.73)$$

This expression (4.73) is used in the next section to derive the master equation in the cavity.

We can also simplify the Heisenberg-Langevin equation for $c(t)$ as:

$$\dot{c}(t) = -\left(i\omega_0 + \frac{\Gamma_c}{2}\right)c(t) - \sqrt{\Gamma_c}b_{\text{in}}(t) - ig\sigma(t). \quad (4.74)$$

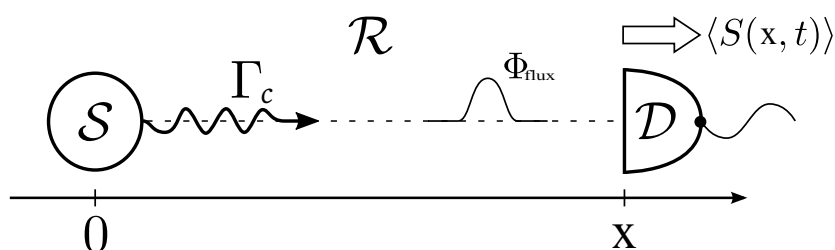


Figure 4.4: Sketch of the photodetection: The source system \mathcal{S} emits a photon with leakage Γ_c at position 0, towards a detector \mathcal{D} at a position x through the reservoir \mathcal{R} . The photon flux Φ_{flux} is measured using the data on the averaged quantized Poynting vector $\langle S(x, t) \rangle$.

Using the results obtained in the previous section, we can write the Poynting vector (4.62) in the inside-outside representation as follows:

$$S_{\text{outs}}(x > 0, t) = \frac{\hbar\omega_0}{\mathcal{A}} b^\dagger\left(t - \frac{x}{c}\right) b\left(t - \frac{x}{c}\right), \quad (4.75)$$

leading to the following expression for the photon flux (written here for $x > 0$):

$$\Phi_{\text{flux}}(x, t) = \left\langle b^\dagger\left(t - \frac{x}{c}\right) b\left(t - \frac{x}{c}\right) \right\rangle. \quad (4.76)$$

Recalling that $b(t - x/c)$ is the output operator (4.71), we emphasize that this relation gives the connection between the photon flux and this output operator.

If we choose the state of the reservoir to be initially a vacuum state: $\rho(t_0) = \rho_S(t_0) \otimes |\emptyset\rangle\langle\emptyset|$, the average of the terms involving $b_{\text{in}}, b_{\text{in}}^\dagger$ in the expression of the flux (4.76) is nullified. This gives the expression of the outgoing photon flux through the semi-transparent mirror for $t > t_0 + \frac{x}{c}, x > 0$:

$$\Phi_{\text{flux}}(x, t) = \Gamma_c \left\langle c^\dagger\left(t - \frac{x}{c}\right) c\left(t - \frac{x}{c}\right) \right\rangle. \quad (4.77)$$

This key result shows that one can determine the flux from the quantum average of the dynamics of the cavity photon number [74].

In the following section, we derive the effective master equation reduced to the system \mathcal{S} which is used to calculate the quantum average of (4.76) in order to derive the flux.

4.2.4 The master equation for the system dynamics

The dynamics of the system $\mathcal{S} = \mathcal{A} \oplus \mathcal{C}$, consisting of the atom and the cavity, derived from the above inside-outside representation can be characterized by a master equation which is shown to be of Lindblad form. We follow the derivation of Refs. [20, 26, 69, 127]. We need first to derive the Heisenberg equation of motion of the operators $X_S(t) = U^\dagger(t, t_0)X_S U(t, t_0)$ of the system in the Heisenberg picture.

The dynamics of $X_S(t)$ is determined from the Heisenberg-Langevin equation (see details of the following calculation in Appendix A.9):

$$\begin{aligned} \frac{d}{dt}X_S(t) = & -\frac{i}{\hbar}\left[X_S(t), H_S^{(H)}(t)\right] + \mathcal{D}_{\text{in},t}^\dagger(X_S(t)) \\ & + \Gamma_c\left(c^\dagger(t)X_S(t)c(t) - \frac{1}{2}\{c^\dagger(t)c(t), X_S(t)\}\right), \end{aligned} \quad (4.78)$$

where $\{A, B\} = AB + BA$ denotes the anticommutation relation, $\mathcal{D}_{\text{in},t}^\dagger(\cdot)$ is a time-dependent dissipator part involving $b_{\text{in}}(t)$, acting on $X_S(t)$, and $H_S^{(H)}(t) = U^\dagger(t, t_0)H_S(t)U(t, t_0)$, with H_S being the system Hamiltonian:

$$H_S(t) = H_A + H_{AC} + H_C. \quad (4.79)$$

In Eq. (4.78) we have used the integrated reservoir operator (4.73) at the position $x = 0$ of the cavity.

We define the expectation value of X_S :

$$\langle X_S(t) \rangle = \text{Tr}_S\{X_S\rho_S(t)\} = \text{Tr}\{X_S(t)\rho(t_0)\}, \quad (4.80)$$

where $\rho(t_0) = \rho_S(t_0) \otimes \rho_R(t_0)$ is the complete density operator and $\rho_S(t) = \text{Tr}_R\{U(t, t_0)\rho(t_0)U^\dagger(t, t_0)\}$ is the reduced density operator describing \mathcal{S} with partial trace $\text{Tr}_R\{\cdot\}$ eliminating the degrees of freedom corresponding to its subscript.

We here assume that the reservoir is initially a vacuum state $\rho_R(t_0) \equiv |\emptyset\rangle\langle\emptyset|$ such that $\mathcal{D}_{\text{in},t}^\dagger(\cdot)$ cancels out in averaging. Finally, averaging Eq. (4.78), we find the master equation of Lindblad form for $\rho_S(t)$:

$$\frac{d}{dt}\rho_S(t) = -\frac{i}{\hbar}[H_S(t), \rho_S(t)] + \Gamma_c\left(c\rho_S(t)c^\dagger - \frac{1}{2}\{c^\dagger c, \rho_S(t)\}\right). \quad (4.81)$$

Here, all system operators σ, c are time independent (Schrödinger picture), and the remaining time dependence of $H_S(t)$ is due to the driving field $\Omega(t)$.

Single photon shaping

In the previous chapter, we derived models to characterize the single photon production from a trapped atom in an open cavity. As an application, in the following, we derive from the preceding analysis a model for the generation and modification of the shape of a single photon using a leaky cavity containing one atom driven by a pulsed laser of Rabi frequency $\Omega(t)$. The production of a single photon in such a system has been demonstrated with an atom flying through the cavity in a resonant stimulated Raman adiabatic passage configuration [108, 143, 195] and for a trapped ion in a cavity [95]. We apply the model for a non-resonant scheme and show that it allows a direct and simple way to design and control the photonic wavepacket on demand. This is obtained for a particular coupling regime, which ensures single photon production without populating the cavity state. This leads to the production of a single photon with broad bandwidth, which can be of advantage when coupling photon states with materials of distinct resonances.

5.1 The model

Since the system of interest involves only the atom and the cavity, in the effective model, the basis introduced in the inside-outside representation reduces to $\{|g, \emptyset\rangle, |e, \emptyset\rangle, |f, 1\rangle, |f, \emptyset\rangle\}$ (see Fig. 4.2), where the third label is dropped due to the elimination of the reservoir degrees of freedom and the label “in” is omitted. Such dynamics involves the Lindblad equation derived previously (we omit the subscript S for ρ):

$$\frac{d}{dt}\rho(t) = -\frac{i}{\hbar}[H_S(t), \rho(t)] + \mathcal{L}[\rho(t)], \quad (5.1)$$

with the dissipator $\mathcal{L}[\rho] = \Gamma_c(c\rho c^\dagger - \frac{1}{2}\{\rho, c^\dagger c\})$. Equation (5.1) can be rewritten as

$$\frac{d}{dt}\rho(t) = -\frac{i}{\hbar}(\check{H}(t)\rho(t) - \rho(t)\check{H}^\dagger(t)) + \Gamma_c c\rho(t)c^\dagger, \quad (5.2)$$

where we introduced a non-Hermitian dissipative Hamiltonian $\check{H}(t) = H_S(t) - i\hbar\frac{\Gamma_c}{2}c^\dagger c$, equivalent to (4.11). Expressing the Hamiltonian in a matrix form (in a two photon

resonance regime: $\Delta = \Delta_c$)

$$H_S(t) = \hbar \begin{bmatrix} \mathcal{H}(t) & [0]_{3 \times 1} \\ [0]_{1 \times 3} & -\omega_0 \end{bmatrix}, \quad (5.3a)$$

$$\mathcal{H}(t) = \begin{bmatrix} 0 & \Omega(t) & 0 \\ \Omega(t) & \Delta & g \\ 0 & g & 0 \end{bmatrix} \quad (5.3b)$$

shows two decoupled dynamical blocks $\mathcal{H}(t)$ and $\{-\omega_0\}$. From the density matrix

$$\rho(t) = \begin{bmatrix} \rho_{\mathbf{AA}}(t) & \rho_{\mathbf{A0}}(t) \\ \rho_{\mathbf{0A}}(t) & \rho_{\mathbf{00}}(t) \end{bmatrix}, \quad (5.4)$$

we split Eq. (5.2) into two equations:

$$\dot{\rho}_{\mathbf{AA}} = -i(\tilde{\mathcal{H}}(t)\rho_{\mathbf{AA}}(t) - \rho_{\mathbf{AA}}(t)\tilde{\mathcal{H}}^\dagger(t)), \quad (5.5a)$$

$$\dot{\rho}_{\mathbf{00}} = \Gamma_c \mathbf{D} \rho_{\mathbf{AA}}(t) \mathbf{D}^\dagger, \quad (5.5b)$$

where $\mathbf{D} = [0, 0, 1]$ is a block from the matrix representation \mathbf{c} of the annihilation operator c , $\tilde{\mathcal{H}}(t) = \mathcal{H}(t) - \frac{i}{2}\Gamma_c \mathbf{D}^\dagger \mathbf{D}$. Choosing the initial condition in $|g, \emptyset\rangle$ makes the dynamics not involve $\rho_{\mathbf{A0}}$ and Eq. (5.5a) corresponds thus to a Schrödinger equation with losses (i.e. with a non-Hermitian Hamiltonian) derived in Eq. (4.32), i.e. $\text{Tr}\rho_{\mathbf{AA}} < 1$:

$$i\frac{\partial}{\partial t}|\psi_{\text{eff}}\rangle = \begin{bmatrix} 0 & \Omega(t) & 0 \\ \Omega(t) & \Delta & g \\ 0 & g & -i\frac{\Gamma_c}{2} \end{bmatrix} |\psi_{\text{eff}}\rangle, \quad (5.6)$$

with $|\psi_{\text{eff}}\rangle$ being the state in the pseudomode picture. The population lost from the subspace spanned by the states $\{|g, \emptyset\rangle, |e, \emptyset\rangle, |f, 1\rangle\}$ (on which the block \mathbf{A} is defined) is collected in state $|f, \emptyset\rangle$ (on which the block $\{-\omega_0\}$ is defined), so that the whole system is closed: $P_{g,0}(t) + P_{e,0}(t) + P_{f,1}(t) + P_{f,0}(t) = 1$ with the population $P_{i,n}(t) = \langle i, n | \rho(t) | i, n \rangle = |c_{i,n}|^2$. We highlight that Eq. (5.6) is obtained from the inside-outside picture, for the cavity of mode c . This equation coincides with Eq. (4.32), obtained from pseudomode picture; hence in this limit the modes c and a are the same.

Rewriting (5.5b), we get:

$$\frac{d}{dt}P_{f,0}(t) = \Gamma_c P_{f,1}(t). \quad (5.7)$$

On the other hand, from the definition of the average $\langle \mathcal{O} \rangle = \text{Tr}(\rho \mathcal{O})$, one can write the photon flux (4.77) in terms of the populations:

$$\Phi_{\text{flux}}(t) \equiv \frac{dn(t)}{dt} = \Gamma_c P_{f,1}(t). \quad (5.8)$$

We can then identify $P_{f,0}(t)$ as the number of outgoing photons: $P_{f,0}(t) \equiv n(t)$. The scheme enables us to derive the shape of the leaking photon, through its temporal flux $\Phi_{\text{flux}}(t)$ from the atom-cavity dynamics, which is determined by the Schrödinger equation (5.6).

5.2 The scheme for a large detuning

Here we start by analyzing the dynamics for different coupling regimes for a single-mode cavity ($\ell_c = \ell_0$). We compare the strong coupling regime $g > \Gamma_c$ with an intermediate coupling regime $g \lesssim \Gamma_c$. The parameters are chosen such that the approximate models described in Chapter 4 remain valid. Particular cases for intermediate and strong coupling regimes are presented in Fig. 5.1. As expected, in the strong coupling regime the single-photon state inside the cavity is more populated than the one in an intermediate coupling regime. In Fig. 5.2, we study cavities with different decay rates and analyze the produced photon inside and outside the cavity, using the full inside-outside representation [Eq.(4.35)]. In Fig. 5.2(a) the produced photon inside the cavity is presented ($P_{f,1}$). As one would expect, with the decrease in Γ_c the probability of the photon state inside the cavity increases. We also notice that for the given symmetric $\Omega(t)$ the shape of the photon takes an asymmetric form with the decrease in Γ_c . Figure 5.2(b) shows the shape of the leaked photon in the frequency domain ($P_{p,\text{outs}}$). As we can see from the figure, the better the effective quality of the cavity is, the more the leaked photon is centered around the cavity resonance frequency. As expected, the bandwidth of the photon gets narrower with the decrease in Γ_c .

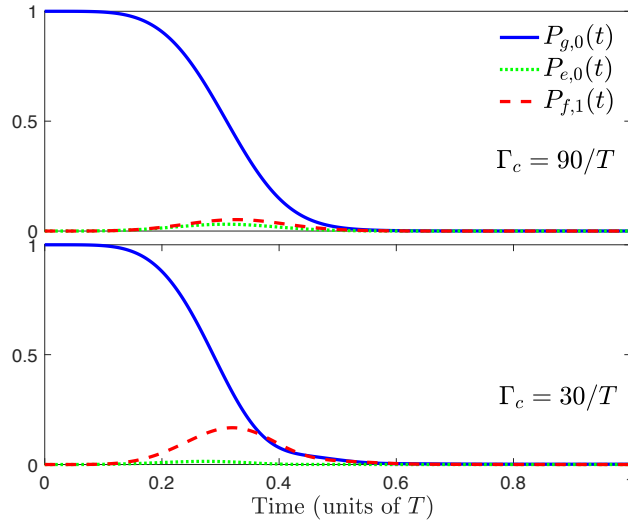


Figure 5.1: Dynamics corresponding to Eq. (5.6) for cavities with different Γ_c factors. The system parameters are $\Omega(t) = \Omega_0 \sin^2\left(\frac{\pi t}{T}\right)$, $(g, \Delta, \Omega_0, \omega_0) \times T = (60, 150, 60, 2416)$. As we can see from the figure, the stronger the leakage of the cavity is, the less the cavity state is populated [see the curve for $P_{f,1}$].

The direct control of production of the shape of a single leaking photon can be achieved for a large detuning $\Delta \gg \Omega, g$ (allowing the adiabatic elimination of the excited state $|e, \emptyset\rangle$ [173]) and an effective weak coupling regime: $\Gamma_c \gg G, g^2/\Delta$ with $G = -g\Omega/\Delta$ being the (assumed positive) effective Raman coupling [allowing the adiabatic elimination of the state $|f, 1\rangle$ (Fig. 5.1)].

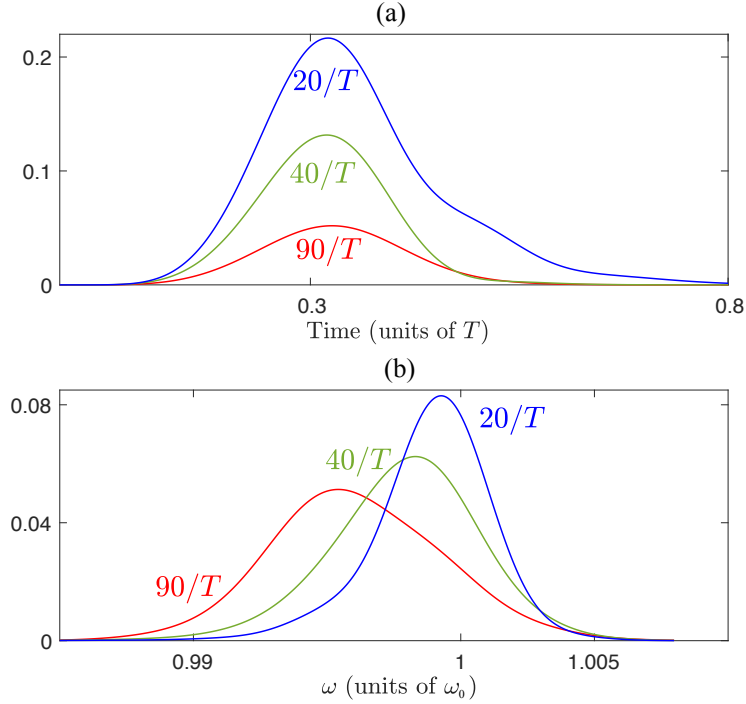


Figure 5.2: Produced single-photon shape in time (a) and frequency (b) domains for different values of the cavity linewidth Γ_c . The other parameters are the same as in Fig. 5.1.

The adiabatic eliminations lead to

$$c_{g,0}(t) = e^{i\zeta(t)} e^{-\frac{\theta(t)}{2}}, \quad (5.9a)$$

$$\zeta(t) = \int_{t_i}^t dt' \frac{\Omega^2(t')}{\Delta}, \quad (5.9b)$$

$$\theta(t) = \int_{t_i}^t dt' \frac{4G^2(t')}{\Gamma_c}. \quad (5.9c)$$

We denote the initial time $t_i = 0$. From $c_{g,0}(t)$, i.e. for given g , Δ , and $\Omega(t)$, one can infer $c_{f,1}(t) = -i2(G(t)/\Gamma_c)c_{g,0}(t)$ and Eq. (5.8) then gives the shape of the photon flux:

$$\Phi_{\text{flux}}(t) = \dot{\theta}(t) e^{-\theta(t)}. \quad (5.10)$$

The inverse calculation allows one to tailor a desired photon flux by deriving explicitly the corresponding $\Omega(t)$ (for given g and Δ). This is achieved by determining $\theta(t)$ from (5.10):

$$\theta(t) = -\ln \left[1 - \int_0^t dt' \Phi_{\text{flux}}(t') \right]. \quad (5.11)$$

We get the simple expression for the Rabi frequency by deriving this latter equation and from (5.9c):

$$\Omega(t) = \frac{\Delta\sqrt{\Gamma_c}}{2g} \sqrt{\frac{\Phi_{\text{flux}}(t)}{1 - \int_0^t dt' \Phi_{\text{flux}}(t')}}. \quad (5.12)$$

We remark that this definition of the Rabi frequency can diverge at large time. To prevent this, we introduce an efficiency parameter $\nu < 1$ which will ensure that $\Omega(t \rightarrow +\infty) = 0$ when $\Phi_{\text{flux}}(t \rightarrow +\infty) = 0$ [143, 195].

Numerical results for a chosen Gaussian probability for the single photon shape

$$\Phi_{\text{flux}}(t) = \frac{\nu\sqrt{\pi}}{T} e^{-(\frac{\pi t}{T})^2}, \quad \int_{-\infty}^{+\infty} \Phi_{\text{flux}}(t) dt = \nu, \quad (5.13)$$

are shown in Figs. 5.3(a) and 5.3(b). Using $\Gamma_c = 90/T$, we obtain $\max_t G(t) \approx 13/T \ll \Gamma_c$. We have also checked numerically the resulting flux by determining it from the numerical solution of the Schrödinger equation (5.6) (without considering the adiabatic elimination) with the Rabi frequency (5.12). The derived photon flux closely follows the desired shape as expected.

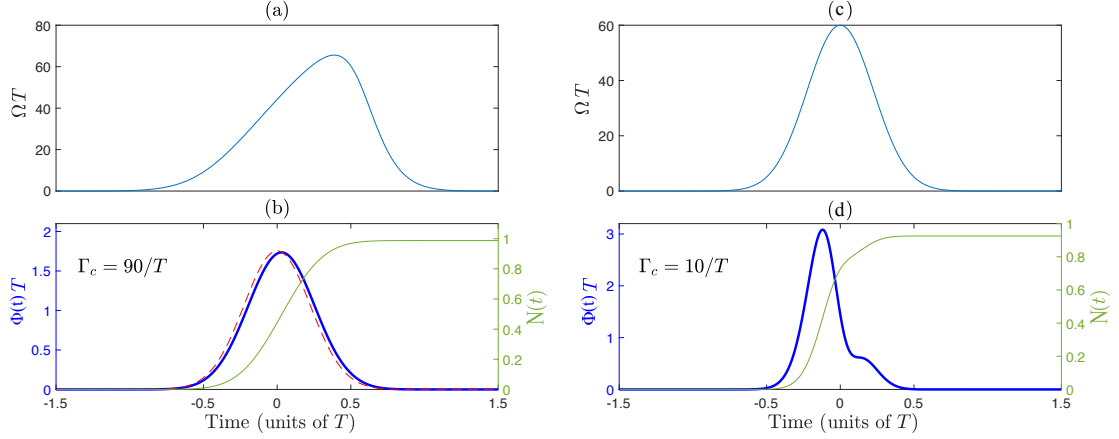


Figure 5.3: (a) and (b) Rabi frequency $\Omega(t)T$ (5.12) with $(|g|, \Gamma_c, \Delta) \times T = (60, 90, 300)$, $\eta = 0.99$, determined from the desired Gaussian shape flux $\Phi_{\text{flux}}(t)$ (5.13) [desired (dashed line) and numerically determined from the original model (5.6) (thick line)] of the single photon through the semitransparent mirror (in units of T); number of outgoing photons $N = \int_{-\infty}^t dt' \Phi_{\text{flux}}(t') = \Gamma_c \int_{-\infty}^t dt' |c_{f,1}(t')|^2$ during the process (thin line). (c) and (d) Same as (a) and (b) but for $\Gamma_c = 10/T$ and a chosen Gaussian Rabi frequency $\Omega(t) = 60 \exp[-(\pi t/T)^2]/T$.

Other, more complex forms can be investigated through (5.12) [30, 104, 154] such as the ones obtained by the resonant process with flying atoms in Refs. [143, 195].

Figures 5.3(c) and 5.3(d) show a different situation with a cavity of better effective quality: $\Gamma_c = 10/T$ and $\max_t G(t) = 12/T \approx \Gamma_c$, where the second adiabatic elimination cannot be made. In this case, the production of the photon occurs earlier and faster due to the earlier peak in Ω compared to the case in (a). The smaller decay rate of the cavity leads to a deformation of the tail of the photonic shape (due to Rabi oscillations).

Summary

In this part, we have derived and analyzed models for the system of a Λ atom trapped in a cavity, featuring a semitransparent mirror and driven by laser pulses allowing the production of a single photon leaking out from the cavity. We introduced true-mode, inside-outside and pseudomode representations for describing the system from first principles. From the exact modes of the system (the true-mode representation), we explicitly introduce the cavity-reservoir coupling which allows one to describe the dynamics without any *a priori* approximations. We have demonstrated that under suitable approximations that we formulate, these different representations give accurate results that are similar to each other, yet generally differ. We particularly analyze a high- Q cavity scenario and show that this requirement alone, in general, is not enough for these approximate models to work. This is especially significant for the models where one considers cavities with higher losses and mode overlaps, namely cavities with low refractive indices, such as plasmonic cavities.

In the literature, it is common to phenomenologically introduce the pseudomode representation. However, this kind of phenomenological approach does not provide the full description of the produced photon, namely, the outgoing photon shape in the frequency domain. In contrast, here, we recover the phenomenological model derived from first principles; moreover, it is complemented with the complete description of the system, including the full characteristics of the photon in the time domain as well as in the frequency domain. This derivation justifies explicitly the Markov approximation producing an input-output relation from first principles via the non-trivial cavity-reservoir coupling (4.10).

Finally, concepts, such as the Poynting vector, photon flux, input-output operators, and photon state, that characterize the propagation of the resulting leaking photons, have been defined and connected: We have formulated an input-output relation taking into account the propagating effects, which allows a direct interpretation of the b_{out} operator through the Poynting vector and the photon flux. The generated flux is then determined from the quantum average of the dynamics of the photon number in the cavity, which results from a standard master equation that we have derived using the operators at $x = 0$. Different coupling regimes have been discussed. In particular, we have studied an effective weak coupling regime with a large detuning and a strong cavity leakage, such that the adiabatic elimination of the cavity state is performed. In this case, one can directly link the envelope of the driving field to the pulse shape of the outgoing single photon which can be tailored at will.

In order to demonstrate the concepts in a straightforward way, here we have considered a simple model for the mirror as a single layer with a fictitious large refractive index. In practice, the large index is produced via a multilayer mirror, made of dielectric stacks. In the upcoming part, we study the light-matter interaction

in such, more realistic cavities, and analyze the effects induced by the structure of the mirror.

A.1 Quantization of the electromagnetic field

In this appendix we demonstrate the quantization of the classical electromagnetic field in a discrete Hilbert space, obtained from Maxwell's equations. When using the standard definition of the vector potential ($\nabla \times \mathbf{A} = \mathbf{B}$), and assuming that in the expression of the vector potential the variables can be separated: $\mathbf{A}(\mathbf{r}, t) = \mathbf{A}(\mathbf{r})A(t)$, the Maxwell's equations (3.5) in the Coulomb gauge ($\nabla \cdot (\varepsilon(\mathbf{r})\mathbf{A}) = 0$, $U = 0$) reduce to the following wave equation:

$$\left(\hat{\Omega}^2 - \omega_k^2\right) \tilde{\mathbf{A}}(\mathbf{r}) = 0, \quad (\text{A.1})$$

$$\left(\frac{\partial^2}{\partial t^2} + \omega_k^2\right) A(t) = 0, \quad (\text{A.2})$$

where we have used the definition $\hat{\Omega}^2 = \frac{c}{\sqrt{\varepsilon(\mathbf{r})}} \nabla \times \nabla \times \frac{c}{\sqrt{\varepsilon(\mathbf{r})}}$ and made the change of variables: $\tilde{\mathbf{A}} = \sqrt{\varepsilon_0 \varepsilon(\mathbf{r})} \mathbf{A}$. We recall that ω_k are the eigenvalues of the operator $\hat{\Omega}$, with the index $k = (\mathbf{k}, \sigma)$, where \mathbf{k} represents the wavevector with $|\mathbf{k}| = \omega_k/c$, and σ represents a possible degeneracy.

Having the classical description of the field, we now want to quantize this field. In the standard canonical quantization procedure, one considers a discrete mode structure of the field that extends over an N -dimensional Hilbert space. We can achieve such discrete modes by formally considering the electromagnetic field to be in a box with a volume V , satisfying certain boundary conditions (e.g., periodic boundary condition). Each mode can then be treated as a harmonic oscillator described by the canonical variables (q_k, p_k) that satisfy the Hamiltonian equations of motion [33, 115]

$$\frac{dq_k}{dt} = \frac{\partial H}{\partial p_k}, \quad (\text{A.3})$$

$$\frac{dp_k}{dt} = -\frac{\partial H}{\partial q_k}. \quad (\text{A.4})$$

Quantization of such harmonic oscillators is achieved by following the principle of correspondence, i.e., replacing the canonically conjugate variables with the corre-

sponding operators - (\hat{q}_k, \hat{p}_k) - acting on a well-defined Hilbert space:

$$q_k \rightarrow \hat{q}_k \quad (\text{A.5})$$

$$p_k \rightarrow \hat{p}_k := -i\hbar \frac{\partial}{\partial q_k}, \quad (\text{A.6})$$

where q_k and p_k are discrete variables, and the corresponding operators satisfy the following commutation relations:

$$[\hat{q}_k, \hat{q}_{k'}] = [\hat{p}_k, \hat{p}_{k'}] = 0 \quad (\text{A.7})$$

$$[\hat{q}_k, \hat{p}_{k'}] = i\hbar \delta_{kk'}. \quad (\text{A.8})$$

Following this procedure, we can quantize the field for the system given by the Hamiltonian (A.10). Unlike the above-described case, the modes in this Hamiltonian are, however, continuous. The transition from discrete to continuous modes can be achieved by pushing the walls of the volume V to infinity. This, however, leads to having a Hilbert space with infinite degrees of freedom. Such a Hilbert space is not well defined, which makes the total space not well-defined either. This difficulty can be avoided if we reformulate the theory in a well-defined Fock space, which is isomorphic to the finite-dimensional Hilbert space [48, 59, 157]. Taking these into account, we perform the quantization of the continuous electromagnetic field following the under-listed steps:

- Defining a Hamiltonian model satisfying the constraints imposed by Coulomb gauge (namely, the transversality constraint);
- Defining canonically conjugate, independent variables in a well-defined finite-dimensional Hilbert space and applying the principle of correspondence to these variables;
- Constructing a Fock space which is isomorphic to the considered finite-dimensional Hilbert space and writing the corresponding operators of the physical observables in the Fock space representation;
- Taking the limit of the finite degrees of freedom to infinity (which is well-defined in Fock space representation) and deriving the quantized Hamiltonian corresponding to Eq. (A.10).

We commence by writing the energy density of the classical electromagnetic field [80]

$$\mathcal{H} = \frac{1}{2} \left(\varepsilon_0 \varepsilon(\mathbf{r}) \mathbf{E}(\mathbf{r}) \cdot \mathbf{E}(\mathbf{r}) + \frac{1}{\mu_0} \mathbf{B}(\mathbf{r}) \cdot \mathbf{B}(\mathbf{r}) \right), \quad (\text{A.9})$$

leading to the full energy expression over all space

$$H = \int d^3\mathbf{r} \mathcal{H}. \quad (\text{A.10})$$

Taking into account the definitions of $\hat{\Omega}^2$, $\tilde{\mathbf{A}}(\mathbf{r})$ and defining a canonically conjugate variable to $\tilde{\mathbf{A}}(\mathbf{r})$ as $\tilde{\mathbf{\Pi}} = -\sqrt{\varepsilon_0 \varepsilon(\mathbf{r})} \mathbf{E}$, the Hamiltonian (A.10) becomes:

$$H = \int d^3\mathbf{r} \frac{1}{2} \left(\tilde{\mathbf{\Pi}} \cdot \tilde{\mathbf{\Pi}} + \tilde{\mathbf{A}} \hat{\Omega}^2 \tilde{\mathbf{A}} \right), \quad (\text{A.11})$$

where to obtain this form, in the term containing $\mathbf{B}(\mathbf{r}) \cdot \mathbf{B}(\mathbf{r}) = (\nabla \times \mathbf{A}(\mathbf{r})) \cdot (\nabla \times \mathbf{A}(\mathbf{r}))$ we have performed integration by parts and used the definition of $\hat{\Omega}^2$. Hamiltonian equations corresponding to Eq. (A.11) read as follows:

$$\frac{\partial \tilde{\mathbf{A}}(\mathbf{r}, t)}{\partial t} = \frac{\delta H}{\delta \tilde{\mathbf{\Pi}}(\mathbf{r}, t)} = \tilde{\mathbf{\Pi}}, \quad (\text{A.12})$$

$$\frac{\partial \tilde{\mathbf{\Pi}}(\mathbf{r}, t)}{\partial t} = -\frac{\delta H}{\delta \tilde{\mathbf{A}}(\mathbf{r}, t)} = -\hat{\Omega}^2 \tilde{\mathbf{A}}, \quad (\text{A.13})$$

where the symbol δ represents the variational derivative, i.e., for a functional $L = \int dx \mathcal{L}(x, f(x), f'(x))$

$$\frac{\delta L}{\delta f(x)} = \frac{\partial \mathcal{L}}{\partial f(x)} - \frac{d}{dx} \frac{\partial \mathcal{L}}{\partial f'(x)}. \quad (\text{A.14})$$

The canonical conjugate variables $(\tilde{\mathbf{A}}, \tilde{\mathbf{\Pi}})$ are, however, not independent, due to the constraint $\nabla \cdot \sqrt{\varepsilon(\mathbf{r})} \tilde{\mathbf{A}}$. Instead, to have independent parameters for quantization, we perform a canonical transformation $(\tilde{\mathbf{A}}, \tilde{\mathbf{\Pi}}) \rightarrow (q_k, p_k)$, where the variables q_k and p_k are independent, canonically conjugate variables, corresponding to the development of $\tilde{\mathbf{A}}$ and $\tilde{\mathbf{\Pi}}$ in normal modes that satisfy the transversality condition. As a last step before performing the quantization, we introduce the following variable in complex space:

$$\mathbf{Z} = \frac{1}{\sqrt{2\hbar}} \left(\hat{\Omega}^{1/2} \tilde{\mathbf{A}} + i\hat{\Omega}^{-1/2} \tilde{\mathbf{\Pi}} \right). \quad (\text{A.15})$$

The variable \mathbf{Z} can be expanded in terms of monochromatic modes $\Phi_k(\mathbf{r})$ that form complete set of basis:

$$\mathbf{Z} = \sum_k \Phi_k(\mathbf{r}) a_k. \quad (\text{A.16})$$

Indeed, if we derive the expression of $\tilde{\mathbf{A}}$ via inverting expression (A.15) and using expansion (A.16), then from Eq. (A.1) we can deduce that the functions $\Phi_k(\mathbf{r})$ satisfy the eigenmode equation:

$$\hat{\Omega}^2 \Phi_k(\mathbf{r}) = \omega_k^2 \Phi_k(\mathbf{r}), \quad (\text{A.17})$$

with the following ortho-normalization relations:

$$\int d^3\mathbf{r} \Phi_k^*(\mathbf{r}) \Phi_{k'}(\mathbf{r}) = \delta_{kk'}, \quad (\text{A.18})$$

$$\sum_k \Phi_k(\mathbf{r}) \Phi_k^*(\mathbf{r}') = \delta^\perp(\mathbf{r} - \mathbf{r}'), \quad (\text{A.19})$$

where $\delta^\perp(\mathbf{r} - \mathbf{r}')$ is the transverse delta function. Additionally, these modes automatically satisfy the transversality condition: $\nabla \cdot (\sqrt{\varepsilon(\mathbf{r})} \Phi_k(\mathbf{r})) = 0$.

Having the expansion (A.16) and recalling that the eigenvalue corresponding to the operator $\hat{\Omega}$ is ω_k [see Eq. (A.17)], we can now quantize the field using the coefficients a_k that can be expressed in terms of the variables (q_k, p_k) as follows:

$$a_k = \frac{1}{\sqrt{2\hbar}} \left(\omega_k^{1/2} q_k + i\omega_k^{-1/2} p_k \right). \quad (\text{A.20})$$

Applying the principle of correspondence to these new coordinates we get the quantized expression of \mathbf{Z} :

$$\hat{\mathbf{Z}} = \sum_k \Phi_k(\mathbf{r}) \hat{a}_k, \quad (\text{A.21})$$

where the creation and annihilation operators $\hat{a}_k^\dagger, \hat{a}_k$ satisfy the commutation relations

$$[\hat{a}_k, \hat{a}_{k'}^\dagger] = \delta_{kk'}, \quad (\text{A.22})$$

$$[\hat{a}_k, \hat{a}_{k'}] = [\hat{a}_k^\dagger, \hat{a}_{k'}^\dagger] = 0. \quad (\text{A.23})$$

Using the definition (A.15), we can write the original variables $(\tilde{\mathbf{A}}, \tilde{\mathbf{\Pi}})$ in terms of the operators $\hat{a}_k, \hat{a}_k^\dagger$:

$$\tilde{\mathbf{A}}(\mathbf{r}) = \sum_k \sqrt{\frac{\hbar}{2\omega_k}} \left(\Phi_k(\mathbf{r}) \hat{a}_k + \Phi_k^*(\mathbf{r}) \hat{a}_k^\dagger \right), \quad (\text{A.24})$$

$$\tilde{\mathbf{\Pi}}(\mathbf{r}) = -i \sum_k \sqrt{\frac{\hbar\omega_k}{2}} \left(\Phi_k(\mathbf{r}) \hat{a}_k - \Phi_k^*(\mathbf{r}) \hat{a}_k^\dagger \right). \quad (\text{A.25})$$

Taking these expression into account, the Hamiltonian in (A.11) becomes

$$H = \frac{1}{2} \sum_k \hbar\omega_k \left(\hat{a}_k^\dagger \hat{a}_k + \hat{a}_k \hat{a}_k^\dagger \right). \quad (\text{A.26})$$

So far, we have considered finite-dimensional Hilbert space, however, as mentioned earlier, in such a Hilbert space the transition from discrete modes to continuous ones is not well-defined. Thus, to be able to make such a transition without difficulty we can construct an associated Fock space based on a coordinate that combines all the modes a_k as a vector: $\underline{a} = (a_{k_1}, \dots, a_{k_N})$, where N is the dimension of the Hilbert space described above (the details of such analysis can be found in Refs. [48, 59]). In this representation, the annihilation operator analogous to \hat{a}_k becomes

$$\hat{\underline{a}} := \frac{1}{\sqrt{2\hbar}} \left(\omega_k^{1/2} \hat{\underline{q}} + i\omega_k^{-1/2} \hat{\underline{p}} \right), \quad (\text{A.27})$$

where $(\underline{q}, \underline{p})$ are the new canonical coordinates: $\underline{q} = (q_{k_1}, \dots, q_{k_N})$, $\underline{p} = (p_{k_1}, \dots, p_{k_N})$. In such a Fock space representation we can now consider the continuous modes. In the considered volume V , the wave vector takes discrete values: $\mathbf{k} = 2\pi \left(\frac{m_1}{L_1}, \frac{m_2}{L_2}, \frac{m_3}{L_3} \right)$, where m_i is an integer, and L_i represents the sides of the box of volume V . When we increase the volume V , the modes accommodated by this volume become denser up to becoming continuous, transforming the discrete operators to continuous ones: $\hat{a}_k \rightarrow \hat{a}(k)$. We can define the following quantity

$$d\mathbf{k} = \lim_{V \rightarrow \infty} \frac{2\pi}{V^{1/3}} \quad (\text{A.28})$$

and write Eq. (A.24) in the form of an integral ($\int d^3k$ being equivalent to $\int d\mathbf{k} \sum_\sigma$), leading to the full quantization of the continuous modes:

$$\tilde{\mathbf{A}}(\mathbf{r}) = \int d^3k \sqrt{\frac{\hbar}{2\omega_k}} \left(\psi(k, \mathbf{r}) \hat{a}(k) + \psi^*(k, \mathbf{r}) \hat{a}^\dagger(k) \right), \quad (\text{A.29})$$

with

$$\hat{a}(k) = \frac{\hat{a}_k}{\sqrt{(d\mathbf{k})^3}} = \sqrt{\frac{V}{(2\pi)^3}} \hat{a}_k, \quad (\text{A.30})$$

$$\psi(k, \mathbf{r}) = \sqrt{\frac{V}{(2\pi)^3}} \Phi_k(\mathbf{r}), \quad (\text{A.31})$$

and the commutation relations

$$[\hat{a}(k), \hat{a}^\dagger(k')] = \delta(k - k'), \quad (\text{A.32})$$

$$[\hat{a}(k), \hat{a}(k')] = [\hat{a}^\dagger(k), \hat{a}^\dagger(k')] = 0. \quad (\text{A.33})$$

A.2 Boundary conditions for a cavity with a single-layered dielectric mirror

As mentioned in Section 3.2, in order to find the modes of the structure depicted in Fig. 3.1, we need to solve Eq. (3.17) taking into account the following boundary conditions:

$$\left\{ \begin{array}{ll} \Phi_\omega(-\ell_c) = 0, & \\ \Phi_\omega(-\epsilon) = \Phi_\omega(+\epsilon), & \text{when } \epsilon \rightarrow 0, \\ \frac{\partial}{\partial x} \Phi_\omega(x) \Big|_{x=-\epsilon} - \frac{\partial}{\partial x} \Phi_\omega(x) \Big|_{x=\epsilon} = 0, & \text{when } \epsilon \rightarrow 0, \\ \Phi_\omega(\delta - \epsilon) = \Phi_\omega(\delta + \epsilon), & \text{when } \epsilon \rightarrow 0, \\ \frac{\partial}{\partial x} \Phi_\omega(x) \Big|_{x=\delta-\epsilon} - \frac{\partial}{\partial x} \Phi_\omega(x) \Big|_{x=\delta+\epsilon} = 0, & \text{when } \epsilon \rightarrow 0. \end{array} \right. \quad (\text{A.34})$$

The mode functions for the different regions, corresponding to the decomposition in Eq. (3.21) can be written as

$$\left\{ \begin{array}{ll} \Phi_{\omega,\text{ins}}(x) = c_1(\omega) e^{i\frac{\omega}{c}x} + c_2(\omega) e^{-i\frac{\omega}{c}x}, & \text{when } -\ell_c \leq x \leq 0, \\ \Phi_{\omega,\text{mirror}}(x) = d_1(\omega) e^{i\frac{\omega}{c}n_1x} + d_2(\omega) e^{-i\frac{\omega}{c}n_1x}, & \text{when } 0 \leq x \leq \delta, \\ \Phi_{\omega,\text{outs}}(x) = b_1(\omega) e^{i\frac{\omega}{c}x} + b_2(\omega) e^{-i\frac{\omega}{c}x}, & \text{when } x \geq \delta. \end{array} \right. \quad (\text{A.35})$$

Applying the boundary conditions (A.34) to the modes in (A.35), we can get the following modes:

$$\begin{aligned} \Phi_{\omega,\text{ins}}(x) &= C_\omega \left(e^{i\frac{\omega}{c}(x+\ell_c)} - e^{-i\frac{\omega}{c}(x+\ell_c)} \right), \\ \Phi_{\omega,\text{mirror}}(x) &= \frac{C_\omega}{1+r_1} \left[(e^{i\frac{\omega}{c}\ell_c} - r_1 e^{-i\frac{\omega}{c}\ell_c}) e^{i\frac{\omega}{c}n_1x} + (r_1 e^{i\frac{\omega}{c}\ell_c} - e^{-i\frac{\omega}{c}\ell_c}) e^{-i\frac{\omega}{c}n_1x} \right], \\ \Phi_{\omega,\text{outs}}(x) &= \frac{C_\omega}{1-r_1^2} \left[\left([e^{i\frac{\omega}{c}\ell_c} - e^{-i\frac{\omega}{c}\ell_c} r_1] e^{in_1\frac{\omega}{c}\delta} - [e^{i\frac{\omega}{c}\ell_c} r_1^2 - e^{-i\frac{\omega}{c}\ell_c} r_1] e^{-in_1\frac{\omega}{c}\delta} \right) e^{i\frac{\omega}{c}(x-\delta)} \right. \\ &\quad \left. - \left([e^{-i\frac{\omega}{c}\ell_c} - e^{i\frac{\omega}{c}\ell_c} r_1] e^{-in_1\frac{\omega}{c}\delta} - [e^{-i\frac{\omega}{c}\ell_c} r_1^2 - e^{i\frac{\omega}{c}\ell_c} r_1] e^{in_1\frac{\omega}{c}\delta} \right) e^{-i\frac{\omega}{c}(x-\delta)} \right], \end{aligned} \quad (\text{A.36})$$

where we have introduced the quantity

$$r_1 = \frac{n_1 - 1}{n_1 + 1}.$$

Using the normalization condition, we derive the following expression for the coefficient C_ω :

$$C_\omega = \frac{1}{\sqrt{2\pi c\mathcal{A}}} e^{i\frac{\omega}{c}\ell_c} T(\omega), \quad (\text{A.37})$$

leading to the modes in Eq. (3.22).

A.3 Lorentzian structure of cavity response function

Following the derivation of the modes of a single-layered cavity in Section 3.2, in this Appendix we demonstrate the expansion of the cavity response function as a sum of Lorentzian-like functions. According to Eq. (3.24), the response function of a single-layered cavity is

$$T(\omega) = \frac{t(\omega)}{1 + r(\omega)e^{2i\frac{\omega}{c}(\ell_c + \frac{\delta}{2})}}. \quad (\text{A.38})$$

Taking the absolute value squared of this expression, and using the relations in Eq (3.27) we get:

$$|T(\omega)|^2 = 1 - \frac{|r(\omega)|e^{i\theta}}{1 + |r(\omega)|e^{i\theta}} - \frac{|r(\omega)|e^{-i\theta}}{1 + |r(\omega)|e^{-i\theta}}, \quad (\text{A.39})$$

where $\theta = 2\frac{\omega}{c}(\ell_c + \delta/2) + \phi_r(\omega)$. We can modify each term of this expression using the geometric series formula $\sum_{n=1}^{\infty} q^n = q/(1 - q)$, when $|q| < 1$:

$$-\frac{|r(\omega)|e^{i\theta}}{1 + |r(\omega)|e^{i\theta}} = \sum_{n=1}^{\infty} (-|r(\omega)|e^{i\theta})^n = \sum_{n=1}^{\infty} |r(\omega)|^n e^{in(\theta+\pi)}, \quad (\text{A.40})$$

$$-\frac{|r(\omega)|e^{-i\theta}}{1 + |r(\omega)|e^{-i\theta}} = \sum_{n=1}^{\infty} |r(\omega)|^n e^{-in(\theta+\pi)} = \sum_{n=-\infty}^{-1} |r(\omega)|^{|n|} e^{in(\theta+\pi)}. \quad (\text{A.41})$$

Taking these into account, the expression in (A.39) becomes:

$$|T(\omega)|^2 = \sum_{n=-\infty}^{\infty} |r(\omega)|^{|n|} e^{in(\theta+\pi)}. \quad (\text{A.42})$$

Furthermore, recalling the Poisson summation formula, which states that

$$\sum_{n=-\infty}^{\infty} f(n) = \sum_{m=-\infty}^{\infty} \int_{-\infty}^{\infty} dx f(x) e^{-i2\pi mx} = \sum_{m=-\infty}^{\infty} \tilde{f}(m), \quad (\text{A.43})$$

with $\tilde{f}(m)$ being the Fourier transform of $f(x)$, we can define $f(x)$ as follows:

$$f(x) = |r(\omega)|^{|x|} e^{ix(\theta+\pi)} = e^{|x| \ln |r(\omega)| + ix(\theta+\pi)}, \quad (\text{A.44})$$

leading to

$$\begin{aligned}
\tilde{f}(m) &= \int_{-\infty}^{\infty} dx e^{|x| \ln |r(\omega)| + ix(\theta + \pi)} e^{-i2\pi mx} \\
&= \int_0^{\infty} dx e^{x \ln |r(\omega)|} e^{-ix(\theta + \pi - 2\pi m)} + \int_0^{\infty} dx e^{x \ln |r(\omega)|} e^{ix(\theta + \pi - 2\pi m)} \\
&= \int_0^{\infty} dx e^{-xa} 2 \cos(x\alpha),
\end{aligned} \tag{A.45}$$

where $a = -\ln |r(\omega)|$, $\alpha = \theta + \pi - 2\pi m$. Evaluating the integral in Eq. (A.45) (via performing integration by parts), we get

$$\tilde{f}(m) = \frac{2a}{a^2 + \alpha^2} = \frac{-2 \ln |r(\omega)|}{(\ln |r(\omega)|)^2 + (\theta + \pi - 2\pi m)}. \tag{A.46}$$

For the response function we get

$$|T(\omega)|^2 = \sum_{m=-\infty}^{\infty} \frac{-2 \ln |r(\omega)|}{(\ln |r(\omega)|)^2 + (\theta + \pi - 2\pi m)} = \sum_{m=-\infty}^{\infty} \frac{c}{2L_1} \frac{\gamma_1(\omega)}{(\omega - \tilde{\omega}_m(\omega))^2 + \left(\frac{\gamma_1(\omega)}{2}\right)^2},$$

where

$$\begin{aligned}
\gamma_1(\omega) &= -\frac{c}{L_1} \ln |r(\omega)|, \\
\tilde{\omega}_m(\omega) &= m \frac{\pi c}{L_1} + \frac{c}{2L_1} (\pi - \phi_r(\omega)), \\
L_1 &= \ell_c + \frac{\delta}{2}.
\end{aligned} \tag{A.47}$$

A.4 Input-output relation with the use of a Dirac delta distribution

In the following, we show the mathematical inconsistency of the standard development of the input-output relation (4.72) from the Heisenberg-Langevin equations (4.61) within the Markov approximation applied without a model for the coupling (see, e.g., Ref. [69]). By assuming a “flat” continuum via the approximation

$$\kappa_c(\omega) \approx \sqrt{\frac{\Gamma_c}{2\pi}} \tag{A.48}$$

and pushing the ω integration from $-\infty$, we approximate the double integral in (4.68b) (considering for simplicity the case $x = 0$) as

$$\int_{t_0}^t dt' \int_0^{+\infty} d\omega \frac{|\kappa_c(\omega)|^2}{\sqrt{\Gamma_c}} c(t') e^{-i\omega(t-t')} \approx \sqrt{\Gamma_c} \int_{t_0}^t dt' c(t') \int_{-\infty}^{+\infty} \frac{d\omega}{2\pi} e^{-i\omega(t-t')} \tag{A.49a}$$

$$= \sqrt{\Gamma_c} \int_{t_0}^t dt' c(t') \delta(t-t') = \frac{\sqrt{\Gamma_c}}{2} c(t). \tag{A.49b}$$

The last step, which can be reformulated in a simpler case as

$$\int_{-\infty}^0 dt c(t) \delta(t) = \frac{1}{2} c(0), \tag{A.50}$$

is mathematically undefined. Since the distributions are defined on the real line via the integration on a test function, it indeed necessitates the introduction of a multiplication with the Heaviside distribution:

$$\int_{-\infty}^{+\infty} dt c(t) H(-t) \delta(t) = \int_{-\infty}^0 dt c(t) \delta(t). \quad (\text{A.51})$$

However such a product of two non regular distributions is undefined, here more specifically the product of the Dirac delta distribution with the Heaviside distribution of discontinuity localized where the Dirac delta is infinite. This has been analyzed in Ref. [79].

An explicit analysis can be conducted by defining a model for the Dirac delta distribution using a family of (noneven) functions represented in Fig. A.1,

$$h_\epsilon^a(t) = \begin{cases} 0 & \text{for } t < (a-1)\epsilon \\ 1/\epsilon & \text{for } (a-1)\epsilon \leq t \leq a\epsilon \\ 0 & \text{for } t > a\epsilon, \end{cases} \quad (\text{A.52})$$

parametrized by a real number $0 < a < 1$, in the limit $\epsilon \rightarrow 0$. We can indeed check that they satisfy the Dirac delta distribution [applied on a test function $\varphi(t)$]:

$$\lim_{\epsilon \rightarrow 0} \int_{-\infty}^{+\infty} dt \varphi(t) h_\epsilon^a(t) = \lim_{\epsilon \rightarrow 0} \frac{1}{\epsilon} \int_{(a-1)\epsilon}^{a\epsilon} dt \varphi(t) = \lim_{\epsilon \rightarrow 0} \int_{a-1}^a ds \varphi(\epsilon s) = \varphi(0), \quad (\text{A.53})$$

where we have applied the change of variable $s = t/\epsilon$. We note that the limit $\epsilon \rightarrow 0$ guarantees that $\delta(t) = \lim_{\epsilon \rightarrow 0} h_\epsilon^a(t)$ is an even distribution.

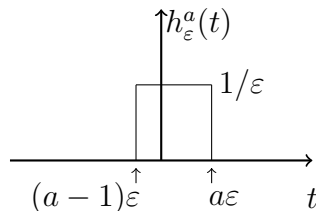


Figure A.1: Representation of a family of non-even functions parametrized by a real number $0 < a < 1$ tending to the Dirac delta distribution in the limit $\epsilon \rightarrow 0$.

Applying this model on (A.50), we obtain

$$\lim_{\epsilon \rightarrow 0} \int_{-\infty}^0 dt c(t) h_\epsilon^a(t) = \lim_{\epsilon \rightarrow 0} \frac{1}{\epsilon} \int_{(a-1)\epsilon}^0 dt c(t) = \lim_{\epsilon \rightarrow 0} \int_{a-1}^0 ds c(\epsilon s) = (1-a)c(0). \quad (\text{A.54})$$

This shows that the result depends on the details of the model of the Dirac delta distribution [163]. We recover the result of (A.50) only for a particular even-function model (i.e., $a = 1/2$).

As a consequence, the derivation (A.49) is not valid in general. It necessitates a specific model for the coupling $\kappa_c(\omega)$, as considered from first principles in this work.

A.5 Derivation of the pseudomode representation

In this appendix, we derive the pseudomode representation directly from the true-mode representation featuring the approximate coupling function (4.6). Taking into account the dynamical equations (4.17), which are derived for the true-mode representation via solving the Schrödinger equation with the Hamiltonian (4.2) and the wavefunction (4.14), we define the following term:

$$\hat{c}_{f,1} = \frac{1}{\hat{g}} \int_0^\infty d\omega \eta(\omega) \tilde{c}_{f,1}(\omega, t) = \frac{1}{\hat{g}} \int_0^\infty d\omega \eta(\omega) e^{-i(\Delta - \Delta_c + \omega - \omega_0)t} \tilde{c}_{f,1}(\omega, t), \quad (\text{A.55})$$

where $\tilde{c}_{f,1}(\omega, t) = e^{i(\Delta - \Delta_c + \omega - \omega_0)t} \tilde{c}_{f,1}(\omega, t)$ satisfies the following equation:

$$\frac{d}{dt} \tilde{c}_{f,1}(\omega, t) = -\eta^*(\omega) e^{i(\Delta - \Delta_c + \omega - \omega_0)t} \tilde{c}_{e,0}(t). \quad (\text{A.56})$$

Calculating the time derivative of Eq. (A.55) using the relation (A.56) we obtain:

$$\begin{aligned} \frac{d}{dt} \hat{c}_{f,1}(t) &= \frac{d}{dt} \hat{c}_{f,1}^{(0)}(t) - \frac{1}{\hat{g}} \int_0^{+\infty} d\omega |\eta(\omega)|^2 \tilde{c}_{e,0}(t) \\ &\quad + \frac{i}{\hat{g}} \int_0^t dt' \tilde{c}_{e,0}(t') \int_0^{+\infty} d\omega |\eta(\omega)|^2 (\Delta - \Delta_c + \omega - \omega_0) e^{-i(\Delta - \Delta_c + \omega - \omega_0)(t-t')}, \end{aligned} \quad (\text{A.57})$$

where we introduce the time derivative of the initial time defined as follows:

$$\hat{c}_{f,1}^{(0)}(t) = \frac{1}{\hat{g}} \int_0^{+\infty} d\omega \eta(\omega) e^{-i(\Delta - \Delta_c + \omega - \omega_0)t} \tilde{c}_{f,1}(\omega, 0). \quad (\text{A.58})$$

In the following we evaluate the integral

$$\mathcal{I}_1 = \int_0^{+\infty} d\omega |\eta(\omega)|^2. \quad (\text{A.59})$$

In order to evaluate this integral we rewrite $\eta(\omega)$ using the expansion $\sin^2 \alpha = (1 - (e^{2i\alpha} + e^{-2i\alpha})/2)/2$:

$$|\eta(\omega)|^2 \approx \frac{\omega_0 |d_{fe}|^2}{\hbar \varepsilon_0 \mathcal{A} l_c} \frac{1}{2} \left(1 - \frac{e^{2i\frac{\omega}{c}(x_A + l_c)}}{2} - \frac{e^{-2i\frac{\omega}{c}(x_A + l_c)}}{2} \right) \frac{\Gamma_c}{2\pi} \frac{1}{(\omega - \omega_0)^2 + \left(\frac{\Gamma_c}{2}\right)^2}.$$

This splits the integral \mathcal{I}_1 into three parts

$$\mathcal{I}_1 = \mathcal{I}_0 + \mathcal{I}_+ + \mathcal{I}_-, \quad (\text{A.60})$$

with

$$\mathcal{I}_0 = \frac{\omega_0 |d_{fe}|^2}{2\hbar \varepsilon_0 \mathcal{A} l_c} \int_{-\infty}^{\infty} d\tilde{\Delta} \frac{\Gamma_c}{2\pi} \frac{1}{\tilde{\Delta}^2 + \left(\frac{\Gamma_c}{2}\right)^2}, \quad (\text{A.61})$$

where we introduced the change of variables $\tilde{\Delta} = \omega - \omega_0$, and assumed $\Gamma_c/\omega_0 \ll 1$, such that the integration limits can be extended from $-\infty$ to ∞ , leading to

$$\mathcal{I}_0 = \frac{\omega_0 |d_{fe}|^2}{2\hbar \varepsilon_0 \mathcal{A} l_c} \frac{\Gamma_c}{2\pi} \frac{2}{\Gamma_c} \arctan \frac{2\tilde{\Delta}}{\Gamma_c} \Big|_{-\infty}^{\infty} = \frac{\omega_0 |d_{fe}|^2}{2\hbar \varepsilon_0 \mathcal{A} l_c}. \quad (\text{A.62})$$

Similarly,

$$\mathcal{I}_{\pm} = -\frac{\omega_0 |d_{fe}|^2}{4\hbar\varepsilon_0 \mathcal{A} \ell_c} e^{\pm i2\frac{\omega_0}{c}(x_A + \ell_c)} \int_{-\infty}^{\infty} d\tilde{\Delta} \frac{\Gamma_c}{2\pi} \frac{e^{\pm i2\frac{\tilde{\Delta}}{c}(x_A + \ell_c)}}{\tilde{\Delta}^2 + \left(\frac{\Gamma_c}{2}\right)^2}. \quad (\text{A.63})$$

The integrals \mathcal{I}_{\pm} can be evaluated by using complex contour integration. For \mathcal{I}_{+} , since the term $x_A + \ell_c > 0$, the integration can be done over upper half complex plane [see Fig. A.2]:

$$\mathcal{I}_{+} = \lim_{R \rightarrow \infty} \left(\oint - \int_{\mathcal{C}_R} \right).$$

The integral over \mathcal{C}_R is 0, when $R \rightarrow \infty$, and

$$\oint dz f(z) = 2\pi i \text{Res} f(z), \quad (\text{A.64})$$

where

$$f(z) = \frac{\Gamma_c}{2\pi} \frac{e^{i2\frac{z}{c}(x_A + \ell_c)}}{z^2 + \left(\frac{\Gamma_c}{2}\right)^2}.$$

Taking this into account

$$\mathcal{I}_{+} = -\frac{\omega_0 |d_{fe}|^2}{4\hbar\varepsilon_0 \mathcal{A} \ell_c} e^{i2\frac{\omega_0}{c}(x_A + \ell_c)} e^{-\frac{\Gamma_c}{c}(x_A + \ell_c)}. \quad (\text{A.65})$$

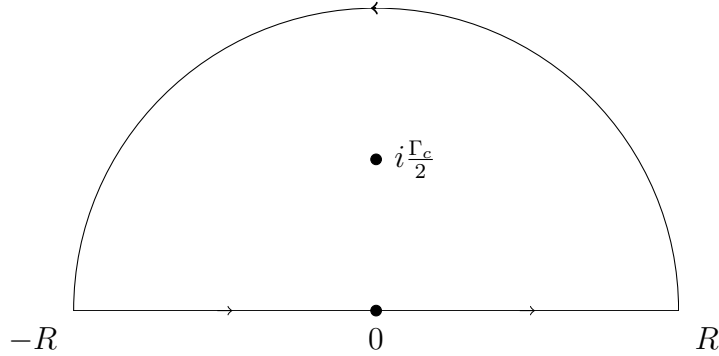


Figure A.2: Curve over which the integral \mathcal{I}_{+} is evaluated.

Similarly, performing integration in lower half plane we can evaluate \mathcal{I}_{-} :

$$\mathcal{I}_{-} = -\frac{\omega_0 |d_{fe}|^2}{4\hbar\varepsilon_0 \mathcal{A} \ell_c} e^{-i2\frac{\omega_0}{c}(x_A + \ell_c)} e^{-\frac{\Gamma_c}{c}(x_A + \ell_c)}. \quad (\text{A.66})$$

Finally, the integral \mathcal{I}_1 becomes

$$\mathcal{I}_1 = \frac{\omega_0 |d_{fe}|^2}{2\hbar\varepsilon_0 \mathcal{A} \ell_c} \left(1 - e^{-\frac{\Gamma_c}{c}(x_A + \ell_c)} \cos \left[2\frac{\omega_0}{c}(x_A + \ell_c) \right] \right). \quad (\text{A.67})$$

Having obtained the value of \mathcal{I}_1 , we now perform similar calculation to evaluate the integral \mathcal{I}_2 :

$$\mathcal{I}_2 = \int_0^{+\infty} d\omega |\eta(\omega)|^2 (\Delta - \Delta_c + \omega - \omega_0) e^{-i(\Delta - \Delta_c + \omega - \omega_0)(t-t')}, \quad (\text{A.68})$$

which leads to the evaluation of integrals of the form

$$g_0(z) = \frac{\Gamma_c (\Delta - \Delta_c + z) e^{-i(\Delta - \Delta_c + z)(t-t')}}{2\pi z^2 + \left(\frac{\Gamma_c}{2}\right)^2}, \quad (\text{A.69})$$

and

$$g_{\pm}(z) = \frac{\Gamma_c e^{\pm i 2 \frac{\omega_0}{c} (x_A + \ell_c)} (\Delta - \Delta_c + z) e^{-i(\Delta - \Delta_c + z)(t-t')} e^{\pm i 2 \frac{z}{c} (x_A + \ell_c)}}{2\pi z^2 + \left(\frac{\Gamma_c}{2}\right)^2}. \quad (\text{A.70})$$

Performing similar complex plane integration as in the case of \mathcal{I}_1 , we obtain

$$\begin{aligned} \int dz g_0(z) &= \left(\Delta - \Delta_c - i \frac{\Gamma_c}{2} \right) e^{-\frac{\Gamma_c}{2}(t-t')} e^{-i(\Delta - \Delta_c)(t-t')}, \\ \int dz g_{-}(z) &= \left(\Delta - \Delta_c - i \frac{\Gamma_c}{2} \right) e^{-\frac{\Gamma_c}{2}(t-t')} e^{-i(\Delta - \Delta_c)(t-t')} e^{-i 2 \frac{\omega_0}{c} (x_A + \ell_c)} e^{-\frac{\Gamma_c}{c} (x_A + \ell_c)}. \end{aligned}$$

The integral of the function $g_{+}(z)$ can be evaluated in the lower half-plane if $t' < t - \frac{2}{c}(x_A + \ell_c)$, and upper half-plane if $t - \frac{2}{c}(x_A + \ell_c) < t' < t$. The quantity $\frac{2}{c}(x_A + \ell_c)$ is of the order of $\frac{\ell_c}{c}$ (half-round trip time of a photon) and the typical time scale at which we observe the dynamics of the system is much greater than this time, hence the contribution of the interval $t - \frac{2}{c}(x_A + \ell_c) < t' < t$ is negligible, thus we evaluate the integral at the lower half plane, and obtain

$$\int dz g_{+}(z) = \left(\Delta - \Delta_c - i \frac{\Gamma_c}{2} \right) e^{-\frac{\Gamma_c}{2}(t-t')} e^{-i(\Delta - \Delta_c)(t-t')} e^{i 2 \frac{\omega_0}{c} (x_A + \ell_c)} e^{\frac{\Gamma_c}{c} (x_A + \ell_c)}.$$

Taking these results into account for the integral \mathcal{I}_2 we obtain

$$\begin{aligned} \mathcal{I}_2 &= \frac{\omega_0 |d_{fe}|^2}{2\hbar \varepsilon_0 \mathcal{A} \ell_c} \left(\Delta - \Delta_c - i \frac{\Gamma_c}{2} \right) e^{-i(\Delta - \Delta_c - i \frac{\Gamma_c}{2})(t-t')} \\ &\times \left[1 - \cos \left[2 \frac{\omega_0}{c} (x_A + \ell_c) \right] \cosh \left[\frac{\Gamma_c}{c} (x_A + \ell_c) \right] \right. \\ &\left. - i \sin \left[2 \frac{\omega_0}{c} (x_A + \ell_c) \right] \sinh \left[\frac{\Gamma_c}{c} (x_A + \ell_c) \right] \right]. \end{aligned} \quad (\text{A.71})$$

Recalling that the condition $\Gamma_c \ll \omega_0$ holds true, the terms containing $2 \frac{\omega_0}{c} (x_A + \ell_c)$ can be regarded as fast oscillating terms compared to the ones with $\frac{\Gamma_c}{c} (x_A + \ell_c)$. We can expand this slow-varying terms using the following Taylor expansion

$$\cosh[\epsilon_1] = 1 + \mathcal{O}(\epsilon_1^2) \quad (\text{A.72})$$

$$\sinh[\epsilon_1] = 0 + \mathcal{O}(\epsilon_1^2) \quad (\text{A.73})$$

$$e^{-\epsilon_1} = 1 + \mathcal{O}(\epsilon_1^2), \quad (\text{A.74})$$

where $\epsilon_1 = \frac{\Gamma_c}{c}(x_A + \ell_c)$. With these, the expressions in (A.67) and (A.71) become

$$\mathcal{I}_1 = \frac{\omega_0 |d_{fe}|^2}{\hbar \epsilon_0 \mathcal{A} \ell_c} \sin^2 \left[\frac{\omega_0}{c} (x_A + \ell_c) \right], \quad (\text{A.75})$$

$$\mathcal{I}_2 = \frac{\omega_0 |d_{fe}|^2}{2\hbar \epsilon_0 \mathcal{A} \ell_c} \left(\Delta - \Delta_c - i \frac{\Gamma_c}{2} \right) e^{-i(\Delta - \Delta_c - i \frac{\Gamma_c}{2})(t-t')} \sin^2 \left[\frac{\omega_0}{c} (x_A + \ell_c) \right]. \quad (\text{A.76})$$

A.6 Discretization of the continuous integrals

In this Appendix we demonstrate how one can numerically solve the equations (4.17) and (4.35) via discretizing the continuum. In order to perform discretization properly, we analyze the continuous parts of the states (4.14) and (4.34), where the photon states $|1_\omega\rangle$ and $|1_{\omega, \text{outs}}\rangle$ and the coefficients $\tilde{c}_{f,1}(\omega, t)$ and $c_{f,0,1}(\omega, t)$ all have units of $1/\sqrt{\omega}$, making the corresponding integrals dimensionless. Thus we can do the following discretization:

$$\int_0^\infty d\omega \tilde{c}_{f,1}(\omega, t) |1_\omega\rangle = \sum_{i=1}^m \sqrt{d\omega} \tilde{c}_{f,1}(\omega_i, t) \sqrt{d\omega} |1_{\omega_i}\rangle,$$

$$\int_0^\infty d\omega c_{f,0,1}(\omega, t) |1_{\omega, \text{outs}}\rangle = \sum_{i=1}^m \sqrt{d\omega} c_{f,0,1}(\omega_i, t) \sqrt{d\omega} |1_{\omega_i, \text{outs}}\rangle,$$

where $d\omega$ is the step of the discretization. By denoting the dimensionless quantities of the sum as $\tilde{\mathbf{c}}_{f,1}(\omega_i, t) = \sqrt{d\omega} \tilde{c}_{f,1}(\omega_i, t)$, $|\tilde{\mathbf{1}}_{\omega_i}\rangle = \sqrt{d\omega} |1_{\omega_i}\rangle$ and $\mathbf{c}_{f,0,1}(\omega_i, t) = \sqrt{d\omega} c_{f,0,1}(\omega_i, t)$, $|\mathbf{1}_{\omega_i, \text{outs}}\rangle = \sqrt{d\omega} |1_{\omega_i, \text{outs}}\rangle$, we can calculate the probability amplitudes of finding the photon in states $|\tilde{\mathbf{1}}_{\omega_i}\rangle$ and $|\mathbf{1}_{\omega_i, \text{outs}}\rangle$, respectively:

$$\tilde{P}(\omega_i, t) = |\langle \tilde{\mathbf{1}}_{\omega_i} | \tilde{\psi} \rangle|^2 = |\tilde{\mathbf{c}}_{f,1}(\omega_i, t)|^2,$$

$$P(\omega_i, t) = |\langle \mathbf{1}_{\omega_i, \text{outs}} | \psi \rangle|^2 = |\mathbf{c}_{f,0,1}(\omega_i, t)|^2.$$

Taking this discretization into account, in Eq. (4.17), the discretization of the function $\eta(\omega)$ becomes $\sqrt{d\omega} \eta(\omega_1), \sqrt{d\omega} \eta(\omega_2), \dots, \sqrt{d\omega} \eta(\omega_m)$, and the equations become:

$$\begin{aligned} i \frac{d}{dt} \tilde{c}_{g,0}(t) &= \Omega \tilde{c}_{e,0}(t), \\ i \frac{d}{dt} \tilde{c}_{e,0}(t) &= \Delta \tilde{c}_{e,0}(t) + \Omega \tilde{c}_{g,0}(t) + i \sum_m \tilde{\eta}_{\omega_m} \tilde{\mathbf{c}}_{f,1}(\omega_m, t), \\ i \frac{d}{dt} \tilde{\mathbf{c}}_{f,1}(\omega_1, t) &= (\Delta - \Delta_c + \omega_1 - \omega_0) \tilde{\mathbf{c}}_{f,1}(\omega_1, t) - i \tilde{\eta}_{\omega_1}^* \tilde{c}_{e,0}(t), \\ &\vdots \\ i \frac{d}{dt} \tilde{\mathbf{c}}_{f,1}(\omega_m, t) &= (\Delta - \Delta_c + \omega_m - \omega_0) \tilde{\mathbf{c}}_{f,1}(\omega_m, t) - i \tilde{\eta}_{\omega_m}^* \tilde{c}_{e,0}(t), \end{aligned}$$

with $\tilde{\eta}_{\omega_m} = \sqrt{d\omega} \eta(\omega_m)$.

Similarly, Eq. (4.35) becomes

$$\begin{aligned}
i\dot{c}_{g,0}(t) &= \Omega c_{e,0}(t), \\
i\dot{c}_{e,0}(t) &= \Delta c_{e,0}(t) + \Omega c_{g,0}(t) + g c_{f,1,0}(t), \\
i\dot{c}_{f,1,0}(t) &= (\Delta - \Delta_c) c_{f,1,0} + g c_{e,0}(t) - i \sum_m \tilde{\kappa}_c^*(\omega_m) \mathbf{c}_{f,0,1}(\omega_m, t), \\
i\dot{c}_{f,0,1}(\omega_1, t) &= (\Delta - \Delta_c + \omega_1 - \omega_0) \mathbf{c}_{f,0,1}(\omega_1, t) + i\tilde{\kappa}_c(\omega_1) c_{f,1,0}(t), \\
&\vdots \\
i\dot{c}_{f,0,1}(\omega_m, t) &= (\Delta - \Delta_c + \omega_m - \omega_0) \mathbf{c}_{f,0,1}(\omega_m, t) + i\tilde{\kappa}_c(\omega_m) c_{f,1,0}(t),
\end{aligned}$$

where $\tilde{\kappa}_c(\omega_m) = \sqrt{d\omega} \kappa_c(\omega_m)$.

By solving these systems of equations numerically using a sufficiently large number of states (typically 100000) discretizing the continuum, we obtain the solutions presented in Fig. 4.3.

A.7 Single photon spatial distribution

In this appendix, we demonstrate that the definition in Eq. (4.55) can be interpreted as a photon number operator. As discussed in Ref. [70], the attempts to define a local photon number operator in a finite volume V showed that, in general, such an operator can not be defined since it does not satisfy the commutation relation for nonoverlapping volumes. However, in the particular system discussed here, where linearly polarized light produced from a high-finesse cavity propagates in one-dimensional space, we are able to define such an operator. In order to show that the definition in Eq. (4.55) is an observable, we evaluate the following commutator (for convenience we work in Schrödinger representation)

$$\begin{aligned}
[b_x^\dagger b_x, b_{x'}^\dagger b_{x'}] &= \frac{1}{(c\Gamma_c)^2} \int d\omega d\omega' d\omega'' d\tilde{\omega} \kappa_c(\omega) \kappa_c^*(\omega') \kappa_c(\omega'') \kappa_c^*(\tilde{\omega}) \\
&\quad \times e^{-i\frac{\omega}{c}x} e^{i\frac{\omega'}{c}x} e^{-i\frac{\omega''}{c}x'} e^{i\frac{\tilde{\omega}}{c}x'} [b_\omega^\dagger b_{\omega'}, b_{\omega''}^\dagger b_{\tilde{\omega}}]. \tag{A.79}
\end{aligned}$$

The commutator appearing on the right side of the equation (A.79) can be simplified as follows

$$\begin{aligned}
[b_\omega^\dagger b_{\omega'}, b_{\omega''}^\dagger b_{\tilde{\omega}}] &= b_\omega^\dagger b_{\omega'} b_{\omega''}^\dagger b_{\tilde{\omega}} - b_{\omega''}^\dagger b_{\tilde{\omega}} b_\omega^\dagger b_{\omega'} = b_\omega^\dagger (\delta(\omega' - \omega'') + b_{\omega''}^\dagger b_{\omega'}) b_{\tilde{\omega}} - b_{\omega''}^\dagger b_{\tilde{\omega}} b_\omega^\dagger b_{\omega'} \\
&= b_\omega^\dagger b_{\tilde{\omega}} \delta(\omega' - \omega'') + b_\omega^\dagger b_{\omega''}^\dagger b_{\omega'} b_{\tilde{\omega}} - b_{\omega''}^\dagger b_{\tilde{\omega}} b_\omega^\dagger b_{\omega'} \\
&= b_\omega^\dagger b_{\tilde{\omega}} \delta(\omega' - \omega'') - b_{\omega''}^\dagger b_{\omega'} \delta(\omega - \tilde{\omega}).
\end{aligned}$$

Taking this into account Eq. (A.79) becomes

$$\begin{aligned}
[b_x^\dagger b_x, b_{x'}^\dagger b_{x'}] &= \frac{1}{(c\Gamma_c)^2} \int d\omega d\omega' d\tilde{\omega} \kappa_c(\omega) \kappa_c^*(\tilde{\omega}) |\kappa_c(\omega')|^2 e^{i\frac{\omega'}{c}(x-x')} e^{-i\frac{\omega}{c}x} e^{i\frac{\tilde{\omega}}{c}x'} b_\omega^\dagger b_{\tilde{\omega}} \\
&\quad - \frac{1}{(c\Gamma_c)^2} \int d\omega d\omega' d\omega'' \kappa_c^*(\omega') \kappa_c(\omega'') |\kappa_c(\omega)|^2 e^{-i\frac{\omega}{c}(x-x')} e^{i\frac{\omega'}{c}x} e^{-i\frac{\omega''}{c}x'} b_{\omega''}^\dagger b_{\omega'}.
\end{aligned}$$

To evaluate these integrals, below we estimate the value of the integral

$$\begin{aligned}
\mathcal{I} &= \int_0^\infty d\omega' |\kappa_c(\omega')|^2 e^{i\frac{\omega'}{c}(x-x')} = \frac{\Gamma_c}{2\pi} \left(\frac{c}{\ell_c}\right)^2 \int_0^\infty d\omega' \frac{\sin^2(\omega' - \omega_0) \frac{\ell_c}{c}}{(\omega' - \omega_0)^2} e^{i\frac{\omega'}{c}(x-x')} \\
&= \frac{\Gamma_c}{2\pi} \left(\frac{c}{\ell_c}\right)^2 \frac{1}{2} \int_0^\infty d\omega' \frac{1 - \cos 2(\omega' - \omega_0) \frac{\ell_c}{c}}{(\omega' - \omega_0)^2} e^{i\frac{\omega'}{c}(x-x')} \\
&= \frac{\Gamma_c}{2\pi} \left(\frac{c}{\ell_c}\right)^2 \frac{1}{2} e^{i\frac{\omega_0}{c}(x-x')} \left[\int_0^\infty d\omega' \frac{e^{i(\omega' - \omega_0) \frac{(x-x')}{c}}}{(\omega' - \omega_0)^2} \right. \\
&\quad \left. - \frac{1}{2} \left(\int_0^\infty d\omega' \frac{e^{i\frac{(\omega' - \omega_0)}{c}(x-x'+2\ell_c)}}{(\omega' - \omega_0)^2} + \int_0^\infty d\omega' \frac{e^{i\frac{(\omega' - \omega_0)}{c}(x-x'-2\ell_c)}}{(\omega' - \omega_0)^2} \right) \right]. \tag{A.80}
\end{aligned}$$

To calculate the individual terms of this integral, we can evaluate the corresponding integrals in complex plane, i.e., we evaluate integrals of the following form (details of this calculation is shown in Appendix A.8):

$$\int_{-\omega_0}^\infty dz \frac{e^{i\frac{z}{c}\zeta}}{z^2} \approx \int_{-\infty}^\infty dz \frac{e^{i\frac{z}{c}\zeta}}{z^2},$$

where we have extended the limits of the integration, assuming that $c/\ell_c \ll \omega_0$, which is satisfied when we consider high-finesse cavities, where the number of modes inside the cavity is high. Calculating the integrals in the complex plane one can show that

$$\mathcal{I} = \frac{\Gamma_c}{2\pi} \left(\frac{c}{\ell_c}\right)^2 \frac{1}{2} e^{i\frac{\omega_0}{c}(x-x')} \begin{cases} 0, & x' < x - 2\ell_c \\ -\frac{\pi}{c}(x - x' - 2\ell_c), & x - 2\ell_c < x' < x \\ \frac{\pi}{c}(x - x' + 2\ell_c), & x < x' < x + 2\ell_c \\ 0, & x' > x + 2\ell_c \end{cases}.$$

Taking this result into account, we can conclude that commutator (A.79) is 0 when $|x' - x| > 2\ell_c$. Equivalently, if we formulate this condition in terms of the propagation time of the photon, we can write $x' = x + ct$, where $t > 2\ell_c/c$, which is known as the coarse-grained approximation, which assumes that the time of flight of a photon through the cavity is small compared with the time resolution of interest [201]. Thus, at this limit, we can interpret $b_x^\dagger b_x$ as the photon number density.

We highlight that integral \mathcal{I} is the integral also appearing in the commutation relation

$$\begin{aligned}
[b_x, b_{x'}^\dagger] &= \frac{1}{c\Gamma_c} \int_0^\infty d\omega d\omega' \kappa_c^*(\omega) \kappa_c(\omega') e^{i\frac{\omega}{c}x} e^{-i\frac{\omega'}{c}x'} [b_\omega, b_{\omega'}^\dagger] \\
&= \frac{1}{c\Gamma_c} \int_0^\infty d\omega |\kappa_c(\omega)|^2 e^{i\frac{\omega}{c}(x-x')} = \frac{1}{c\Gamma_c} \mathcal{I}, \tag{A.81}
\end{aligned}$$

leading to

$$[b_x, b_x^\dagger] = \frac{1}{2\ell_c}. \tag{A.82}$$

A.8 Evaluation of the integral (4.68b)

In order to evaluate the integral in (4.68b), we use the following expression for $\kappa_c(\omega)$:

$$\kappa_c(\omega) = \sqrt{\frac{\Gamma_c}{2\pi}} e^{-i\frac{\omega}{c}\ell_c} \text{sinc}\left((\omega - \omega_0)\frac{\ell_c}{c}\right).$$

We calculate the following integral:

$$I = \int_0^\infty d\omega |\kappa_c(\omega)|^2 e^{-i\omega\tau} = \frac{\Gamma_c}{2\pi} \left(\frac{c}{\ell_c}\right)^2 \int_0^\infty d\omega \frac{\sin^2\left((\omega - \omega_0)\frac{\ell_c}{c}\right)}{(\omega - \omega_0)^2} e^{-i\omega\tau}, \quad (\text{A.83})$$

where $\tau = t - t' - \frac{x}{c}$. This leads to the evaluation of integrals of the following form (where we have extended the limits of the integration, assuming that $c/\ell_{\text{eff}} \ll \omega_m$, which is satisfied when we consider high finesse cavities, where the number of modes inside the cavity is high):

$$\begin{aligned} I_1 &= \int_{-\infty}^{\infty} dz \frac{e^{-iz\tau}}{z^2}, \\ I_2 &= \int_{-\infty}^{\infty} dz \frac{e^{-iz(\tau - \frac{2\ell_c}{c})}}{z^2}, \\ I_3 &= \int_{-\infty}^{\infty} dz \frac{e^{-iz(\tau + \frac{2\ell_c}{c})}}{z^2}, \end{aligned} \quad (\text{A.84})$$

making

$$I = \frac{\Gamma_c}{2\pi} \left(\frac{c}{\ell_c}\right)^2 \frac{e^{-i\omega_0\tau}}{2} \left[I_1 - \frac{1}{2}I_2 - \frac{1}{2}I_3 \right].$$

The integrals in Eq. (A.84) can be evaluated using complex plane integration techniques. The integral I_1 can be evaluated in upper half-plane [Fig. A.3] if $\tau < 0$ and lower half-plane if $\tau > 0$. Thus, we analyze the following complex integral

$$\oint_C dz f(z) = \oint_C dz \frac{e^{-iz\tau}}{z^2} = 0 = \int_{-R}^{-r} dz f(z) + \int_{C_r} dz f(z) + \int_r^R dz f(z) + \int_{C_R} dz f(z).$$

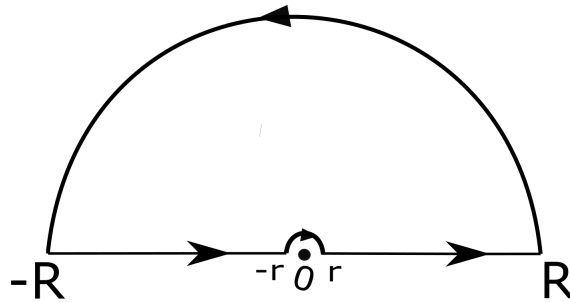


Figure A.3: Integration path in the upper half-plane. The integrals in (A.84) can be estimated on this path, when $r \rightarrow 0$ and $R \rightarrow \infty$.

The integral over the curve C_R becomes 0, when $R \rightarrow \infty$. We can evaluate the integral over C_r , as follows

$$\int_{C_r} dz f(z) = \int_{C_r} dz \frac{e^{-iz\tau}}{z^2} = \begin{cases} -i\pi \text{Res}(f, 0), & \tau < 0, \\ i\pi \text{Res}(f, 0), & \tau > 0. \end{cases} \quad (\text{A.85})$$

Since we have a second order pole at $z = 0$, in order to calculate the residue we use the following formula:

$$\text{Res}(f, 0) = \frac{1}{(n-1)!} \lim_{z \rightarrow 0} \frac{d^{n-1}}{dz^{n-1}} (z^n f(z)) = \frac{d}{dz} e^{-iz\tau} = -i\tau,$$

thus, Eq. (A.85) becomes

$$\int_{C_r} dz f(z) = \begin{cases} -\pi\tau, & \tau < 0, \\ \pi\tau, & \tau > 0. \end{cases} \quad (\text{A.86})$$

Finally,

$$I_1 = \int_{-\infty}^{\infty} dz f(z) = \lim_{R \rightarrow \infty, r \rightarrow 0} \int_{-R}^{-r} dz f(z) + \int_r^R dz f(z) = - \int_{C_r} dz f(z) = \begin{cases} \pi\tau, & \tau < 0, \\ -\pi\tau, & \tau > 0. \end{cases} \quad (\text{A.87})$$

Applying similar estimation for integrals I_2 and I_3 , we can show that

$$I_2 = \int_{-\infty}^{\infty} dz \frac{e^{-iz(\tau - \frac{2\ell_c}{c})}}{z^2} = \begin{cases} \pi(\tau - \frac{2\ell_c}{c}), & \tau < \frac{2\ell_c}{c}, \\ -\pi(\tau - \frac{2\ell_c}{c}), & \tau > \frac{2\ell_c}{c}, \end{cases} \quad (\text{A.88})$$

$$I_3 = \int_{-\infty}^{\infty} dz \frac{e^{-iz(\tau + \frac{2\ell_c}{c})}}{z^2} = \begin{cases} \pi(\tau + \frac{2\ell_c}{c}), & \tau < -\frac{2\ell_c}{c}, \\ -\pi(\tau + \frac{2\ell_c}{c}), & \tau > -\frac{2\ell_c}{c}. \end{cases} \quad (\text{A.89})$$

Taking these results into account, the integral in Eq. (A.83) becomes

$$I = \frac{\Gamma_c}{2\pi} \left(\frac{c}{\ell_c}\right)^2 \frac{1}{2} e^{-i\omega_0(t-t'-\frac{x}{c})} \begin{cases} 0, & t' > t - \frac{x}{c} + \frac{2\ell_c}{c}, \\ -\pi(t' - t + \frac{x}{c} - \frac{2\ell_c}{c}), & t - \frac{x}{c} < t' < t - \frac{x}{c} + \frac{2\ell_c}{c}, \\ \pi(t' - t + \frac{x}{c} + \frac{2\ell_c}{c}), & t - \frac{x}{c} - \frac{2\ell_c}{c} < t' < t - \frac{x}{c}, \\ 0, & t' < t - \frac{x}{c} - \frac{2\ell_c}{c}. \end{cases} \quad (\text{A.90})$$

Having calculated the integral over the frequency, we can now evaluate the time integral in (4.68b). Taking into account the results in (A.90), we can reduce the integration range to the following ones

$$\begin{aligned} \int_{t_0}^t &= \int_{t - \frac{x}{c} - \frac{2\ell_c}{c}}^{t - \frac{x}{c}} + \int_{t - \frac{x}{c}}^{t - \frac{x}{c} + \frac{2\ell_c}{c}}, & \text{when } x > 2\ell_c, \\ \int_{t_0}^t &= \int_{t - \frac{x}{c} - \frac{2\ell_c}{c}}^{t - \frac{x}{c}} + \int_{t - \frac{x}{c}}^t, & \text{when } 0 < x < 2\ell_c \end{aligned}$$

with $t > t_0 + \frac{x}{c} + \frac{2\ell_c}{c}$. Considering that we analyze the dynamics for times much longer than the round trip time of the produced photon, i.e., $t \gg \frac{2\ell_c}{c}$ (coarse-grained approximation), the integral for the case $x < 2\ell_c$ can be evaluated the same way as

the integral for $x > 2\ell_c$, since $t + 2\ell_c/c > t - x/c + 2\ell_c/c \approx t$. Hence the integrals above can be evaluated as follows:

$$\begin{aligned} \int_{t-\frac{x}{c}}^{t-\frac{x}{c}+\frac{2\ell_c}{c}} dt' f(t') &= \frac{1}{2} \left[f\left(t - \frac{x}{c} + \frac{2\ell_c}{c}\right) + f\left(t - \frac{x}{c}\right) \right] \frac{2\ell_c}{c}, \\ \int_{t-\frac{x}{c}-\frac{2\ell_c}{c}}^{t-\frac{x}{c}} dt' f(t') &= \frac{1}{2} \left[f\left(t - \frac{x}{c} - \frac{2\ell_c}{c}\right) + f\left(t - \frac{x}{c}\right) \right] \frac{2\ell_c}{c}. \end{aligned}$$

Hence, for the full integral, we obtain

$$\int_{t_0}^t dt' \int_0^\infty d\omega |\kappa_c(\omega)|^2 e^{-i\omega(t-t'-\frac{x}{c})} c(t') = \Gamma_c c\left(t - \frac{x}{c}\right).$$

For the case $x = 0$, the integration over the frequency in (A.83) gives the following result:

$$\frac{\Gamma_c}{2\pi} \left(\frac{c}{\ell_c}\right)^2 \frac{1}{2} e^{-i\omega_0(t-t')} \begin{cases} 0, & t' > \frac{2\ell_c}{c} \\ -\pi(t' - t + \frac{x}{c} - \frac{2\ell_c}{c}), & t < t' < t + \frac{2\ell_c}{c} \\ \pi(t' - t + \frac{x}{c} + \frac{2\ell_c}{c}), & t - \frac{2\ell_c}{c} < t' < t \\ 0, & t' < t - \frac{2\ell_c}{c}. \end{cases} \quad (\text{A.91})$$

Since the upper limit of the time integration is t , the second line of (A.91) does not contribute to the integration over the time, and the overall integral becomes:

$$\int_{t_0}^t dt' \int_0^\infty d\omega |\kappa_c(\omega)|^2 e^{-i\omega(t-t')} c(t') = \frac{\Gamma_c}{2} c(t).$$

A.9 Derivation of the master equation

In the following, we derive the dynamics of $X_S(t)$ from the Heisenberg equation, using Eqs. (4.7) and (4.79):

$$\begin{aligned} \frac{d}{dt} X_S(t) &= -\frac{i}{\hbar} [X_S(t), H^{(H)}(t)] = -\frac{i}{\hbar} [X_S(t), H_S^{(H)}(t)] \\ &\quad + \int_0^\infty d\omega \left(\kappa_c(\omega) b_\omega^\dagger(t) [X_S(t), c(t)] - \kappa_c^*(\omega) [X_S(t), c^\dagger(t)] b_\omega(t) \right). \end{aligned} \quad (\text{A.92})$$

From the definition (4.68a), we have $\int_0^\infty d\omega \kappa_c^*(\omega) b_\omega(t) = \sqrt{\Gamma_c} b(x=0, t)$, for which we can use the relation (4.73); hence

$$\begin{aligned} \frac{d}{dt} X_S(t) &= -\frac{i}{\hbar} [X_S(t), H_S^{(H)}(t)] \\ &\quad + \left(\sqrt{\Gamma_c} b_{in}^\dagger(t) + \frac{\Gamma_c}{2} c^\dagger(t) \right) [X_S(t), c(t)] - [X_S(t), c^\dagger(t)] \left(\sqrt{\Gamma_c} b_{in}(t) + \frac{\Gamma_c}{2} c(t) \right) \\ &= -\frac{i}{\hbar} [X_S(t), H_S^{(H)}(t)] + \sqrt{\Gamma_c} b_{in}^\dagger(t) [X_S(t), c(t)] - [X_S(t), c^\dagger(t)] \sqrt{\Gamma_c} b_{in}(t) \\ &\quad + \Gamma_c \left(c^\dagger(t) X_S(t) c(t) - \frac{1}{2} \{c^\dagger(t) c(t), X_S(t)\} \right). \end{aligned}$$

We further define the time-dependent dissipator

$$\mathcal{D}_{in,t}^\dagger(X_S(t)) = \sqrt{\Gamma_c} b_{in}^\dagger(t) [X_S(t), c(t)] - [X_S(t), c^\dagger(t)] \sqrt{\Gamma_c} b_{in}(t),$$

leading to

$$\begin{aligned} \frac{d}{dt}X_S(t) &= -\frac{i}{\hbar}[X_S(t), H_S^{(H)}(t)] + \mathcal{D}_{\text{in},t}^\dagger(X_S(t)) \\ &\quad + \Gamma_c \left(c^\dagger(t)X_S(t)c(t) - \frac{1}{2} \{c^\dagger(t)c(t), X_S(t)\} \right). \end{aligned} \quad (\text{A.93})$$

The expectation value of X_S can be calculated as follows:

$$\begin{aligned} \langle X_S(t) \rangle &= \text{Tr} \{X_S(t)\rho(t_0)\} = \text{Tr} \{X_S U(t, t_0)\rho(t_0)U^\dagger(t, t_0)\} \\ &= \text{Tr}_S \left\{ \text{Tr}_R \left\{ X_S U(t, t_0)\rho(t_0)U^\dagger(t, t_0) \right\} \right\} = \text{Tr}_S \{X_S \rho_S(t)\}, \end{aligned}$$

where we have used the cyclic property of the trace, and defined

$$\rho_S(t) = \text{Tr}_R \left\{ U(t, t_0)\rho(t_0)U^\dagger(t, t_0) \right\}.$$

Similarly, using the property $\text{Tr} \{A + B\} = \text{Tr} \{A\} + \text{Tr} \{B\}$, $\forall A, B$, we can calculate the averages on the right hand side of Eq. (A.93):

$$\begin{aligned} \langle [X_S(t), H_S^{(H)}(t)] \rangle &= \text{Tr} \{[X_S(t), H_S^{(H)}(t)]\rho(t_0)\} = \text{Tr} \{[X_S, H_S(t)] U(t, t_0)\rho(t_0)U^\dagger(t, t_0)\} \\ &= \text{Tr}_S \{[X_S, H_S(t)] \rho_S(t)\} = \text{Tr}_S \{X_S [H_S(t), \rho_S(t)]\}, \end{aligned}$$

$$\begin{aligned} \langle c^\dagger(t)X_S(t)c(t) \rangle &= \text{Tr}_S \{c^\dagger X_S c \rho_S(t)\} = \text{Tr}_S \{X_S c \rho_S(t) c^\dagger\}, \\ \langle \{c^\dagger(t)c(t), X_S(t)\} \rangle &= \text{Tr}_S \left\{ \{c^\dagger c, X_S\} \rho_S(t) \right\} = \text{Tr}_S \left\{ X_S \{ \rho_S(t), c^\dagger c \} \right\}. \end{aligned}$$

Assuming that the reservoir is initially a vacuum state $\rho_R(t_0) = |\emptyset\rangle\langle\emptyset|$, for the dissipator part $\mathcal{D}_{\text{in},t}^\dagger$ we get

$$\begin{aligned} \text{Tr} \{b_{\text{in}}^\dagger(t) [X_S(t), c(t)] \rho(t_0)\} &= \text{Tr} \{[X_S(t), c(t)] \rho(t_0) b_{\text{in}}^\dagger(t)\} \\ &= \text{Tr} \{[X_S(t), c(t)] \rho_S(t_0) \otimes \rho_R(t_0) b_{\text{in}}^\dagger(t)\} \\ &= \text{Tr} \{[X_S(t), c(t)] \rho_S(t_0) \otimes |\emptyset\rangle\langle\emptyset| b_{\text{in}}^\dagger(t)\} = 0. \end{aligned}$$

Similarly

$$\text{Tr} \left\{ [X_S(t), c^\dagger(t)] b_{\text{in}}(t) \rho(t_0) \right\} = 0.$$

Finally, Eq. (A.93) becomes

$$\begin{aligned} \text{Tr}_S \left\{ X_S \frac{d\rho_S(t)}{dt} \right\} &= \text{Tr}_S \{X_S [H_S(t), \rho_S(t)]\} \\ &\quad + \Gamma_c \left(\text{Tr}_S \{X_S c \rho_S(t) c^\dagger\} - \frac{1}{2} \text{Tr}_S \{X_S \{ \rho_S(t), c^\dagger c \} \} \right). \end{aligned}$$

Furthermore, using the property $\forall A, \text{Tr} \{AB\} = \text{Tr} \{AC\} \Leftrightarrow B = C$, we obtain the master equation for $\rho_S(t)$:

$$\frac{d}{dt}\rho_S(t) = [H_S(t), \rho_S(t)] + \Gamma_c \left(c \rho_S(t) c^\dagger - \frac{1}{2} \{ \rho_S(t), c^\dagger c \} \right).$$

Part III

Light-matter interaction in open cavities with dielectric stacks

Cavities with multilayer dielectric stacks

In the models discussed so far, the cavity mirror is modeled as a single dielectric layer with a fictitiously high refractive index. In practice, to achieve high mirror reflectivity, highly reflective dielectric coatings, or Bragg stacks are used as standard [130]. These comprise layer pairs of quarter-wavelength optical thickness dielectric material, with alternating refractive indices. Generally, a high reflectivity is only achieved for a large number of such layers, implying a notable penetration of the stack by incident light. A common strategy for enhancing the Purcell factor is the minimization of mode volume, which generally requires reducing mirror spacing. At its extreme, the mirror spacing can be of the same order as the resonant wavelength of interest [97]. This unintentionally increases the relative portion of the cavity mode within the dielectric stack [6, 130, 207], rendering inaccurate the standard spectral properties of a Fabry-Pérot resonator, such as its resonance frequency, linewidth and free spectral range. The propagation of light in cavities limited by dielectric mirrors has been studied before under the resonance condition where the frequency of the light matches a resonance frequency of the Fabry-Perot cavity as well as the design frequency of the dielectric stack forming the mirror [6, 130, 189]. Additionally, this problem has also been studied numerically for calculating the mode volume of leaky optical cavities [107, 106, 167]. Here we go a step further in considering the more general case of a wave of arbitrary wavelength traveling through the stack. Note that this is always the case if the emitter coupled to the cavity is not resonant with the cavity mode. To this end, in the following we derive a closed expression for the coupling between an atom and the field within a cavity whose mirrors are dielectric multilayer stacks.

As we can see from the previous derivation for a single-layered cavity case [Section 3.2], the modes of such a system are normalized in terms of the mode volume, which is the geometric volume of the optical resonator ($V = \mathcal{A}l_c$). However, in the case of the strong coupling resonator we consider below, the concept of mode volume departs from the standard notion of a geometric volume, suitably modifying the calculation of the Purcell Factor. This goes substantially beyond the aspects that have been addressed before [62, 188], now taking into account a large number of

dielectric layers and the off-resonant case, where the field and the design wavelength of the dielectric stacks are different.

In the following, we revise the concept of mode volume and cavity resonance frequency for a cavity formed from dielectric mirrors. Just like in the case for a cavity with a single-layered mirror, here we start by describing the system in the true-mode representation. We expand the theory, derived in the previous part, for the case of a multilayer stack. From this, we obtain a general expression for the coupling strength between the field and the atom. This allows for a discussion on a more realistic specification of effective cavity length and corresponding mode volume for short cavities. We show that the expected resonance frequency of the cavity, the resonant frequency of the emitter and the design frequency of the dielectric stack may differ substantially from one another. By considering the boundary to these effects, we demonstrate that the standard models of optical resonance are asymptotically re-achieved at extended cavity lengths.

6.1 The model

Having obtained the propagation of light in a cavity with a thin single-layered mirror in Section 3.2, we now extend this analysis to describe the field modes in Bragg stacks. This is done by considering an alternating stack of two dielectric materials. The first type of layer has a width δ with refractive index n_1 , while the second one has a width α with index n_2 . The stack has $2N - 1$ layers: $N - 1$ pairs of dielectric and one additional layer of index n_1 . As such, the first and last layers of the stack have the higher refractive index ($n_1 > n_2$) [8]. For the sake of simplicity, we disregard the substrate on which the coating is deposited, which would normally correspond to a final, significantly thicker, layer of low index material. An updated cavity model is shown in Fig. 6.1 and the corresponding relative permittivity is given by:

$$\varepsilon_r(x) = \begin{cases} 1 & -\ell_c < x \leq 0 \\ n_1^2 & j_1(\delta + \alpha) < x \leq j_1(\delta + \alpha) + \delta \\ n_2^2 & (j_2 - 1)(\delta + \alpha) + \delta < x \leq j_2(\delta + \alpha) \\ 1 & x > N(\delta + \alpha) - \alpha \end{cases}, \quad (6.1)$$

where $j_1 \in \{0, 1, 2, \dots, N - 1\}$ and $j_2 \in \{1, 2, \dots, N - 1\}$. Similar to the single-layered case, the mirror is designed to reflect best at wavelength λ_0 , which is used to specify the quarter wave dielectric layer optical thickness: $\delta = \lambda_0/4n_1$ and $\alpha = \lambda_0/4n_2$. For simplicity, we further consider $n_2 = 1$. By following the continuity of the field and its derivative, and imposing a perfect mirror at $x = -\ell_c$, we solve the equation (3.17) and find that the mode can be described in terms of the following functions:

$$\begin{aligned} B_0(\omega, x) &= e^{i\frac{\omega}{c}(x+\ell_c)}, \\ B_j(\omega, x) &= \begin{cases} \frac{1}{1-r_1} \left(B_{j-1}(\omega, x_2(j)) + r_1 B_{j-1}^*(\omega, x_2(j)) \right) e^{i\frac{\omega}{c}(x-x_2(j))} & j \text{ even,} \\ \frac{1}{1+r_1} \left(B_{j-1}(\omega, x_1(j)) - r_1 B_{j-1}^*(\omega, x_1(j)) \right) e^{i\frac{\omega}{c}n_1(x-x_1(j))} & j \text{ odd,} \end{cases} \end{aligned} \quad (6.2)$$

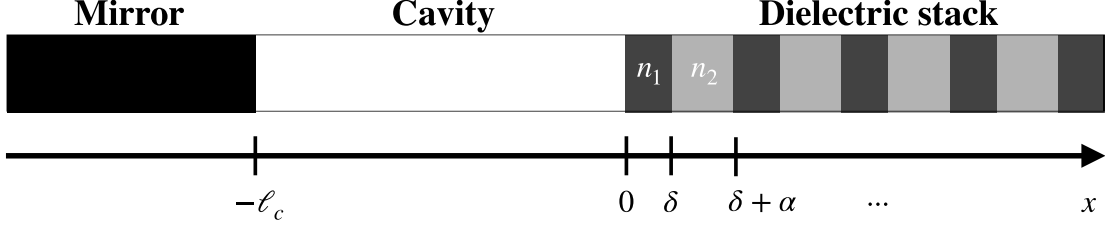


Figure 6.1: Description of the considered model. A perfect mirror stands at $x = -\ell_c$, delimiting a cavity of length ℓ_c with an alternating dielectric stack standing from zero.

where

$$x_1(j) = \frac{j-1}{2}(\delta + \alpha), \quad (6.3)$$

$$x_2(j) = \frac{j}{2}(\delta + \alpha) - \alpha. \quad (6.4)$$

The solution to the Eq. (3.17) is then given by

$$\Phi_\omega(x) = \sum_{j=0}^{2N} CA_j(\omega, x) \chi_{\Theta_j}, \quad (6.5)$$

where j runs over the $2N - 1$ possible layers, labelled as $\Theta_j \subset \mathbb{R}$. The $2N$ th term describes the mode exiting the cavity. C is a normalization factor common to all terms and

$$A_j(\omega, x) = B_j(\omega, x) - B_j^*(\omega, x), \quad j = 0, \dots, 2N. \quad (6.6)$$

In particular, Θ_j has the form

$$\Theta_0 = [-\ell_c, 0], \quad (6.7)$$

$$\Theta_j = \begin{cases} [x_2(j), x_2(j) + \alpha], & j \text{ even,} \\ [x_1(j), x_1(j) + \delta], & j \text{ odd.} \end{cases} \quad j = 1, \dots, 2N \quad (6.8)$$

For a mismatch of the light propagation frequency, ω , with the stack design frequency, $\omega_0 = 2\pi c/\lambda_0$, the intensity of the mode can either decay or grow exponentially through the stack. This can potentially be a combination of each, achieving extremal points of intensity within the dielectric-layer stack. Some examples are shown in Fig. 6.2.

6.2 Effective cavity response function

After the modes have been described in the form of Eq. (6.5), we consider the effective optical response of the structure. Following the normalization of the modes in (6.5), the inside and outside modes have the form

$$\Phi_{\omega, \text{ins}}(x) = \frac{2i}{\sqrt{2\pi c \mathcal{A}}} e^{i\frac{\omega}{c}\ell_c} \mathcal{T}_\omega \sin\left[\frac{\omega}{c}(x + \ell_c)\right], \quad (6.9a)$$

$$\Phi_{\omega, \text{outs}}(x) = \frac{1}{\sqrt{2\pi c \mathcal{A}}} \left(e^{2i\frac{\omega}{c}\ell_c} \frac{\mathcal{T}_\omega}{\mathcal{T}_\omega^*} e^{i\frac{\omega}{c}x} - e^{-i\frac{\omega}{c}x} \right), \quad (6.9b)$$

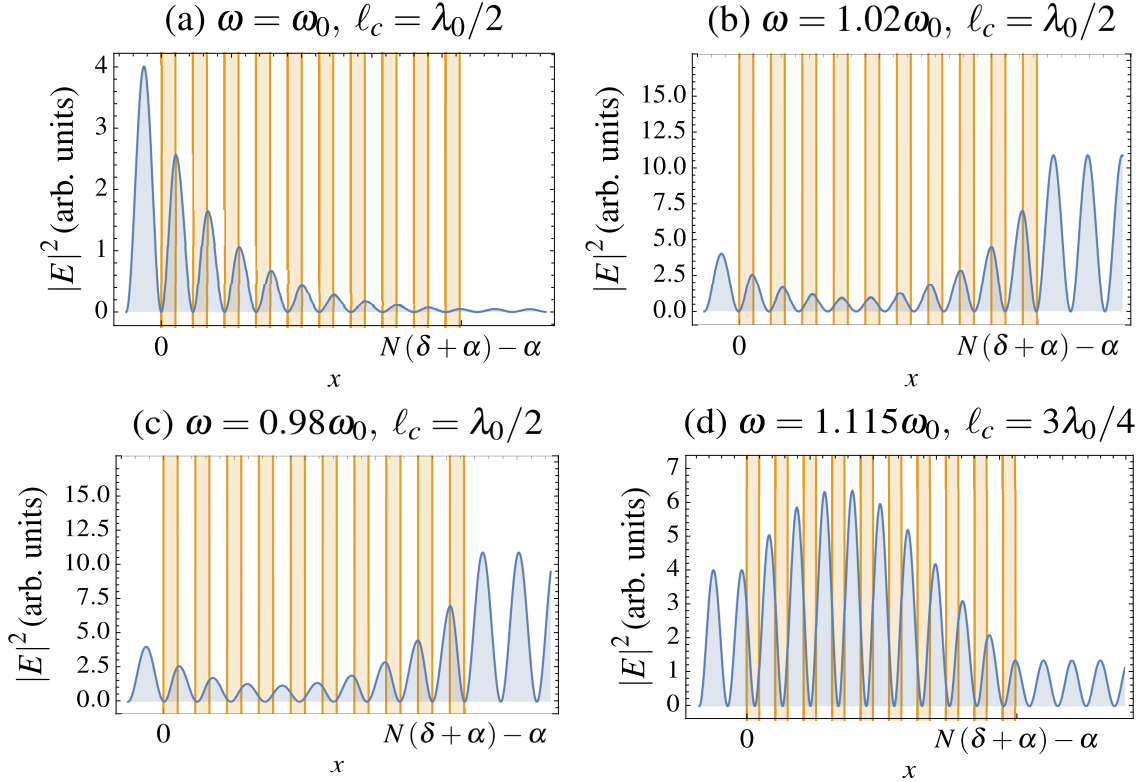


Figure 6.2: Mode propagation of a wave of wavelength λ , for a cavity with a multilayered stack with an index of $n_1 = 1.25$. A perfect mirror stands at $x = -\ell_c$, forming a cavity of length ℓ_c with an alternating dielectric stack of $2N - 1 = 21$ alternating layers of width $\delta = \lambda_0/4n_1$ and $\alpha = \lambda_0/4n_2$ (n_2 is taken to be 1). The propagation frequency $\omega = 2\pi c/\lambda$ is varied to observe the mode propagation. In (a), the case when $\ell_c = \lambda_0/2$ and ω exactly matches with the cavity design resonance frequency ω_0 is shown, obtaining the strongest confinement of light inside of the cavity. In (b) and (c), we can see how the intensity changes when the propagating light is slightly off resonance. Finally, in (d) we increase the cavity length to reach $\ell_c = 3\lambda_0/4$ and observe that we achieve resonance coupling when $\omega = 1.1022\omega_0$. Moreover, we can see that in this case the intensity of the light within the layer stack exceeds the intensity of the light inside of the cavity.

where $\Phi_{\omega,\text{ins}}(x)$ describes the mode between the perfect mirror and the first layer of the multilayered mirror, and $\Phi_{\omega,\text{outs}}(x)$ describes the mode outside the cavity, where there are no dielectric layers anymore. Here, \mathcal{T}_ω is the response function of the structure, which has the form

$$\mathcal{T}_\omega = \frac{e^{-i\frac{\omega}{c}(\ell_c + (N-1)(\delta + \alpha))}}{B_{2N-2}^*(\omega)} \frac{t(\omega)}{1 + e^{i\frac{\omega}{c}\delta} e^{i\phi_B(\omega)} r(\omega)}, \quad (6.10)$$

where $\phi_B(\omega) = \arg\left(B_{2N-2}/B_{2N-2}^*\right)$ and for simplicity we have omitted the argument of $B_{2N-2} = B_{2N-2}(\omega, x_1(2N-1))$. Here, $t(\omega)$ and $r(\omega)$ remain the same as for the single-layer case.

If we introduce an indexing of the response function defined above, such that $\mathcal{T}_\omega = \mathcal{T}_\omega^N$, where the label N stands for the $2N - 1$ layers, then it can be shown that

$$\frac{e^{-i\frac{\omega}{c}(\ell_c+(N-1)(\delta+\alpha))}}{B_{2N-2}^*(\omega)} = \mathcal{T}_\omega^{N-1}, \quad (6.11)$$

where \mathcal{T}_ω^{N-1} is the response function of a cavity having a dielectric stack with $2N - 3$ dielectric layers. Figure 6.3 shows a series of different cavity response functions for different numbers of layer stacks and cavity lengths. Here, our model is seen to exhibit the standard behavior of an optical cavity by showing a decreased linewidth as the number of layers increases, as would be expected from increased mirror reflectivity. Furthermore, the free spectral range of the cavity decreases as its length is increased.

Similar to the single-layer case, here we can decompose the square modulus of the response function as a sum of Lorentzian-like functions, analogous to the one in Eq. (3.28):

$$|\mathcal{T}_\omega|^2 = \sum_{m=-\infty}^{\infty} \left(\frac{c}{\delta |B_{2N-2}(\omega)|^2} \frac{\gamma_N(\omega)}{(\omega - \hat{\omega}_m(\omega))^2 + \left(\frac{\gamma_N(\omega)}{2}\right)^2} \right), \quad (6.12)$$

where

$$\gamma_N(\omega) = -c \frac{\ln |r(\omega)|}{\delta/2}, \quad (6.13)$$

$$\hat{\omega}_m = \frac{c\pi}{\delta/2} m - c \frac{(\phi_r(\omega) + \phi_B(\omega) + \pi)}{\delta}. \quad (6.14)$$

The term $\phi_B(\omega)$ in the expression of $\hat{\omega}_m$ accounts for the multilayer nature of the mirror. In the single-layered case, this has the simple, analytical form $\phi_{B_1}(\omega) = 2\ell_c\omega/c$.

As we can see from Fig. 6.3, the multilayer structure leads to a narrowly peaked Lorentzian response function. In order to obtain the individual Lorentzians corresponding to each peak in the response function, we fit each individual peak to the exact cavity response function shown in Eq. (6.12), obtaining numerical parameters for the values of $L_N^{(m)}$, $\gamma_N^{(m)}$ and $\omega_N^{(m)}$:

$$|\mathcal{T}_\omega|^2 = \sum_m \frac{c}{2L_N^{(m)}} \frac{\gamma_N^{(m)}}{(\omega - \omega_N^{(m)})^2 + \left(\frac{\gamma_N^{(m)}}{2}\right)^2}. \quad (6.15)$$

In the case of a single-layered mirror, we obtain the individual Lorentzians by evaluating the parameters in (3.29) at the resonance frequencies ω_m . Here, however, we can not follow the same procedure due to the complicated nature of the coefficient $|B_{2N-2}(\omega)|^2$. Therefore, we apply a numerical fitting to recover the accuracy of the procedure described above.

We now examine what happens when we vary the spacing between the mirrors. By taking into account the multilayer structure of the mirror, we also observe resonance frequency shifts from the expected resonances, i.e., for a cavity having a mirror spacing ℓ_c , the expected resonance frequency would be $\omega_m = 2\pi c/\lambda_0 = \pi m (c/\ell_c)$, where m is the number of antinodes between the mirrors. However, the resonance

frequencies that we obtain with a multilayered structure, in general, do not match the values of ω_m described above (see Fig. 6.4). In other words, if in the multilayered case we write $\omega_{\text{eff}} = \omega_N^{(m)} = \pi m (c/\ell_{\text{eff}})$ for the resonance frequencies, then, in general ℓ_{eff} is different from ℓ_c . In particular, ℓ_{eff} is the same as ℓ_c only if $\ell_c = p\lambda_0/2$, where p is an integer. Moreover, the shorter the cavity, the greater the difference between ω_{eff} and ω_m .

Since here we study cavities inducing strong coupling and the more layers, the higher the cavity finesse, the individual Lorentzian terms in Eq. (6.15) are well separated. Thus, for the response function we can write

$$\mathcal{T}_\omega \approx \sum_m \sqrt{\frac{c}{2L_N^{(m)}}} \frac{\sqrt{\gamma_N^{(m)}}}{(\omega - \omega_N^{(m)}) + i\frac{\gamma_N^{(m)}}{2}} = \sum_m \mathcal{T}_m(\omega). \quad (6.16)$$

In Chapter 7 we study the accuracy of this estimation in more details, considering high as well as low finesse cavities.

6.3 Trapped atom interacting with a multilayer cavity

Having obtained the response function for the multilayer cavity, we can now study the single photon production from the atom trapped in such a multilayer cavity. Starting from the true-mode representation introduced in Section 4.1.1, we can write the atom-field coupling strength analogous to Eq. (4.6):

$$\eta_\omega = \sum_m \left(i \sqrt{\frac{\omega}{\hbar\epsilon_0 L_N^{(m)}}} d_{\text{fe}} e^{i\frac{\omega}{c}\ell_c} \sin\left[\frac{\omega}{c}(x_A + \ell_c)\right] \sqrt{\frac{\gamma_N^{(m)}}{2\pi} \frac{1}{(\omega - \omega_N^{(m)}) + i\frac{\gamma_N^{(m)}}{2}}} \right). \quad (6.17)$$

Comparing this result with the single-layer case, we can see that the expressions are the same, with the exception that for the multilayer case we have $L_N^{(m)}$ instead of ℓ_c and $\gamma_N^{(m)}$ instead of Γ_c . Similarly, if we interpret the product $L_N^{(m)}\mathcal{A}$ in the pre-factor as the mode volume, it is no longer defined through the geometric length of the cavity, due to the discrepancy between $L_N^{(m)}$ and ℓ_c .

Over the width $\gamma_N^{(m)}$ of a single Lorentzian, the prefactor $\sqrt{\omega}$ can be considered as constant for $\omega \simeq \omega_N^{(m)} \pm \gamma_N^{(m)}$, therefore we can further approximate the mode selective coupling $\eta_{\omega,m}$ as:

$$\eta_{\omega,m} \approx i \sqrt{\frac{\omega_N^{(m)}}{\hbar\epsilon_0 L_N^{(m)}}} d_{\text{fe}} e^{i\frac{\omega}{c}\ell_c} \sin\left[\frac{\omega}{c}(x_A + \ell_c)\right] \sqrt{\frac{\gamma_N^{(m)}}{2\pi} \frac{1}{(\omega - \omega_N^{(m)}) + i\frac{\gamma_N^{(m)}}{2}}}, \quad (6.18)$$

where x_A is the position of the atom inside the cavity.

Using the expression (6.18), we can now move from true-mode representation to pseudo-mode representation. Analogous to the definition in (4.13), we define the following operator:

$$\hat{a}_m = \frac{1}{g_m} \int_0^\infty d\omega \eta_{\omega,m} \hat{a}_\omega, \quad (6.19)$$

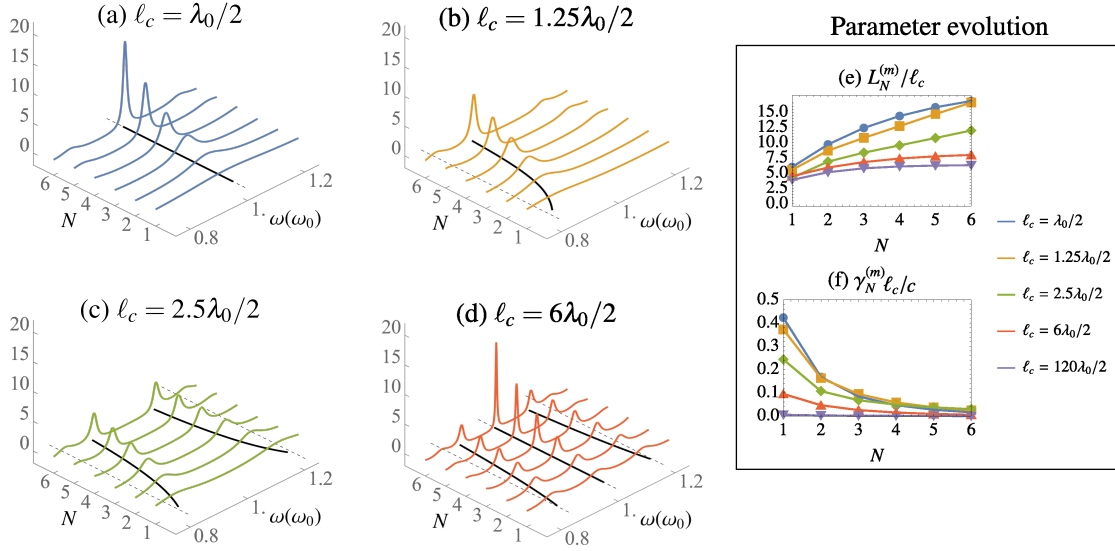


Figure 6.3: Cavity response function, $|\mathcal{T}_\omega|^2$, as a function of the angular frequency of the light and the number of layers, $2N - 1$, for a cavity with a multilayered stack with a refractive index $n_1 = 1.25$. A perfect mirror stands at $x = -\ell_c$, and there is an alternating dielectric stack with a varying number of N layers of width $\delta = \lambda_0/4n_1$ and $N - 1$ layers of width $\alpha = \lambda_0/4n_2$ (where n_2 is taken to be 1). Both the number of dielectric layers and the spacing of the cavity are varied to observe different sorts of cavity response functions: (a) shows $\ell_c = \lambda_0/2$, (b) $\ell_c = 1.25\lambda_0/2$, (c) $\ell_c = 2.5\lambda_0/2$, and (e) $\ell_c = 6\lambda_0/2$. All of these can be decomposed as a sum of Lorentzian functions in ω . The dashed lines correspond to perfect cavity resonances: $\omega_m = m\pi c/\ell_c$, where m is the number of antinodes between the mirrors. The black, solid lines correspond to $\omega_N^{(m)}$, the peak responses followed by the modes. These do not coincide with ω_m and are strongly dependent on the number of layers. (e) and (f) also follow the values of $L_N^{(m)}$ and $\gamma_N^{(m)}$ for different values of ℓ_c .

which satisfies the commutation relations:

$$\begin{aligned} [\hat{a}_m, \hat{a}_{m'}^\dagger] &= \delta_{mm'}, \\ [\hat{a}_m, \hat{a}_{m'}] &= 0. \end{aligned}$$

The normalization coefficient g_m can be calculated performing similar calculation as presented in Appendix A.5 leading to

$$g_m = -\sqrt{\frac{\omega_N^{(m)}}{\hbar\epsilon_0 L_N^{(m)} \mathcal{A}}} d_{\text{fe}} e^{i\frac{\omega_N^{(m)}}{c}\ell_c} \sin\left[\frac{\omega_N^{(m)}}{c}(x_A + \ell_c)\right] + \mathcal{O}(\epsilon^2), \quad (6.20)$$

up to an error of the order ϵ^2 , where $\epsilon = \gamma_N^{(m)} \frac{x_A + \ell_c}{c}$. The width $\gamma_N^{(m)}$ decreases with increasing the number of layers and cavity length, hence ϵ becomes smaller (see Fig. 6.3) and the approximation is well validated.

If we compare the expression (6.20) with the atom-perfect cavity coupling g introduced in Eq. (4.7), which explicitly reads as follows:

$$g = -\sqrt{\frac{\omega_m}{\hbar\epsilon_0 \ell_c \mathcal{A}}} d_{\text{fe}} e^{i\frac{\omega_m}{c}\ell_c} \sin\left[\frac{\omega_m}{c}(x_A + \ell_c)\right], \quad (6.21)$$

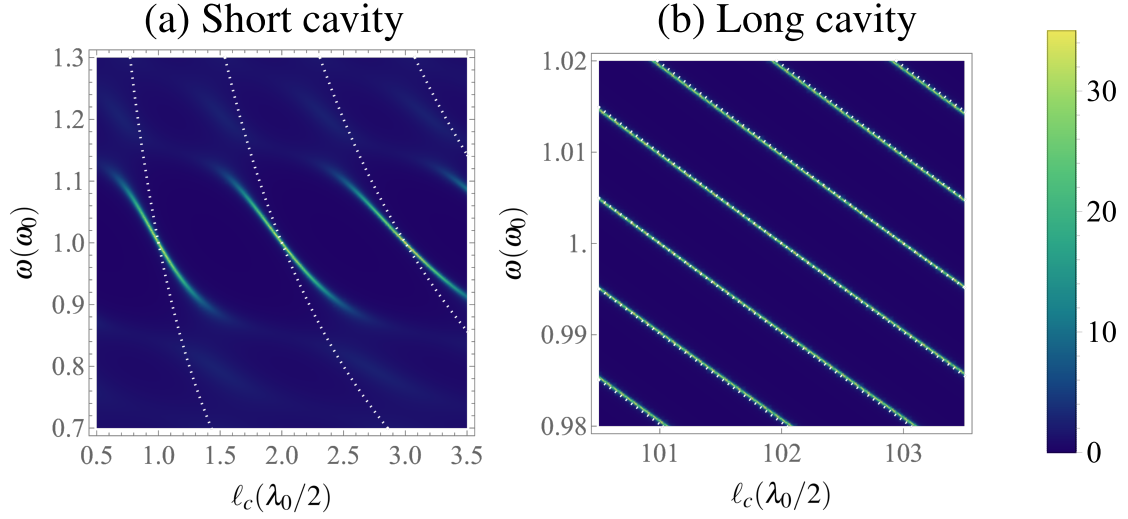


Figure 6.4: Calculated Inside/Outside intensity ratio using the electromagnetic propagation of the mode versus $\pi mc/\ell_c$ shown in white, dotted lines. When cavities are very short, the mismatch is appreciable and the maximum Inside/Outside ratio lines predicted conventionally differ significantly with respect to the mode prediction. We can see that, only at the points where we have a cavity of length $\ell_c = p\lambda_0/2$, where p is an integer, the predicted and actual lines match.

(with $\omega_m = m\pi c/\ell_c$), we can see that it is different from (6.20) by an error factor $\mathcal{O}(\epsilon^2)$, and due to the mismatch between ℓ_c and $L_N^{(m)}$ and ω_m and $\omega_N^{(m)}$.

Obtaining the description of the atom-multilayer cavity system in true-mode and pseudo-mode representations, we now move to the inside-outside representation, the derivation of which is explicitly shown in the next chapter.

Effective models for multilayer cavity dynamics

As we have discussed in Chapter 4, by using frequency dependent cavity-reservoir coupling function (4.10) corresponding to the inside-outside representation, one can have the complete characterization of the open cavity dynamics derived from first principles. We showed that for the approximate inside-outside model to work, the cavity must be of high finesse. If we consider Fabry-Pérot type cavities, in practice the high finesse is achieved via increasing the number of dielectric layers forming the cavity mirrors. As discussed in the previous chapter, the dielectric structure of the cavity mirrors may alter the characteristic parameters of the cavity, such as cavity free spectral range, mode volume and the effective length determining the cavity resonances. Taking into account these results, in this chapter, we extend the effective models derived in Chapter 4 for a cavity featuring multilayer mirrors. In particular, we derive the frequency-dependent cavity-reservoir coupling function for cavities made of multilayer dielectric mirrors, starting from first-principles. This provides the complete characterization of the cavity dynamics, explicitly taking into account the effects induced by the geometrical structure of the mirror. Based on this derivation, we introduce a generalized cavity response function and an effective reflectivity that allow to describe the behavior of the multilayer cavity in terms of a single-layered one, whose characteristic parameters account for the actual multilayer nature of the cavity. We estimate the error of such a reformulated description with respect to the number of dielectric layers and the cavity length. We follow the same derivation scheme described in Ref. [52], where the cavity-reservoir coupling is derived by comparing the modes of a closed system consisting of an open cavity and its surroundings to the modes of a system where a perfect cavity is coupled to the semi-infinite reservoir of continuous modes. This allows us to derive a generalized cavity-environment coupling function that accounts for the effects caused by the actual structure of the mirror. We apply this model to study the dynamics of an atom trapped in such a multilayer cavity and study the properties of a photon produced from such a system. In particular, we demonstrate that apart from having the time profile of the produced photon inside the cavity, with this formulation, one can obtain the spectral shape of the photon as well as its spatial distribution outside the cavity.

7.1 True-mode representation for a multilayer cavity

Just like for the single-layered cavity, here we start by analyzing a global closed system consisting of a non-perfect multilayered cavity and its surroundings. In this representation, we can quantize the model according to the modes (6.9) that extend over inside as well as outside the cavity:

$$\Phi_{\omega,\text{ins}}(x) = \frac{2i}{\sqrt{2\pi c\mathcal{A}}} e^{i\frac{\omega}{c}\ell_c} \mathcal{T}_\omega \sin\left[\frac{\omega}{c}(x + \ell_c)\right], \quad (7.1a)$$

$$\Phi_{\omega,\text{outs}}(x) = \frac{1}{\sqrt{2\pi c\mathcal{A}}} \left(e^{2i\frac{\omega}{c}\ell_c} \frac{\mathcal{T}_\omega}{\mathcal{T}_\omega^*} e^{i\frac{\omega}{c}x} - e^{-i\frac{\omega}{c}x} \right). \quad (7.1b)$$

\mathcal{T}_ω is the multilayer cavity response function derived in Eq. (6.10), which can be written in the following form:

$$\mathcal{T}_\omega \approx \sum_m \mathcal{T}_m(\omega), \quad (7.2a)$$

$$\mathcal{T}_m(\omega) = \sqrt{\frac{c}{2L_N^{(m)}}} \frac{\sqrt{\gamma_N^{(m)}}}{(\omega - \omega_N^{(m)}) + i\frac{\gamma_N^{(m)}}{2}}, \quad (7.2b)$$

where the index m spans through $2p - 1 + 2N + \lceil 2(\ell_c - p\frac{\lambda_0}{2}) \rceil$, with p being the number of antinodes within the length ℓ_c . We recall that $L_N^{(m)}$ is the length determining the light amplification strength inside the cavity, while $\ell_{\text{eff}}^{(m)}$ is the effective cavity length determined from the resonance frequencies $\omega_N^{(m)} = m\pi c/\ell_{\text{eff}}^{(m)}$.

While for a cavity with a single-layered mirror, a similar expression to (7.2) can be obtained with analytically defined $\gamma_1^{(m)}$ and $\omega_1^{(m)}$ [see Eqs. (3.29) and (3.31)], for multilayer structure this expression is obtained numerically via imposing $|\mathcal{T}_\omega| \approx |\sum \mathcal{T}_m(\omega)|$, leading to numerically defined $\gamma_N^{(m)}$, $\omega_N^{(m)}$ and $L_N^{(m)}$. We highlight that, unlike here, in Section 6.2 we performed the fitting of the function $|\mathcal{T}_\omega|^2$, since we considered a regime where $\mathcal{T}_m(\omega)\mathcal{T}_{m'}(\omega) = \delta_{mm'}$. However, here we want to consider a more general case, where there can be overlap between different $\mathcal{T}_m(\omega)$. In Fig. 7.1, we illustrate the response function \mathcal{T}_ω [Eq. (6.10)] and the individual terms $\mathcal{T}_m(\omega)$ for cavities with different mirror spacing and dielectric layers. As we can see, for certain scenarios, the overlap between the neighboring $\mathcal{T}_m(\omega)$ is significant, and given the representation of finesse as the ratio of cavity free spectral range to its linewidth, the significant overlap implies that the cavity is of low finesse. For the situations where the overlap is negligible, around the resonance peak ω_0 the full response function (7.2a) can be reduced to a single term $\mathcal{T}_m(\omega)$: $\mathcal{T}_\omega \approx \mathcal{T}_m(\omega)$ (high-finesse), where $m = 1$ for the Lorentzian centred around ω_0 . In particular, in Fig. 7.2(a), we show the error of such an approximation for cavities of different mirror spacing ℓ_c and dielectric structure. The error is estimated by calculating the term

$$1 - \left| \frac{\langle \mathcal{T}_\omega, \mathcal{T}_m(\omega) \rangle}{\langle \mathcal{T}_\omega, \mathcal{T}_\omega \rangle} \right| = 1 - \left| \frac{\int d\omega \mathcal{T}_\omega \mathcal{T}_m^*(\omega)}{\int d\omega |\mathcal{T}_\omega|^2} \right|, \quad (7.3)$$

where the integration is done over the region $\omega_N^{(m)} - \gamma_N^{(m)}/2 < \omega < \omega_N^{(m)} + \gamma_N^{(m)}/2$. As we can see, for the cases where the number of nodes inside the cavity is not

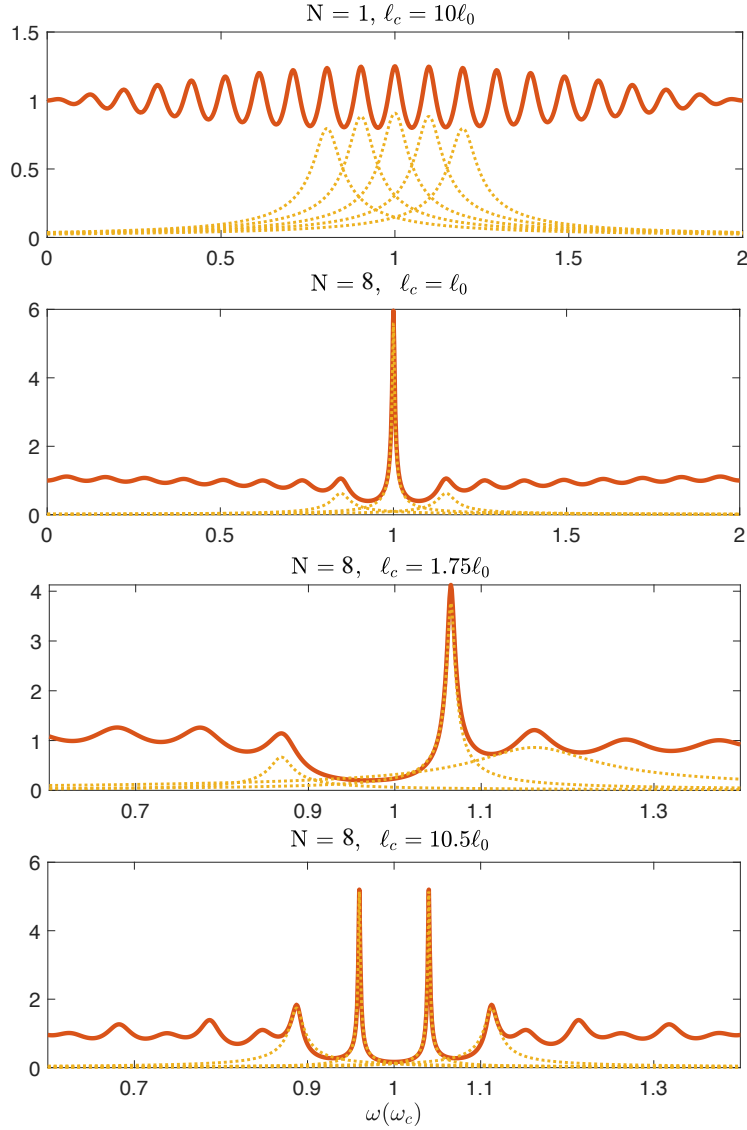


Figure 7.1: Response function of a multilayer cavity. Solid lines represent the actual response function $|\mathcal{T}_\omega|$, while dashed lines correspond to each term $|\mathcal{T}_m(\omega)|$ close to the resonance frequency ω_0 . N is the number of dielectric pairs and ℓ_c is the mirror spacing, with $\ell_0 = \lambda_0/2$.

exact, i.e., $\ell_c/\ell_0 \neq p$, the main resonance peak is not symmetric with respect to the neighboring peaks, and while it is well separated from one, it can be significantly overlapped with the other, increasing the error in the approximation.

Taking into account this analysis of the response function, in the following, we reformulate $\mathcal{T}_m(\omega)$ around each peak $\omega_N^{(m)}$ in terms of a single-layered cavity response function derived in Section 3.2. This reformulation can be thought of as replacing a multilayer mirror with an effective single-layered one with negligible thickness, which is positioned such that it forms a cavity of mirror spacing $\ell_{\text{eff}}^{(m)}$ and the resonance frequency $\omega_N^{(m)}$. The spectral transmission and reflection functions for this fictitious

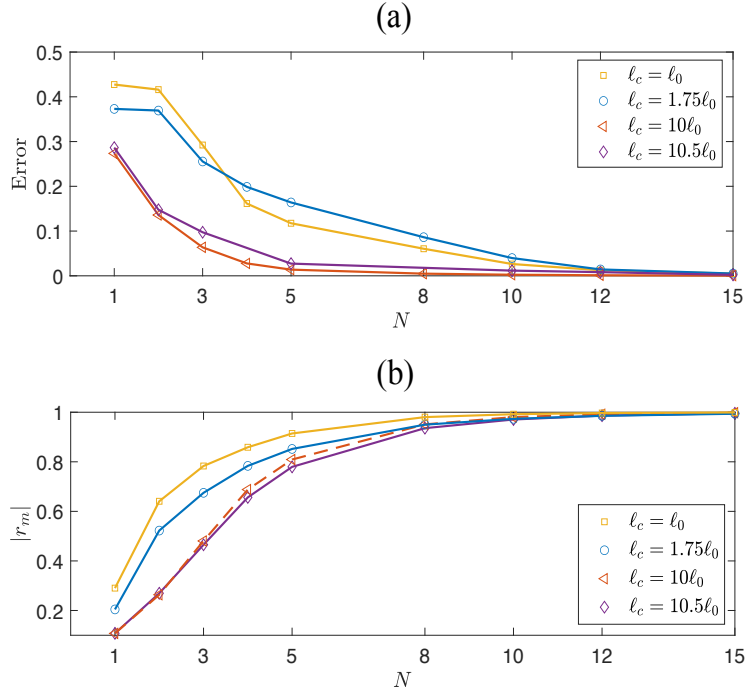


Figure 7.2: (a): The error of approximating the full response function by a single term of the form (7.2b) around the resonance peak ω_0 for cavities with different lengths ℓ_c and with different number of dielectric layer pairs N . (b): Reflectivity of a mirror replacing the partially transparent multilayer mirror: $|r_m| = r_m(\omega_N^{(m)}) = e^{-\gamma_N^{(m)} \ell_{\text{eff}}^{(m)}}/c$.

mirror are $t_m(\omega)$ and $r_m(\omega)$ respectively, such that (see the details in Appendix B.1):

$$\mathcal{T}_m(\omega) \approx T_{m,\omega} = \sqrt{\frac{\ell_{\text{eff}}^{(m)}}{L_N^{(m)}}} \frac{t_m(\omega)}{1 + r_m(\omega) e^{2i\frac{\omega}{c} \ell_{\text{eff}}^{(m)}}}, \quad (7.4)$$

with $|r_m(\omega_N^{(m)})| = e^{-\gamma_N^{(m)} \ell_{\text{eff}}^{(m)}/c}$, $r_m(\omega) = |r_m(\omega)| e^{i\varphi_r(\omega)}$ and $\varphi_r(\omega_N^{(m)}) = \pi$. As we can see, the expression (7.4) is different from the standard single-layered mirror response function [Eq. (3.24)] by the factor $\sqrt{\ell_{\text{eff}}^{(m)}/L_N^{(m)}}$, which tends to 1 only in particular cases [see Fig. 6.3]. Thus, Eq. (7.4) can be considered as the generalized cavity response function, that incorporates the effects induced by the cavity structure. We remark that the function $t_m(\omega)$ ($r_m(\omega)$) is not uniquely defined in the whole spectrum, and the way we define it here does not provide the complete spectral information of the phase factor $\varphi_t(\omega)$ ($\varphi_r(\omega)$). Additionally, we can interpret the term $|r_m| := |r_m(\omega_N^{(m)})|$ as the effective reflectivity of the multilayer cavity and in Fig. 7.2(b), we show the dependence of this effective reflectivity on the number of dielectric layer pairs and the mirror spacing of the actual cavity. Comparing Fig. 7.2(b) with the error figure Fig. 7.2(a), we can estimate the value of the mirror reflectivity for which the complete modes of the cavity can be replaced by individual ones.

7.1.1 Electromagnetic field in the true-mode representation

Using the modes in Eq. (7.1), we can write the quantized electric and magnetic fields expressions in true-mode representation [59, 60]. In particular, the fields inside and outside of the cavity read as follows:

$$\begin{aligned} E_{\text{ins}}(x) &= -i \int_0^\infty d\omega \sqrt{\frac{\hbar\omega}{2\varepsilon_0}} \left(\Phi_{\omega,\text{ins}}(x) a_\omega - \Phi_{\omega,\text{ins}}^*(x) a_\omega^\dagger \right), \\ &= \int_0^\infty d\omega \sqrt{\frac{\hbar\omega}{\pi c \mathcal{A} \varepsilon_0}} \left(\sin \left[\frac{\omega}{c} (x + \ell_c) \right] e^{i\frac{\omega}{c} \ell_c} \mathcal{T}_\omega a_\omega + H.c. \right), \end{aligned} \quad (7.5a)$$

$$\begin{aligned} E_{\text{outs}}(x) &= -i \int_0^\infty d\omega \sqrt{\frac{\hbar\omega}{2\varepsilon_0}} \left(\Phi_{\omega,\text{outs}}(x) a_\omega - \Phi_{\omega,\text{outs}}^*(x) a_\omega^\dagger \right), \\ &= -i \int_0^\infty d\omega \sqrt{\frac{\hbar\omega}{4\pi c \mathcal{A} \varepsilon_0}} \left(\left[e^{2i\frac{\omega}{c} \ell_c} \frac{\mathcal{T}_\omega}{\mathcal{T}_\omega^*} e^{i\frac{\omega}{c} x} - e^{-i\frac{\omega}{c} x} \right] a_\omega - H.c. \right), \end{aligned} \quad (7.5b)$$

$$B_{\text{ins}}(x) = \frac{i}{c} \int_0^\infty d\omega \sqrt{\frac{\hbar\omega}{\pi c \mathcal{A} \varepsilon_0}} \left(\cos \left[\frac{\omega}{c} (x + \ell_c) \right] e^{i\frac{\omega}{c} \ell_c} \mathcal{T}_\omega a_\omega - H.c. \right), \quad (7.6a)$$

$$B_{\text{outs}}(x) = \frac{i}{c} \int_0^\infty d\omega \sqrt{\frac{\hbar\omega}{4\pi c \mathcal{A} \varepsilon_0}} \left(\left[e^{2i\frac{\omega}{c} \ell_c} \frac{\mathcal{T}_\omega}{\mathcal{T}_\omega^*} e^{i\frac{\omega}{c} x} + e^{-i\frac{\omega}{c} x} \right] a_\omega - H.c. \right), \quad (7.6b)$$

where a_ω is the annihilation operator of the true modes describing the whole cavity-environment closed system. These operators satisfy the commutation relations

$$[a_\omega, a_{\omega'}^\dagger] = \delta(\omega - \omega'), \quad (7.7a)$$

$$[a_\omega, a_{\omega'}] = 0. \quad (7.7b)$$

Furthermore, the Hamiltonian for such a closed system in the true-mode representation can be written

$$H = \int_0^\infty d\omega \hbar\omega a_\omega^\dagger a_\omega. \quad (7.8)$$

After writing the modes in the true-mode representation, in the following we separate these true modes into inside and outside ones.

7.2 Inside-outside representation

In the previous section, we introduced the model in the true-mode representation, where the modes describe the full cavity-environment closed system. In this section, we analyze the system in the inside-outside representation presented in Section 4.1.2, where the inside modes correspond to the discrete modes of a perfect cavity and the outside modes are the continuous reservoir modes that are delimited by the perfect cavity. This separation of the modes into the inside and the outside allows one to study the dynamics of the cavity separated from its environment while still providing the characterization of the full closed system.

In the derivation below, we consider a regime with relatively high effective reflectivity, so that we can approximate the full response function with a single term $\mathcal{T}_m(\omega)$, corresponding to the strongest resonance peak. Since we consider a single peak m , for readability, here after we drop the indexing m for the terms $\ell_{\text{eff}}^{(m)} := \ell_{\text{eff}}$ and $L_N^{(m)} := L_N$, and redefine the resonance frequency $\omega_m := \omega_N^{(m)}$ and the cavity linewidth $\gamma_N^{(m)} = \gamma_m$.

7.2.1 Electromagnetic field in the inside-outside representation

The electric and magnetic fields in a perfect cavity of length ℓ_{eff} , the left mirror of which is placed at $-\ell_c$ read as follows:

$$E_{0,\text{ins}}(x) = \sum_{m=1}^{\infty} \sqrt{\frac{\hbar\omega_m}{\ell_{\text{eff}}\mathcal{A}_r\varepsilon_0}} (c_m + c_m^\dagger) \sin\left[\frac{\omega_m}{c}(x + \ell_c)\right], \quad (7.9a)$$

$$B_{0,\text{ins}}(x) = \frac{i}{c} \sum_{m=1}^{\infty} \sqrt{\frac{\hbar\omega_m}{\ell_{\text{eff}}\mathcal{A}_r\varepsilon_0}} (c_m - c_m^\dagger) \cos\left[\frac{\omega_m}{c}(x + \ell_c)\right], \quad (7.9b)$$

where c_m/c_m^\dagger is the discrete annihilation/creation operator describing the perfect cavity mode with the resonance frequencies $\omega_m = \pi cm/\ell_{\text{eff}}$. These operators satisfy the following relations:

$$[c_m, c_{m'}^\dagger] = \delta_{mm'}, \quad (7.10a)$$

$$[c_m, c_{m'}] = 0. \quad (7.10b)$$

\mathcal{A}_r is the transverse area of the mode of the perfect cavity, which is related to the actual mode area of the multilayer mirror with the following relation: $\mathcal{A}_r = (L_N/\ell_{\text{eff}})\mathcal{A}$. Taking this into account the fields in Eq. (7.9) become

$$E_{0,\text{ins}}(x) = \sum_{m=1}^{\infty} \sqrt{\frac{\hbar\omega_m}{L_N\mathcal{A}\varepsilon_0}} (c_m + c_m^\dagger) \sin\left[\frac{\omega_m}{c}(x + \ell_c)\right], \quad (7.11a)$$

$$B_{0,\text{ins}}(x) = \frac{i}{c} \sum_{m=1}^{\infty} \sqrt{\frac{\hbar\omega_m}{L_N\mathcal{A}\varepsilon_0}} (c_m - c_m^\dagger) \cos\left[\frac{\omega_m}{c}(x + \ell_c)\right]. \quad (7.11b)$$

Analogously, we can define the fields for the outside:

$$E_{0,\text{outs}}(x) = \int_0^\infty d\omega \sqrt{\frac{\hbar\omega}{\pi c\mathcal{A}\varepsilon_0}} (b_\omega + b_\omega^\dagger) \sin\left[\frac{\omega}{c}(x - d)\right], \quad (7.12a)$$

$$B_{0,\text{outs}}(x) = \frac{i}{c} \int_0^\infty d\omega \sqrt{\frac{\hbar\omega}{\pi c\mathcal{A}\varepsilon_0}} (b_\omega - b_\omega^\dagger) \cos\left[\frac{\omega}{c}(x - d)\right], \quad (7.12b)$$

which are derived considering that the outside is delimited by a perfect mirror on the left, placed at $d = \ell_{\text{eff}} - \ell_c$. Here, unlike for the inside modes, the mode area \mathcal{A} for the outside is the same as the one for the multilayer cavity. $b_\omega/b_\omega^\dagger$ is the annihilation/creation operator of the outside, i.e., the reservoir, satisfying the commutation relations

$$[b_\omega, b_{\omega'}^\dagger] = \delta(\omega - \omega'), \quad (7.13a)$$

$$[b_\omega, b_{\omega'}] = 0. \quad (7.13b)$$

7.3 Cavity-reservoir coupling function

If the separation into discrete cavity modes (inside) and the semi-infinite reservoir modes (outside) is correct, then the modes in this representation should be equivalent to those obtained from the true-mode representation. In the following, we impose such equivalence and analyze its validity via deriving the corresponding cavity-reservoir coupling function. In order to obtain the relation between the true modes a_ω and the inside and the outside modes a_m and b_ω we equate the corresponding electric and magnetic fields of the inside and the outside parts:

$$E_{0,\text{ins}}(x) = E_{\text{ins}}(x), \quad (7.14a)$$

$$B_{0,\text{ins}}(x) = B_{\text{ins}}(x), \quad (7.14b)$$

$$E_{0,\text{outs}}(x) = E_{\text{outs}}(x), \quad (7.14c)$$

$$B_{0,\text{outs}}(x) = B_{\text{outs}}(x). \quad (7.14d)$$

From these equivalences, for the cavity operator c_m we obtain (see the details in Appendix B.2)

$$c_m = \frac{1}{\ell_{\text{eff}}} \sqrt{\frac{cL_N}{\pi}} \int_0^\infty d\omega \sqrt{\frac{\omega}{\omega_m}} \times \left(\frac{\sin\left[(\omega - \omega_m)\frac{\ell_{\text{eff}}}{c}\right]}{\omega - \omega_m} e^{i\frac{\omega}{c}\ell_c} \mathcal{T}_\omega a_\omega - \frac{\sin\left[(\omega + \omega_m)\frac{\ell_{\text{eff}}}{c}\right]}{\omega + \omega_m} e^{-i\frac{\omega}{c}\ell_c} \mathcal{T}_\omega^* a_\omega^\dagger \right), \quad (7.15)$$

and for the reservoir operator we get (see the details in Appendix B.3):

$$b_\omega = \frac{1}{2\pi c} \int_d^\infty dx \int_0^\infty d\omega' \sqrt{\frac{\omega'}{\omega}} \times \left(\left[G_{\omega'} e^{i\frac{\omega' - \omega}{c}(x-d)} + e^{-i\frac{\omega'}{c}d} e^{-i\frac{\omega' - \omega}{c}(x-d)} \right] a_{\omega'} - \left[G_{\omega'}^* e^{-i\frac{\omega' + \omega}{c}(x-d)} + e^{i\frac{\omega'}{c}d} e^{i\frac{\omega' + \omega}{c}(x-d)} \right] a_{\omega'}^\dagger \right), \quad (7.16)$$

where $d = \ell_{\text{eff}} - \ell_c$ and

$$G_\omega = e^{2i\frac{\omega}{c}\ell_c} \frac{\mathcal{T}_\omega}{\mathcal{T}_\omega^*} e^{i\frac{\omega}{c}d}. \quad (7.17)$$

Applying the limit $\mathcal{T}_\omega \approx \mathcal{T}_m(\omega) \approx T_{m,\omega}$, G_ω simplifies to

$$G_{\omega'} \approx e^{-i\frac{\omega'}{c}d} + 2ie^{i\frac{\omega'}{c}\ell_c} T_{m,\omega'} \sqrt{\frac{L_{\text{eff}}}{\ell_{\text{eff}}}} \frac{\cos\left(\frac{\omega'}{c}\ell_{\text{eff}} + \varphi_r(\omega')\right) + |r_m(\omega')| \cos\left(\frac{\omega'}{c}\ell_{\text{eff}}\right)}{|t_m(\omega')|}. \quad (7.18)$$

Using this simplification the expression in Eq. (7.16) becomes (see the details in Appendix B.3):

$$b_\omega = e^{-i\frac{\omega}{c}d} a_\omega + \frac{1}{\pi} \int_0^\infty d\omega' \sqrt{\frac{\omega'}{\omega}} \sqrt{\frac{L_N}{\ell_{\text{eff}}}} \frac{\cos\left(\frac{\omega'}{c}\ell_{\text{eff}} + \varphi_r(\omega')\right) + |r_m(\omega')| \cos\left(\frac{\omega'}{c}\ell_{\text{eff}}\right)}{|t_m(\omega')|} \times \left(e^{i\frac{\omega'}{c}\ell_c} T_{m,\omega'} \lim_{\epsilon \rightarrow 0} \frac{1}{\omega - \omega' - i\epsilon} a_{\omega'} + e^{-i\frac{\omega'}{c}\ell_c} T_{m,\omega'}^* \lim_{\epsilon \rightarrow 0} \frac{1}{\omega + \omega' - i\epsilon} a_{\omega'}^\dagger \right).$$

7.3.1 Separation of the true modes into inside and outside modes

Above, we derived the expressions of the inside and the outside mode operators in terms of the true modes a_ω . Here, we derive the inverse relation, expanding the true modes in terms of the inside operator c_m and the outside operator b_ω . We start by assuming that the true modes can be decomposed in terms of the separated modes as follows:

$$a_\omega = \sum_{m=1}^{\infty} [\alpha_{m_1}(\omega)c_m + \alpha_{m_2}(\omega)c_m^\dagger] + \int_0^\infty d\omega' (\beta_1(\omega, \omega')b_{\omega'} + \beta_2(\omega, \omega')b_{\omega'}^\dagger). \quad (7.19)$$

Taking the discrete and continuous parts of this definition separately, we further define the following operators:

$$a_D(\omega) = \sum_{m=1}^{\infty} [\alpha_{m_1}(\omega)c_m + \alpha_{m_2}(\omega)c_m^\dagger], \quad (7.20a)$$

$$a_C(\omega) = \int_0^\infty d\omega' (\beta_1(\omega, \omega')b_{\omega'} + \beta_2(\omega, \omega')b_{\omega'}^\dagger), \quad (7.20b)$$

such that

$$a_\omega = a_D(\omega) + a_C(\omega). \quad (7.21)$$

If the decomposition (7.19) is indeed true, then the following commutation relation should hold:

$$[a_\omega, a_{\omega'}^\dagger] = [a_D(\omega), a_D^\dagger(\omega')] + [a_C(\omega), a_C^\dagger(\omega')]. \quad (7.22)$$

In order to check this relation we first calculate the coefficients $\alpha_{m_1}(\omega)$, $\alpha_{m_2}(\omega)$ and $\beta_1(\omega, \omega')$, $\beta_2(\omega, \omega')$ (see the details in Appendix B.4):

$$\alpha_{m_1}(\omega) = [a_\omega, c_m^\dagger] = \sqrt{\frac{L_N}{\pi c}} \sqrt{\frac{\omega}{\omega_m}} \text{sinc}\left[(\omega - \omega_m) \frac{\ell_{\text{eff}}}{c}\right] e^{-i\frac{\omega}{c}\ell_c} \mathcal{T}_\omega^*, \quad (7.23a)$$

$$\alpha_{m_2}(\omega) = [c_m, a_\omega] = \sqrt{\frac{L_N}{\pi c}} \sqrt{\frac{\omega}{\omega_m}} \text{sinc}\left[(\omega + \omega_m) \frac{\ell_{\text{eff}}}{c}\right] e^{-i\frac{\omega}{c}\ell_c} \mathcal{T}_\omega^*, \quad (7.23b)$$

$$\beta_1(\omega, \omega') = [a_\omega, b_{\omega'}^\dagger] = e^{i\frac{\omega}{c}d} \delta(\omega - \omega') \quad (7.24a)$$

$$+ \frac{1}{\pi} \sqrt{\frac{\omega}{\omega'}} \left(T_{m,\omega}^* \sqrt{\frac{L_N}{\ell_{\text{eff}}}} \lim_{\epsilon \rightarrow 0} \frac{e^{-i\frac{\omega}{c}\ell_c}}{\omega' - \omega + i\epsilon} \frac{\cos\left(\frac{\omega}{c}\ell_{\text{eff}} + \varphi_r(\omega)\right) + |r_m(\omega)| \cos\left(\frac{\omega}{c}\ell_{\text{eff}}\right)}{|t_m(\omega)|} \right),$$

$$\beta_2(\omega, \omega') = [b_{\omega'}, a_\omega] \quad (7.24b)$$

$$= -\frac{1}{\pi} \sqrt{\frac{\omega}{\omega'}} \left(T_{m,\omega}^* \sqrt{\frac{L_N}{\ell_{\text{eff}}}} \lim_{\epsilon \rightarrow 0} \frac{e^{-i\frac{\omega}{c}\ell_c}}{\omega' + \omega - i\epsilon} \frac{\cos\left(\frac{\omega}{c}\ell_{\text{eff}} + \varphi_r(\omega)\right) + |r_m(\omega)| \cos\left(\frac{\omega}{c}\ell_{\text{eff}}\right)}{|t_m(\omega)|} \right).$$

In general, operators (7.20) with coefficients (7.23) and (7.24) do not satisfy the commutation relation (7.22), however, as we show below, since we are in the limit where $\mathcal{T}_\omega \approx \mathcal{T}_m(\omega) \approx T_{m,\omega}$, we can approximate these coefficients such that they satisfy the commutation relations, therefore justifying the separation of the modes

into inside and outside. To demonstrate that, we proceed by approximating the coefficients $\alpha_{m_i}(\omega)$ and $\beta_i(\omega, \omega')$:

$$\alpha_{m_1}(\omega) \approx e^{-i\frac{\omega}{c}\ell_c} \sqrt{\frac{\gamma_m}{2\pi}} \frac{1}{(\omega - \omega_m) - i\frac{\gamma_m}{2}}, \quad (7.25a)$$

$$\alpha_{m_2}(\omega) \approx 0, \quad (7.25b)$$

$$\begin{aligned} \beta_1(\omega, \omega') &\approx e^{i\frac{\omega'}{c}d} \delta(\omega - \omega') \\ &+ \frac{1}{\pi} \left(e^{-i\frac{\omega}{c}\ell_c} T_{m,\omega}^* \sqrt{\frac{L_N}{\ell_{\text{eff}}}} \lim_{\epsilon \rightarrow 0} \frac{1}{\omega' - \omega + i\epsilon} (-1)^m \frac{-1 + |r_m(\omega_m)|}{|t_m(\omega_m)|} \right), \end{aligned} \quad (7.25c)$$

$$\beta_2(\omega, \omega') \approx 0, \quad (7.25d)$$

where we have evaluated $\alpha_{m_1}(\omega)$ and $\beta_1(\omega, \omega')$ around the resonance peak ω_m and discarded α_{m_2} and $\beta_2(\omega, \omega')$ treating them as fast oscillating terms. These approximations lead to the following relation between the true and the separated inside-outside modes:

$$a_\omega \approx \sum_{m=1}^{\infty} \alpha_{m_1}(\omega) c_m + \int_0^\infty d\omega' \beta_1(\omega, \omega') b_{\omega'}. \quad (7.26)$$

With this separation the commutation relation (7.22) is satisfied as long as the terms of the order $(\gamma_m \frac{\ell_{\text{eff}}}{c})^2$ are negligible, i.e., the reflectivity of the mirror is close to 1 [Fig. 7.2(b)] (see the details in Appendix B.5). With these relations between the true and inside-outside modes, it can also be shown that the modes of the inside and the outside indeed commute at this limit: $[c_m, b_\omega^\dagger] = 0$.

7.3.2 Hamiltonian

Having obtained the relation between the modes of the true-mode and the inside-outside representations, we can now derive the Hamiltonian describing the separated inside-outside system from the true-mode Hamiltonian (7.8) (see the details in Appendix B.6):

$$\begin{aligned} H &= \sum_{m=1} \hbar \omega_m c_m^\dagger c_m + \int_0^\infty d\omega \hbar \omega b_\omega^\dagger b_\omega \\ &+ i\hbar \sum_{m=1} \int_0^\infty d\omega \left(\kappa_m(\omega) b_\omega^\dagger c_m - \kappa_m^*(\omega) c_m^\dagger b_\omega \right), \end{aligned} \quad (7.27)$$

with

$$\kappa_m(\omega) = -ie^{-i\frac{\omega}{c}\ell_{\text{eff}}} \sqrt{\frac{\gamma_m}{2\pi}} \text{sinc} \left[(\omega - \omega_m) \frac{\ell_{\text{eff}}}{c} \right] \quad (7.28)$$

being the coupling between the cavity and the reservoir. As we can see, this term is not constant and unlike the one obtained for a cavity with a single-layered mirror of negligible thickness [Eq. (4.10)], Eq. (7.28) features the effective length ℓ_{eff} of the multilayer cavity. Just like the response function (7.4), the coupling function (7.28) can also be considered as the generalization of the similar expression derived for a single-layered cavity. Only in a certain limit, where $\ell_{\text{eff}} = \ell_c$ these formulas coincide.

7.3.3 Poynting vector

Now that we have a complete description of the model in inside-outside representation, here we focus on characterizing the field propagating outside the cavity. Performing similar derivation to the one demonstrated in Section 4.2.1, we derive the Poynting vector for the cavity with multilayer mirror. The Poynting vector in the true-mode representation with the electromagnetic fields (7.5b) and (7.6b), for the propagation in the positive x direction reads as follows:

$$S_{\text{outs}}(x) = \frac{\hbar}{2\pi\mathcal{A}} \int_0^\infty d\omega d\omega' \sqrt{\omega\omega'} \text{Re} \left\{ G_\omega G_{\omega'}^* e^{i\frac{(\omega-\omega')x}{c}} a_{\omega'}^\dagger a_\omega \right\}. \quad (7.29)$$

Taking the definition in Eq. (7.17) and the expression of the coefficient $\alpha_{m_1}(\omega)$ given in Eq. (7.25a), we can reformulate G_ω as follows:

$$G_\omega \approx e^{2i\frac{\omega}{c}l_c} \frac{\mathcal{T}_m(\omega)}{\mathcal{T}_m^*(\omega)} e^{i\frac{\omega}{c}d} \approx e^{i\frac{\omega}{c}l_{\text{eff}}} \alpha_{m_1}^*(\omega) \sqrt{\frac{2\pi}{\gamma_m}} \left(\omega - \omega_m - i\frac{\gamma_m}{2} \right). \quad (7.30)$$

Using Eq. (7.30) and the expansion of true modes in terms of outside modes: $a_\omega = \int_0^\infty d\omega'' \beta_1(\omega, \omega'') b_{\omega''}$ (since we derive the Poynting vector for the outside part we do not consider the discrete part of the decomposition (7.26), corresponding to the inside modes), we can write the Poynting vector for the outgoing field in the inside-outside representation:

$$S_{\text{outs}}(x) \approx \frac{\hbar\omega_m}{\mathcal{A}\gamma_m} \int_0^\infty d\omega d\omega' \kappa_m^*(\omega) \kappa_m(\omega') b_{\omega'}^\dagger b_\omega, \quad (7.31)$$

where we have evaluated the integral

$$\int_0^\infty d\omega'' \left(\omega - \omega_m - i\frac{\gamma_m}{2} \right) \alpha_{m_1}^*(\omega) \beta_1(\omega, \omega'') b_{\omega''} = -i\kappa_m^*(\omega) b_\omega,$$

similar to the one calculated in Appendix B.6.

Having obtained the expression for the Poynting vector, we next define the following operator analogous to Eq. (4.44) that characterizes the spatial distribution of the photon propagating outside:

$$b(x) := \frac{1}{\sqrt{\gamma_m}} \int_0^\infty d\omega \kappa_m^*(\omega) e^{i\frac{\omega}{c}x} b_\omega, \quad (7.32)$$

and the Poynting vector can be written as

$$S_{\text{outs}}(x) = \frac{\hbar\omega_m}{\mathcal{A}} b^\dagger(x) b(x). \quad (7.33)$$

Corresponding coarse-grained photon number density becomes

$$\Phi_{\text{density}}(x, t) = \frac{\mathcal{A}}{\hbar\omega_m} \frac{\langle S_{\text{outs}}(x) \rangle_{|\psi(t)\rangle}}{c} = \frac{1}{c} \langle b^\dagger(x) b(x) \rangle = \langle b_x^\dagger b_x \rangle, \quad (7.34)$$

where we have defined an operator similar to Eq. (4.67)

$$b_x^\dagger = \frac{1}{\sqrt{c}} b^\dagger(x) = \frac{1}{\sqrt{c\gamma_m}} \int_0^\infty d\omega \kappa_m(\omega) e^{-i\frac{\omega}{c}x} b_\omega^\dagger, \quad (7.35)$$

which satisfies the following commutation relations:

$$[b_x, b_x^\dagger] = \frac{1}{2\ell_{\text{eff}}}, \quad (7.36)$$

$$[b_x, b_{x'}^\dagger] = 0, \quad \text{when } |x - x'| > 2\ell_{\text{eff}}. \quad (7.37)$$

Hence, the total photon number outside the cavity reads

$$N(t) = \int_0^\infty dx \langle b_x^\dagger b_x \rangle_{|\psi(t)\rangle}. \quad (7.38)$$

The general photon state outside the multilayer cavity can be defined the same way as (4.58)

$$|1_{\text{outs}}(t)\rangle = \int_0^{+\infty} d\omega \Psi(\omega, t) b_\omega^\dagger |\emptyset\rangle. \quad (7.39)$$

In the following, we use the definitions presented here to analyze the production and the propagation of a single photon produced from an atom trapped in a cavity.

7.4 Numerical verification of the inside-outside representation

To verify the validity of the above mode separation, we next study the dynamics of a Λ -type atom of ground state $|g\rangle$, excited state $|e\rangle$ and a metastable state $|f\rangle$, trapped in the multilayer cavity (Fig. 7.3). The atom is excited by a classical laser field of Rabi frequency $\Omega(t)$, introducing a detuning between the laser frequency ω_L and the frequency of excited state ω_{eg} : $\Delta = \omega_{\text{eg}} - \omega_L$. Furthermore, the atom decays from the excited to the metastable state by coupling to the cavity mode, emitting a photon, which eventually leaks out of the cavity through the transparent mirror. To study the dynamics of this process, we start by analysing this model in terms of the true modes. For this case the overall Hamiltonian can be written as:

$$\tilde{H}(t) = H_A(t) + H_{\text{int}} + H_E \quad (7.40a)$$

$$H_A(t) = \hbar(\omega_{\text{fg}} - \omega_L)\sigma_f + \hbar\Delta\sigma_e + \hbar\Omega(\sigma_{\text{ge}} + \sigma_{\text{eg}}), \quad (7.40b)$$

$$H_E = \int_0^{+\infty} d\omega \hbar\omega a_\omega^\dagger a_\omega, \quad (7.40c)$$

$$H_{\text{int}} = i\hbar \int_0^{+\infty} d\omega \left(\eta_\omega a_\omega \sigma^\dagger - \eta_\omega^* a_\omega^\dagger \sigma \right), \quad (7.40d)$$

where the Hamiltonian H_E represents the part describing the environment, which is the multilayer cavity and the reservoir, considered as a single entity. We have also introduced the atomic operators $\sigma_{ij} = |i\rangle\langle j|$. η_ω describes the coupling of the emitter with the true modes a_ω [Eq. (4.5)]:

$$\eta_\omega = i\sqrt{\frac{\omega}{\hbar\epsilon_0\pi c\mathcal{A}}} d_{\text{fe}} e^{i\frac{\omega}{c}\ell_c} \sin\left(\frac{\omega}{c}(x_A + \ell_c)\right) \mathcal{T}_\omega. \quad (7.41)$$

The state corresponding to this representation can be written as follows:

$$|\tilde{\psi}\rangle = \tilde{c}_{g,0}(t)|g, \emptyset\rangle + \tilde{c}_{e,0}(t)|e, \emptyset\rangle + \int_0^{+\infty} d\omega \tilde{c}_{f,1}(\omega, t)|f, \mathbf{1}_\omega\rangle, \quad (7.42)$$

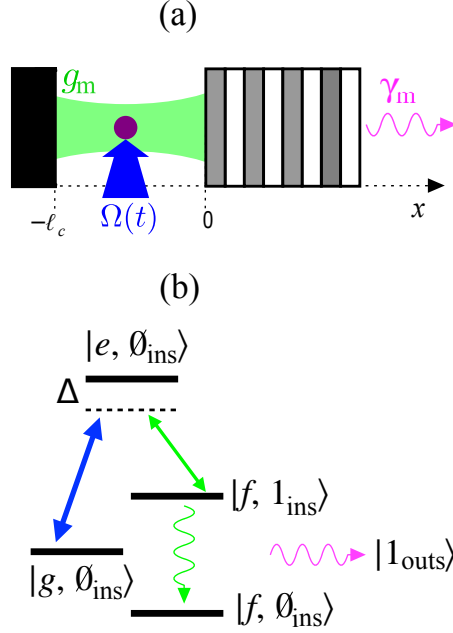


Figure 7.3: (a) Λ -type atom trapped in a non-perfect cavity. The cavity is formed by a perfect mirror placed at $x = -\ell_c$ and a partially transparent mirror standing from $x = 0$ and made of a dielectric stack of alternating layers. The atom is driven by an external classical laser field of Rabi frequency $\Omega(t)$. g_m is the coupling strength between the atom and the m -th mode of the cavity, and γ_m is the corresponding linewidth. (b) Inside-outside representation of the considered model. Initially the atom is in the ground state $|g\rangle$. In the course of the excitation process, one photon is taken from the laser field and transferred to the cavity, corresponding to the state $|f, 1_{\text{ins}}\rangle$. Due to the cavity leakage γ_m , this photon eventually leaks out of the cavity to the environment transferring the photon state to the outside ($|1_{\text{outs}}\rangle$).

where

$$|1_{\omega}\rangle = a_{\omega}^{\dagger}|\emptyset\rangle. \quad (7.43)$$

Dynamical equations corresponding to the Hamiltonian in (7.40) with the state (7.42) are:

$$i\frac{d}{dt}\tilde{c}_{g,0}(t) = \Omega(t)\tilde{c}_{e,0}(t), \quad (7.44a)$$

$$i\frac{d}{dt}\tilde{c}_{e,0}(t) = \Delta\tilde{c}_{e,0}(t) + \Omega(t)\tilde{c}_{g,0}(t) + i\int_0^{+\infty}d\omega\eta_{\omega}\tilde{c}_{f,1}(\omega,t), \quad (7.44b)$$

$$i\frac{d}{dt}\tilde{c}_{f,1}(\omega,t) = (\omega + \omega_{\text{fg}} - \omega_L)\tilde{c}_{f,1}(\omega,t) - i\eta_{\omega}^*\tilde{c}_{e,0}(t). \quad (7.44c)$$

Same system in the inside-outside representation has the following Hamiltonian:

$$H(t) = H_A(t) + H_{AC} + H_C + H_{RS} + H_R \quad (7.45a)$$

$$H_C = \sum_m \hbar \omega_m c_m^\dagger c_m, \quad (7.45b)$$

$$H_{AC} = \sum_m \hbar g_m (c_m^\dagger \sigma + \sigma^\dagger c_m), \quad (7.45c)$$

$$H_R = \int_0^{+\infty} d\omega \hbar \omega b_\omega^\dagger b_\omega, \quad (7.45d)$$

$$H_{RC} = i\hbar \sum_m \int_0^{+\infty} d\omega (\kappa_m(\omega) b_\omega^\dagger c_m - \kappa_m^*(\omega) c_m^\dagger b_\omega), \quad (7.45e)$$

where g_m is the coupling of the atom with the m -th mode of the perfect cavity:

$$g_m = -d_{fe} \sqrt{\frac{\omega_m}{\hbar \epsilon_0 L_N \mathcal{A}}} \sin \left[\frac{\omega_m}{c} (x_A + \ell_c) \right]. \quad (7.46)$$

The state in this representation reads as follows:

$$\begin{aligned} |\psi\rangle &= c_{g,0,0}(t) |g, \emptyset_{\text{ins}}, \emptyset_{\text{outs}}\rangle + c_{e,0,0}(t) |e, \emptyset_{\text{ins}}, \emptyset_{\text{outs}}\rangle + \sum_m c_{f,1,0}^{(m)}(t) |f, 1_{\text{ins}}^{(m)}, \emptyset_{\text{outs}}\rangle \\ &+ \int_0^{+\infty} d\omega c_{f,0,1}(\omega, t) |f, \emptyset_{\text{ins}}, 1_{\text{outs},\omega}\rangle, \end{aligned}$$

with

$$|1_{\text{ins}}^{(m)}\rangle = c_m^\dagger |\emptyset\rangle, \quad (7.47a)$$

$$|1_{\omega,\text{outs}}\rangle = b_\omega^\dagger |\emptyset_{\text{outs}}\rangle. \quad (7.47b)$$

The corresponding dynamical equations can be written as

$$i \frac{d}{dt} c_{g,0,0}(t) = \Omega(t) c_{e,0,0}(t), \quad (7.48a)$$

$$i \frac{d}{dt} c_{e,0,0}(t) = \Delta c_{e,0,0}(t) + \Omega(t) c_{g,0,0}(t) + \sum_m g_m c_{f,1,0}^{(m)}(t), \quad (7.48b)$$

$$i \frac{d}{dt} c_{f,1,0}^{(m)}(t) = (\omega_{\text{fg}} + \omega_m - \omega_L) c_{f,1,0}^{(m)}(t) + g_m c_{e,0,0}(t) + \int_0^{+\infty} d\omega \kappa_m^*(\omega) c_{f,0,1}(\omega, t), \quad (7.48c)$$

$$i \frac{d}{dt} c_{f,0,1}(\omega, t) = (\omega_{\text{fg}} - \omega_L + \omega) c_{f,0,1}(\omega, t) + \sum_m \kappa_m(\omega) c_{f,1,0}^{(m)}(t). \quad (7.48d)$$

In a regime where the cavity is such that after some time the photon leaks out of it completely ($t \rightarrow \infty$), the outside photon state becomes $c_{f,0,1}(\omega, t) \rightarrow \mathbf{c}_{f,0,1}(\omega) e^{-i(\omega_{\text{fg}} - \omega_L + \omega)t}$, with

$$\int_0^\infty d\omega |c_{f,0,1}(\omega, t)|^2 = \int_0^\infty d\omega |\mathbf{c}_{f,0,1}(\omega)|^2 = 1. \quad (7.49)$$

Thus, at this limit we can identify the function $\Psi(\omega, t)$ in Eq. (7.39) as

$$\Psi(\omega, t) = \mathbf{c}_{f,0,1}(\omega) e^{-i(\omega_{\text{fg}} - \omega_L + \omega)t}. \quad (7.50)$$

Following the definition of the operator (7.35) and taking the solutions of Eq. (7.48), we can determine the density of photon number at a position x by calculating the mean value in Eq. (7.38):

$$\Phi_{\text{density}}(x, t) = |c_{0,1}(x, t)|^2 = \langle \psi(t) | b_x^\dagger b_x | \psi(t) \rangle. \quad (7.51)$$

with

$$c_{0,1}(x, t) = \frac{1}{\sqrt{c\gamma_m}} \int_0^\infty d\omega \kappa_m^*(\omega) e^{i\frac{\omega}{c}x} c_{f,0,1}(\omega, t). \quad (7.52)$$

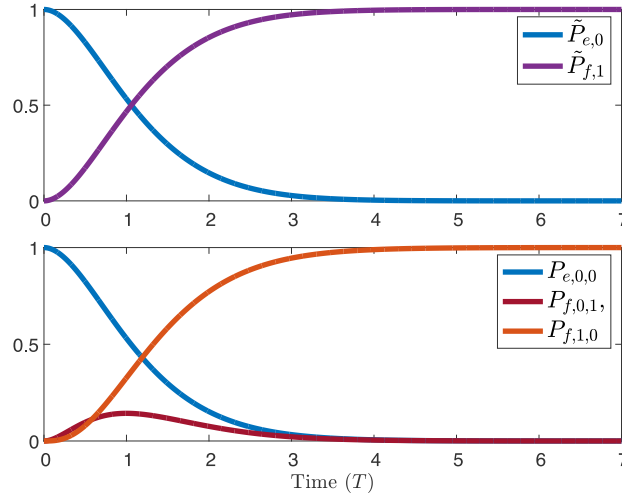


Figure 7.4: The dynamics in true-mode (top figure) and inside-outside representations (bottom figure). The figures are obtained for the case where the atom is initially in the excited state trapped in a cavity having a multilayer mirror with $N = 8$ dielectric layer pairs and the mirror spacing $\ell_c = 10\ell_0$. We consider the following parameters $\Omega(t) = 0$, $\Delta = 0$, $d_{fe}/\sqrt{\hbar\epsilon_0 c \bar{A}} = 0.0025$ and $x_A = -4.5\ell_0$. The lines correspond to the coefficients $\tilde{P}_{e,0} = |\tilde{c}_{e,0}(t)|^2$, $\tilde{P}_{f,1} = \int_0^\infty d\omega |\tilde{c}_{f,1}(\omega, t)|^2$ in the true-mode representation and $P_{e,0,0} = |c_{e,0,0}(t)|^2$, $P_{f,1,0} = |c_{f,1,0}(t)|^2$ and $P_{f,0,1} = \int_0^\infty d\omega |c_{f,0,1}(\omega, t)|^2$ in the inside-outside representation.

In Fig. 7.4 we show the numerical solutions of dynamical equations (7.44) and (7.48). We study an intermediate coupling regime, where the atom-cavity coupling is such that there are no Rabi oscillations between them and the photon leaks out of the cavity after being produced: $g_m \lesssim \gamma_m$. In the inside-outside representation the function $P_{f,1,0}$ describes the shape of the produced photon inside the cavity and the function $P_{f,0,1}$ corresponds to the photon outside the cavity, while in the true-mode representation, since there is no separation between the inside and the outside, there is one term describing the photon: $\tilde{P}_{f,1}$, which incorporates the inside and the outside photon states, such that at the limit of validity of inside-outside representation $\tilde{P}_{f,1} \approx P_{f,1,0} + P_{f,0,1}$. In Fig. 7.5, we compare the outgoing photon shape obtained via each representation in the frequency domain. Additionally, taking into account the fact that one can obtain the spectral distribution of the photon via the Fourier transform of the state $c_{f,1,0}(t)$, we define a photon state

$$\hat{P}_{\text{outs}} = \sigma \left| \int_0^t dt c_{f,1,0}^*(t) e^{-i\omega t} \right|^2, \quad (7.53)$$

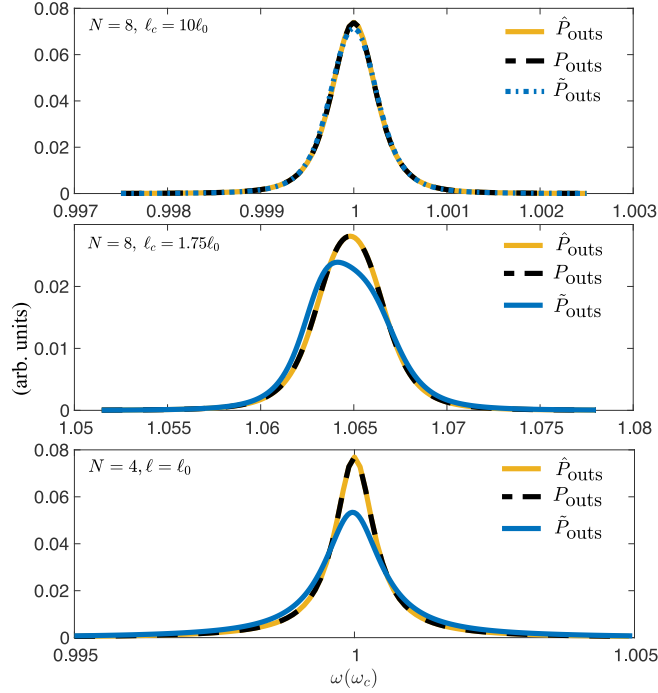


Figure 7.5: The shape of the outgoing photon in the frequency domain, obtained from true-mode representation (\tilde{P}_{outs}), inside-outside representation (P_{outs}) and via a Fourier transform of the inside photon state (\hat{P}_{outs}). The parameters are defined as follows: $\tilde{P}_{\text{outs}} = |\tilde{c}_{f,1}(\omega, t_f)|^2$, $P_{\text{outs}} = |c_{f,0,1}(\omega, t_f)|^2$, where t_f is a time corresponding to the steady state of the photon, i.e., the time when the photon has leaked out of the cavity, and $\hat{P}_{\text{outs}} = |\sqrt{\gamma_m/2\pi}\text{FT}\{c_{f,1,0}(t)\}|^2$. The top figure corresponds to the case described in Fig. 7.4, with an effective reflectivity $|r_m| \approx 0.953$. In the middle figure, the effective reflectivity is $|r_m| \approx 0.949$ with $\ell_c = 1.75\ell_0$, and $x_A \approx -0.342\ell_0$, such that the atom of transition frequency $\omega \approx 1.065\omega_c$ is placed at the field maximum. In the bottom figure $N = 4$, $\ell_c = \ell_0$ and $x_A = -0.5\ell_0$, making the effective reflectivity $|r_m| \approx 0.858$. The transition frequency of the atom is $\omega = \omega_c$ with $d_{fe}/\sqrt{\hbar\epsilon_0 c \mathcal{A}} = 0.01$.

where $c_{f,1,0}(t)$ is the photon state inside the cavity in the inside-outside representation and $\sigma = \gamma_m/2\pi$ is the normalization constant, obtained by taking into account the fact that at $t \rightarrow \infty$ the photon is completely outside the cavity, such that $\int d\omega \hat{P}_{\text{outs}} = 1$. As we can see from Fig. 7.5, at such a long time limit, in the case when the cavity mirror has enough layers such that we are in a regime of high effective reflectivity, the photon derived from the inside-outside representation and the corresponding Fourier transform definition almost exactly matches with the photon shape derived from the true-mode representation. On the other hand, when the leakage through the multilayer mirror is strong, i.e., the effective reflectivity is relatively low, the mismatch between the two representations is significant. Additionally, in the regime where $\ell_c/\ell_0 \neq k$, the mismatch is also significant. These mismatches are due to the fact that at these regimes the individual Lorentzians of the response function have overlaps and the emitter couples to more than one mode. In such an overlapped regime, the Lorentzians neighboring the main peak can not be directly added to the inside-outside model as a separate mode m' , since, due to this overlap, the quantized modes associated to each of these Lorentzians will not satisfy the commutation

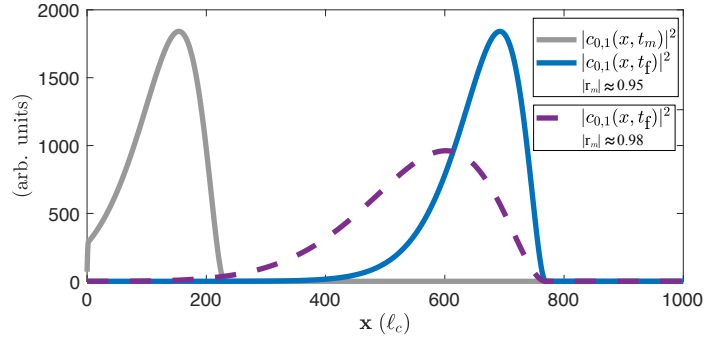


Figure 7.6: Propagating single-photon state along the propagation direction. The cavity mirror of the inside-outside representation is placed at $d = 0$ (for the actual multilayer mirror $\ell_c = 10\ell_0$, thus $\ell_{\text{eff}} = \ell_c$). The solid curves are obtained with the same parameters as the ones in Fig. 7.4(a), leading to effective reflectivity $|r_m| \approx 0.95$. The curve corresponding to $|c_{0,1}(x, t_m)|^2$ describes the photon state at a time t_m , when the photon is not completely out of the cavity yet (in the simulation the value of t_m corresponds to the point $t_m = 3$ in Fig. 7.4(a)). Similarly, $|c_{0,1}(x, t_f)|^2$ corresponds to the time t_f when the photon has left the cavity and propagates along the positive x direction. The dashed line is $|c_{0,1}(x, t_f)|^2$ but for a cavity with higher effective reflectivity $|r_m| \approx 0.98$ ($N = 10$).

relations. Finally, in Fig. 7.6, we study the photon shape along the propagation direction, corresponding to the term defined in Eq. (7.52). From Fig. 7.4 we can determine the time after which the photon is completely outside the cavity. Using the expression (7.52) with the solutions of Eq. (7.48), we can describe the propagation of the photon outside the cavity. As we can see from Fig. 7.6, for the given cavity length, the width of the spatial distribution of the single photon is of the order $\sim 200\ell_c$, and the better the effective reflectivity, the broader the distribution of the photon outside the cavity. Additionally, we highlight that the sharp start of the single photon distribution in space is due to the strict limitation imposed by the speed of light. Notably, this special relativity feature is preserved during the calculations.

Summary

In this part, we have extended the analysis of Part II for the more realistic cavity scenarios, i.e., cavities with mirrors made of multilayer dielectric material. We have shown that the geometric structure of the mirror can affect the characteristic parameters of the cavity, such as cavity mode volume, length and resonance frequencies. In particular, the effective cavity length ℓ_{eff} , as defined in the literature [36, 180, 207], determines the cavity resonance and, as we have shown here, does not correspond to the coupling factor cavity length $L_N^{(m)}$ used for determining the strength of the cavity-emitter coupling. We have found that these two lengths do not correspond to each other whenever a multilayer structure is taken into consideration. Additionally, the resonance frequencies through which ℓ_{eff} is defined no longer coincide with the expected resonances at integer multiples of $\pi c/\ell_c$. A pronounced side effect of this discrepancy is that the most common approach for determining a cavity length by means of measuring its free-spectral range [164] is bound to fail for very short cavities. The geometric length of the cavity might differ by up to $\lambda_0/2$ from its effective length determining the free spectral range. This difference may be of importance in applications where the cavity spacings used are very short and the mirrors are made of dielectric coatings [131, 186].

Moreover, the standard model for light-matter interaction in optical cavities considers the mode volume of the cavity to be the product between the longitudinal extent of the mode (considered to be only the separation between the mirrors) and a factor accounting for the transverse behavior of the mode [174]. However, here we have shown that this is only valid if the mirrors can be seen as hard mode-delimiting boundaries. Any physical cavity is very different to that respect. The mode penetrates into the dielectric mirror stack, couples to the outside and the light frequency is not quantized in these open systems. However, even though we do not explicitly consider a mode volume, we show that the atom-cavity coupling involves a factor having the unit of volume. Only in the case of a perfect cavity having hard boundaries at the positions of the mirrors, this factor coincides with the geometric definition of the mode volume. This discrepancy can lead to a Purcell factor different from the one calculated by using a standard approach, especially with short mirror spacings.

After obtaining the description of such a multilayer cavity, we then demonstrated the first-principle derivation of the cavity-reservoir coupling function for such more realistic cavities. This derivation is done in the limit where the structure of the cavity is such that the cavity resonances can be characterized via well-separated Lorentzian-like functions. In particular, we explicitly estimated the accuracy of such an approximation with respect to the cavity length and the number of dielectric layers forming the mirror. We have shown that in this limit one can replace the

multilayer mirror with an effective single-layered mirror of negligible thickness. We introduced the generalized cavity response function for this replaced mirror, which, in general, is different from a single-layered cavity response function and incorporates the effects caused by the multilayer structure of the actual cavity. Based on this, we defined the effective reflectivity and showed that even in the regime where the effective reflectivity is high, i.e., the cavity is of high finesse, the cavity-reservoir coupling function derived for the multilayer cavity is different from that derived for a single-layered cavity.

The models derived here lead to a more general description of the cavity-reservoir system, where one can take into account the structure of the mirror and freely vary the frequency of light, the multilayer structure and the position of the cavity mirror. This is different from the standard open cavity analysis, where the cavity-reservoir interaction is modeled phenomenologically and is treated as a loss. With the derivation presented here one can describe the full cavity-reservoir closed system, while being able to describe the state of the open cavity separated from the reservoir. Such a model allows to study the spectral shape and the propagation of the produced single photon outside the cavity. This is particularly useful when studying the reverse process of photon absorption and the full process of generation and absorption in more realistic cavity QED systems.

B.1 Effective single-layered cavity response function

In this appendix we demonstrate how one can reformulate the results derived for the multilayer cavity in terms of a single-layered one. As it is shown in Appendix A.3, for a single-layered cavity whose thickness is negligible with respect to the mirror spacing ℓ_c , the response function has the following form:

$$T(\omega) = \frac{t(\omega)}{1 + r(\omega)e^{2i\frac{\omega}{c}\ell_c}} = \sum_m \sqrt{\frac{c}{2\ell_c}} \frac{\sqrt{\gamma_1(\omega)}}{\omega - \tilde{\omega}_m(\omega) + i\frac{\gamma_1(\omega)}{2}} \approx \sum_m \sqrt{\frac{c}{2\ell_c}} \frac{\sqrt{\gamma_{1m}}}{\omega - \omega_m + i\frac{\gamma_{1m}}{2}}, \quad (\text{B.1})$$

with

$$\gamma_1(\omega) = -\frac{c}{\ell_c} \ln |r(\omega)|; \quad \gamma_{1m} := \gamma_1(\omega_m) = -\frac{c}{\ell_c} \ln |r(\omega_m)|, \quad (\text{B.2})$$

$$\tilde{\omega}_m(\omega) = m\frac{\pi c}{\ell_c} + \frac{c}{2\ell_c} (\pi - \phi_r(\omega)); \quad \omega_m := \tilde{\omega}_m(\omega_m) \approx m\frac{\pi c}{\ell_c}, \quad (\text{B.3})$$

with $r(\omega) = |r(\omega)|e^{i\phi_r(\omega)}$, and $\phi_r(\omega_m) \approx \pi$ for a high finesse cavity.

Similar to the expansion (B.1), Eq. (6.10) can be approximated as:

$$|\mathcal{T}_\omega| \approx \left| \sum_m \mathcal{T}_m(\omega) \right| \quad (\text{B.4})$$

$$\mathcal{T}_m(\omega) = \sqrt{\frac{c}{2L_N^{(m)}}} \frac{\sqrt{\gamma_N^{(m)}}}{(\omega - \omega_N^{(m)}) + i\frac{\gamma_N^{(m)}}{2}}, \quad (\text{B.5})$$

where $\gamma_N^{(m)}$, $L_N^{(m)}$ and $\omega_N^{(m)} = m\pi c/\ell_{\text{eff}}^{(m)}$ are obtained numerically. Taking these parameters into account and the definitions in (B.2), for the multilayer cavity we can define a function $\gamma_m(\omega)$ around each peak m , such that $\gamma_m(\omega_N^{(m)}) = \gamma_N^{(m)}$ and $\gamma_m(\omega) = a\gamma_1(\omega)$, where a is a constant defined as: $a = \gamma_N^{(m)}/\gamma_1(\omega_N^{(m)})$. This can be interpreted as replacing the multilayer mirror by a single-layered one forming a cavity of length $\ell_{\text{eff}}^{(m)}$ with a spectral reflection function $r_m(\omega)$ determined from the following expression:

$$\gamma_m(\omega) = a\gamma_1(\omega) = -a\frac{c}{\ell_c} \ln |r(\omega)| = -\frac{c}{\ell_{\text{eff}}^{(m)}} a \frac{\ell_{\text{eff}}^{(m)}}{\ell_c} \ln |r(\omega)| = -\frac{c}{\ell_{\text{eff}}^{(m)}} \ln |r_m(\omega)|, \quad (\text{B.6})$$

with $|r_m(\omega)| = |r(\omega)|^a \frac{\ell_{\text{eff}}^{(m)}}{\ell_c}$. Consequently, we can define the spectral transmission function $t_m(\omega)$ from the following relations:

$$r_m(\omega) = |r_m(\omega)|e^{i\varphi_r(\omega)}, \quad (\text{B.7})$$

$$t_m(\omega) = |t_m(\omega)|e^{i\varphi_t(\omega)}, \quad (\text{B.8})$$

$$|t_m(\omega)|^2 + |r_m(\omega)|^2 = 1, \quad (\text{B.9})$$

$$t_m(\omega)r_m^*(\omega) + t_m^*(\omega)r_m(\omega) = 0, \quad (\text{B.10})$$

$$\varphi_r(\omega) - \varphi_t(\omega) = \frac{\pi}{2}, \quad (\text{B.11})$$

We highlight that the way we obtain $r_m(\omega)$ and $t_m(\omega)$ does not provide the explicit information about the phase factors $\varphi_r(\omega)$ and $\varphi_t(\omega)$.

Taking into account the definitions above we can reformulate the actual response function in terms of a single-layered cavity response function equivalent to the multilayer one around each resonance peak:

$$T_{m,\omega} = \sqrt{\frac{\ell_{\text{eff}}^{(m)}}{L_N^{(m)}}} \frac{t_m(\omega)}{1 + r_m(\omega)e^{2i\frac{\omega}{c}\ell_{\text{eff}}^{(m)}}}. \quad (\text{B.12})$$

Indeed, we can simplify eq. (B.12) as follows:

$$\begin{aligned} |T_{m,\omega}|^2 &= \frac{\ell_{\text{eff}}^{(m)}}{L_N^{(m)}} \frac{|t_m(\omega)|^2}{\left|1 + |r_m(\omega)|e^{i\left(2\frac{\omega}{c}\ell_{\text{eff}}^{(m)} + \varphi_r(\omega)\right)}\right|^2} = \frac{\ell_{\text{eff}}^{(m)}}{L_N^{(m)}} \frac{1 - |r_m(\omega)|^2}{\left|1 + |r_m(\omega)|e^{i\left(2\frac{\omega}{c}\ell_{\text{eff}}^{(m)} + \varphi_r(\omega)\right)}\right|^2} \\ &= \frac{\ell_{\text{eff}}^{(m)}}{L_N^{(m)}} \left[1 - \frac{|r_m(\omega)|e^{i\left(2\frac{\omega}{c}\ell_{\text{eff}}^{(m)} + \varphi_r(\omega)\right)}}{1 + |r_m(\omega)|e^{i\left(2\frac{\omega}{c}\ell_{\text{eff}}^{(m)} + \varphi_r(\omega)\right)}} - \frac{|r_m(\omega)|e^{-i\left(2\frac{\omega}{c}\ell_{\text{eff}}^{(m)} + \varphi_r(\omega)\right)}}{1 + |r_m(\omega)|e^{-i\left(2\frac{\omega}{c}\ell_{\text{eff}}^{(m)} + \varphi_r(\omega)\right)}} \right] \\ &= \frac{\ell_{\text{eff}}^{(m)}}{L_N^{(m)}} \left[1 + \sum_{k=1}^{\infty} |r_m(\omega)|^k \left(e^{ik\left(2\frac{\omega}{c}\ell_{\text{eff}}^{(m)} + \varphi_r(\omega) - \pi\right)} + e^{-ik\left(2\frac{\omega}{c}\ell_{\text{eff}}^{(m)} + \varphi_r(\omega) - \pi\right)} \right) \right] \\ &= \frac{\ell_{\text{eff}}^{(m)}}{L_N^{(m)}} \sum_{k=-\infty}^{\infty} |r_m(\omega)|^k e^{ik\left(2\frac{\omega}{c}\ell_{\text{eff}}^{(m)} + \varphi_r(\omega) - \pi\right)} \\ &= \frac{\ell_{\text{eff}}^{(m)}}{L_N^{(m)}} \sum_{k=-\infty}^{\infty} \frac{-2 \ln |r_m(\omega)|}{\left(\ln |r_m(\omega)|\right)^2 + \left(2\frac{\omega}{c}\ell_{\text{eff}}^{(m)} + \varphi_r(\omega) - \pi - 2\pi k\right)^2} \\ &= \frac{\ell_{\text{eff}}^{(m)}}{L_N^{(m)}} \sum_{k=-\infty}^{\infty} \left(\frac{c}{2\ell_{\text{eff}}^{(m)}}\right)^2 \frac{-2 \ln |r_m(\omega)|}{\left(\ln |r_m(\omega)|\frac{c}{2\ell_{\text{eff}}^{(m)}}\right)^2 + \left(\omega + \frac{c}{2\ell_{\text{eff}}^{(m)}}(\varphi_r(\omega) - \pi - 2\pi k)\right)^2}. \end{aligned}$$

Recalling the definition in (B.6) and defining $\hat{\omega}_k(\omega) = k\pi c/\ell_{\text{eff}}^{(m)} + (\pi - \varphi_r(\omega))c/2\ell_{\text{eff}}^{(m)}$, we obtain

$$|T_{m,\omega}|^2 = \sum_{k=-\infty}^{\infty} \left(\frac{c}{2L_N^{(m)}}\right) \frac{\gamma_m(\omega)}{\left(\omega - \hat{\omega}_k(\omega)\right)^2 + \left(\frac{\gamma_m(\omega)}{2}\right)^2} \approx \left(\frac{c}{2L_N^{(m)}}\right) \frac{\gamma_N^{(m)}}{\left(\omega - \omega_N^{(m)}\right)^2 + \left(\frac{\gamma_N^{(m)}}{2}\right)^2}, \quad (\text{B.13})$$

where we considered the fact that the above expansion is done for each resonance peak of the actual response function separately, hence the sum reduces to a single term around $\omega_N^{(m)}$, i.e., $\hat{\omega}_k(\omega_N^{(m)}) = \omega_N^{(m)}$, which makes the phase $\varphi_r(\omega_N^{(m)}) = \pi$. Further, by taking the square root of the above equation, we obtain

$$T_{m,\omega} = \sqrt{\frac{c}{2L_N^{(m)}}} \frac{\sqrt{\gamma_N^{(m)}}}{(\omega - \omega_N^{(m)}) + i\frac{\gamma_N^{(m)}}{2}}, \quad (\text{B.14})$$

which is exactly the same as eq. (B.5). Doing similar expansion around each peak $\omega_N^{(m)}$, for the full response function we get:

$$\mathcal{T}_\omega \approx \sum_m \sqrt{\frac{c}{2L_N^{(m)}}} \frac{\sqrt{\gamma_N^{(m)}}}{(\omega - \omega_N^{(m)}) + i\frac{\gamma_N^{(m)}}{2}}, \quad (\text{B.15})$$

We highlight that this reformulation does not give uniquely defined expressions for the functions $t_m(\omega)$ and $r_m(\omega)$, however just knowing this functions at the corresponding resonances, i.e. $r(\omega_N^{(m)})$, is enough for the further derivation.

B.2 Discrete cavity modes in terms of to the true modes

In this appendix, we demonstrate the relation between the cavity operator in the inside-outside representation c_m and the true modes a_ω . From the equations

$$\begin{aligned} E_{0,\text{ins}}(x) &= E_{\text{ins}}(x), \\ B_{0,\text{ins}}(x) &= B_{\text{ins}}(x) \end{aligned}$$

we have

$$\begin{aligned} \sum_{m=1}^{\infty} \sqrt{\frac{\hbar\omega_m}{L_N \mathcal{A} \varepsilon_0}} (c_m + c_m^\dagger) \sin \left[\frac{\omega_m}{c} (x + \ell_c) \right] &= \int_0^\infty d\omega \sqrt{\frac{\hbar\omega}{\pi c \mathcal{A} \varepsilon_0}} \left(\sin \left[\frac{\omega}{c} (x + \ell_c) \right] e^{i\frac{\omega}{c} \ell_c} \mathcal{T}_\omega a_\omega \right. \\ &\quad \left. + \sin \left[\frac{\omega}{c} (x + \ell_c) \right] e^{-i\frac{\omega}{c} \ell_c} \mathcal{T}_\omega^* a_\omega^\dagger \right), \end{aligned} \quad (\text{B.16a})$$

$$\begin{aligned} \sum_{m=1}^{\infty} \sqrt{\frac{\hbar\omega_m}{L_N \mathcal{A} \varepsilon_0}} (c_m - c_m^\dagger) \cos \left[\frac{\omega_m}{c} (x + \ell_c) \right] &= \int_0^\infty d\omega \sqrt{\frac{\hbar\omega}{\pi c \mathcal{A} \varepsilon_0}} \left(\cos \left[\frac{\omega}{c} (x + \ell_c) \right] e^{i\frac{\omega}{c} \ell_c} \mathcal{T}_\omega a_\omega \right. \\ &\quad \left. - \cos \left[\frac{\omega}{c} (x + \ell_c) \right] e^{-i\frac{\omega}{c} \ell_c} \mathcal{T}_\omega^* a_\omega^\dagger \right). \end{aligned} \quad (\text{B.16b})$$

which simplifies to

$$\begin{aligned} \sum_{m=1}^{\infty} \sqrt{\frac{\omega_m}{L_N}} (c_m + c_m^\dagger) \sin \left[\frac{\omega_m}{c} (x + \ell_c) \right] &= \int_0^\infty d\omega \sqrt{\frac{\omega}{\pi c}} \left(\left[\sin \left[\frac{\omega}{c} (x + \ell_c) \right] e^{i\frac{\omega}{c} \ell_c} \mathcal{T}_\omega \right] a_\omega \right. \\ &\quad \left. + \left[\sin \left[\frac{\omega}{c} (x + \ell_c) \right] e^{-i\frac{\omega}{c} \ell_c} \mathcal{T}_\omega^* \right] a_\omega^\dagger \right), \end{aligned} \quad (\text{B.17a})$$

$$\begin{aligned} \sum_{m=1}^{\infty} \sqrt{\frac{\omega_m}{L_N}} (c_m - c_m^\dagger) \cos \left[\frac{\omega_m}{c} (x + \ell_c) \right] &= \int_0^\infty d\omega \sqrt{\frac{\omega}{\pi c}} \left(\cos \left[\frac{\omega}{c} (x + \ell_c) \right] e^{i\frac{\omega}{c} \ell_c} \mathcal{T}_\omega a_\omega \right. \\ &\quad \left. - \cos \left[\frac{\omega}{c} (x + \ell_c) \right] e^{-i\frac{\omega}{c} \ell_c} \mathcal{T}_\omega^* a_\omega^\dagger \right). \end{aligned} \quad (\text{B.17b})$$

If we multiply both sides of Eq. (B.17a) by $\sin\left[\frac{\omega_n}{c}(x + \ell_c)\right]$ and integrate over the interval $x = (-\ell_c, d)$, where $d = \ell_{\text{eff}} - \ell_c$, we get

$$(c_m + c_m^\dagger) = \frac{1}{\ell_{\text{eff}}} \sqrt{\frac{cL_N}{\pi}} \int_0^\infty d\omega \sqrt{\frac{\omega}{\omega_m}} \left(\frac{\sin\left[(\omega - \omega_m)\frac{\ell_{\text{eff}}}{c}\right]}{\omega - \omega_m} - \frac{\sin\left[(\omega + \omega_m)\frac{\ell_{\text{eff}}}{c}\right]}{\omega + \omega_m} \right) \times \left(e^{i\frac{\omega}{c}\ell_c} \mathcal{T}_\omega a_\omega + e^{-i\frac{\omega}{c}\ell_c} \mathcal{T}_\omega^* a_\omega^\dagger \right). \quad (\text{B.18})$$

Similarly, if we multiply both sides of Eq. (B.17b) by $\cos\left[\frac{\omega_n}{c}(x + \ell_c)\right]$ and integrate we get

$$(c_m - c_m^\dagger) = \frac{1}{\ell_{\text{eff}}} \sqrt{\frac{cL_N}{\pi}} \int_0^\infty d\omega \sqrt{\frac{\omega}{\omega_m}} \left(\frac{\sin\left[(\omega - \omega_m)\frac{\ell_{\text{eff}}}{c}\right]}{\omega - \omega_m} + \frac{\sin\left[(\omega + \omega_m)\frac{\ell_{\text{eff}}}{c}\right]}{\omega + \omega_m} \right) \times \left(e^{i\frac{\omega}{c}\ell_c} \mathcal{T}_\omega a_\omega - e^{-i\frac{\omega}{c}\ell_c} \mathcal{T}_\omega^* a_\omega^\dagger \right). \quad (\text{B.19})$$

By taking the sum of equations (B.18) and (B.19), we get the expression for the discrete cavity operator a_m :

$$c_m = \frac{1}{\ell_{\text{eff}}} \sqrt{\frac{cL_N}{\pi}} \int_0^\infty d\omega \sqrt{\frac{\omega}{\omega_m}} \left(\frac{\sin\left[(\omega - \omega_m)\frac{\ell_{\text{eff}}}{c}\right]}{\omega - \omega_m} e^{i\frac{\omega}{c}\ell_c} \mathcal{T}_\omega a_\omega - \frac{\sin\left[(\omega + \omega_m)\frac{\ell_{\text{eff}}}{c}\right]}{\omega + \omega_m} e^{-i\frac{\omega}{c}\ell_c} \mathcal{T}_\omega^* a_\omega^\dagger \right). \quad (\text{B.20})$$

B.3 Continuous reservoir modes in terms of the true modes

Analogously to Appendix B.2, in this one we derive the relation between the reservoir operator b_ω and the operator a_ω . From the equations

$$\begin{aligned} E_{0,\text{outs}}(x) &= E_{\text{outs}}(x), \\ B_{0,\text{outs}}(x) &= B_{\text{outs}}(x), \end{aligned}$$

we get

$$2 \int_0^\infty d\omega \sqrt{\omega} (b_\omega + b_\omega^\dagger) \sin\left[\frac{\omega}{c}(x - d)\right] = -i \int_0^\infty d\omega \sqrt{\omega} \left(\left[e^{2i\frac{\omega}{c}\ell_c} \frac{\mathcal{T}_\omega}{\mathcal{T}_\omega^*} e^{i\frac{\omega}{c}x} - e^{-i\frac{\omega}{c}x} \right] a_\omega - H.c. \right), \quad (\text{B.21})$$

$$2 \int_0^\infty d\omega \sqrt{\omega} (b_\omega - b_\omega^\dagger) \cos\left[\frac{\omega}{c}(x - d)\right] = \int_0^\infty d\omega \sqrt{\omega} \left(\left[e^{2i\frac{\omega}{c}\ell_c} \frac{\mathcal{T}_\omega}{\mathcal{T}_\omega^*} e^{i\frac{\omega}{c}x} + e^{-i\frac{\omega}{c}x} \right] a_\omega - H.c. \right). \quad (\text{B.22})$$

We multiply both sides of Eq. (B.21) by $\sin\left[\frac{\omega'}{c}(x - d)\right]$ and integrate over the interval (d, ∞) , which gives:

$$(b_{\omega'} + b_{\omega'}^\dagger) = -\frac{i}{\pi c} \int_d^\infty dx \int_0^\infty d\omega \sqrt{\frac{\omega}{\omega'}} \left(\left[e^{2i\frac{\omega}{c}\ell_c} \frac{\mathcal{T}_\omega}{\mathcal{T}_\omega^*} e^{i\frac{\omega}{c}x} - e^{-i\frac{\omega}{c}x} \right] a_\omega - H.c. \right) \sin\left[\frac{\omega'}{c}(x - d)\right]. \quad (\text{B.23})$$

Similarly, if we multiply both sides of equation (B.22) by $\cos\left[\frac{\omega'}{c}(x-d)\right]$ we obtain:

$$(b_{\omega'} - b_{\omega'}^\dagger) = \frac{1}{\pi c} \int_d^\infty dx \int_0^\infty d\omega \sqrt{\frac{\omega}{\omega'}} \left(\left[e^{2i\frac{\omega}{c}\ell_c} \frac{\mathcal{T}_\omega}{\mathcal{T}_\omega^*} e^{i\frac{\omega}{c}x} + e^{-i\frac{\omega}{c}x} \right] a_\omega - H.c. \right) \cos\left[\frac{\omega'}{c}(x-d)\right]. \quad (\text{B.24})$$

If now we sum the expressions in (B.23) and (B.24) we obtain:

$$b_{\omega'} = \frac{1}{2\pi c} \int_d^\infty dx \int_0^\infty d\omega \sqrt{\frac{\omega}{\omega'}} \left(\left[e^{2i\frac{\omega}{c}\ell_c} \frac{\mathcal{T}_\omega}{\mathcal{T}_\omega^*} e^{i\frac{\omega}{c}d} e^{i\frac{\omega-\omega'}{c}(x-d)} + e^{-i\frac{\omega}{c}d} e^{-i\frac{\omega-\omega'}{c}(x-d)} \right] a_\omega - \left[e^{-2i\frac{\omega}{c}\ell_c} \frac{\mathcal{T}_\omega^*}{\mathcal{T}_\omega} e^{-i\frac{\omega}{c}d} e^{-i\frac{\omega+\omega'}{c}(x-d)} + e^{i\frac{\omega}{c}d} e^{i\frac{\omega+\omega'}{c}(x-d)} \right] a_\omega^\dagger \right). \quad (\text{B.25})$$

We define

$$G_\omega := e^{2i\frac{\omega}{c}\ell_c} \frac{\mathcal{T}_\omega}{\mathcal{T}_\omega^*} e^{i\frac{\omega}{c}d}. \quad (\text{B.26})$$

Considering the limit where $\mathcal{T}_\omega \approx \mathcal{T}_m(\omega) \approx T_{m,\omega}$, the above expression can be simplified using the formulation in Eq. (7.4):

$$\begin{aligned} G_\omega &\approx e^{2i\frac{\omega}{c}\ell_c} \frac{T_{m,\omega}}{T_{m,\omega}^*} e^{i\frac{\omega}{c}d} = e^{2i\frac{\omega}{c}\ell_c} e^{i\frac{\omega}{c}d} \frac{t_m(\omega)}{t_m^*(\omega)} \frac{1 + r_m^*(\omega) e^{-2i\frac{\omega}{c}\ell_{\text{eff}}}}{1 + r_m(\omega) e^{2i\frac{\omega}{c}\ell_{\text{eff}}}} \\ &= -e^{2i\frac{\omega}{c}\ell_c} e^{i\frac{\omega}{c}d} e^{2i\varphi_r(\omega)} \frac{1 + |r_m(\omega)| e^{-i\varphi_r(\omega)} e^{-2i\frac{\omega}{c}\ell_{\text{eff}}}}{1 + |r_m(\omega)| e^{i\varphi_r(\omega)} e^{2i\frac{\omega}{c}\ell_{\text{eff}}}} \\ &= -e^{-i\frac{\omega}{c}d} \left(e^{2i\frac{\omega}{c}\ell_c} e^{2i\frac{\omega}{c}d} e^{2i\varphi_r(\omega)} \frac{1 + |r_m(\omega)| e^{-i(\varphi_r(\omega) + 2\frac{\omega}{c}\ell_{\text{eff}})}}{1 + |r_m(\omega)| e^{i(\varphi_r(\omega) + 2\frac{\omega}{c}\ell_{\text{eff}})}} + 1 - 1 \right) \\ &= e^{-i\frac{\omega}{c}d} - e^{i\frac{\omega}{c}\ell_c} e^{i\varphi_r(\omega)} \frac{2 \cos\left(\frac{\omega}{c}d + \frac{\omega}{c}\ell_c + \varphi_r(\omega)\right) + |r_m(\omega)| 2 \cos\left(\frac{\omega}{c}\ell_{\text{eff}}\right)}{1 + |r_m(\omega)| e^{i\varphi_r(\omega)} e^{2i\frac{\omega}{c}\ell_{\text{eff}}}} \\ &= e^{-i\frac{\omega}{c}d} + ie^{i\frac{\omega}{c}\ell_c} \frac{2 \cos\left(\frac{\omega}{c}d + \frac{\omega}{c}\ell_c + \varphi_r(\omega)\right) + |r_m(\omega)| 2 \cos\left(\frac{\omega}{c}\ell_{\text{eff}}\right)}{|t_m(\omega)|} T_{m,\omega} \sqrt{\frac{L_N}{\ell_{\text{eff}}}} \\ &= e^{-i\frac{\omega}{c}d} + 2ie^{i\frac{\omega}{c}\ell_c} \frac{\cos\left(\frac{\omega}{c}\ell_{\text{eff}} + \varphi_r(\omega)\right) + |r_m(\omega)| \cos\left(\frac{\omega}{c}\ell_{\text{eff}}\right)}{|t_m(\omega)|} T_{m,\omega} \sqrt{\frac{L_N}{\ell_{\text{eff}}}}. \end{aligned}$$

Using this simplification we can calculate the integral over x in Eq. (7.16)

$$\begin{aligned}
b_\omega &= \frac{1}{2\pi c} \int_d^\infty dx \int_0^\infty d\omega' \sqrt{\frac{\omega'}{\omega}} \left(\left[G_{\omega'} e^{i\frac{\omega'-\omega}{c}(x-d)} + e^{-i\frac{\omega'}{c}d} e^{-i\frac{\omega'-\omega}{c}(x-d)} \right] a_{\omega'} \right. \\
&\quad \left. - \left[G_{\omega'}^* e^{-i\frac{\omega'+\omega}{c}(x-d)} + e^{i\frac{\omega'}{c}d} e^{i\frac{\omega'+\omega}{c}(x-d)} \right] a_{\omega'}^\dagger \right) \\
&= \frac{1}{2\pi c} \int_d^\infty dx \int_0^\infty d\omega' \sqrt{\frac{\omega'}{\omega}} \\
&\quad \times \left(\left[\frac{2ie^{i\frac{\omega'}{c}l_c} \cos\left(\frac{\omega'}{c}l_{\text{eff}} + \varphi_r(\omega')\right) + |r_m(\omega')| \cos\left(\frac{\omega'}{c}l_{\text{eff}}\right)}{|t_m(\omega')|} T_{m,\omega'} \sqrt{\frac{L_N}{l_{\text{eff}}}} e^{i\frac{\omega'-\omega}{c}(x-d)} \right. \right. \\
&\quad \left. \left. + e^{-i\frac{\omega'}{c}d} e^{i\frac{\omega'-\omega}{c}(x-d)} + e^{-i\frac{\omega'}{c}d} e^{-i\frac{\omega'-\omega}{c}(x-d)} \right] a_{\omega'} \right. \\
&\quad \left. - \left[-\frac{2ie^{-i\frac{\omega'}{c}l_c} \cos\left(\frac{\omega'}{c}l_{\text{eff}} + \varphi_r(\omega')\right) + |r_m(\omega')| \cos\left(\frac{\omega'}{c}l_{\text{eff}}\right)}{|t_m(\omega')|} T_{m,\omega'}^* \sqrt{\frac{L_N}{l_{\text{eff}}}} e^{-i\frac{\omega'+\omega}{c}(x-d)} \right. \right. \\
&\quad \left. \left. + e^{i\frac{\omega'}{c}d} e^{-i\frac{\omega'+\omega}{c}(x-d)} + e^{i\frac{\omega'}{c}d} e^{i\frac{\omega'+\omega}{c}(x-d)} \right] a_{\omega'}^\dagger \right).
\end{aligned}$$

Knowing that:

$$\int_0^\infty dy e^{\pm i\frac{\omega \pm \omega'}{c}y} = -\lim_{\epsilon \rightarrow 0} \frac{c}{(\pm i(\omega \pm \omega') - \epsilon)},$$

and taking into account that we integrate only over positive frequencies, for the above integral we get

$$\begin{aligned}
b_\omega &= e^{-i\frac{\omega}{c}d} a_\omega + \frac{1}{\pi} \int_0^\infty d\omega' \sqrt{\frac{\omega'}{\omega}} \sqrt{\frac{L_N}{l_{\text{eff}}}} \frac{\cos\left(\frac{\omega'}{c}l_{\text{eff}} + \varphi_r(\omega')\right) + |r_m(\omega')| \cos\left(\frac{\omega'}{c}l_{\text{eff}}\right)}{|t_m(\omega')|} \\
&\quad \times \left(e^{i\frac{\omega'}{c}l_c} T_{m,\omega'} \lim_{\epsilon \rightarrow 0} \frac{1}{\omega - \omega' - i\epsilon} a_{\omega'} + e^{-i\frac{\omega'}{c}l_c} T_{m,\omega'}^* \lim_{\epsilon \rightarrow 0} \frac{1}{\omega + \omega' - i\epsilon} a_{\omega'}^\dagger \right).
\end{aligned}$$

B.4 Coefficients relating the true modes to the inside-outside modes

In this appendix, we derive the coefficients $\alpha_{m_1}(\omega)$, $\alpha_{m_2}(\omega)$ and $\beta_1(\omega, \omega')$, $\beta_2(\omega, \omega')$, corresponding to the decomposition of true modes into inside-outside modes [Eq. (7.19)]. We start by calculating the following commutators:

$$\begin{aligned}
\alpha_{m_1}(\omega) &= [a_\omega, c_m^\dagger] = \frac{1}{l_{\text{eff}}} \sqrt{\frac{cL_N}{\pi}} \int d\omega' \sqrt{\frac{\omega'}{\omega_m}} \left(\frac{\sin\left[(\omega' - \omega_m) \frac{l_{\text{eff}}}{c}\right]}{\omega' - \omega_m} e^{-i\frac{\omega'}{c}l_c} \mathcal{T}_{\omega'}^* [a_\omega, a_{\omega'}^\dagger] \right. \\
&\quad \left. - \frac{\sin\left[(\omega' + \omega_m) \frac{l_{\text{eff}}}{c}\right]}{\omega' + \omega_m} e^{i\frac{\omega'}{c}l_c} \mathcal{T}_{\omega'} [a_\omega, a_{\omega'}] \right) = \frac{1}{l_{\text{eff}}} \sqrt{\frac{cL_N}{\pi}} \sqrt{\frac{\omega}{\omega_m}} \frac{\sin\left[(\omega - \omega_m) \frac{l_{\text{eff}}}{c}\right]}{\omega - \omega_m} e^{-i\frac{\omega}{c}l_c} \mathcal{T}_\omega^*,
\end{aligned}$$

where we have used the commutation relations (7.7). Similarly,

$$\begin{aligned} \alpha_{m_2}(\omega) = [c_m, a_\omega] &= \frac{1}{\ell_{\text{eff}}} \sqrt{\frac{cL_N}{\pi}} \int d\omega' \sqrt{\frac{\omega'}{\omega_m}} \left(\frac{\sin[(\omega' - \omega_m) \frac{\ell_{\text{eff}}}{c}]}{\omega' - \omega_m} e^{i\frac{\omega'}{c}\ell_c} \mathcal{T}_{\omega'} [a_{\omega'}, a_\omega] \right. \\ &\left. - \frac{\sin[(\omega' + \omega_m) \frac{\ell_{\text{eff}}}{c}]}{\omega' + \omega_m} e^{-i\frac{\omega'}{c}\ell_c} \mathcal{T}_{\omega'}^* [a_{\omega'}^\dagger, a_\omega] \right) = \frac{1}{\ell_{\text{eff}}} \sqrt{\frac{cL_N}{\pi}} \sqrt{\frac{\omega}{\omega_m}} \frac{\sin[(\omega + \omega_m) \frac{\ell_{\text{eff}}}{c}]}{\omega + \omega_m} e^{-i\frac{\omega}{c}\ell_c} \mathcal{T}_\omega^*. \end{aligned}$$

Similar calculation can be done to obtain the coefficients $\beta_1(\omega, \omega')$ and $\beta_2(\omega, \omega')$:

$$\begin{aligned} \beta_1(\omega, \omega') &= [a_\omega, b_{\omega'}^\dagger] = e^{i\frac{\omega'}{c}d} [a_\omega, a_{\omega'}^\dagger] \\ &+ \frac{1}{\pi} \int_0^\infty d\omega'' \sqrt{\frac{\omega''}{\omega'}} \sqrt{\frac{L_N}{\ell_{\text{eff}}}} \frac{\cos\left(\frac{\omega''}{c}\ell_{\text{eff}} + \varphi_r(\omega'')\right) + |r_m(\omega'')| \cos\left(\frac{\omega''}{c}\ell_{\text{eff}}\right)}{|t_m(\omega'')|} \\ &\times \left(e^{-i\frac{\omega''}{c}\ell_c} T_{m,\omega''}^* \lim_{\epsilon \rightarrow 0} \frac{1}{\omega' - \omega'' + i\epsilon} [a_\omega, a_{\omega''}^\dagger] + e^{i\frac{\omega''}{c}\ell_c} T_{m,\omega''} \lim_{\epsilon \rightarrow 0} \frac{1}{\omega' + \omega'' + i\epsilon} [a_\omega, a_{\omega''}] \right) \\ &= e^{i\frac{\omega'}{c}d} \delta(\omega - \omega') \\ &+ \frac{1}{\pi} \sqrt{\frac{\omega}{\omega'}} \sqrt{\frac{L_N}{\ell_{\text{eff}}}} \frac{\cos\left(\frac{\omega}{c}\ell_{\text{eff}} + \varphi_r(\omega)\right) + |r_m(\omega)| \cos\left(\frac{\omega}{c}\ell_{\text{eff}}\right)}{|t_m(\omega)|} e^{-i\frac{\omega}{c}\ell_c} T_{m,\omega}^* \lim_{\epsilon \rightarrow 0} \frac{1}{\omega' - \omega + i\epsilon}. \end{aligned}$$

Similarly,

$$\begin{aligned} \beta_2(\omega, \omega') &= [b_{\omega'}, a_\omega] = e^{-i\frac{\omega'}{c}d} [a_{\omega'}, a_\omega] \\ &+ \frac{1}{\pi} \int_0^\infty d\omega'' \sqrt{\frac{\omega''}{\omega'}} \sqrt{\frac{L_N}{\ell_{\text{eff}}}} \frac{\cos\left(\frac{\omega''}{c}\ell_{\text{eff}} + \varphi_r(\omega'')\right) + |r_m(\omega'')| \cos\left(\frac{\omega''}{c}\ell_{\text{eff}}\right)}{|t_m(\omega'')|} \\ &\times \left(e^{i\frac{\omega''}{c}\ell_c} T_{m,\omega''} \lim_{\epsilon \rightarrow 0} \frac{1}{\omega' - \omega'' - i\epsilon} [a_{\omega''}, a_\omega] + e^{-i\frac{\omega''}{c}\ell_c} T_{m,\omega''}^* \lim_{\epsilon \rightarrow 0} \frac{1}{\omega' + \omega'' - i\epsilon} [a_{\omega'}^\dagger, a_\omega] \right) \\ &= -\frac{1}{\pi} \sqrt{\frac{\omega}{\omega'}} \sqrt{\frac{L_N}{\ell_{\text{eff}}}} \frac{\cos\left(\frac{\omega}{c}\ell_{\text{eff}} + \varphi_r(\omega)\right) + |r_m(\omega)| \cos\left(\frac{\omega}{c}\ell_{\text{eff}}\right)}{|t_m(\omega)|} e^{-i\frac{\omega}{c}\ell_c} T_{m,\omega}^* \lim_{\epsilon \rightarrow 0} \frac{1}{\omega' + \omega - i\epsilon}. \end{aligned}$$

B.5 Commutation relation for the separated modes

In this appendix we verify the validity of the commutation relation (7.22) using the separation (7.26) with the coefficients (7.25):

$$\begin{aligned} [a_D(\omega), a_D^\dagger(\omega')] &= \sum_{m=1} \sum_{m'=1} \alpha_{m_1}(\omega) \alpha_{m'_1}^*(\omega') [c_m, c_{m'}^\dagger] = \sum_{m=1} \alpha_{m_1}(\omega) \alpha_{m_1}^*(\omega') \\ &= \sum_{m=1} e^{-i\frac{\omega}{c}\ell_c} \sqrt{\frac{\gamma_m}{2\pi}} \frac{1}{(\omega - \omega_m) - i\frac{\gamma_m}{2}} e^{i\frac{\omega'}{c}\ell_c} \sqrt{\frac{\gamma_m}{2\pi}} \frac{1}{(\omega' - \omega_m) + i\frac{\gamma_m}{2}} \\ &= \sum_{m=1} e^{-i(\omega - \omega')\frac{\ell_c}{c}} \frac{\gamma_m}{2\pi} \frac{1}{(\omega - \omega_m) - i\frac{\gamma_m}{2}} \frac{1}{(\omega' - \omega_m) + i\frac{\gamma_m}{2}} \\ &\approx \sum_{m=1} \frac{\gamma_m}{2\pi} \frac{1}{(\omega - \omega_m) - i\frac{\gamma_m}{2}} \frac{1}{(\omega' - \omega_m) + i\frac{\gamma_m}{2}} \end{aligned} \quad (\text{B.27})$$

For the corresponding continuous part we get:

$$\begin{aligned}
[a_C(\omega), a_C^\dagger(\omega'')] &= \int_0^\infty \int_0^\infty d\omega' d\tilde{\omega} \beta_1(\omega, \omega') \beta_1^*(\omega'', \tilde{\omega}) [b_{\omega'}, b_{\tilde{\omega}}^\dagger] \\
&= \delta(\omega'' - \omega) + e^{i\frac{\omega''}{c}d} \frac{1}{\pi} \left(e^{i\frac{\omega''}{c}l_c} T_{m,\omega''} \sqrt{\frac{L_N}{\ell_{\text{eff}}}} (-1)^m \frac{-1 + |r_m(\omega_m)|}{|t_m(\omega_m)|} \lim_{\epsilon \rightarrow 0} \frac{1}{\omega - \omega'' - i\epsilon} \right) \\
&+ e^{-i\frac{\omega''}{c}d} \frac{1}{\pi} \left(e^{-i\frac{\omega''}{c}l_c} T_{m,\omega}^* \sqrt{\frac{L_N}{\ell_{\text{eff}}}} (-1)^m \frac{-1 + |r_m(\omega_m)|}{|t_m(\omega_m)|} \lim_{\epsilon \rightarrow 0} \frac{1}{\omega'' - \omega + i\epsilon} \right) \\
&+ \frac{L_N}{\ell_{\text{eff}}\pi^2} \left(\frac{-1 + |r_m(\omega_m)|}{|t_m(\omega_m)|} \right)^2 T_{m,\omega}^* T_{m,\omega''} \int_0^\infty d\omega' \lim_{\epsilon \rightarrow 0} \frac{e^{i(\omega'' - \omega)\frac{\ell_c}{c}}}{\omega' - \omega + i\epsilon} \lim_{\epsilon \rightarrow 0} \frac{1}{\omega' - \omega'' - i\epsilon}.
\end{aligned}$$

We proceed by applying the following approximation, which is justified by the fact that we consider a cavity of high reflectivity:

$$\begin{aligned}
\frac{-1 + |r_m(\omega_m)|}{|t_m(\omega_m)|} &= \frac{-1 + e^{-\gamma_m \frac{\ell_{\text{eff}}}{c}}}{\sqrt{1 - e^{-2\gamma_m \frac{\ell_{\text{eff}}}{c}}}} = \frac{-1 + 1 - \gamma_m \frac{\ell_{\text{eff}}}{c} + \mathcal{O}\left(\left(\gamma_m \frac{\ell_{\text{eff}}}{c}\right)^2\right)}{\sqrt{1 - 1 + 2\gamma_m \frac{\ell_{\text{eff}}}{c} - \mathcal{O}\left(\left(\gamma_m \frac{\ell_{\text{eff}}}{c}\right)^2\right)}} \\
&\approx -\frac{\gamma_m \frac{\ell_{\text{eff}}}{c}}{\sqrt{2\gamma_m \frac{\ell_{\text{eff}}}{c}}} = -\sqrt{\frac{\gamma_m \ell_{\text{eff}}}{2c}}, \tag{B.28}
\end{aligned}$$

where the terms of the order of $\left(\gamma_m \frac{\ell_{\text{eff}}}{c}\right)^2$ and higher are neglected based on the above assumption. With this assumption and using the explicit expression of $\mathcal{T}_m(\omega)$ (since $T_{m,\omega} \approx \mathcal{T}_m(\omega)$) the commutator becomes:

$$\begin{aligned}
[a_C(\omega), a_C^\dagger(\omega'')] &\approx \delta(\omega'' - \omega) \\
&- \sum_m (-1)^m \frac{\gamma_m}{2\pi} \lim_{\epsilon \rightarrow 0} \frac{1}{\omega - \omega'' - i\epsilon} \left(\frac{e^{i\frac{\omega''}{c}d} e^{i\frac{\omega''}{c}l_c}}{\omega'' - \omega_m + i\frac{\gamma_m}{2}} - \frac{e^{-i\frac{\omega''}{c}d} e^{-i\frac{\omega''}{c}l_c}}{\omega - \omega_m - i\frac{\gamma_m}{2}} \right) \\
&+ \frac{1}{\pi^2} \sum_m \frac{\gamma_m^2}{4} \frac{e^{i(\omega'' - \omega)\frac{\ell_c}{c}}}{\omega - \omega_m - i\frac{\gamma_m}{2}} \frac{1}{\omega'' - \omega_m + i\frac{\gamma_m}{2}} \int_0^\infty d\omega' \lim_{\epsilon \rightarrow 0} \frac{1}{\omega' - \omega + i\epsilon} \lim_{\epsilon \rightarrow 0} \frac{1}{\omega' - \omega'' - i\epsilon} \\
&= \delta(\omega'' - \omega) - \sum_m \frac{\gamma_m}{2\pi} \lim_{\epsilon \rightarrow 0} \frac{1}{\omega - \omega'' - i\epsilon} \left(\frac{1}{\omega'' - \omega_m + i\frac{\gamma_m}{2}} - \frac{1}{\omega - \omega_m - i\frac{\gamma_m}{2}} \right) \\
&+ \frac{1}{\pi^2} \sum_m \frac{\gamma_m^2}{4} \frac{e^{i(\omega'' - \omega)\frac{\ell_c}{c}}}{\omega - \omega_m - i\frac{\gamma_m}{2}} \frac{1}{\omega'' - \omega_m + i\frac{\gamma_m}{2}} \int_0^\infty d\omega' \lim_{\epsilon \rightarrow 0} \frac{1}{\omega' - \omega + i\epsilon} \lim_{\epsilon \rightarrow 0} \frac{1}{\omega' - \omega'' - i\epsilon} \\
&\approx \delta(\omega'' - \omega) - \sum_m \frac{\gamma_m}{2\pi} \frac{1}{\left(\omega'' - \omega_m + i\frac{\gamma_m}{2}\right) \left(\omega - \omega_m - i\frac{\gamma_m}{2}\right)}, \tag{B.29}
\end{aligned}$$

where we have neglected the terms of the order $(\gamma_m/\omega_m)^2$ since we consider cavities of high quality, i.e., $\gamma_m/\omega_m \ll 1$. We also evaluate the following term at the resonance frequency ω_m : $e^{i\frac{\omega}{c}d} e^{i\frac{\omega''}{c}l_c} = e^{i\frac{\omega_m}{c}d} e^{i\frac{\omega_m}{c}l_c} = e^{i\frac{\omega_m}{c}(\ell_{\text{eff}} - l_c)} e^{i\frac{\omega_m}{c}l_c} = (-1)^m$.

If we sum equations (B.27) and (B.29) we get the required commutation relation:

$$[a_\omega, a_{\omega'}^\dagger] = [a_D(\omega), a_D^\dagger(\omega')] + [a_C(\omega), a_C^\dagger(\omega')] = \delta(\omega' - \omega). \tag{B.30}$$

B.6 Hamiltonian representation

In this appendix we derive the Hamiltonian for the inside-outside representation, starting from Hamiltonian (7.8) derived for the true modes. Using the relation (7.26) we can write the following:

$$\begin{aligned}
 H &= \int_0^\infty d\omega \hbar \omega a_\omega^\dagger a_\omega \\
 &= \int_0^\infty d\omega \hbar \omega \left[\sum_{m=1}^\infty \alpha_{m_1}^*(\omega) c_m^\dagger + \int_0^\infty d\omega' \beta_1^*(\omega, \omega') b_{\omega'}^\dagger \right] \left[\sum_{m=1}^\infty \alpha_{m_1}(\omega) c_m + \int_0^\infty d\omega' \beta_1(\omega, \omega') b_{\omega'} \right] \\
 &= \int_0^\infty d\omega \hbar \omega \left[\sum_{m=1}^\infty \sum_{m'=1}^\infty \alpha_{m_1}(\omega) \alpha_{m'_1}^*(\omega) c_{m'}^\dagger c_m \right. \\
 &\quad + \sum_{m=1}^\infty \int_0^\infty d\omega' \left(\alpha_{m_1}^*(\omega) \beta_1(\omega, \omega') c_m^\dagger b_{\omega'} + \alpha_{m_1}(\omega) \beta_1^*(\omega, \omega') b_{\omega'}^\dagger c_m \right) \\
 &\quad \left. + \int_0^\infty d\omega' d\omega'' \beta_1^*(\omega, \omega') \beta_1(\omega, \omega'') b_{\omega'}^\dagger b_{\omega''} \right].
 \end{aligned}$$

We proceed by analyzing each term of the above equation separately:

$$H_C = \int_0^\infty d\omega \hbar \omega \sum_{m=1}^\infty \sum_{m'=1}^\infty \alpha_{m_1}(\omega) \alpha_{m'_1}^*(\omega) c_m^\dagger c_{m'}. \quad (\text{B.31})$$

Since we are considering a regime where individual resonance peaks of the cavity are well separated, we can apply the following estimation: $\alpha_{m_1}(\omega) \alpha_{m'_1}^*(\omega) \approx \delta_{mm'} |\alpha_{m_1}(\omega)|^2$, which follows from the assumption $\mathcal{T}_m(\omega) \mathcal{T}_{m'}^*(\omega) \approx \delta_{mm'}$. Taking this into account the expression (B.31) becomes

$$H_C = \int_0^\infty d\omega \hbar \omega \sum_{m=1}^\infty |\alpha_{m_1}(\omega)|^2 c_m^\dagger c_m, \quad (\text{B.32})$$

where the following integral can be evaluated by using the corresponding complex integral, assuming that $\gamma_m/\omega_m \ll 1$:

$$\int_0^\infty d\omega \omega |\alpha_{m_1}(\omega)|^2 \approx \int_0^\infty d\omega \frac{\gamma_m}{2\pi} \frac{\omega}{(\omega - \omega_m)^2 + \left(\frac{\gamma_m}{2}\right)^2}, \quad (\text{B.33})$$

the corresponding complex integral being $\oint_C dz \frac{z+b}{z^2+a}$, integrated in the upper half of the complex plane. Taking this into account the integral in (B.33) becomes

$$\int_0^\infty d\omega \omega |\alpha_{m_1}(\omega)|^2 = \omega_m,$$

which leads to

$$H_C = \sum_{m=1}^\infty \hbar \omega_m c_m^\dagger c_m. \quad (\text{B.34})$$

Next we evaluate the continuous part of the Hamiltonian describing the reservoir:

$$H_R = \int_0^\infty d\omega \int_0^\infty d\omega' \int_0^\infty d\omega'' \hbar \omega \beta_1^*(\omega, \omega') \beta_1(\omega, \omega'') b_{\omega'}^\dagger b_{\omega''}. \quad (\text{B.35})$$

Using the approximation in (B.28) the expression of $\beta_1(\omega, \omega')$ can be written as follows:

$$\begin{aligned}
\beta_1(\omega, \omega') &\approx e^{i\frac{\omega'}{c}d}\delta(\omega - \omega') - \frac{1}{\pi}e^{-i\frac{\omega}{c}\ell_c}\mathcal{T}_m^*(\omega)(-1)^m\sqrt{\frac{\gamma_m\ell_{\text{eff}}}{2c}}\sqrt{\frac{L_N}{\ell_{\text{eff}}}}\lim_{\epsilon\rightarrow 0}\frac{1}{\omega' - \omega + i\epsilon} \\
&= e^{i\frac{\omega'}{c}d}\delta(\omega - \omega') - \frac{\gamma_m}{2\pi}e^{-i\frac{\omega}{c}\ell_c}\sum_m\frac{1}{\omega - \omega_m - i\frac{\gamma_m}{2}}(-1)^m\lim_{\epsilon\rightarrow 0}\frac{1}{\omega' - \omega + i\epsilon} \\
&= e^{i\frac{\omega'}{c}d}\delta(\omega - \omega') - \sqrt{\frac{\gamma_m}{2\pi}}\sum_m\alpha_{m_1}(\omega)(-1)^m\lim_{\epsilon\rightarrow 0}\frac{1}{\omega' - \omega + i\epsilon}.
\end{aligned} \tag{B.36}$$

Taking this into account, the Hamiltonian in (B.35) becomes:

$$\begin{aligned}
H_R &\approx \int_0^\infty d\omega \hbar\omega b_\omega^\dagger b_\omega \\
&+ \frac{1}{2\pi} \int_0^\infty d\omega' \int_0^\infty d\omega'' \hbar \left(\lim_{\epsilon\rightarrow 0} \frac{\gamma_m}{\omega'' - \omega' + i\epsilon} \frac{-\omega''(\omega_m + i\frac{\gamma_m}{2}) + \omega'(\omega_m - i\frac{\gamma_m}{2})}{(\omega' - \omega_m - i\frac{\gamma_m}{2})(\omega'' - \omega_m + i\frac{\gamma_m}{2})} \right. \\
&+ \left. \int_0^\infty d\omega \frac{\gamma_m^2}{(\omega - \omega_m)^2 + (\frac{\gamma_m}{2})^2} \lim_{\epsilon\rightarrow 0} \frac{\omega}{\omega' - \omega - i\epsilon} \lim_{\epsilon\rightarrow 0} \frac{1}{\omega'' - \omega + i\epsilon} \right) b_{\omega'}^\dagger b_{\omega''}.
\end{aligned}$$

By estimating the integral in the last term via corresponding complex plane integral (similar to eq. (B.33)), and neglecting the terms of the order $(\gamma_m/\omega_m)^2$, the above expression reduces to the following:

$$H_R = \int_0^\infty d\omega \hbar\omega b_\omega^\dagger b_\omega.$$

Finally, we evaluate the term describing the interaction between the perfect cavity and the reservoir modes:

$$H_{CR} = \int_0^\infty d\omega \hbar\omega \sum_{m=1}^\infty \int_0^\infty d\omega' \left(\alpha_{m_1}^*(\omega)\beta_1(\omega, \omega')c_m^\dagger b_{\omega'} + \alpha_{m_1}(\omega)\beta_1^*(\omega, \omega')b_{\omega'}^\dagger c_m \right). \tag{B.37}$$

To simplify this expression we again use the approximated expression (B.36) for

$\beta_1(\omega, \omega')$, leading to an integral of the form

$$\begin{aligned}
 \mathcal{I}_1 &= \int_0^\infty d\omega \hbar\omega \sum_{m=1}^\infty \int_0^\infty d\omega' \alpha_{m_1}^*(\omega) \beta_1(\omega, \omega') c_m^\dagger b_{\omega'} \\
 &= \int_0^\infty d\omega \hbar\omega \sum_{m=1}^\infty \int_0^\infty d\omega' \alpha_{m_1}^*(\omega) \left(e^{i\frac{\omega'}{c}d} \delta(\omega - \omega') \right. \\
 &\quad \left. - \frac{1}{\sqrt{\pi}} \sum_{m'} \alpha_{m_1'}(\omega) (-1)^{m'} \sqrt{\frac{\gamma_{m'}}{2}} \lim_{\epsilon \rightarrow 0} \frac{1}{\omega' - \omega + i\epsilon} \right) c_m^\dagger b_{\omega'} \\
 &= \int_0^\infty d\omega \sum_{m=1}^\infty \hbar\omega \alpha_{m_1}^*(\omega) e^{i\frac{\omega}{c}d} c_m^\dagger b_\omega \\
 &\quad - \int_0^\infty d\omega \sum_{m=1}^\infty \int_0^\infty d\omega' \sum_{m'=1}^\infty \hbar\omega (-1)^{m'} \alpha_{m_1}^*(\omega) \alpha_{m_1'}(\omega) \sqrt{\frac{\gamma_{m'}}{2\pi}} \lim_{\epsilon \rightarrow 0} \frac{1}{\omega' - \omega + i\epsilon} c_m^\dagger b_{\omega'} \\
 &= \int_0^\infty d\omega \sum_{m=1}^\infty \hbar\omega \alpha_{m_1}^*(\omega) e^{i\frac{\omega}{c}d} c_m^\dagger b_\omega \\
 &\quad - \int_0^\infty d\omega \sum_{m=1}^\infty \int_0^\infty d\omega' \hbar\omega (-1)^m |\alpha_{m_1}(\omega)|^2 \sqrt{\frac{\gamma_m}{2\pi}} \lim_{\epsilon \rightarrow 0} \frac{1}{\omega' - \omega + i\epsilon} c_m^\dagger b_{\omega'}.
 \end{aligned}$$

The last term can be evaluated similarly to the integral in (B.33), leading to

$$\begin{aligned}
 \mathcal{I}_1 &= \int_0^\infty d\omega \sum_{m=1}^\infty \hbar\omega \alpha_{m_1}^*(\omega) e^{i\frac{\omega}{c}d} a_m^\dagger b_\omega - \int_0^\infty d\omega \sum_{m=1}^\infty \hbar(-1)^m \sqrt{\frac{\gamma_m}{2\pi}} \frac{\omega_m - i\frac{\gamma_m}{2}}{\omega - \omega_m + i\frac{\gamma_m}{2}} c_m^\dagger b_\omega \\
 &= \int_0^\infty d\omega \sum_{m=1}^\infty \hbar \left(e^{i\frac{\omega}{c}d_{\text{eff}}} \sqrt{\frac{\gamma_m}{2\pi}} \frac{\omega}{\omega - \omega_m + i\frac{\gamma_m}{2}} - (-1)^m \sqrt{\frac{\gamma_m}{2\pi}} \frac{\omega_m - i\frac{\gamma_m}{2}}{\omega - \omega_m + i\frac{\gamma_m}{2}} \right) c_m^\dagger b_\omega \\
 &\approx \int_0^\infty d\omega \sum_{m=1}^\infty \hbar \left((-1)^m \sqrt{\frac{\gamma_m}{2\pi}} \frac{\omega}{\omega - \omega_m + i\frac{\gamma_m}{2}} - (-1)^m \sqrt{\frac{\gamma_m}{2\pi}} \frac{\omega_m - i\frac{\gamma_m}{2}}{\omega - \omega_m + i\frac{\gamma_m}{2}} \right) c_m^\dagger b_\omega \\
 &= \int_0^\infty d\omega \sum_{m=1}^\infty \hbar e^{i\frac{\omega}{c}d_{\text{eff}}} \sqrt{\frac{\gamma_m}{2\pi}} \text{sinc} \left[(\omega - \omega_m) \frac{\ell_{\text{eff}}}{c} \right] c_m^\dagger b_\omega,
 \end{aligned}$$

where when writing the last term we recovered the terms we had previously evaluated at the resonance frequency ω_m , i.e., $\text{sinc} \left[(\omega - \omega_m) \frac{\ell_{\text{eff}}}{c} \right]$ and $e^{i\frac{\omega}{c}d_{\text{eff}}}$. Further, by defining a coupling function as follows:

$$\kappa_m(\omega) = -ie^{-i\frac{\omega}{c}d_{\text{eff}}} \sqrt{\frac{\gamma_m}{2\pi}} \text{sinc} \left[(\omega - \omega_m) \frac{\ell_{\text{eff}}}{c} \right], \quad (\text{B.38})$$

the full Hamiltonian in terms of separated inside-outside modes becomes:

$$H = \sum_{m=1}^\infty \hbar\omega_m c_m^\dagger c_m + \int_0^\infty d\omega \hbar\omega b_\omega^\dagger b_\omega + i\hbar \sum_{m=1}^\infty \int_0^\infty d\omega \left(\kappa_m(\omega) b_\omega^\dagger c_m - \kappa_m^*(\omega) c_m^\dagger b_\omega \right). \quad (\text{B.39})$$

Part IV

Conclusion and perspectives

*The important thing in science
is not so much to obtain new
facts as to discover new ways of
thinking about them.*

William Henry Bragg

As a conclusion, in this manuscript, we have examined different models for describing the light-matter interaction in optical cavities. In particular, we have proposed approximate methods derived from first principles, to efficiently characterize such a process of light-matter interfacing by obtaining the dynamics and complete characterization of a single photon produced in such a system. While in theoretical models considered in the literature, this is usually done by phenomenologically constructing the cavity leakage, in more realistic scenarios, since the cavity can never be isolated from its environment, the light-matter interaction in the cavity can be affected by the continuous modes of the environment. To account for these effects, we derived the dynamics of an atom trapped in an open cavity. Based on this derivation, we defined effective models that allow the characterization of the cavity-environment closed system, directly providing the spectral and spatial properties of the propagating photon outside the cavity. This analysis is extended for more realistic cavities that are made of multilayered dielectric mirrors.

The analysis of the multilayer structure enabled a more realistic description of the characteristic parameters of the cavity, namely cavity resonance frequencies, effective cavity length and corresponding mode volume. In particular, we have found that the length parameter defining the cavity resonances, the length parameter describing the cavity-emitter coupling strength and the geometric length describing the distance between the cavity mirrors, in general, do not coincide. This can lead to a Purcell factor different from the one calculated by using a standard approach. Additionally, by applying the effective models derived from first principles, we were able to characterize the single photon produced in such a multilayered cavity and leaking out to the environment. In particular, we focused on the representation where the quantized modes of the full cavity-environment system can be separated into inside and outside cavity parts, featuring frequency-dependent cavity-reservoir coupling. In this representation, we derived the propagating photon state along the propagation direction outside the cavity, as well as the photon shape in the frequency domain. This is particularly important when considering the reverse process, where we can use the spectral and spatial shape of the photon derived here to efficiently feed it to a distant cavity with a loaded emitter, acting as a stationary qubit. In this context, the output photon derived here can be considered as an initial photon state, specifically representing the input state corresponding to the term b_{in} of Eq. (4.72). This leads to the term $\mathcal{D}_{\text{in},t}^\dagger$ in Eq. (4.78) being different from

0. By correspondingly modifying the master equation, through the incorporation of the contribution of this term, one can, in principle, characterize the entire process of single-photon production and absorption. As discussed in the literature [42, 64], such a process requires optimal driving pulses for efficient state mapping between the distant cavities, and this process is strongly dependent on the duration of the input photon (time profile) and its spectral distribution, ensuring complete impedance matching.

Furthermore, we demonstrated that at a high-finesse cavity limit, the multilayer nature of the mirror can be reformulated in terms of an effective single-layered one, featuring corrected parameters accounting for the effects induced by the multilayer nature of the cavity. The discrepancy between these parameters and the ones standardly used, is particularly significant for cavities with short mirror spacing, hence the effects induced by the structure of the cavity mirrors may be of importance in applications where the cavity spacings used are very short and the mirrors are made of dielectric coatings [131, 186]. This can be relevant when studying the coupling of ions [189] and atoms to fibre-tip optical cavities [19], quantum dots [125], NV-centers [89, 97, 186], the use of two different frequencies within a short multilayered cavity [68] and, in general, whenever there is a very short cavity that couples strongly to a discrete quantum emitter. In sum, the substantial deviations from the simple model discussed here would make it impossible to establish strong coupling unless these corrections were considered. Additionally, in an intermediate coupling regime, where the photon can escape the cavity easily, to characterize the propagation of this photon the corrected parameters, derived from the multilayer analysis need to be taken into account. These results could also prove useful for the spectral characterization of devices with multilayered structures [85]. Finally, the models derived here can be applied to study more complex dynamics with a laser-driven atom trapped in a multilayer cavity, in particular for controlling the photonic states produced from such cavities. These models can be extended to study the produced photon as a flying qubit, where the information, for example, can be encoded in the polarization of the photon.

We also note that submicrometric confinement of light in (dissipative and dispersive) metallic media gives rise to surface plasmon polaritons that can be used for quantum optics at the nanoscale [28]. Albeit these are no multilayered structures, the construction of quantized models taking into account the resulting losses follow a similar approach and is based on a microscopic oscillator model for the medium coupled to the electromagnetic field [86] with a particular care for finite-size media [47, 49].

C.1 Microscopic and phenomenological models of driven systems in structured reservoirs

In this appendix, we study the case of a driven qubit interacting with a structured environment by means of a microscopic model and analyze the consequences of the FD assumption. This includes the possibility of using reservoir engineering as a tool for quantum control. For that purpose, we mainly study the dynamics on asymptotic timescales and compare the steady states reachable with a microscopic master equation (MME) with the ones given by a master equation based on a fixed dissipator (FDME). We show that manipulating the environment through reservoir engineering, which is possible when the environment spectrum is not flat, allows one to obtain a collection of stationary states that can be very different from the ones given by the FDME.

C.1.1 The model system

For the sake of simplicity, we tackle the problem of comparing microscopic and phenomenological models of driven systems in structured environments by revisiting a simple quantum system made of a qubit of frequency ω_0 driven by a monochromatic control laser field whose frequency is ω_L and whose initial phase is φ . We define the detuning as $\Delta = \omega_0 - \omega_L$ and we refer to the Rabi frequency Ω , related to the intensity of the laser field, as the driving amplitude. We assume henceforth that ω_0 and ω_L are much larger than Δ and Ω . The starting Hamiltonian is given by

$$\bar{H}_S = \frac{\hbar\omega_0}{2}\sigma_z + \hbar\Omega \cos(\omega_L t + \varphi)\sigma_x, \quad (\text{C.1})$$

where σ_z and σ_x are Pauli matrices. Under the above condition on the parameters we may apply the rotating wave approximation on \bar{H}_S , obtaining

$$\bar{H}_S^{RW} = \frac{\hbar\omega_0}{2}\sigma_z + \frac{\hbar\Omega}{2}[e^{-i(\omega_L t + \varphi)}\sigma_+ + e^{i(\omega_L t + \varphi)}\sigma_-], \quad (\text{C.2})$$

where σ_+ and σ_- are, respectively, the raising and the lowering qubit operator. We also move to a frame rotating at frequency ω_L , by means of the unitary operator $U_L = \exp[-i(\omega_L t + \varphi)\sigma_z/2]$ (also absorbing the time-independent phase factor φ). In such a rotating frame, any state $|\bar{\psi}\rangle$ is mapped into $|\psi\rangle = U_L^\dagger|\bar{\psi}\rangle$, and the

Schrödinger equation $i\hbar\partial_t|\bar{\psi}\rangle = \bar{H}_S^{RW}|\bar{\psi}\rangle$ becomes $i\hbar\partial_t(U_L|\psi\rangle) = \bar{H}_S^{RW}U_L|\psi\rangle$, that can be rewritten as $i\hbar\partial_t|\psi\rangle = H_S|\psi\rangle$, where $H_S = U_L^\dagger\bar{H}_S^{RW}U_L - i\hbar(\partial_t U_L^\dagger)U_L$, which leads to

$$H_S = \frac{\hbar\Delta}{2}\sigma_z + \frac{\hbar\Omega}{2}\sigma_x. \quad (\text{C.3})$$

The interaction between the system and the environment, which is assumed not to depend on the control field (see, for instance, Ref. [204]), reads as follows:

$$\bar{H}_I = \sum_k \hbar \left(g_k a_k + g_k^* a_k^\dagger \right) \sigma_x, \quad (\text{C.4})$$

where a_k and a_k^\dagger are, respectively, the annihilation and the creation operators of the bosonic bath and g_k are the coupling constants. In the above rotating frame, \bar{H}_I becomes $H_I = U_L^\dagger\bar{H}_I U_L$, which gives

$$H_I = \sum_k \hbar (g_k a_k + g_k^* a_k^\dagger) \left[e^{i(\omega_L t + \varphi)} \sigma_+ + e^{-i(\omega_L t + \varphi)} \sigma_- \right]. \quad (\text{C.5})$$

The free Hamiltonian of the environment has the form $H_E = \sum_k \hbar\omega_k a_k^\dagger a_k$, and, of course, is not touched by the change of frame. H_S can be diagonalized as $H_S = \frac{\hbar\nu}{2}(|\phi_+\rangle\langle\phi_+| - |\phi_-\rangle\langle\phi_-|)$, with $\nu = \sqrt{\Delta^2 + \Omega^2}$. Its eigenstates are

$$\begin{aligned} |\phi_+\rangle &= C|e\rangle + S|g\rangle, \\ |\phi_-\rangle &= C|g\rangle - S|e\rangle, \end{aligned} \quad (\text{C.6})$$

where $|g\rangle$ and $|e\rangle$ are, respectively, the ground and the excited state of the qubit free Hamiltonian $(\hbar\omega_0/2)\sigma_z$, $C = \cos(\theta/2)$, $S = \sin(\theta/2)$ and

$$\theta = 2 \arctan[(\nu - \Delta)/\Omega]. \quad (\text{C.7})$$

For example, for a given $\Delta > 0$, θ goes from 0 to $\pi/2$ when Ω goes from 0 to infinity.

C.1.2 Microscopic master equation

To derive a microscopic master equation, the qubit driven by the field is treated first. The resulting dressed qubit is next coupled to the environment by expressing H_I in terms of the eigenoperators of H_S represents the standard Born and Markov approximations are applied.

Defining $\tilde{\sigma}_z = |\phi_+\rangle\langle\phi_+| - |\phi_-\rangle\langle\phi_-|$ and $\tilde{\sigma}_\pm = |\phi_\pm\rangle\langle\phi_\mp|$, these are connected to σ_z , σ_+ , and σ_- by

$$\begin{aligned} \sigma_\pm &= C^2\tilde{\sigma}_\pm - S^2\tilde{\sigma}_\mp + SC\tilde{\sigma}_z, \\ \sigma_z &= \cos\theta\tilde{\sigma}_z - \sin\theta\tilde{\sigma}_x. \end{aligned} \quad (\text{C.8})$$

Using the expressions for σ_+ and σ_- , the qubit operators in H_I can be written in terms of eigenoperators of H_S . The detailed derivation of the MME is presented in the supplementary Section C.3. Its final form in the Schrödinger picture is

$$\dot{\rho} = -\frac{i}{\hbar}[H_S + H_{LS}, \rho] + \mathcal{D}^{\text{sec}}(\rho) + \mathcal{D}^{\text{nsec}}(\rho), \quad (\text{C.9})$$

where H_{LS} is the Lamb shift Hamiltonian, whose role is discussed in Section C.3, while $\mathcal{D}^{sec}(\rho)$ and $\mathcal{D}^{nsec}(\rho)$ are, respectively, the secular and the non-secular parts of the dissipator, the latter featuring terms oscillating at frequencies ν and 2ν .

With regards to $\mathcal{D}^{sec}(\rho)$, it is given by:

$$\mathcal{D}^{sec}(\rho) = \gamma_-^\theta \mathcal{L}[\tilde{\sigma}_+](\rho) + \gamma_+^\theta \mathcal{L}[\tilde{\sigma}_-](\rho) + \gamma_z^\theta \mathcal{L}[\tilde{\sigma}_z](\rho), \quad (\text{C.10})$$

where the Lindblad superoperator is $\mathcal{L}[\hat{X}](\rho) = \hat{X}\rho\hat{X}^\dagger - \{\rho, \hat{X}^\dagger\hat{X}\}/2$, with

$$\begin{aligned} \gamma_-^\theta &= 2\pi \left\{ C^4 J(\omega_L + \nu) n(\omega_L + \nu) + S^4 J(\omega_L - \nu) \right. \\ &\quad \left. \times [1 + n(\omega_L - \nu)] \right\}, \\ \gamma_+^\theta &= 2\pi \left\{ C^4 J(\omega_L + \nu) [1 + n(\omega_L + \nu)] + S^4 J(\omega_L - \nu) \right. \\ &\quad \left. \times n(\omega_L - \nu) \right\}, \\ \gamma_z^\theta &= 2\pi \left\{ S^2 C^2 J(\omega_L) [1 + 2n(\omega_L)] \right\}, \end{aligned} \quad (\text{C.11})$$

where $J(\omega)$ is the spectral density of the environment and $n(\omega) = 1/[e^{(\hbar\omega)/(k_B T)} - 1]$ is the average number of excitations in the bath at frequency ω , with k_B being the Boltzmann constant. The above coefficients can be rewritten as

$$\begin{aligned} \gamma_-^\theta &= C^4 \gamma_+ n_+ + S^4 \gamma_- (1 + n_-), \\ \gamma_+^\theta &= C^4 \gamma_+ (1 + n_+) + S^4 \gamma_- n_-, \\ \gamma_z^\theta &= S^2 C^2 \gamma_0 (1 + 2n_0), \end{aligned} \quad (\text{C.12})$$

where $\gamma_p = 2\pi J(\omega_L + p\nu)$ and $n_p = n(\omega_L + p\nu)$, where $p = \{-1, +1, 0\}$ (for any parameter l depending on p we use the shorthand notation $l_{-1} = l_-$ and $l_{+1} = l_+$). Because of the control field, the qubit experiences dephasing- and thermal-like dissipative effects already in the case of a zero-temperature bath ($n_p = 0$), as shown by the fact that also in this case all the γ_p^θ contribute to the dynamics and the steady state is not expected to be pure anymore.

The operator $\mathcal{D}^{nsec}(\rho)$ and its coefficients are reported in supplementary Section C.3. In Sec. C.1.4, we give some comments about when their effect cannot be neglected. A detailed analysis of the limits of validity of the secular approximation in our system can be found in Ref. [170].

C.1.3 The reference case: the fixed dissipator

In Sec. C.1.2, we have seen that, in the microscopic approach, the dissipator depends on the control field acting on the qubit. The FD approach consists in neglecting this dependence and in assuming that the dissipative part of the master equation is equal to the one in the absence of the control field, i.e., the qubit coupled to the environment is treated first, and this single entity is next coupled to the laser. The application of this procedure is well known in optimal control protocols. Recently, this approach has been used to determine the control Hamiltonian that counteracts a given dissipation [166]. In this context, we consider a density matrix evolving according to a general (Lindblad) master equation

$$\dot{\rho} = -\frac{i}{\hbar} [H, \rho] + \mathcal{D}^{fd}(\rho). \quad (\text{C.13})$$

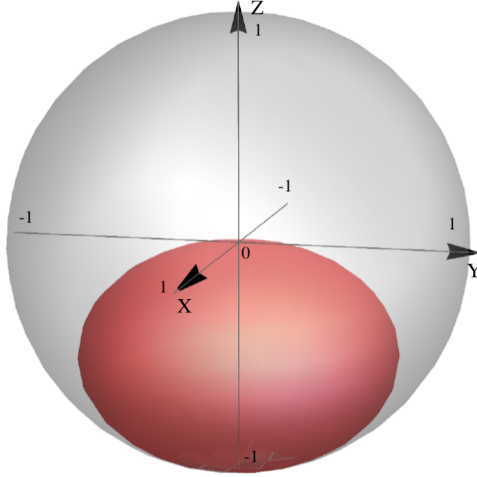


Figure C.1: Bloch sphere (gray) and steady-state ellipsoid (red). The components of the Bloch vector of an arbitrary state ρ are $r_x = 2\text{Re}[\rho_{eg}]$, $r_y = -2\text{Im}[\rho_{eg}]$, and $r_z = 2\rho_{ee} - 1$. The ellipsoid has been drawn by taking $T = 0$.

The set of stationary solutions $\dot{\rho}^{\text{fd}} = 0$, which are compatible with the fixed dissipator $\mathcal{D}^{\text{fd}}(\rho^{\text{fd}})$ can be computed by disregarding the coherent part. Since the coherent part of the master equation can not change the spectrum and then the purity of the state, the same must also be true for the dissipator [166, 116]. Then, the collection of stationary states ρ^{fd} must obey the relation:

$$\text{Tr}[(\rho^{\text{fd}})^{n-1}\mathcal{D}^{\text{fd}}(\rho^{\text{fd}})] = 0, \quad \forall n \in \{2, \dots, d\}, \quad (\text{C.14})$$

where d is the dimension of the Hilbert space. Thus, we have defined a (fixed) dissipator and a family of Hamiltonians. For any steady state, we can find the Hamiltonian H such that $\dot{\rho}^{\text{fd}} = 0$. Writing the steady state as $\rho^{\text{fd}} = \sum_{\alpha=1}^d \lambda_{\alpha} |\alpha\rangle\langle\alpha|$, it follows that

$$H = \hbar \sum_{\alpha, \beta: \lambda_{\alpha} \neq \lambda_{\beta}} \frac{i\langle\alpha|\mathcal{D}^{\text{fd}}(\rho^{\text{fd}})|\beta\rangle}{\lambda_{\alpha} - \lambda_{\beta}} |\alpha\rangle\langle\beta|. \quad (\text{C.15})$$

For the case of the qubit introduced in Sec. C.1.1, we only need to satisfy

$$\text{Tr}[\rho^{\text{fd}}\mathcal{D}^{\text{fd}}(\rho^{\text{fd}})] = 0.$$

In this model, at a given bath temperature T , the FD is equal to the dissipator one would obtain in the absence of the control field ($\Omega \rightarrow 0$). This can be obtained from the microscopic dissipator of Eq. (C.9) taking $\theta = 0$ and $\nu = \Delta$. In this limit, the decay rates of Eq. (C.12) tend to: $\gamma_{-}^0 = \gamma_{\text{fd}}n_{\text{fd}}$, $\gamma_{+}^0 = \gamma_{\text{fd}}(1 + n_{\text{fd}})$ and $\gamma_z^0 = 0$, where $\gamma_{\text{fd}} = 2\pi J(\omega_0)$ and $n_{\text{fd}} = n(\omega_0)$. The fixed dissipator is then of the form

$$D^{\text{fd}}(\rho) = \gamma_{\text{fd}}n_{\text{fd}}\mathcal{L}[\sigma_{+}](\rho) + \gamma_{\text{fd}}(1 + n_{\text{fd}})\mathcal{L}[\sigma_{-}](\rho). \quad (\text{C.16})$$

It follows that in the FD approach the steady state depends on γ_{fd} . To compute it, we use $H = H_S$ in Eq. (C.13), neglecting the Lamb shift. We observe that when it is present and not negligible, it could be taken into account by considering that it just leads to a different value of the parameter Δ . In this sense, in all the parts where the result depends only on the ratio Ω/Δ , the same result could be obtained by just changing Ω according to the change of Δ . In particular, in the

limit of flat spectrum, it is possible to see that the Lamb shift computed in this phenomenological framework is zero (see the Section C.3 for an explanation of how this can be found in the microscopic approach). The nonsecular terms that one could obtain using a microscopic derivation applied to the qubit coupled to the environment in the absence of the driving laser will not be considered here since the FDME is introduced on phenomenological grounds. The steady states can be then expressed in the σ_z basis in terms of some of its density matrix elements (hereafter we use the notation $\rho_{ij} = \langle i|\rho|j\rangle$) as (restoring the dependence on φ):

$$\begin{aligned}\rho_{ee}^{\text{fd}} &= \frac{n_{\text{fd}}}{1 + 2n_{\text{fd}}} + \frac{\Omega^2/(1 + 2n_{\text{fd}})}{\gamma_{\text{fd}}^2(1 + 2n_{\text{fd}})^2 + 4\Delta^2 + 2\Omega^2}, \\ \rho_{eg}^{\text{fd}} &= -\Omega \frac{2\Delta/(1 + 2n_{\text{fd}}) + i\gamma_{\text{fd}}}{\gamma_{\text{fd}}^2(1 + 2n_{\text{fd}})^2 + 4\Delta^2 + 2\Omega^2} e^{-i\varphi},\end{aligned}\quad (\text{C.17})$$

being, of course, for any ρ , $\rho_{gg} = 1 - \rho_{ee}$ and $\rho_{ge} = \rho_{eg}^*$. The FD steady solutions by varying the control field parameters, Ω , Δ and φ , are represented in Fig. C.1 (for $T = 0$) where they are shown to lie on the surface of an ellipsoid inside the Bloch sphere. This ellipsoid is a standard geometric structure in Nuclear Magnetic Resonance [54, 116, 120]. For $T \neq 0$, the steady states lie on a smaller ellipsoid inside the one depicted in Fig. C.1.

C.1.4 Reservoir engineering through microscopic master equation with structured environment

We present in this section the control of steady states by using the MME of Sec. C.1.2. In particular, we compare the steady-state solutions of the FDME with the ones provided by the MME to discuss how the control of the system is modified when the environment is used as a tool to suitably tailor the asymptotic states. We also compare some specific dynamics to highlight our results.

In the case of flat spectrum, it holds $\gamma_- = \gamma_+ = \gamma_0 = \gamma_{\text{fd}}$ and one can show the remarkable property that, under the approximation $n_- \approx n_+ \approx n_0 \approx n_{\text{fd}}$, the MME coincides exactly with the FDME (see the supplementary Section C.3 for a complete derivation). The steady states of the MME and of the FDME are thus the same for any T . In particular, in the secular limit, in the frame rotating at the laser frequency (after restoring the phase φ), the MME steady solutions are equal to the ones of Eq. (C.17) after discarding the terms containing γ_{fd} , which are indeed negligible in this limit. One can show that the geometric form of the steady-state solutions obtained by varying the control field parameters, Ω , Δ , and φ , corresponds to the very same ellipsoid of Fig. C.1. When nonsecular terms are added, the microscopic steady states coincide with the ones obtained with the FD, given in Eq. (C.17). We consider below the case of structured environments in which relevant differences can instead occur.

We consider in particular the MME in the secular regime, noting that this regime is typically encountered in several contexts such as quantum optics setups [20]. The steady state ρ^{sec} , which satisfies both $[\rho^{\text{sec}}, H_S + H_{LS}] = 0$ and $\mathcal{D}^{\text{sec}}(\rho^{\text{sec}}) = 0$, is

$$\rho^{\text{sec}} = \frac{\gamma_-^\theta}{\gamma_+^\theta + \gamma_-^\theta} |\phi_+\rangle\langle\phi_+| + \frac{\gamma_+^\theta}{\gamma_+^\theta + \gamma_-^\theta} |\phi_-\rangle\langle\phi_-|, \quad (\text{C.18})$$

where the superscript “sec” refers to the secular master equation. The collection of steady states that are obtained as functions of the control parameter θ and of the phase φ (once it is restored) describes a surface in the Bloch vector representation which is invariant under a rotation around the z axis.

We consider structured environments characterized by a spectral density varying notably around ω_L on the scale of the dressed frequency ν . In this scenario, even in the limit where the secular approximation holds, the microscopic approach provides target steady states that may be not close to the ones obtained with the FDME. In the Markovian limit, while in the FD case there is only one value of the spectral density that matters, the two additional sidebands at $\omega_L \pm \nu$ must be considered according to the microscopic derivation [see Eq. (C.11)].

When $n_+ \approx n_- \approx n_0 \approx n_{\text{fd}}$, Eq. (C.18) gives (after restoring the phase φ)

$$\begin{aligned}\rho_{ee}^{\text{sec}} &\approx \frac{n_{\text{fd}}}{1 + 2n_{\text{fd}}} + \frac{S^2 C^2}{1 + 2n_{\text{fd}}} \frac{S^2 \gamma_- + C^2 \gamma_+}{S^4 \gamma_- + C^4 \gamma_+}, \\ \rho_{eg}^{\text{sec}} &\approx \frac{SC}{1 + 2n_{\text{fd}}} \frac{S^4 \gamma_- - C^4 \gamma_+}{S^4 \gamma_- + C^4 \gamma_+} e^{-i\varphi}.\end{aligned}\tag{C.19}$$

Exploiting the dependence on the two frequencies $\omega_L \pm \nu$ opens the possibility for taking profit from reservoir engineering. It indeed allows one to deform the ellipsoid of Fig. (C.1), thus modifying the family of target states. For instance, one of the possible consequences is that the equator of the ellipsoid can be broadened, allowing one to get higher values for the absolute value of the nondiagonal elements of the density matrix, as it is always possible to reduce the weight of the smaller term in Eq. (C.18) and then to obtain purer states. We observe that $2|\rho_{eg}|$ is a measure of the resource named quantum coherence [179].

The case of zero temperature

We start the analysis with the zero-temperature case. The scenarios where $J(\omega_L + \nu) \gtrless J(\omega_L - \nu)$ are compared with the flat spectral density case in Fig. C.2, where the components x and z of the Bloch vector of the steady states, $r_x = 2 \text{Re}[\rho_{eg}]$ and $r_z = 2\rho_{ee} - 1$, are plotted. In Fig. C.2(a), we consider fixed values for the ratio $\mu = \gamma_-/\gamma_+ = J(\omega_L - \nu)/J(\omega_L + \nu)$ for all values of the dressed energy. This analysis permits to visualize for any value of the control parameters θ of Eq. (C.7) (or equivalently of Ω/Δ) and φ how much the steady states differ in the two approaches for a given μ . In the two panels, all the parts of the different lines are obtained by considering a fixed positive Δ and using Ω , assuming values ≥ 0 , and φ , being equal to 0 or π , as control parameters. In particular, with respect to the FDME, purer states can be obtained ($|\rho_{eg}|$ may become closer to the maximum allowed value of $1/2$) and even the population inversion can be reached. We observe that the FDME is considered in the case when its dependence on γ_{fd} is negligible, and so the steady state practically coincides with the microscopic secular one in the limit of flat spectrum (or more in general when $\mu = 1$).

As an example, let us consider the case where the target state reached using the FD dynamics at zero temperature is one of the states with maximally allowed $|\rho_{eg}|$, that is, a point that lies on its equator [166]. This class of states is obtained using $\Omega = \pm\sqrt{2}\Delta$ and, written in the Bloch form, is $\vec{r}_{\text{mc}} = \{\mp \cos \varphi/\sqrt{2}, \mp \sin \varphi/\sqrt{2}, -1/2\}$. We focus

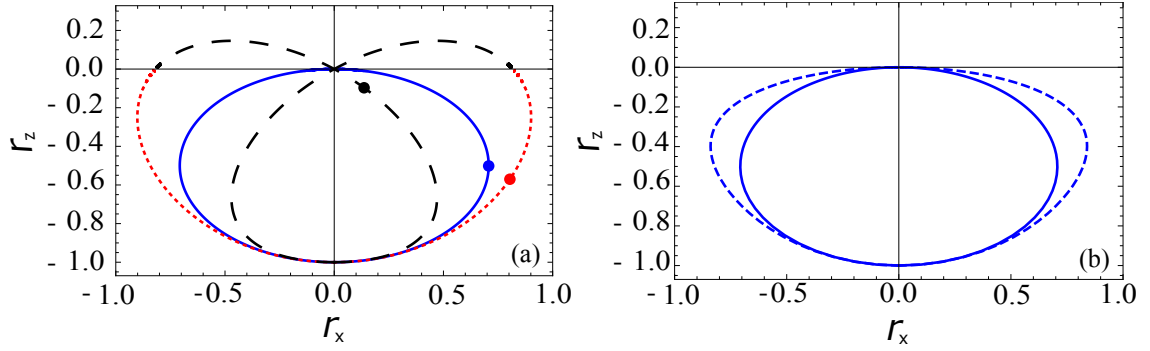


Figure C.2: Families of steady states (components x and z of the Bloch vector, r_x and r_z) determined from the FDME (the dependence on γ_{fd} is assumed to be negligible) and from the secular MME by varying the control field parameters Ω , assuming values ≥ 0 , and φ , being equal to 0 or π , for a positive fixed value of Δ . (a) The FDME case is represented by the blue solid line while the red dotted and the black dashed lines represent the microscopic steady states when $\mu = \gamma_-/\gamma_+$ is kept fixed for any ν and equal to, respectively, 0.1 and 10. The three enlightened points represent the three steady states obtained by using $\Omega = \sqrt{2}\Delta$ and $\varphi = \pi$, which, in the FDME case, gives the maximum allowed $|\rho_{eg}|$. (b) The family of stationary states has been calculated either assuming the FDME (solid line) or the Lorentzian density of states given in Eq. (C.20) with $\omega_c = \omega_0$ and $\lambda = \Delta$ (dashed line).

on the case $\Omega = \sqrt{2}\Delta$ and $\varphi = \pi$, obtaining then $\vec{r}_{\text{mc}} = \{1/\sqrt{2}, 0, -1/2\}$. On the other hand, in the presence of structured reservoir, taking $\Omega = \sqrt{2}\Delta$ and $\varphi = \pi$, we would end up in $\vec{r} \simeq \{0.805, 0, -0.569\}$ using $\mu = 0.1$ or in $\vec{r} \simeq \{0.134, 0, -0.095\}$ using $\mu = 10$. The three states, reached with the same control field, are visualized with points in Fig. C.2(a). The distances between these points clearly point out how much could be the error due to using the FDME to predict the steady state in a given control protocol.

In order to treat a specific physical scenario where μ varies when the control field parameters are changed, we now consider the case in which the spectral density has the Lorentzian profile

$$J_{\text{Lor}}(\omega) = \frac{\gamma_l}{2\pi} \frac{\lambda^2}{(\omega - \omega_c)^2 + \lambda^2}, \quad (\text{C.20})$$

where the parameter λ defines the width of the curve and ω_c its center. We consider values of λ much greater than γ_l , such that the Markovian approximation used for the derivation of the MME is satisfied. The flat spectral density case is recovered in the limit $\lambda \rightarrow \infty$. Using Eq. (C.20), one can expect that only in some parts of the parameter space the deformation is relevant. On the tails of the curve, we fall for instance in something similar to the flat spectral density case, which gives the same results of the FDME. The differences in the case of a Lorentzian spectral density are depicted in Fig. C.2(b), where we have assumed that the dependence on γ_{fd} of the FDME steady solutions is negligible and calculated the steady states by varying Ω/Δ in the case of a fixed Lorentzian, with $\lambda = \Delta$ (we have fixed a positive value for Δ and varied Ω , assuming values ≥ 0 , and φ , being equal to 0 or π).

We have numerically compared the secular MME curve in Fig. C.2(b) with the one obtained by adding the nonsecular terms at zero temperature and for values of γ_{fd} much smaller than Δ . In general, the nonsecular curve is very close to the MME

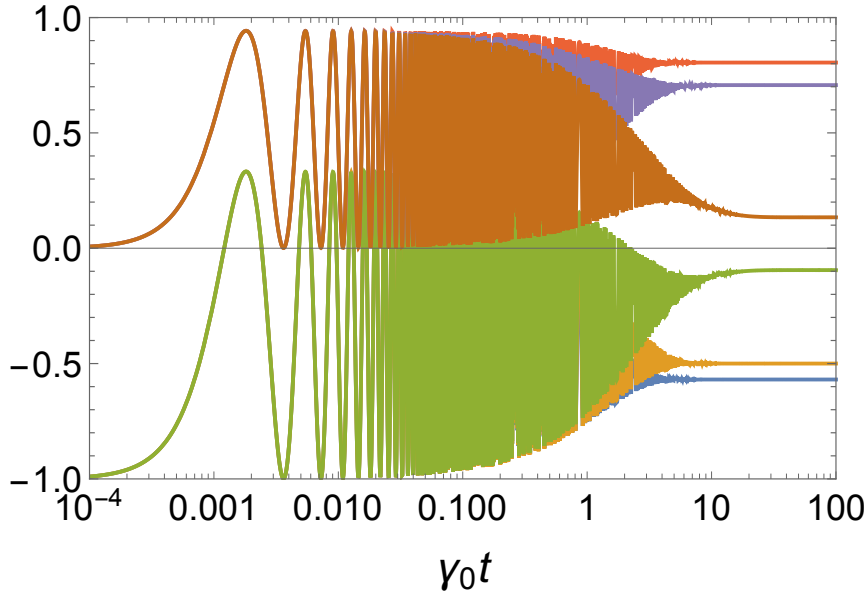


Figure C.3: The Bloch vector components r_x and r_z , as a function of time (in units of γ_0^{-1} and in logarithmic scale). The initial state is $|g\rangle$, $\Omega = \sqrt{2}\Delta$, $\varphi = \pi$, and $\gamma_0 = 0.001\Delta$. Three cases are considered: the MME with $\mu = 0.1$ ($\gamma_- = 0.2\gamma_0$ and $\gamma_+ = 2\gamma_0$), the FDME with $\gamma_{\text{fd}} = \gamma_0$, and the MME with $\mu = 10$ ($\gamma_- = 2\gamma_0$ and $\gamma_+ = 0.2\gamma_0$). All the r_x curves start from 0 and reach the larger value for the case $\mu = 0.1$, the intermediate one for the FDME, and the lower one for the case $\mu = 10$. All the r_z curves start from -1 and reach the larger value (in modulus) for the case $\mu = 0.1$, the intermediate one (in modulus) for the FDME, and the lower one (in modulus) for the case $\mu = 10$. The fixed dissipator dynamics is practically identical to the one of the MME in the limit of flat spectrum, $\gamma_- = \gamma_+ = \gamma_0 = \gamma_{\text{fd}}$ ($\mu = 1$).

curve except when one approaches the origin of the axis, for values of Ω much larger than Δ . For instance, for $\gamma_{\text{fd}}/\Delta = 0.001$ we observe differences for Ω/Δ greater than 100. When this ratio overcomes a given value, we observe steady values of r_x different from zero, with r_z becoming positive but very close to zero, and at a certain point the nonsecular MME starts to predict nonphysical steady states. The occurrence of differences between secular and nonsecular master equations has been discussed in Ref. [170].

In order to show how different steady states for the same values of the control field parameters are dynamically obtained, we report in Fig. C.3 the time evolution of r_x and r_z for the same cases of the points highlighted in Fig. C.2(a), obtained with $\Omega = \sqrt{2}\Delta$ and $\varphi = \pi$. In particular, we choose $\gamma_- = 0.2\gamma_0$ and $\gamma_+ = 2\gamma_0$ for the case $\mu = 0.1$, the FDME for the fixed dissipator case ($\mu = 1$), and $\gamma_- = 2\gamma_0$ and $\gamma_+ = 0.2\gamma_0$ for the case $\mu = 10$. The FDME dynamics is practically identical to the one of the MME in the limit of flat spectrum, $\gamma_- = \gamma_+ = \gamma_0 = \gamma_{\text{fd}}$ ($\mu = 1$) for values of γ_{fd} small enough, as in this case where $\gamma_{\text{fd}} = 0.001\Delta$. The qubit is initially in the ground state $|g\rangle$. The values of the rates γ_p are chosen without referring to a specific spectral density (no Lamb shift is considered).

We have then shown that, in general, using the FDME can cause a lack of accuracy in determining the steady state, which would be detrimental in a quantum control

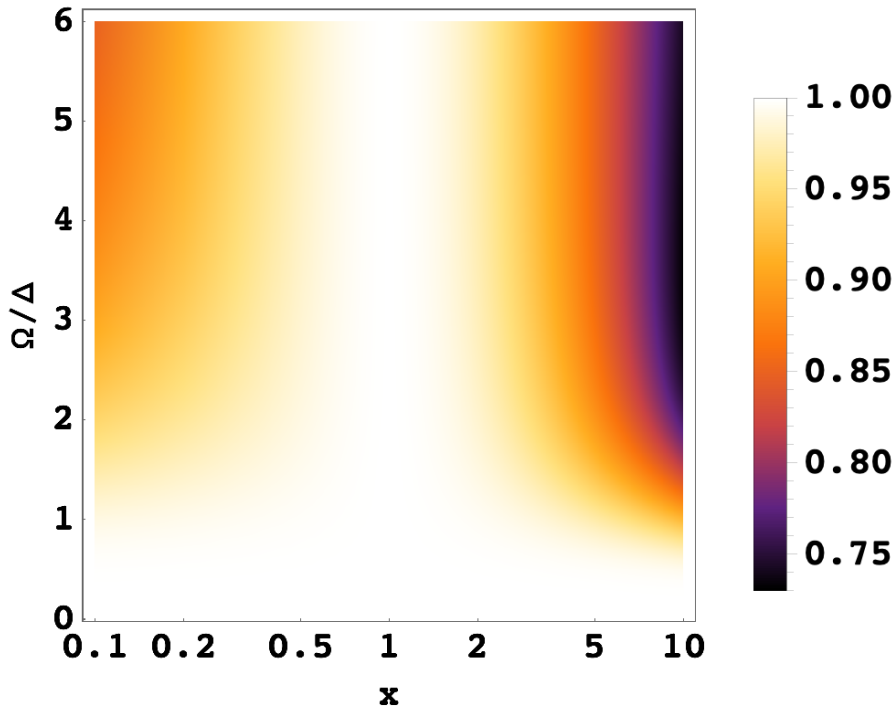


Figure C.4: Fidelity between the FDME steady states (their dependence on γ_{fd} is assumed to be negligible) and the ones obtained with the secular MME by releasing the flat-spectrum assumption, as a function of the control field parameter Ω/Δ and of the ratio $\mu = \gamma_-/\gamma_+$ (in logarithmic scale).

protocol. This effect can be enlightened by considering the distance between the stationary state induced by a structured spectral density, as predicted by the MME, and the one given by the FDME as a function of the control field parameter Ω/Δ (this distance does not depend on φ). In Fig. C.4 we use the fidelity as a measure of such distance. For two arbitrary states ρ and σ it is defined as $\text{Tr}[\sqrt{\sqrt{\rho}\sigma\sqrt{\rho}}]^2$. It is important to stress that a fidelity of the order of $3/4$ is already an indication of a dramatic difference between two states. For instance, the fidelity between a two-qubit Bell state and the state obtained from it by removing the coherence is $1/\sqrt{2}$. In Fig. C.4, an important discrepancy may be observed for $\Omega/\Delta \gtrsim 1$. In particular, for a given value of Ω/Δ , smaller values of fidelity are obtained when μ moves away from 1. The behavior for $\Omega/\Delta < 1$ is instead reminiscent of the fact that for small angles θ the microscopic dissipator tends to the FD one, as shown before Eq. (C.16).

One may raise doubts about the freedom in the choice of the spectral density. In particular, the Markovian approximation could break down for some frequency region. Here, we remark that the results of this section hold for values of the system-bath coupling such that we are well behind the weak-coupling limit and the Markovian character of the dynamics is warranted. In any case, even for an intermediate coupling constant, we are interested in the stationary regime that takes place long after all the possible non-Markovian effects have been washed out.

The case of non zero temperature

According to what has been said so far, a structured spectral density allows for a broader family of target states but, at the same time, would typically give solutions that are distinct from the ellipsoid predicted by the FDME. We now show that zero-temperature FDME steady states can be recovered in the case of a structured environment by exploiting tailored thermal effects.

To this aim, we consider the FDME steady states of Eq. (C.17) in the limit when the terms depending on γ_{fd} are negligible (being always $n_- \approx n_+ \approx n_0 \approx n_{\text{fd}}$):

$$\begin{aligned}\rho_{ee}^{\text{sec}}(\mu = 1) &\approx \frac{n_{\text{fd}}}{1 + 2n_{\text{fd}}} + \frac{\Omega^2/(1 + 2n_{\text{fd}})}{4\Delta^2 + 2\Omega^2}, \\ \rho_{eg}^{\text{sec}} &\approx -\frac{\Omega\Delta/(1 + 2n_{\text{fd}})}{2\Delta^2 + \Omega^2}e^{-i\varphi},\end{aligned}\tag{C.21}$$

We indicate them with superscript “sec” since they coincide with the steady states of the secular MME [see Eq. (C.19)] in the limit of flat spectrum ($\mu = 1$). We compare them at zero temperature with the general case of Eq. (C.19) that depends both on n_{fd} and on the ratio $\mu = \gamma_-/\gamma_+$, and look, for any given μ , for the existence of solutions of

$$\begin{aligned}\rho_{ee}^{\text{sec}}(\mu = 1, n_{\text{fd}} = 0) &= \rho_{ee}^{\text{sec}}(\mu, n_{\text{fd}}) \\ \rho_{eg}^{\text{sec}}(\mu = 1, n_{\text{fd}} = 0) &= \rho_{eg}^{\text{sec}}(\mu, n_{\text{fd}}).\end{aligned}\tag{C.22}$$

The solution of both equations is given by

$$n_{\text{fd}}(\mu) = \frac{S^4 C^4 (1 - \mu)}{(C^2 - S^2)(C^4 + \mu S^4)}.\tag{C.23}$$

Solutions corresponding to physical values of n_{fd} (that is $n_{\text{fd}} \geq 0$) only appear for $0 \leq \mu \leq 1$, which is easy to understand looking at Fig. C.2(a). In fact, thermal effects are expected to reduce the value of $|\rho_{eg}|$ of any state, making it impossible to move from the black line ($\mu = 10$) to the blue one ($\mu = 1$). The behavior of $n_{\text{fd}}(\mu = 0.1)$ is plotted in Fig. C.5 as a function of the control field parameter Ω/Δ . The needed thermal correction is very small as long as $\Omega < \Delta$, as the same argument used to explain the behavior observed in Fig. C.4 holds.

C.2 Discussion and conclusions

Master equations are a powerful tool to analyze the dissipative dynamics of quantum systems. They are usually obtained by making a series of assumptions that need to be fulfilled and to be verified in realistic setups, as, in general, exact solutions are not available. They are often introduced on the basis on phenomenological assumptions. Here, we have derived a microscopic master equation for a driven qubit and compared it with the fixed dissipator model, which is widely used, especially in the quantum control community, as it allows one to explore the behavior of entire families of control Hamiltonians in a simple way. We have found that, in the weak-coupling regime, the steady states of the two approaches can be very different in the case of a structured environment, while they are practically identical for a flat spectrum.

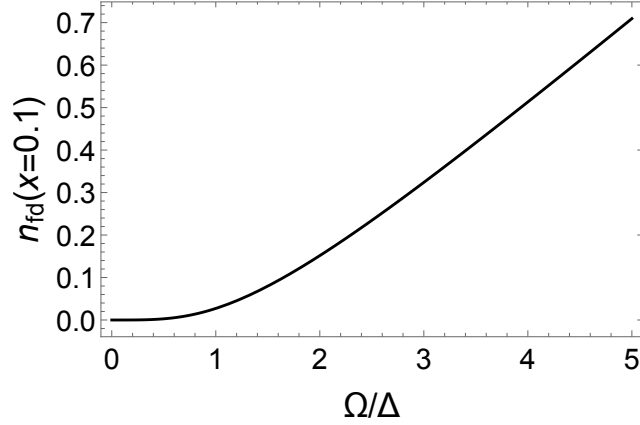


Figure C.5: Thermal factor $n_{\text{fd}}(\mu = 0.1)$ as a function of Ω/Δ necessary to compensate the effects due to a ratio $\mu = \gamma_-/\gamma_+ = 0.1$ in order for the MME steady state at the temperature corresponding to $n_{\text{fd}}(\mu = 0.1)$ to end up in the zero - temperature flat-spectrum ellipsoid formed by the (approximated) FDME steady states.

In conclusion, considering the simplest case of a driven qubit, we have assessed the limit of validity of the phenomenological approach for the specific task on asymptotic timescales. We have explored the possibility of implementing reservoir engineering techniques to widen the family of target states, which are correctly predicted by using microscopic master equations.

Quantum control protocols most often use time-dependent fields, implying time-dependent Rabi frequency, detuning, and phase as control parameters. For slowly varying parameters, one expects that the FDME and MME still coincide for a flat environment spectrum and that the difference between them still persists for structured environments. The expected rich variety of target states resulting from structured environments could then be exploited using microscopic models in quantum control and reservoir engineering schemes.

C.3 Derivation of the microscopic master equation

In this section, we derive the microscopic master equation of the driven qubit, presenting its various parts. Using Eq. (C.8), in the interaction picture with respect to $H_S + H_E$, the interaction Hamiltonian of Eq. (C.5) reads

$$\tilde{H}_I(t) = B(t) \left(f_+^t \tilde{\sigma}_+ + f_-^t \tilde{\sigma}_- + f_z^t \tilde{\sigma}_z \right), \quad (\text{C.24})$$

with $B(t) = \sum_k \hbar(g_k a_k e^{-i\omega_k t} + g_k^* a_k^\dagger e^{i\omega_k t})$ and where

$$\begin{aligned} f_+^t &= [C^2 e^{i(\omega_L t + \varphi)} - S^2 e^{-i(\omega_L t + \varphi)}] e^{i\nu t}, \\ f_-^t &= [C^2 e^{-i(\omega_L t + \varphi)} - S^2 e^{i(\omega_L t + \varphi)}] e^{-i\nu t}, \\ f_z^t &= SC[e^{i(\omega_L t + \varphi)} + e^{-i(\omega_L t + \varphi)}]. \end{aligned} \quad (\text{C.25})$$

The operators entering the master equation are multiplied by $f_i^t f_j^{t-s}$, with $i, j = +, -, z$. Thus, there will be secular terms for $\{i, j\}$ such that $f_i^t = f_j^{t*}$ and nonsecular

terms in all other cases. In general, the products $f_i^t f_j^{t-s}$ may have parts oscillating at the laser frequency $e^{\pm 2i\omega_L t}$. For instance,

$$f_+^t f_+^{t-s} = [C^4 e^{i[\omega_L(2t-s)+2\varphi]} + S^4 e^{-i[\omega_L(2t-s)+2\varphi]} - 2C^2 S^2 \cos \omega_L s] e^{i\nu(2t-s)}. \quad (\text{C.26})$$

On the basis of the condition assumed in Sec. C.1.1, $\omega_L \gg \Delta, \Omega$, we note that the first two fast-oscillating terms in Eq. (C.26) can be neglected. We observe that neglecting this kind of terms is completely equivalent to obtain the master equation writing the interaction Hamiltonian in rotating wave approximation:

$$H_I = \sum_k \hbar [g_k a_k e^{i(\omega_L t + \varphi)} \sigma_+ + g_k^* a_k^\dagger e^{-i(\omega_L t + \varphi)} \sigma_-]. \quad (\text{C.27})$$

In this limit, the products linked to the secular terms

$$\begin{aligned} f_-^t f_+^{t-s} &\approx e^{-i\nu s} [C^4 e^{-i\omega_L s} + S^4 e^{i\omega_L s}], \\ f_+^t f_-^{t-s} &\approx e^{i\nu s} [C^4 e^{i\omega_L s} + S^4 e^{-i\omega_L s}], \\ f_z^t f_z^{t-s} &\approx 2S^2 C^2 \cos \omega_L s, \end{aligned} \quad (\text{C.28})$$

determine the coefficients of Eq. (C.11). Nonsecular terms are determined by the products

$$\begin{aligned} f_+^t f_+^{t-s} &\approx -2C^2 S^2 e^{i\nu(2t-s)} \cos \omega_L s, \\ f_+^t f_z^{t-s} &\approx CS(C^2 e^{i\omega_L s} - S^2 e^{-i\omega_L s}) e^{i\nu t}, \\ f_z^t f_+^{t-s} &\approx e^{i\nu(t-s)} CS(C^2 e^{-i\omega_L s} - S^2 e^{i\omega_L s}), \end{aligned} \quad (\text{C.29})$$

together with $f_-^t f_-^{t-s} = (f_+^t f_+^{t-s})^*$, $f_-^t f_z^{t-s} = (f_+^t f_z^{t-s})^*$, and $f_z^t f_-^{t-s} = (f_z^t f_+^{t-s})^*$. The factors $e^{\pm i\nu t}$ and $e^{\pm 2i\nu t}$ are taken out when one moves back to the Schrödinger picture. We indicate with $\overline{f_i^t f_j^{t-s}}$ the products $f_i^t f_j^{t-s}$ after the elimination of the factors $e^{\pm i\nu t}$ and $e^{\pm 2i\nu t}$ and, taking the continuum limit, we introduce the spectral density $J(\omega) = \sum_k |g_k|^2 \delta(\omega - \omega_k)$, such that the trace over the bath's degrees of freedom is transformed into an integral over all the frequencies. The Born-Markov master equation, assuming a factorized initial condition for the system and its bath, is then given by [20, 69]

$$\begin{aligned} \dot{\rho} = & -\frac{i}{\hbar} [H_S, \rho] + \frac{1}{\hbar^2} \sum_{i,j=+,-,z} \int_0^\infty ds \\ & \left[\overline{f_i^{t*} f_j^{t-s}} \langle B(t) B(t-s) \rangle (\tilde{\sigma}_j \rho \tilde{\sigma}_i^\dagger - \tilde{\sigma}_i^\dagger \tilde{\sigma}_j \rho) + H.c. \right], \end{aligned} \quad (\text{C.30})$$

where H.c. denotes Hermitian conjugation and the bath correlation functions, taking a thermal equilibrium state ρ_B at temperature T , are given by

$$\text{Tr}_B \{ B(t) B(t-s) \rho_B \} = \hbar^2 \int_0^\infty d\omega J(\omega) [(1 + n(\omega)) e^{-i\omega s} + n(\omega) e^{i\omega s}]. \quad (\text{C.31})$$

The explicit development of Eq. (C.30) leads to Eq. (C.9). In particular, in order to calculate the coefficients of the master equation, in the Markovian limit, one makes use of the identity

$$\int_0^\infty e^{\pm i\varepsilon t} dt = \pi \delta(\varepsilon) \pm i\mathcal{P} \frac{1}{\varepsilon}, \quad (\text{C.32})$$

where $\delta(\varepsilon)$ is the Dirac δ function and \mathcal{P} denotes the Cauchy principal value.

The Lamb shift Hamiltonian of Eq. (C.9) is given by

$$H_{LS} = \hbar[s_+^\theta \tilde{\sigma}_+ \tilde{\sigma}_- + s_-^\theta \tilde{\sigma}_- \tilde{\sigma}_+ + s_z^\theta \tilde{\sigma}_z^2], \quad (\text{C.33})$$

where

$$\begin{aligned} s_+^\theta &= \mathcal{P} \int_0^\infty d\omega J(\omega) \left[\frac{C^4(1+n(\omega))}{(\omega_L + \nu) - \omega} - \frac{S^4 n(\omega)}{(\omega_L - \nu) - \omega} \right], \\ s_-^\theta &= \mathcal{P} \int_0^\infty d\omega J(\omega) \left[\frac{S^4(1+n(\omega))}{(\omega_L - \nu) - \omega} - \frac{C^4 n(\omega)}{(\omega_L + \nu) - \omega} \right], \\ s_z^\theta &= \mathcal{P} \int_0^\infty d\omega J(\omega) \frac{S^2 C^2}{\omega_L - \omega}. \end{aligned} \quad (\text{C.34})$$

We observe that it holds $[H_S, H_{LS}] = 0$.

As for the nonsecular part $\mathcal{D}^{\text{nsec}}(\rho)$, we have

$$\begin{aligned} \mathcal{D}^{\text{nsec}}(\rho) &= (\gamma_{++}^\theta + i s_{++}^\theta) \tilde{\sigma}_+ \rho \tilde{\sigma}_+ + (\gamma_{+z}^\theta + i s_{+z}^\theta) (\tilde{\sigma}_+ \tilde{\sigma}_z \rho - \tilde{\sigma}_z \rho \tilde{\sigma}_+) \\ &\quad + (\gamma_{-z}^\theta + i s_{-z}^\theta) (\tilde{\sigma}_- \tilde{\sigma}_z \rho - \tilde{\sigma}_z \rho \tilde{\sigma}_-) + (\gamma_{z+}^\theta + i s_{z+}^\theta) (\tilde{\sigma}_z \tilde{\sigma}_+ \rho - \tilde{\sigma}_+ \rho \tilde{\sigma}_z) \\ &\quad + (\gamma_{z-}^\theta + i s_{z-}^\theta) (\tilde{\sigma}_z \tilde{\sigma}_- \rho - \tilde{\sigma}_- \rho \tilde{\sigma}_z) + \text{H.c.}, \end{aligned} \quad (\text{C.35})$$

where the various coefficients γ_{ij}^θ and s_{ij}^θ can be computed by explicitly developing Eq. (C.30):

$$\begin{aligned} \gamma_{++}^\theta &= -\frac{1}{2} C^2 S^2 (\gamma_-(1+2n_-) + \gamma_+(1+2n_+)), \\ \gamma_{z+}^\theta &= -\frac{1}{2} C S [\gamma_+ n_+ C^2 - \gamma_-(1+n_-) S^2], \\ \gamma_{z-}^\theta &= -\frac{1}{2} C S [\gamma_+(1+n_+) C^2 - \gamma_- n_- S^2], \\ \gamma_{+z}^\theta &= -\frac{1}{2} \gamma_0 C S [(1+n_0) C^2 - n_0 S^2], \\ \gamma_{-z}^\theta &= -\frac{1}{2} \gamma_0 C S [n_0 C^2 - (1+n_0) S^2], \end{aligned} \quad (\text{C.36})$$

and

$$\begin{aligned} s_{++}^\theta &= -\mathcal{P} \int_0^\infty d\omega J(\omega) C^2 S^2 \left[\frac{1+2n(\omega)}{(\omega_L - \nu) - \omega} - \frac{1+2n(\omega)}{(\omega_L + \nu) - \omega} \right], \\ s_{z+}^\theta &= \mathcal{P} \int_0^\infty d\omega J(\omega) C S \left[\frac{S^2(1+n(\omega))}{(\omega_L - \nu) - \omega} + \frac{C^2 n(\omega)}{(\omega_L + \nu) - \omega} \right], \\ s_{z-}^\theta &= -\mathcal{P} \int_0^\infty d\omega J(\omega) C S \left[\frac{S^2 n(\omega)}{(\omega_L - \nu) - \omega} + \frac{C^2(1+n(\omega))}{(\omega_L + \nu) - \omega} \right], \\ s_{+z}^\theta &= -\mathcal{P} \int_0^\infty d\omega J(\omega) C S \left[\frac{C^2 + n(\omega)}{\omega_L - \omega} \right], \\ s_{-z}^\theta &= \mathcal{P} \int_0^\infty d\omega J(\omega) C S \left[\frac{S^2 + n(\omega)}{\omega_L - \omega} \right], \end{aligned} \quad (\text{C.37})$$

For each pair of i, j in Eq. (C.30) the part of the integrals involving the δ function, gives us the decay rates of Eq. (C.11) when $i = j$ and the ones of Eq. (C.36) when $i \neq j$, for any spectral density. The principal part in Eq. (C.32) leads to the Lamb shift Hamiltonian of Eq. (C.33). Note that the subscripts of γ_i^θ , s_i^θ , γ_{ij}^θ , and s_{ij}^θ are chosen independently of the actual values of i and j in Eq. (C.30), leading to the various terms where these parameters appear.

It can be shown (see for instance Ref. [103]) that, in the case of a flat spectral density, all the terms deriving from the principal part of Eq. (C.32) vanish. This can be obtained by first performing the integrals by using a Lorentzian spectral density and by then taking the width of this Lorentzian to infinity. In the case of a non-flat spectrum, we treat these terms, taking again the Lorentzian spectral density. In the secular MME, the terms in the Lamb shift Hamiltonian lead to nothing but energy shift, and then their effect is not relevant for the steady states. Instead, the contribution of the terms deriving from the principal part of Eq. (C.32) appearing in the nonsecular MME [see Eq. (C.37)], in general, cannot be neglected (see comment in Sec. C.1.4 on the comparison between secular and nonsecular master equations).

Finally, keeping the terms of Eq. (C.35) in Eq. (C.9), it is possible to show that in the flat-spectrum limit, under the approximation $n_- \approx n_+ \approx n_0 \approx n_{\text{fd}}$, the nonsecular MME gives exactly the same result as FDME, i.e, using $H = H_S$, Eq. (C.9) becomes Eq. (C.13), for any γ_{fd} .

Bibliography

- [1] Cavity QED approaches to quantum information processing and quantum computing. https://qist.lanl.gov/pdfs/rm_intro.pdf, 2004.
- [2] Jérôme Abadie *et al.* A gravitational wave observatory operating beyond the quantum shot-noise limit. *Nature Physics*, 7(12):962–965, 2011.
- [3] Benjamin P. Abbott *et al.* Prospects for observing and localizing gravitational-wave transients with advanced ligo, advanced virgo and kagra. *Living Reviews in Relativity*, 23(1):3, 2020.
- [4] Antonio Acín, Immanuel Bloch, Harry Buhrman, Tommaso Calarco, Christopher Eichler, Jens Eisert, Daniel Esteve, Nicolas Gisin, Steffen J Glaser, Fedor Jelezko, Stefan Kuhr, Maciej Lewenstein, Max F Riedel, Piet O Schmidt, Rob Thew, Andreas Wallraff, Ian Walmsley, and Frank K Wilhelm. The quantum technologies roadmap: a european community view. *New Journal of Physics*, 20(8):080201, 2018.
- [5] Moteb M Alqahtani, Mark S Everitt, and Barry M Garraway. Cavity qed photons for quantum information processing. *Journal of Physics B: Atomic, Molecular and Optical Physics*, 55(18):184004, 2022.
- [6] Joseph H. Apfel. Optical coating design with reduced electric field intensity. *Applied Optics*, 16(7):1880, July 1977.
- [7] Koji Azuma, Kiyoshi Tamaki, and Hoi-Kwong Lo. All-photonic quantum repeaters. *Nature Communications*, 6, 2015.
- [8] Mary Banning. Practical methods of making and using multilayer filters. *J. Opt. Soc. Am.*, 37(10):792–797, October 1947.
- [9] Ladislaus Alexander Banyai and Stephan W Koch. *Semiconductor quantum dots*, volume 2. World Scientific, 1993.
- [10] Thomas D Barrett, Dustin Stuart, Oliver Barter, and Axel Kuhn. Nonlinear zeeman effects in the cavity-enhanced emission of polarised photons. *New Journal of Physics*, 20(7):073030, 2018.
- [11] Bruno Bellomo, Riccardo Messina, Didier Felbacq, and Mauro Antezza. Quantum systems in a stationary environment out of thermal equilibrium. *Phys. Rev. A*, 87:012101, Jan 2013.

- [12] Charles H. Bennett, Gilles Brassard, Claude Crépeau, Richard Jozsa, Asher Peres, and William K. Wootters. Teleporting an unknown quantum state via dual classical and Einstein-Podolsky-Rosen channels. *Phys. Rev. Lett.*, 70:1895–1899, 1993.
- [13] K. Bergmann, H. Theuer, and B. W. Shore. Coherent population transfer among quantum states of atoms and molecules. *Rev. Mod. Phys.*, 70:1003–1025, 1998.
- [14] P. Bertet, S. Osnaghi, P. Milman, A. Auffeves, P. Maioli, M. Brune, J. M. Raimond, and S. Haroche. Generating and probing a two-photon fock state with a single atom in a cavity. *Phys. Rev. Lett.*, 88:143601, 2002.
- [15] Alexandre Blais, Steven M. Girvin, and William D. Oliver. Quantum information processing and quantum optics with circuit quantum electrodynamics. *Nature Physics*, 16(3):247–256, 2020.
- [16] K. J. Blow, Rodney Loudon, Simon J. D. Phoenix, and T. J. Shepherd. Continuum fields in quantum optics. *Phys. Rev. A*, 42:4102–4114, Oct 1990.
- [17] J. Borregaard and A. S. Sørensen. Near-heisenberg-limited atomic clocks in the presence of decoherence. *Phys. Rev. Lett.*, 111:090801, 2013.
- [18] Sergey I. Bozhevolnyi and Jacob B. Khurgin. The case for quantum plasmonics. *Nature Photonics*, 11(7):398–400, Jul 2017.
- [19] Manuel Brekenfeld, Dominik Niemietz, Joseph Dale Christesen, and Gerhard Rempe. A quantum network node with crossed optical fibre cavities. *Nature Physics*, 16(6):647+, 2020.
- [20] H. P. Breuer and F. Petruccione. *The theory of open quantum systems*. Oxford University Press, Great Clarendon Street, 2002.
- [21] M.L. Brongersma and P.G. Kik. *Surface Plasmon Nanophotonics*. Springer Series in Optical Sciences. Springer Netherlands, 2007.
- [22] M. Brune, P. Nussenzveig, F. Schmidt-Kaler, F. Bernardot, A. Maali, J. M. Raimond, and S. Haroche. From lamb shift to light shifts: Vacuum and subphoton cavity fields measured by atomic phase sensitive detection. *Phys. Rev. Lett.*, 72:3339–3342, 1994.
- [23] David C. Burnham and Donald L. Weinberg. Observation of simultaneity in parametric production of optical photon pairs. *Phys. Rev. Lett.*, 25:84–87, 1970.
- [24] Angela Sara Cacciapuoti, Marcello Caleffi, Francesco Tafuri, Francesco Saverio Cataliotti, Stefano Gherardini, and Giuseppe Bianchi. Quantum internet: Networking challenges in distributed quantum computing. *IEEE Network*, 34(1):137–143, 2020.
- [25] Yong-Jing Cai, Ming Li, Xi-Feng Ren, Chang-Ling Zou, Xiao Xiong, Hua-Lin Lei, Bi-Heng Liu, Guo-Ping Guo, and Guang-Can Guo. High-visibility on-chip quantum interference of single surface plasmons. *Phys. Rev. Appl.*, 2:014004, Jul 2014.

- [26] Howard J. Carmichael. *Statistical Methods in Quantum Optics*. Springer Berlin, Heidelberg, 1999.
- [27] H. B. G. Casimir. On the attraction between two perfectly conducting plates. *Proc. K. Ned. Akad. Wet.*, 51:793, 1948.
- [28] Darrick E. Chang, Anders S. Sørensen, Eugene A. Demler, and Mikhail D. Lukin. A single-photon transistor using nanoscale surface plasmons. *Nature Physics*, 3(11):807–812, August 2007.
- [29] G. Chiribella, G. M. D’Ariano, P. Perinotti, and M. F. Sacchi. Efficient use of quantum resources for the transmission of a reference frame. *Phys. Rev. Lett.*, 93:180503, 2004.
- [30] J. I. Cirac, L. M. Duan, and P. Zoller. Quantum optical implementation of quantum information processing. In Francesco De Martini and Christopher Monroe, editors, *Experimental quantum computation and information*, volume 148, page 263. IOS Press, Amsterdam, 2002.
- [31] J. I. Cirac, P. Zoller, H. J. Kimble, and H. Mabuchi. Quantum state transfer and entanglement distribution among distant nodes in a quantum network. *Phys. Rev. Lett.*, 78:3221–3224, 1997.
- [32] J. Ignacio Cirac and Peter Zoller. Goals and opportunities in quantum simulation. *Nature Physics*, 8(4):264–266, 2012.
- [33] C. Cohen-Tannoudji, B. Diu, and F. Laloë. *Quantum Mechanics*. Number vol. 1 in A Wiley - Interscience publication. Wiley, 1977.
- [34] C. Cohen-Tannoudji, J. Dupont-Roc, and G. Grynberg. *Photons and Atoms: Introduction to Quantum Electrodynamics*. Wiley, 1989.
- [35] Claude Cohen-Tannoudji, Jacques Dupont-Roc, and Gilbert Grynberg. *Photons and atoms: Introduction to quantum electrodynamics*. Wiley, New York, NY, 1997.
- [36] Larry A. Coldren, Scott W. Corzine, and Milan L. Mashanovitch. *Diode Lasers and Photonic Integrated Circuits*. Wiley-Blackwell, Hoboken, N.J, 2nd edition edition, April 2012.
- [37] S. Cova, M. Ghioni, A. Lacaita, C. Samori, and F. Zappa. Avalanche photodiodes and quenching circuits for single-photon detection. *Appl. Opt.*, 35(12):1956–1976, 1996.
- [38] Adetunmise C. Dada, Jonathan Leach, Gerald S. Buller, Miles J. Padgett, and Erika Andersson. Experimental high-dimensional two-photon entanglement and violations of generalized bell inequalities. *Nature Physics*, 7(9):677–680, 2011.
- [39] B. J. Dalton, Stephen M. Barnett, and B. M. Garraway. Theory of pseudomodes in quantum optical processes. *Phys. Rev. A*, 64:053813, Oct 2001.

- [40] Nathalie P. de Leon, Mikhail D. Lukin, and Hongkun Park. Quantum plasmonic circuits. *IEEE Journal of Selected Topics in Quantum Electronics*, 18(6):1781–1791, 2012.
- [41] D. Deutsch. Quantum theory, the Church-Turing principle and the universal quantum computer. *Proceedings of the Royal Society of London Series A*, 400(1818):97–117, 1985.
- [42] Jerome Dilley, Peter Nisbet-Jones, Bruce W. Shore, and Axel Kuhn. Single-photon absorption in coupled atom-cavity systems. *Phys. Rev. A*, 85:023834, 2012.
- [43] David P DiVincenzo. The physical implementation of quantum computation. *Fortschritte der Physik*, 48(9-11):771–783, 2000.
- [44] Shruti Dogra, John J. McCord, and Gheorghe Sorin Paraoanu. Coherent interaction-free detection of microwave pulses with a superconducting circuit. *Nature Communications*, 13(1):7528, 2022.
- [45] A C Doherty, A S Parkins, S M Tan, and D F Walls. Effects of motion in cavity qed. *Journal of Optics B: Quantum and Semiclassical Optics*, 1(4):475, 1999.
- [46] Thomas H. Doherty, Axel Kuhn, and Ezra Kassa. Multi-resonant open-access microcavity arrays for light matter interaction. *Opt. Express*, 31(4):6342–6355, 2023.
- [47] V. Dorier, J. Lampart, S. Guérin, and H. R. Jauslin. Canonical quantization for quantum plasmonics with finite nanostructures. *Physical Review A*, 100(4), October 2019.
- [48] Vincent Dorier. *Quantum theory of light in linear media : applications to quantum optics and quantum plasmonics*. Theses, Université Bourgogne Franche-Comté, February 2020.
- [49] Vincent Dorier, Stéphane Guérin, and Hans-Rudolf Jauslin. Critical review of quantum plasmonic models for finite-size media. *Nanophotonics*, 9(12):3899–3907, June 2020.
- [50] Vincent Dorier, Stéphane Guérin, and Hans-Rudolf Jauslin. Critical review of quantum plasmonic models for finite-size media. *Nanophotonics*, 9(12):3899–3907, 2020.
- [51] L.-M. Duan, A. Kuzmich, and H. J. Kimble. Cavity qed and quantum-information processing with “hot” trapped atoms. *Phys. Rev. A*, 67:032305, 2003.
- [52] Sergio M. Dutra. *Cavity Quantum Electrodynamics: The Strange Theory of Light in a Box*. Wiley Series in Lasers and Applications. Wiley, Hoboken, NJ, 2005.
- [53] H. S. Eisenberg, J. F. Hodelin, G. Khoury, and D. Bouwmeester. Multiphoton path entanglement by nonlocal bunching. *Phys. Rev. Lett.*, 94:090502, 2005.

- [54] R.R. Ernst, G. Bodenhausen, and A. Wokaun. *Principles of Nuclear Magnetic Resonance in One and Two Dimensions*. International series of monographs on chemistry. Clarendon Press, 1990.
- [55] Mark S. Everitt and Barry M. Garraway. Multiphoton resonances for all-optical quantum logic with multiple cavities. *Phys. Rev. A*, 90:012335, 2014.
- [56] N. Fabre, A. Keller, and P. Milman. Wigner distribution on a double-cylinder phase space for studying quantum error-correction protocols. *Phys. Rev. A*, 102:022411, Aug 2020.
- [57] C. Fabry and A. Pérot. Théorie et applications d 'une nouvelle méthode de spectroscopie interférentielle. *Ann. de Chim. et de Phys.*, 16(7):115, 1899.
- [58] James S. Fakonas, Hyunseok Lee, Yousif A. Kelaita, and Harry A. Atwater. Two-plasmon quantum interference. *Nature Photonics*, 8(4):317–320, Apr 2014.
- [59] M Federico, V Dorier, S Guérin, and H R Jauslin. Space-time propagation of photon pulses in dielectric media, illustrations with beam splitters. *Journal of Physics B: Atomic, Molecular and Optical Physics*, 55(17):174002, aug 2022.
- [60] M Federico and H R Jauslin. Isomorphism between the białynicki-birula and the landau-peierls fock space quantization of the electromagnetic field in position representation. *Journal of Physics A: Mathematical and Theoretical*, 56(23):235302, may 2023.
- [61] M. Federico and H. R. Jauslin. Nonlocality of the energy density for all single-photon states. *Phys. Rev. A*, 108:043720, Oct 2023.
- [62] Xiao-Ping Feng. Theory of short optical cavity with dielectric multilayer film mirrors. *Optics Communications*, 83(1):162–176, May 1991.
- [63] Richard P. Feynman. Simulating physics with computers. *International Journal of Theoretical Physics*, 21(6):467–488, 1982.
- [64] M. Fleischhauer, S.F. Yelin, and M.D. Lukin. How to trap photons? storing single-photon quantum states in collective atomic excitations1this paper is dedicated to marlan o. scully on the occasion of his 60th birthday. we are grateful to him for introducing us to this exciting field and for his continuous inspiration and encouragement.1. *Optics Communications*, 179(1):395–410, 2000.
- [65] R. Foord, R. Jones, C. J. Oliver, and E. R. Pike. The use of photomultiplier tubes for photon counting. *Appl. Opt.*, 8(10):1975–1989, 1969.
- [66] P. Forn-Díaz, L. Lamata, E. Rico, J. Kono, and E. Solano. Ultrastrong coupling regimes of light-matter interaction. *Rev. Mod. Phys.*, 91:025005, 2019.
- [67] Louis Garbe, Matteo Bina, Arne Keller, Matteo G. A. Paris, and Simone Felicetti. Critical quantum metrology with a finite-component quantum phase transition. *Phys. Rev. Lett.*, 124:120504, Mar 2020.

- [68] Sébastien Garcia, Francesco Ferri, Jakob Reichel, and Romain Long. Overlapping two standing waves in a microcavity for a multi-atom photon interface. *Optics Express*, 28(10):15515, may 2020.
- [69] C. W. Gardiner and P. Zoller. *Quantum Noise*. Springer, third edition, 2004.
- [70] J. Garrison and R. Chiao. *Quantum Optics*. Oxford Graduate Texts. OUP Oxford, 2008.
- [71] Klaus M Gheri, Klaus Ellinger, Thomas Pellizzari, and Peter Zoller. Photon-wavepackets as flying quantum bits. *Fortschritte der Physik*, 46(4-5):401–415, 1998.
- [72] Gian Luca Giorgi, Astghik Saharyan, Stéphane Guérin, Dominique Sugny, and Bruno Bellomo. Microscopic and phenomenological models of driven systems in structured reservoirs. *Phys. Rev. A*, 101:012122, Jan 2020.
- [73] Steffen J. Glaser, Ugo Boscain, Tommaso Calarco, Christiane P. Koch, Walter Köckenberger, Ronnie Kosloff, Ilya Kuprov, Burkhard Luy, Sophie Schirmer, Thomas Schulte-Herbrüggen, Dominique Sugny, and Frank K. Wilhelm. Training schrödinger’s cat: quantum optimal control. *The European Physical Journal D*, 69(12):279, 2015.
- [74] A. Gogyan, S. Guérin, H.-R. Jauslin, and Yu. Malakyan. Deterministic source of a train of indistinguishable single-photon pulses with a single-atom-cavity system. *Phys. Rev. A*, 82:023821, Aug 2010.
- [75] G. N. Gol’tsman, O. Okunev, G. Chulkova, A. Lipatov, A. Semenov, K. Smirnov, B. Voronov, A. Dzardanov, C. Williams, and Roman Sobolewski. Picosecond superconducting single-photon optical detector. *Applied Physics Letters*, 79(6):705–707, 08 2001.
- [76] P. Goy, J. M. Raimond, M. Gross, and S. Haroche. Observation of cavity-enhanced single-atom spontaneous emission. *Phys. Rev. Lett.*, 50:1903–1906, 1983.
- [77] R. Graham and H. Haken. Quantum theory of light propagation in a fluctuating laser-active medium. *Zeitschrift für Physik A Hadrons and nuclei*, 213(5):420–450, Oct 1968.
- [78] T. M. Graham, M. Kwon, B. Grinkemeyer, Z. Marra, X. Jiang, M. T. Lichtman, Y. Sun, M. Ebert, and M. Saffman. Rydberg-mediated entanglement in a two-dimensional neutral atom qubit array. *Phys. Rev. Lett.*, 123:230501, 2019.
- [79] David Griffiths and Stephen Walborn. Dirac deltas and discontinuous functions. *American Journal of Physics*, 67(5):446–447, 05 1999.
- [80] David J. Griffiths. *Introduction to Electrodynamics*. Prentice Hall, 3rd ed edition, 1999.
- [81] Laszlo Gyongyosi and Sandor Imre. Opportunistic entanglement distribution for the quantum internet. *Scientific Reports*, 9, 2019.

- [82] Robert H. Hadfield. Single-photon detectors for optical quantum information applications. *Nature Photonics*, 3(12):696–705, 2009.
- [83] Serge Haroche and Daniel Kleppner. Cavity Quantum Electrodynamics. *Physics Today*, 42(1):24–30, 1989.
- [84] Philipp Hauke, Fernando M Cucchietti, Luca Tagliacozzo, Ivan Deutsch, and Maciej Lewenstein. Can one trust quantum simulators? *Reports on Progress in Physics*, 75(8):082401, 2012.
- [85] Christina J. Hood, H. J. Kimble, and Jun Ye. Characterization of high-finesse mirrors: Loss, phase shifts, and mode structure in an optical cavity. *Phys. Rev. A*, 64(3):033804, August 2001.
- [86] Bruno Huttner and Stephen M. Barnett. Quantization of the electromagnetic field in dielectrics. *Physical Review A*, 46(7):4306–4322, October 1992.
- [87] D. Jaksch, J. I. Cirac, P. Zoller, S. L. Rolston, R. Côté, and M. D. Lukin. Fast quantum gates for neutral atoms. *Phys. Rev. Lett.*, 85:2208–2211, 2000.
- [88] E.T. Jaynes and F.W. Cummings. Comparison of quantum and semiclassical radiation theories with application to the beam maser. *Proceedings of the IEEE*, 51(1):89–109, 1963.
- [89] S. Johnson, P. R. Dolan, T. Grange, A. A. P. Trichet, G. Hornecker, Y. C. Chen, L. Weng, G. M. Hughes, A. A. R. Watt, A. Auffèves, and J. M. Smith. Tunable cavity coupling of the zero phonon line of a nitrogen-vacancy defect in diamond. *New J. Phys.*, 17(12):122003, December 2015.
- [90] Tomi H. Johnson, Stephen R. Clark, and Dieter Jaksch. What is a quantum simulator? *EPJ Quantum Technology*, 1(1):10, 2014.
- [91] Seok-Min Jung and Kwang-Seok Yun. Energy-harvesting device with mechanical frequency-up conversion mechanism for increased power efficiency and wideband operation. *Applied Physics Letters*, 96(11):111906, 2010.
- [92] B. E. Kardynał, S. S. Hees, A. J. Shields, C. Nicoll, I. Farrer, and D. A. Ritchie. Photon number resolving detector based on a quantum dot field effect transistor. *Applied Physics Letters*, 90(18):181114, 2007.
- [93] Ivan Kassal, James D. Whitfield, Alejandro Perdomo-Ortiz, Man-Hong Yung, and Alán Aspuru-Guzik. Simulating chemistry using quantum computers. *Annual Review of Physical Chemistry*, 62(1):185–207, 2011. PMID: 21166541.
- [94] M. A. Kastner. The single-electron transistor. *Rev. Mod. Phys.*, 64:849–858, 1992.
- [95] M Keller, B Lange, K Hayasaka, W Lange, and H Walther. A calcium ion in a cavity as a controlled single-photon source. *New Journal of Physics*, 6:95–95, jul 2004.
- [96] Timothy E. Keller and Morton H. Rubin. Theory of two-photon entanglement for spontaneous parametric down-conversion driven by a narrow pump pulse. *Phys. Rev. A*, 56:1534–1541, 1997.

- [97] Andreas M. Kern, Dai Zhang, Marc Brecht, Alexey I. Chizhik, Antonio Virgilio Failla, Frank Wackenhut, and Alfred J. Meixner. Enhanced single-molecule spectroscopy in highly confined optical fields: From $\lambda/2$ -Fabry–Pérot resonators to plasmonic nano-antennas. *Chem. Soc. Rev.*, 43(4):1263–1286, January 2014.
- [98] H J Kimble. Strong interactions of single atoms and photons in cavity qed. *Physica Scripta*, 1998(T76):127, 1998.
- [99] H. J. Kimble. The quantum internet. *Nature*, 453(7198):1023–1030, 2008.
- [100] E Knill, R Laflamme, and GJ Milburn. A scheme for efficient quantum computation with linear optics. *Nature*, 409(6816):46–52, 2001.
- [101] L. Knöll, W. Vogel, and D.-G. Welsch. Resonators in quantum optics: A first-principles approach. *Phys. Rev. A*, 43:543–553, Jan 1991.
- [102] P. Kómár, E. M. Kessler, M. Bishof, L. Jiang, A. S. Sørensen, J. Ye, and M. D. Lukin. A quantum network of clocks. *Nature Physics*, 10(8):582–587, 2014.
- [103] Anna Kowalewska-kudlaszyk and Ryszard Tanaś. Generalized master equation for a two-level atom in a strong field and tailored reservoirs. *Journal of Modern Optics*, 48(2):347–370, 2001.
- [104] Stefan Krastanov, Kurt Jacobs, Gerald Gilbert, Dirk R. Englund, and Mikkel Heuck. Controlled-phase gate by dynamic coupling of photons to a two-level emitter. *npj Quantum Information*, 8(1):103, Sep 2022.
- [105] Hanna Krauter, Christine A. Muschik, Kasper Jensen, Wojciech Wasilewski, Jonas M. Petersen, J. Ignacio Cirac, and Eugene S. Polzik. Entanglement generated by dissipation and steady state entanglement of two macroscopic objects. *Phys. Rev. Lett.*, 107:080503, Aug 2011.
- [106] Philip Trøst Kristensen and Stephen Hughes. Modes and mode volumes of leaky optical cavities and plasmonic nanoresonators. *ACS Photonics*, 1(1):2–10, Jan 2014.
- [107] Philip Trøst Kristensen, C. Van Vlack, and S. Hughes. Generalized effective mode volume for leaky optical cavities. *Optics Letters*, 37(10):1649–1651, 2012.
- [108] A. Kuhn, M. Hennrich, T. Bundo, and G. Rempe. Controlled generation of single photons from a strongly coupled atom-cavity system. *Applied Physics B*, 69(5):373–377, 1999.
- [109] Axel Kuhn, Markus Hennrich, and Gerhard Rempe. Deterministic single-photon source for distributed quantum networking. *Phys. Rev. Lett.*, 89:067901, 2002.
- [110] Axel Kuhn, Jason Smith, Matthias Keller, and David M. Lucas. Short roadmap to quantum networking. https://www.physics.ox.ac.uk/system/files/file_attachments/roadmap-to-quantum-networking-44796.pdf.

- [111] Onur Kuzucu, Marco Fiorentino, Marius A. Albota, Franco N. C. Wong, and Franz X. Kärtner. Two-photon coincident-frequency entanglement via extended phase matching. *Phys. Rev. Lett.*, 94:083601, 2005.
- [112] Paul G. Kwiat, Klaus Mattle, Harald Weinfurter, Anton Zeilinger, Alexander V. Sergienko, and Yanhua Shih. New high-intensity source of polarization-entangled photon pairs. *Phys. Rev. Lett.*, 75:4337–4341, 1995.
- [113] Paul G Kwiat and Harald Weinfurter. Embedded bell-state analysis. *Physical Review A*, 58(4):R2623, 1998.
- [114] X. Lacour, S. Guérin, and H. R. Jauslin. Optimized adiabatic passage with dephasing. *Phys. Rev. A*, 78:033417, Sep 2008.
- [115] L.D. Landau and E.M. Lifshitz. *Quantum Mechanics: Non-Relativistic Theory*. Teoreticheskai fizika. Elsevier Science, 2013.
- [116] M. Lapert, E. Assémat, S. J. Glaser, and D. Sugny. Understanding the global structure of two-level quantum systems with relaxation: Vector fields organized through the magic plane and the steady-state ellipsoid. *Phys. Rev. A*, 88:033407, Sep 2013.
- [117] C. K. Law and H. J. Kimble. Deterministic generation of a bit-stream of single-photon pulses. *Journal of Modern Optics*, 44(11-12):2067–2074, 1997.
- [118] Changhyoup Lee, Benjamin Lawrie, Raphael Pooser, Kwang-Geol Lee, Carsten Rockstuhl, and Mark Tame. Quantum plasmonic sensors. *Chemical Reviews*, 121(8):4743–4804, 2021.
- [119] D. Leibfried, M. D. Barrett, T. Schaetz, J. Britton, J. Chiaverini, W. M. Itano, J. D. Jost, C. Langer, and D. J. Wineland. Toward heisenberg-limited spectroscopy with multiparticle entangled states. *Science*, 304(5676):1476–1478, 2004.
- [120] M.H. Levitt. *Spin Dynamics: Basics of Nuclear Magnetic Resonance*. Wiley, 2013.
- [121] Maciej Lewenstein, Anna Sanpera, Veronica Ahufinger, Bogdan Damski, Aditi Sen(De), and Ujjwal Sen. Ultracold atomic gases in optical lattices: mimicking condensed matter physics and beyond. *Advances in Physics*, 56(2):243–379, 2007.
- [122] Ying Li, Peter C. Humphreys, Gabriel J. Mendoza, and Simon C. Benjamin. Resource costs for fault-tolerant linear optical quantum computing. *Phys. Rev. X*, 5:041007, 2015.
- [123] Seth Lloyd. Universal quantum simulators. *Science*, 273(5278):1073–1078, 1996.
- [124] Peter Lodahl, Arne Ludwig, and Richard J. Warburton. A deterministic source of single photons. *Physics Today*, 75(3):44–50, 03 2022.

- [125] Vivien Loo, Loïc Lanco, Aristide Lemaître, Isabelle Sagnes, Olivier Krebs, Paul Voisin, and Pascale Senellart. Quantum dot-cavity strong-coupling regime measured through coherent reflection spectroscopy in a very high-q micropillar. *Applied Physics Letters*, 97(24):241110, dec 2010.
- [126] E. D. Lopaeva, I. Ruo Berchera, I. P. Degiovanni, S. Olivares, G. Brida, and M. Genovese. Experimental realization of quantum illumination. *Phys. Rev. Lett.*, 110:153603, 2013.
- [127] William H. Louisell. *Quantum statistical properties of radiation*. Wiley, 1973.
- [128] Dawei Lu, Boruo Xu, Nanyang Xu, Zhaokai Li, Hongwei Chen, Xinhua Peng, Ruixue Xu, and Jiangfen Du. Quantum chemistry simulation on quantum computers: theories and experiments. *Phys. Chem. Chem. Phys.*, 14:9411–9420, 2012.
- [129] H. Mabuchi, Q. A. Turchette, M. S. Chapman, and H. J. Kimble. Real-time detection of individual atoms falling through a high-finesse optical cavity. *Opt. Lett.*, 21(17):1393–1395, 1996.
- [130] H. A Macleod. *Thin-Film Optical Filters*. Institute of Physics Publishing, 2018.
- [131] Matthias Mader, Jakob Reichel, Theodor W. Hänsch, and David Hunger. A scanning cavity microscope. *Nature Communications*, 6(1):7249, June 2015.
- [132] X. Maître, E. Hagle, G. Nogues, C. Wunderlich, P. Goy, M. Brune, J. M. Raimond, and S. Haroche. Quantum memory with a single photon in a cavity. *Phys. Rev. Lett.*, 79:769–772, 1997.
- [133] L. Mandel. Configuration-space photon number operators in quantum optics. *Phys. Rev.*, 144:1071–1077, Apr 1966.
- [134] D. Marcos, M. Wubs, J. M. Taylor, R. Aguado, M. D. Lukin, and A. S. Sørensen. Coupling nitrogen-vacancy centers in diamond to superconducting flux qubits. *Phys. Rev. Lett.*, 105:210501, 2010.
- [135] Francois Marquier, Christophe Sauvan, and Jean-Jacques Greffet. Revisiting quantum optics with surface plasmons and plasmonic resonators. *ACS Photonics*, 4(9):2091–2101, Sep 2017.
- [136] Andreas Maser, Benjamin Gmeiner, Tobias Utikal, Stephan Götzinger, and Vahid Sandoghdar. Few-photon coherent nonlinear optics with a single molecule. *Nature Photonics*, 10(7):450–453, Jul 2016.
- [137] J. McKeever, J. R. Buck, A. D. Boozer, A. Kuzmich, H.-C. Nägerl, D. M. Stamper-Kurn, and H. J. Kimble. State-insensitive cooling and trapping of single atoms in an optical cavity. *Phys. Rev. Lett.*, 90:133602, 2003.
- [138] Rodney Van Meter and Joe Touch. Designing quantum repeater networks. *IEEE Communications Magazine*, 51(8):64–71, 2013.
- [139] Pierre Meystre. Theoretical developments in cavity quantum optics: a brief review. *Physics Reports*, 219(3):243–262, 1992.

- [140] C. Monroe. Quantum information processing with atoms and photons. *Nature*, 416(6877):238–246, 2002.
- [141] Paul-Antoine Moreau, Ermes Toninelli, Thomas Gregory, and Miles J. Padgett. Imaging with quantum states of light. *Nature Reviews Physics*, 1(6):367–380, 2019.
- [142] Iii Sargent Murray, Marlan O. Scully, and Jr. Lamb Willis E. *Laser Physics*. Avalon Publishing, 1978.
- [143] Peter B R Nisbet-Jones, Jerome Dilley, Daniel Ljunggren, and Axel Kuhn. Highly efficient source for indistinguishable single photons of controlled shape. *New Journal of Physics*, 13(10):103036, 2011.
- [144] G. Nogues, A. Rauschenbeutel, S. Osnaghi, M. Brune, J. M. Raimond, and S. Haroche. Seeing a single photon without destroying it. *Nature*, 400(6741):239–242, 1999.
- [145] Stefan Nußmann, Karim Murr, Markus Hijlkema, Bernhard Weber, Axel Kuhn, and Gerhard Rempe. Vacuum-stimulated cooling of single atoms in three dimensions. *Nature Physics*, 1(2):122–125, 2005.
- [146] A. Orioux, A. Eckstein, A. Lemaître, P. Filloux, I. Favero, G. Leo, T. Coudreau, A. Keller, P. Milman, and S. Ducci. Direct bell states generation on a iii-v semiconductor chip at room temperature. *Phys. Rev. Lett.*, 110:160502, Apr 2013.
- [147] T. Pellizzari, S. A. Gardiner, J. I. Cirac, and P. Zoller. Decoherence, continuous observation, and quantum computing: A cavity qed model. *Phys. Rev. Lett.*, 75:3788–3791, 1995.
- [148] P. W. H. Pinkse, T. Fischer, P. Maunz, and G. Rempe. Trapping an atom with single photons. *Nature*, 404(6776):365–368, 2000.
- [149] Graeme Pleasance, Barry M. Garraway, and Francesco Petruccione. Generalized theory of pseudomodes for exact descriptions of non-markovian quantum processes. *Phys. Rev. Res.*, 2:043058, Oct 2020.
- [150] Nina Podoliak, Hiroki Takahashi, Matthias Keller, and Peter Horak. Comparative numerical studies of ion traps with integrated optical cavities. *Phys. Rev. Appl.*, 6:044008, 2016.
- [151] E.M. Purcell. Proceedings of the american physical society. *Physical Review*, 69(11-12):681, B10, 1946.
- [152] A. Rauschenbeutel, G. Nogues, S. Osnaghi, P. Bertet, M. Brune, J. M. Raimond, and S. Haroche. Coherent operation of a tunable quantum phase gate in cavity qed. *Phys. Rev. Lett.*, 83:5166–5169, 1999.
- [153] M. G. Raymer and C. J. McKinstrie. Quantum input-output theory for optical cavities with arbitrary coupling strength: Application to two-photon wave-packet shaping. *Phys. Rev. A*, 88:043819, Oct 2013.

- [154] Dileep V. Reddy and Michael G. Raymer. Photonic temporal-mode multiplexing by quantum frequency conversion in a dichroic-finesse cavity. *Opt. Express*, 26(21):28091–28103, Oct 2018.
- [155] Andreas Reiserer. Colloquium: Cavity-enhanced quantum network nodes. *Rev. Mod. Phys.*, 94:041003, 2022.
- [156] Gerhard Rempe, Herbert Walther, and Norbert Klein. Observation of quantum collapse and revival in a one-atom maser. *Phys. Rev. Lett.*, 58:353–356, 1987.
- [157] Benjamin Rousseaux. *Control for quantum technologies at the nanoscale*. Theses, Université de Bourgogne Franche-Comté, November 2016.
- [158] Morton H. Rubin, David N. Klyshko, Y. H. Shih, and A. V. Sergienko. Theory of two-photon entanglement in type-ii optical parametric down-conversion. *Phys. Rev. A*, 50:5122–5133, 1994.
- [159] M. Saffman, T. G. Walker, and K. Mølmer. Quantum information with rydberg atoms. *Rev. Mod. Phys.*, 82:2313–2363, 2010.
- [160] A. Saharyan, B. Rousseaux, Z. Kis, S. Stryzhenko, and S. Guérin. Propagating single photons from an open cavity: Description from universal quantization. *Phys. Rev. Res.*, 5:033056, Jul 2023.
- [161] Astghik Saharyan, Juan-Rafael Álvarez, Thomas H. Doherty, Axel Kuhn, and Stéphane Guérin. Light-matter interaction in open cavities with dielectric stacks. *Applied Physics Letters*, 118(15):154002, 2021.
- [162] Astghik Saharyan, Juan-Rafael Álvarez, Axel Kuhn, and Stéphane Guérin. Effective models for quantum optics with multilayer open cavities. *to be submitted*.
- [163] A.I. Saichev and W. Woyczynski. *Distributions in the Physical and Engineering Sciences, Volume 1: Distributional and Fractal Calculus, Integral Transforms and Wavelets*. Birkhäuser Boston, 1997.
- [164] Bahaa EA Saleh and Malvin Carl Teich. *Fundamentals of Photonics*, volume 22. John Wiley & Sons, 1991.
- [165] Nicolas Sangouard, Christoph Simon, Hugues de Riedmatten, and Nicolas Gisin. Quantum repeaters based on atomic ensembles and linear optics. *Rev. Mod. Phys.*, 83:33–80, 2011.
- [166] Simeon Sauer, Clemens Gneiting, and Andreas Buchleitner. Stabilizing entanglement in the presence of local decay processes. *Phys. Rev. A*, 89:022327, Feb 2014.
- [167] C. Sauvan, J. P. Hugonin, I. S. Maksymov, and P. Lalanne. Theory of the spontaneous optical emission of nanosize photonic and plasmon resonators. *Phys. Rev. Lett.*, 110:237401, Jun 2013.
- [168] Romana Schirhagl, Kevin Chang, Michael Loretz, and Christian L. Degen. Nitrogen-vacancy centers in diamond: Nanoscale sensors for physics and biology. *Annual Review of Physical Chemistry*, 65(1):83–105, 2014. PMID: 24274702.

- [169] Claude Elwood Shannon. A mathematical theory of communication. *The Bell System Technical Journal*, 27:379–423, 623–656, 1948.
- [170] H. Z. Shen, M. Qin, Xiao-Ming Xiu, and X. X. Yi. Exact non-markovian master equation for a driven damped two-level system. *Phys. Rev. A*, 89:062113, Jun 2014.
- [171] Peter W. Shor. Scheme for reducing decoherence in quantum computer memory. *Phys. Rev. A*, 52:R2493–R2496, 1995.
- [172] Peter W. Shor. Polynomial-time algorithms for prime factorization and discrete logarithms on a quantum computer. *SIAM Journal on Computing*, 26(5):1484–1509, 1997.
- [173] Bruce W Shore. *Manipulating quantum structures using laser pulses*. Cambridge University Press, 2011.
- [174] William T. Silfvast. *Laser Fundamentals*. Cambridge University Press, Cambridge ; New York, second edition edition, September 2008.
- [175] Marcus Silva, Martin Rötteler, and Christof Zalka. Thresholds for linear optics quantum computing with photon loss at the detectors. *Phys. Rev. A*, 72:032307, 2005.
- [176] M P Silveri, J A Tuorila, E V Thuneberg, and G S Paraoanu. Quantum systems under frequency modulation. *Reports on Progress in Physics*, 80(5):056002, 2017.
- [177] Sergei Slussarenko and Geoff J. Pryde. Photonic quantum information processing: A concise review. *Applied Physics Reviews*, 6(4):041303, 2019.
- [178] A. M. Steane. Error correcting codes in quantum theory. *Phys. Rev. Lett.*, 77:793–797, 1996.
- [179] Alexander Streltsov, Gerardo Adesso, and Martin B. Plenio. Colloquium: Quantum coherence as a resource. *Rev. Mod. Phys.*, 89:041003, Oct 2017.
- [180] Y. Suematsu, S. Arai, and K. Kishino. Dynamic single-mode semiconductor lasers with a distributed reflector. *Journal of Lightwave Technology*, 1(1):161–176, March 1983.
- [181] M. S. Tame, K. R. McEnery, Ş K. Özdemir, J. Lee, S. A. Maier, and M. S. Kim. Quantum plasmonics. *Nature Physics*, 9(6):329–340, Jun 2013.
- [182] Frank Arute *et al.* Quantum supremacy using a programmable superconducting processor. *Nature*, 574(7779):505–510, 2019.
- [183] Klaas Bergmann *et al.* Roadmap on stirap applications. *Journal of Physics B: Atomic, Molecular and Optical Physics*, 52(20):202001, 2019.
- [184] Yong Yu *et al.* Entanglement of two quantum memories via fibres over dozens of kilometres. *Nature*, 578(7794):240+, 2020.

- [185] R. J. Thompson, G. Rempe, and H. J. Kimble. Observation of normal-mode splitting for an atom in an optical cavity. *Phys. Rev. Lett.*, 68:1132–1135, 1992.
- [186] A. A. P. Trichet, P. R. Dolan, D. James, G. M. Hughes, C. Vallance, and J. M. Smith. Nanoparticle Trapping and Characterization Using Open Microcavities. *Nano Lett.*, 16(10):6172–6177, October 2016.
- [187] Christos Tserkezis, Antonio I Fernández-Domínguez, P A D Gonçalves, Francesco Todisco, Joel D Cox, Kurt Busch, Nicolas Stenger, Sergey I Bozhevolnyi, N Asger Mortensen, and Christian Wolff. On the applicability of quantum-optical concepts in strong-coupling nanophotonics. *Reports on Progress in Physics*, 83(8):082401, jul 2020.
- [188] Kikuo Ujihara, Atsushi Nakamura, Osamu Manba, and Xiao-Ping Feng. Spontaneous Emission in a Very Short Optical Cavity with Plane-Parallel Dielectric Mirrors. *Jpn. J. Appl. Phys.*, 30(12R):3388, December 1991.
- [189] Kerry J. Vahala. Optical microcavities. *Nature*, 424(6950):839–846, August 2003.
- [190] Leo Van-Damme, Daniel Schraft, Genko T. Genov, Dominique Sugny, Thomas Halfmann, and Stéphane Guérin. Robust not gate by single-shot-shaped pulses: Demonstration of the efficiency of the pulses in rephasing atomic coherences. *Phys. Rev. A*, 96:022309, 2017.
- [191] S. J. van Enk, J. I. Cirac, and P. Zoller. Purifying two-bit quantum gates and joint measurements in cavity qed. *Phys. Rev. Lett.*, 79:5178–5181, 1997.
- [192] S. J. van Enk, H. J. Kimble, and H. Mabuchi. Quantum information processing in cavity-qed. *Quantum Information Processing*, 3(1):75–90, 2004.
- [193] Rodney Van Meter and Simon J. Devitt. The path to scalable distributed quantum computing. *Computer*, 49(9):31–42, 2016.
- [194] H. Varguet, A. A. Díaz-Valles, S. Guérin, H. R. Jauslin, and G. Colas des Francs. Collective strong coupling in a plasmonic nanocavity. *The Journal of Chemical Physics*, 154(8):084303, 02 2021.
- [195] Genko S Vasilev, Daniel Ljunggren, and Axel Kuhn. Single photons made-to-measure. *New Journal of Physics*, 12(6):063024, 2010.
- [196] M. Vengalattore, J. M. Higbie, S. R. Leslie, J. Guzman, L. E. Sadler, and D. M. Stamper-Kurn. High-resolution magnetometry with a spinor bose-einstein condensate. *Phys. Rev. Lett.*, 98:200801, 2007.
- [197] Frank Verstraete, Michael M. Wolf, and J. Ignacio Cirac. Quantum computation and quantum-state engineering driven by dissipation. *Nature Physics*, 5(9):633–636, Sep 2009.
- [198] Nikolay V Vitanov, Thomas Halfmann, Bruce W Shore, and Klaas Bergmann. Laser-induced population transfer by adiabatic passage techniques. *Annual Review of Physical Chemistry*, 52(1):763–809, 2001. PMID: 11326080.

- [199] Nikolay V. Vitanov, Andon A. Rangelov, Bruce W. Shore, and Klaas Bergmann. Stimulated raman adiabatic passage in physics, chemistry, and beyond. *Rev. Mod. Phys.*, 89:015006, 2017.
- [200] Nikolay V. Vitanov, Andon A. Rangelov, Bruce W. Shore, and Klaas Bergmann. Stimulated raman adiabatic passage in physics, chemistry, and beyond. *Rev. Mod. Phys.*, 89:015006, 2017.
- [201] Werner Vogel and Dirk-Gunnar Welsch. *Quantum Optics*. Wiley, first edition, May 2006.
- [202] Jelena Vučković, Marko Lončar, Hideo Mabuchi, and Axel Scherer. Design of photonic crystal microcavities for cavity qed. *Phys. Rev. E*, 65:016608, 2001.
- [203] Herbert Walther, Benjamin T H Varcoe, Berthold-Georg Englert, and Thomas Becker. Cavity quantum electrodynamics. *Reports on Progress in Physics*, 69(5):1325, 2006.
- [204] U. Weiss. *Quantum Dissipative Systems*. G - Reference, Information and Interdisciplinary Subjects Series. World Scientific, 2012.
- [205] J. Ye, D. W. Vernooy, and H. J. Kimble. Trapping of single atoms in cavity qed. *Phys. Rev. Lett.*, 83:4987–4990, 1999.
- [206] J. Q. You and Franco Nori. Atomic physics and quantum optics using superconducting circuits. *Nature*, 474(7353):589–597, 2011.
- [207] Pan Zhong, Wu Rong-han, and Wang Qi-ming. Effective cavity length in vertical cavity surface emitting laser. *Acta Physica Sinica (Overseas Edition)*, 4(11):810–815, November 1995.
- [208] Jing-jun Zhu, Kaipeng Liu, Xi Chen, and Stéphane Guérin. Optimal control and ultimate bounds of 1:2 nonlinear quantum systems. *Phys. Rev. A*, 108:042610, Oct 2023.

Titre : Modèles effectifs pour l'optique quantique à photon unique

Mots clés : Optique quantique, cavité QED, photons uniques

Résumé : Au cours des dernières décennies, l'optique quantique a évolué des cavités à facteur de qualité élevé des premières expériences vers de nouvelles conceptions de cavités impliquant des modes à fuite. Bien que les modèles utilisés dans des expériences standard soient efficaces pour reproduire leurs résultats, les fuites de photons sont la plupart du temps traitées de manière phénoménologique ce qui limite l'interprétation des résultats et ne permet pas une étude systématique. Dans ce manuscrit, nous adoptons une approche différente et, à partir des premiers principes, nous dérivons des modèles effectifs qui permettent la caractérisation complète d'un photon unique produit dans la cavité et se propageant dans l'espace libre. Nous proposons un schéma atome-cavité pour la génération de photons uniques et analysons rigoureusement le photon unique sortant dans les domaines temporel et fréquentiel pour différents régimes de couplage. Nous étendons l'analyse en étudiant des modèles de cavités plus réalistes, prenant notamment en compte la structure diélectrique multicouche des miroirs de la cavité.

Nous évaluons la force du couplage dipolaire entre un seul émetteur et le champ de rayonnement dans une telle cavité optique. Notre modèle permet de faire varier librement la fréquence de résonance de la cavité, la fréquence de la transition lumineuse ou atomique, ainsi que la longueur d'onde associée à la mise en forme du miroir diélectrique. En particulier, nous montrons qu'en raison des effets induits par la nature multicouche du miroir de la cavité, même dans le régime de cavité à haute finesse tel que défini habituellement, la description du système cavité-réservoir peut différer de celle où la structure du miroir est négligée. Pour les cavités très courtes, la longueur effective utilisée pour déterminer le volume du mode de la cavité et les longueurs définissant les résonances sont différentes, et diffèrent notablement de la longueur géométrique de la cavité. Sur la base de ces résultats, nous définissons une fonction de réponse généralisée de la cavité et une fonction de couplage cavité-réservoir, qui tiennent compte de la structure géométrique du miroir de la cavité.

Title: Effective models for single-photon quantum optics

Keywords: Quantum optics, cavity QED, single photons

Abstract: Over the last decades, quantum optics has evolved from high-quality-factor cavities in the early experiments toward new cavity designs involving leaky modes. Despite efficient models to describe standard experiments, photon leakage is most of the time treated phenomenologically, which restricts the interpretation of the results and does not allow systematic studies. In this manuscript, we take a different approach, and starting from first principles, we derive effective models that allow complete characterization of a leaking single photon produced in the cavity and propagating in free space. We propose an atom-cavity scheme for single-photon generation, and we rigorously analyze the outgoing single photon in time and frequency domains for different coupling regimes. We extend the analysis by studying more realistic cavity models, namely taking into account the multilayer dielectric structure of cavity mirrors. We evaluate the dipole coupling strength between a

single emitter and the radiation field within such an optical cavity. Our model allows one to freely vary the resonance frequency of the cavity, the frequency of light or atomic transition addressing it, and the design wavelength of the dielectric mirror. In particular, we show that due to the effects induced by the multilayer nature of the cavity mirror, even in the standardly defined high-finesse cavity regime, the cavity-reservoir system description might differ from the one where the structure of the mirror is neglected. For very short cavities, the effective length used to determine the cavity mode volume and the lengths defining the resonances are different, and also found to diverge appreciably from the geometric length of the cavity. Based on these results, we define a generalized cavity response function and cavity-reservoir coupling function, which account for the geometric structure of the cavity mirror.